Theoretical & Phenomenological Explorations of the Dark Sector

HARVARD UNIVERSITY
Graduate School of Arts and Sciences

DISSERTATION ACCEPTANCE CERTIFICATE

The undersigned, appointed by the

Department of Physics

have examined a dissertation entitled

Theoretical & Phenomenological Explorations of the Dark Sector

presented by Aditya Deepak Parikh

candidate for the degree of Doctor of Philosophy and hereby certify that it is worthy of acceptance.

Signature Matthew B. Reece

Typed name: Professor Matthew Reece, Chair

Signature _____

Typed name: Professor Melissa Franklin

Signature Cora Dvorkin

Typed name: Professor Cora Dvorkin

Date: April 18, 2022

Theoretical & Phenomenological Explorations of the Dark Sector

A DISSERTATION PRESENTED
BY
ADITYA DEEPAK PARIKH
TO
THE DEPARTMENT OF PHYSICS

IN PARTIAL FULFILLMENT OF THE REQUIREMENTS
FOR THE DEGREE OF
DOCTOR OF PHILOSOPHY
IN THE SUBJECT OF
PHYSICS

HARVARD UNIVERSITY
CAMBRIDGE, MASSACHUSETTS

APRIL 2022

Thesis advisor: Professor Matthew Reece Aditya Deepak Parikh

Theoretical & Phenomenological Explorations of the Dark Sector

Abstract

The particle nature of dark matter and its interactions are issues of central importance with the current understanding of particle physics and clearly indicate the need to go beyond the Standard Model. The lack of detection of a WIMP has spurred both experimental and theoretical innovation. A wide array of direct and indirect detection techniques have vastly expanded the experimentally probed parameter space. This includes small tabletop experiments, large underground detectors, and ground- and space-based telescopes searching for astrophysical and cosmological signals. In conjunction, theorists have gone beyond the standard dark matter scenario by adding new fields, interactions, and portals connecting to the Standard Model. The rich phenomenology associated with these models predict novel signatures and the experimental data provide exciting avenues to search for signs of new physics.

In this dissertation, we present progress on exploring dark sector and BSM phenomenology from various lenses. In the most dire scenarios, dark matter does not couple to the Standard Model and only possesses self-interactions. Despite this, the underlying interactions produce cross sections which exhibit significantly different behaviors as a function of velocity. We develop a formalism to compute the cross section, that carefully matches the effective quantum mechanics and QFT descriptions, and

takes into account Sommerfeld enhancement, a non-perturbative effect relevant in the nonrelativistic regime. We find that pseudoscalar and axial-vector type interactions don't exhibit this enhancement. This formalism consistently deals with the pseudoscalar potential, which a priori seems singular. This leads us to propose the Quantum Mechanics Swampland, where we begin to delineate the boundary between quantum mechanical potentials which can be completed into a QFT and those which cannot. Next, we consider the more optimistic scenario where that dark sector is connected to the Standard Model via a portal. We propose an explanation to the Galactic Center Excess, a robust gamma-ray signal possibly originating from annihilating dark matter. We consider a CP-violating Higgs portal which allows Majorana fermion dark matter to annihilate to Standard Model final states. Measurements of the electron EDM place stringent constraints on viable parameter space. This builds on a separate analysis of the ACME experiment's constraint on the electron EDM and the implications this has for generic models of BSM physics. Precision measurements are an interesting window into models of new physics. In a similar spirit to the analysis of the EDM results, we also consider the anomalous measurement of the W boson mass from the CDF experiment. We characterize this tension in terms of the oblique parameters, and discuss various models of new physics which can generate the required values to alleviate the tension between the measurement and Standard Model prediction. Finally, we consider a separate portal where the dark sector is endowed with a U(1) and kinetically mixes with the Standard Model U(1). With the expectation that the dark and visible sectors must ultimately embed into a complete theory of quantum gravity, we use the Swampland conjectures to place constraints on the size of the kinetic mixing parameter.

Contents

Citations to previously published research

Parts of this thesis contain research published in the following manuscripts:

Chapter 2 and Appendix A are lightly edited versions of

P. Agrawal, A. Parikh, and M. Reece
Systematizing the Effective Theory of Self-Interacting Dark Matter
JHEP 10 (2020) 191, [arXiv:2003.00021].

Chapter 3 and Appendix B are lightly edited versions of

A. Parikh
The Quantum Mechanics Swampland
Phys. Rev. D 104 (2021) 036005, [arXiv:2012.11606].

Chapter 4 and Appendix C are lightly edited versions of

K. Fraser, A. Parikh, and W. Xu
A Closer Look at CP-Violating Higgs Portal Dark Matter as a Candidate for the GCE
JHEP 03 (2021) 123, [arXiv:2010.15129].

Chapter 5 and Appendix D are lightly edited versions of

C. Cesarotti, Q. Lu, Y. Nakai, A. Parikh, and M. Reece
Interpreting the Electron EDM Constraint
JHEP 05 (2019) 059, [arXiv:1810.07736].

Chapter 6 is a lightly edited version of

P. Asadi, C. Cesarotti, K. Fraser, S. Homiller, and A. Parikh
Oblique Lessons from the W Mass Measurement at CDF II
[arXiv:2204.05283].

Chapter 7 and Appendix E are lightly edited versions of

G. Obied and A. Parikh
A Tale of Two U(1)s: Kinetic Mixing from Lattice WGC States
[arXiv:2109.07913].

List of Figures

For ma, papa, bhai, and goober.

Acknowledgments

Unsurprisingly, the hardest part of writing this dissertation, has been the acknowledgements section. As I take these moments to reflect back on my journey, I begin to truly understand the role played by those around me in helping me succeed.

I owe an enormous debt of gratitude to my advisor, Matt Reece, with whom it has been both a privilege and a pleasure to learn from and work with. Matt welcomed me into his group when I was just starting out as a grad student. Over the next six years, I had the opportunity to not only learn a tremendous amount of physics, but also how to approach research, deconstruct problems, and think like a physicist. I will endlessly aspire to achieve Matt's tremendous breadth of expertise, his creativity, and his ability to have keen insights in each. Moreover, Matt's approach to viewing me more as a collaborator and less as a student has helped me develop into an independent physicist. In Matt, I see all the qualities I hope to emulate as a physicist. Many thanks to Tracy Slatyer, with whom I had the opportunity to collaborate with. I aspire to achieve the intuition with which Tracy approaches problems, her willingness to extend a formalism to tackle a problem no matter how complicated it may be, and her ability to make theory statements grounded in data. Thank you for supporting me in my career and growth as a physicist. I would also like to thank my committee members, Melissa Franklin and Cora Dvorkin, for the insights and support they have provided over the years.

One of the best parts about working with Matt has been the interactions with the students and post-

docs in our group, as well as those we have absorbed along the way. I bring with me fond memories of the kindness, good humor, spirited debates, and $\hbar$ opinions of the group postdocs: Prateek Agrawal, Pouya Asadi, Francis-Yan Cyr-Racine, Sam Homiller, Rashmish Mishra, Julian Muñoz, Yuichiro Nakai, Bryan Ostdiek, David Pinner, and John Stout. In particular, I owe much of my growth to the mentorship of Prateek over the years. And of course, this would have been a very lonely journey without my peers and friends, the students of the group: Hengameh Bagherian, Cari Cesarotti, Nick DePorzio, Katie Fraser, Qianshu Lu, Georges Obied, and Linda Xu. The constant banter, roasting, peanut-gallery content, and contributions to a masterpiece, *The Swapland*[24], made this entire PhD all the more enjoyable. To Linda, Georges, and Katie especially, I appreciate our never ending discussions sharing our confusions, voicing our frustrations, and learning some physics along the way.

Thank you to the Harvard High Energy Theory Group at large for being a constant source of inspiration and support over the years. I have learned a great deal from all of you in conversations, seminars, over coffee, and at the blackboards. In particular, I would like to acknowledge Nick Agia, Anders Andreassen, Adam Ball, Alek Bedroya, Minjae Cho, Scott Collier, Tansu Daylan, Chris Frye, Hofie Hannesdottir, Temple He, Dan Kapec, David Kolchmeyer, Alex Lupsasca, Miguel Montero, Monica Pate, Ana-Maria Raclariu, Tom Rudelius, Houri Tarazi, and Irene Valenzuela. I am also grateful for the deep insights provided by Howard Georgi, Lisa Randall, Matt Schwartz, Matt Strassler, and Cumrun Vafa over many interesting discussions. Thank you as well to the administrative assistants who have kept the HETG functioning and caffeinated: Erica Colwell, Nicole D'Aleo, Rae Gilchrist, Elise Krims, and Jennifer Pollock.

Thank you to the graduate students in my cohort, and at MIT, that I have been lucky to call my

friends. From our darts games, puppet show planning, and the rest of our G1 shenanigans to social hours and department Christmas parties, you've all been sources of friendly comfort over the years and grad school would have been significantly duller without all of you: Will Conway, Emil Khabiboulline, Hongwan Liu, Tim Menke, Marios Michael, Sruthi Narayanan, Lauren Niu, Paloma Ocola, Daniel Pollack, Greg Ridgway, Rhine Samajdar, Daniya Seitova, Jon Vandermause, and Jeremy Yodh. I would like to especially thank Sruthi. It is rare to find someone who becomes a best friend so quickly. Thanks for sharing all our inside jokes, our countless movie nights, and (post)-social hour adventures. I can't imagine having made it through these six years without your friendship and our innumerable conversations working through some aspect of physics that was confusing us. Thank you also to Jacob Barandes, Hannah Belcher, Lisa Cacciabaudo, and Carol Davis. I truly appreciate everything you do for all of the graduate students. Thank you especially to Lisa and Carol for all the hugs, chocolates, advice, and support you have provided. Grad school would truly have been impossible without every single one of you and I will miss you all a lot!

I would be remiss not to mention the faculty and students at Rutgers who have also played a significant role in getting me to where I am today. To my first research advisor, Sevil Salur, thank you for supporting me throughout my undergraduate career. I hope to one day mentor my own students with the same kindness you showed our whole group and instill the tenacity with which to approach research like you did for me. Thanks to David Shih for entertaining countless hours of conversations which helped lead me to a deeper understanding and appreciation for physics. Thank you also for taking the time to introduce me to Matt for the first time during his visit to Rutgers. I've greatly appreciated all the support you've provided. Lastly, I would like to thank Andrew Baker, Raghav

Kunnawalkam Elayavalli, Eric Gawiser, Vedant Sachdeva, Yianni Tamanas, and Ani Thuppul.

Finally, I would like to thank my family for everything they have done. My parents, Dipti and Deepak, have always encouraged me to follow my interests and dreams, no matter what they were. My brother, Ankit, has always been my role model and someone who I continually look up to. Thank you all for instilling in me the beliefs and values which I carry with me everyday and continue to shape me. Lastly, thank you to Anya, for your unconditional love, despite me being away from home for long periods of time. Thank you all for being my strongest support system. No amount of words will ever convey how blessed I am to have you all by my side.

1

Introduction

The Standard Model of particle physics is an extremely well-tested theory describing most of the phenomena in the world around us. It is an effective quantum field theory describing the non-gravitational fundamental forces and matter. In particular, the Standard Model is a gauge theory, implying that the Lagrangian is invariant under a set of local transformations which determine the Standard Model gauge group G_{SM}. The elementary particle content is given by 3 generations of quarks and leptons,

5 gauge bosons, and 1 Higgs boson[1], which all transform under appropriate representations of the Standard Model gauge group $SU(3) \times SU(2)_L \times U(1)_Y$. The generations are ordered by mass, so the first generation contains the up and down quarks and the electron and electron neutrino, the second generation contains the charm and strange quarks and the muon and muon neutrino, and the third generation contains the top and bottom quarks and the tau and tau neutrino. The gauge fields are the photon, the Z boson, the $W^{\pm}$ bosons, and the gluon (of which there are actually 8 varieties), which mediate the electromagnetic, weak, and strong forces respectively. Invariance of the Standard Model Lagrangian under G_{SM} determines the coupling of these fields to each other and precisely determines the nature of their interactions. Since its development starting in the 1970s, the Standard Model has made countless predictions which have been experimentally verified. This has brought the field of particle physics to an interesting crossroads. On one hand, the Standard Model has been stunningly successful and theoretical predictions have been experimentally corroborated to exquisite precision. On the other hand, the Standard Model must break down at sufficiently high energy scales since it fails to explain several phenomena including gravity, the nature of dark energy and a natural explanation for the size of the cosmological constant, the baryon asymmetry of the Universe, the hierarchy between the Planck and weak scales, and the particle nature and interactions of dark matter. Understanding any of these phenomena, will almost certainly lead to physics beyond the Standard Model, and augment our effective theory with new particles, interactions, and possibly even new gauge groups. In this dissertation, we begin to address these questions by exploring the structure of the dark sector and considering the extent to which precision measurements can constrain models of new physics.

[1] "Wait, what is a boson?" – Matt Reece

Dark matter broadly characterizes the invisible, mysterious matter which is non-baryonic and contributes approximately 5 times as much to the global energy budget of the Universe as baryonic Standard Model matter. The non-baryonic nature hints immediately to a non-Standard Model origin, forcing us to consider extensions to the Standard Model. The existence of dark matter was originally proposed by Fritz Zwicky in the 1930s to explain the gravitational anomaly in the Coma cluster. Zwicky estimated the mass of the Coma cluster by measuring the brightness and number of galaxies, and under the assumption that the system is virialized, he predicted the velocities of the galaxies, only to observe that they were moving too fast. To account for this discrepancy, the Coma cluster had to be heavier than expected, which led Zwicky to propose a "dark matter" which filled the Coma cluster and contributed to the majority of its mass. The first definitive observational evidence came from the groundbreaking study of galactic rotation curves by Vera Rubin in 1968 [363,364]. Rubin measured the rotational velocity of stars as a function of distance from the center of the galaxy for various systems. The generic expectation was that inside the galaxy, stars further from the center would rotate faster since they experience a larger gravitational acceleration due to the extra mass enclosed. The light-emitting portion of the galaxy should contain all the mass, so if we measure the rotational velocity of an object outside the galaxy, its velocity should be decreasing since the enclosed mass is constant, but the gravitational acceleration falls off with distance. This behavior is called the Keplerian decline. Instead of exhibiting the expected Keplerian decline at large distances, the rotation curves Rubin observed flattened out, or in some cases even rose, pointing to the existence of a large halo of invisible matter enveloping the visible galaxy. Since the time of her seminal work, more rotation curves have been mapped out to larger and larger distances, and they all lead to the same conclusion as Rubin's.

In addition to rotation curves, exquisite measurements of the anisotropies in the Cosmic Microwave Background [22] as well as gravitational lensing measurements [327] have further strengthened the case for dark matter. These observational signatures come from systems at various different length scales corresponding to various different epochs in the history of the Universe, but all require dark matter to consistently explain them. The current best explanation is the cold dark matter paradigm where we introduce a new, massive, non-relativistic particle species that interacts very weakly with the Standard Model through some interaction, in addition to gravitational interactions.

The original proposal for a dark matter candidate was a Weakly Interacting Massive Particle (WIMP) with a mass in the $\mathcal{O}(100)$ GeV range. WIMPs were expected to have weak scale cross sections, which helped generate the correct relic abundance, and were protected by a discrete $\mathbb{Z}_2$ symmetry, which helped maintain the stability of dark matter over cosmological time scales. Searches for WIMPs, and dark matter more generally, have progressed through three main fronts, which are often colloquially referred to as making it, shaking it, or breaking it. The first is direct production, where Standard Model initial states produce dark matter final states. Dark matter carries away momentum and energy which is not detected by the experiment, leading to a missing energy signature. These searches are conducted mostly at colliders, where two beams of particles collide with each other at fixed interaction points and fixed target experiments, where one particle beam hits a slab of target material [276,57,197,113,192]. The next class is direct detection experiments, where dark matter scatters off a Standard Model particle depositing energy and momentum and leaving a detectable signature [47,42,32,30,154,317]. The kinematics of standard WIMP searches allow dark matter to scatter off Standard Model matter directly, but in recent years, there has been a push towards considering lighter mass dark matter candidates, and

direct detection techniques have evolved to also consider dark matter scattering off of collective excitations, such as phonons, in materials. Finally, the last class is indirect detection searches which look for signals of dark matter annihilating into Standard Model final states [28,387,342,12]. In the early universe, this process set the dark matter relic abundance for the WIMP through a process known as freezeout. At present, annihilations can occur in dark matter rich environments, such as the centers of galaxies, which are the targets of indirect detection searches. In recent years, a fourth avenue searching for dark matter self-interactions has also gained prominence, and attempts have been made to use current astrophysical observations to constrain self-interaction cross sections [374,159]. These self-interactions can modify dark matter distributions in galaxies, so searching for these modifications provide an additional handle on the nature of dark matter. The extensive, complementary experimental program has greatly constrained the WIMP paradigm. In conjunction, there also exist discrepancies between simulations and observations at small scales. The first of these is the missing satellites problem [332,300] where simulations tend to over-predict the amount of satellite galaxies around a Milky Way sized galaxy, as compared to the amount observed. The second is the too-big-to-fail problem [98] where certain dark matter halos predicted by simulations are so large that they definitely should have produced stars and be observable, yet we have not seen them. The third is the core/cusp problem [217,331] where simulations predict a cuspy dark matter density profile in galaxies which grows as we approach the center of the galaxy, but observations have shown a cored dark matter density profile which flattens out towards the center. Finally, there is also the diversity problem [341,304] where simulations predict a fairly unique shape for rotation curves with little variance, but observations of galaxies have shown a diverse array of rotation curve shapes. In principle, observation biases and baryonic physics may address these discrep-

ancies and completely resolve them [243,103,366,102,362,167], but the confluence of both a non-detection and the small scale problems has led to a proliferation of models extending the WIMP paradigm with non-minimal field content and interactions, and are often referred to as dark sectors. These models predict a wide array of signatures which can be detected by the complementary search strategies in place through the extensive experimental program. In this dissertation, we explore in more detail some of these extensions and discuss the constraints placed on them by current and next-generation experiments.

In addition to the purely phenomenological approach motivated by experimental results, there is an orthogonal approach to constrain dark sector and beyond Standard Model physics which uses the notion of theoretical consistency. In particular, in the string theory community, this is known as the Swampland program. From a low-energy perspective, there are a large class of apparently consistent effective quantum field theories which can be written down. At some higher energy scale, we expect to have a theory of quantum gravity, such as string theory, but not all of these effective quantum field theories can be consistently embedded into a theory of quantum gravity. So, the Swampland program aims to delineate the boundary between the consistent theories, which live in the Landscape, and inconsistent theories, which live in the Swampland, through a series of conjectures [101,344]. As low-energy phenomenologists, we can take these conjectures as theoretical input and focus on the subset of theories consistent with quantum gravity. In this dissertation, we also present the implications of the Swampland conjectures on a specific class of dark sector models containing a dark analogue of electromagnetism.

This dissertation is structured as follows. In Chapter 2, we take an effective field theory approach

to the theory of self-interacting dark matter. We develop a new procedure to consistently match an underlying QFT to the effective quantum mechanics description of the scattering process. Using this procedure, we critically analyze the existence of Sommerfeld enhancement in various classes of interactions. The consequences of this matching procedure are further examined in Chapter 3, where we study a variety of tree-level quantum mechanical potentials and explore their singularity structures. The lack of existence of singular potentials descending from a QFT leads us to propose the existence of the Quantum Mechanics Swampland. In Chapter 4, we fit the gamma-ray signal excess from the Galactic Center with a model of annihilating dark matter connected to the Standard Model through a CP-violating Higgs portal. CP-violation generically contributes to the electron EDM, which we study in Chapter 5. We illustrate the power of current null results by constraining various models of new physics. In Chapter 6, we consider the new measurement of the W boson mass made by the CDF experiment, which has a significantly larger value than the Standard Model prediction. We determine the values of the oblique parameters favored by the new measurement, and consider various models which generate these values at tree- and loop-level. In Chapter 7, we consider the implications of the Swampland conjectures on dark sector U(1)s which can kinetically mix with the Standard Model U(1). These conjectures are a set of criteria low-energy QFTs are expected to satisfy so that they can be consistently UV completed into theories of quantum gravity. The goal of this dissertation is to present progress in exploring the structure of the dark sector from purely theoretical as well as phenomenological lenses.

2

Systematizing the Effective Theory of Self-Interacting Dark Matter

2.1 Introduction

The majority of mass in our universe is in the form of dark matter, but the underlying nature of dark matter and its interactions remains elusive. Many attempts to understand the nature of dark matter

rely on searching for its interactions with ordinary matter, through direct or indirect detection experiments or attempts to directly produce dark matter particles at colliders or fixed-target experiments. We may also be able to learn about the particle nature of dark matter if it has significant self-interactions, which can alter the astrophysical and cosmological signals of dark matter in ways that may be detectable[374,159]. In recent years, many aspects of the astrophysics and cosmology of self-interacting dark matter have been extensively studied, so we will of necessity refer to only a small fraction of the literature. An excellent recent review article with extensive references is[383].

Dark matter self-interactions have been posited as a possible explanation for a number of discrepancies on small scales between observation and the results of classic N-body dark matter simulations of standard ΛCDM cosmology, such as the core/cusp problem[217,331], the missing satellites problem[332,300], the too-big-to-fail problem[98], and the diversity problem[341,304]. A weakness of such arguments is that baryonic physics, such as supernovae or AGN activity, can alter the distribution of dark matter in galaxies and clusters in ways that are unaccounted for in dark matter-only simulations. Incorporating baryonic physics in simulations accurately is challenging, and may solve some or even all of the potential problems with ΛCDM on small scales[243,103,366,102,362,167].

We do not take sides in this debate. We expect that in the future our understanding of dark matter and baryonic effects could be refined to allow for an averaged dark matter scattering rate to be extracted from data in systems on a variety of scales, from dwarf galaxies to clusters. Because the typical velocity of a dark matter particle is much lower in a dwarf galaxy than in a galaxy cluster, such observations could map out the velocity dependence of dark matter scattering, which encodes information about the underlying particle physics[210,105,320]. An attempt to do this with current data has been made

in [291] and argued to fit a Yukawa potential with a light mediator. Again, one can debate whether these conclusions are robust to uncertainties in baryonic physics, but in any case an important message to take away from [291] is that observations may eventually tell us the quantity $\langle \sigma v \rangle / m_{\rm DM}$ as a function of the rms velocity v.

With such measurements in hand, we would naturally want to answer the inverse problem: what underlying model of dark matter self-interactions produces the observed velocity dependence of the cross section? This question is nontrivial because dark matter is nonrelativistic, and in the nonrelativistic limit low-velocity scattering can be nonperturbatively enhanced by the Sommerfeld effect [373]. To compute the cross section in the low-velocity regime, we must match the relativistic QFT of interest onto a nonrelativistic effective theory [123,314] in which we can compute the cross section nonperturbatively by (numerically) solving the Schrödinger equation. In the dark matter context, the need for such calculations was first appreciated in the annihilation of heavy WIMPs [260,261,262]. More recently, it has been applied to scattering of dark matter through light mediators that generate an effective Yukawa potential [55,105,320,384]. However, relativistic QFTs can match to a much wider range of nonrelativistic effective interactions than a simple Yukawa potential. The classification of such interactions [176] has been used to study a variety of possible recoil spectra in direct detection experiments [202,215,87] (see also [25,222]). Most relevantly for our current work, it has also been used to classify dark matter self-interactions in [80], the "effective theory of self-interacting dark matter", which is closely related to the results in this chapter, although some of our conclusions differ.

2.1.1 Goals of this work and relation to the previous literature

Our goal in this chapter is to calculate the velocity dependence of dark matter self-interactions for the case of spin-1/2 dark matter interacting via a light boson, which may be a scalar, pseudoscalar, vector, or axial vector. In each case, we match to a nonrelativistic effective theory, then solve the Schrödinger equation numerically to obtain the velocity dependence of the cross section.

Our work differs from, and extends, earlier work on nonrelativistic dark matter scattering in several respects. The first is our matching procedure: we match the Born approximation to short-distance scattering in the quantum mechanical effective theory to the tree-level perturbative QFT approximation to short-distance scattering. This provides a boundary condition at small radius, from which we can integrate outwards to solve the Schrödinger equation and capture long-distance effects of light mediators. The specifics of our matching procedure are inspired by earlier work [123,314], but the details are novel: our procedure is streamlined and easy to apply. A particular difference from some previous work on self-interacting dark matter is that we do not just consider the effective potential generated by t-channel exchange, but include the contact interactions arising in other channels. In the case of pseudoscalar mediators, this is crucial to obtain the correct cross sections at small velocities.

Our approach clarifies a number of issues related to pseudoscalar mediators. We sum over all angular momentum partial waves. While a simple Yukawa potential conserves orbital angular momentum, the exchange of a pseudoscalar or axial vector leads to interactions that couple different ℓ modes (while conserving the total angular momentum j). Some earlier work has considered a toy model aimed at approximating pseudoscalar exchange without treating the coupled channels carefully. This toy model

includes a singular $1/r^3$ potential. We will show that this misses an important aspect of the physics, namely that the Born approximation for the pseudoscalar potential is non-singular at short distances. Furthermore, our matching procedure is robust to variations in the matching scale. Unlike some results in the literature, our cross section is entirely determined by the underlying QFT and does not depend on ad hoc constants introduced in the nonrelativistic effective theory.

In the end, we find that the correct matching of a weakly-coupled effective field theory with a light pseudoscalar or axial vector mediator leads to a nonrelativistic effective theory in which there is no enhancement of the cross section at low velocities. For these theories, unlike the case of light scalar or vector mediators, tree-level QFT is reliable. This simple result is in contrast with some earlier claims in the literature, for instance, in studies of annihilating dark matter with a pseudoscalar mediator[78,319]. A similar claim about the lack of Sommerfeld enhancement for the pseudoscalar potential was made in [288]. In this work, we provide more detailed arguments in support of this claim, incorporating both analytical and numerical evidence.

We proceed as follows: in §2.2, we introduce the basic models of mediators in QFT. We review why the axial vector mediator is special, in that its couplings to dark matter must vanish as the mediator mass goes to zero. In §2.3, we describe our matching procedure, the way in which we set boundary conditions, and the process of extracting the S-matrix from numerical solutions of the Schrödinger equation. In §2.4, we explain the absence of a Sommerfeld enhancement for a pseudoscalar mediator, arguing that a 1-loop calculation in the perturbative QFT also suggests that the effect should be absent. We explain the differences between our results and certain claims in the literature. Then, we present the numerical results of solving the Schrödinger equation and computing the cross section for the

various models. We offer concluding remarks in §2.5.

2.2 SIDM and Our Examples

We consider a weakly coupled dark sector with spin-1/2 fermionic dark matter interacting via scalar or vector mediators. If these mediators are light and generate an attractive potential, then it is possible that Sommerfeld enhancement can significantly boost the scattering cross section. So, it is crucial to analyze the potentials generated by various renormalizable interactions.

The details of the calculation depend on whether the dark matter carries an approximate conserved charge. If dark matter is a Majorana fermion, then the $\chi\chi \to \chi\chi$ scattering process receives contributions from s-, t-, and u-channel diagrams. In the Majorana case, there is no vector interaction, i.e., the coupling $A_\mu \chi^\dagger \bar{\sigma}^\mu \chi$ takes the form of an axial vector interaction when packaged into a 4-component field. If dark matter carries an approximately conserved charge, we should consider a Dirac fermion, and the dark matter abundance may be primarily of one charge (*asymmetric* dark matter[340,290,398]) or it may contain particles of both charges (*symmetric* dark matter). Scattering in the asymmetric case, $\chi\chi \to \chi\chi$, receives contributions from only t- and u-channel diagrams. In the symmetric case, there is additionally the process $\chi\bar{\chi} \to \chi\bar{\chi}$, which receives s- and t-channel contributions but no u-channel contribution.

Our goal in this work is to clarify conceptual issues in matching theories of self-interacting dark matter to a nonrelativistic effective theory, and to understand in which cases a Sommerfeld enhancement is present. These aspects of the physics are not sensitive to the Majorana or Dirac nature of the

fermion or to the symmetric or asymmetric nature of the dark matter population. Thus, for concreteness, in the remainder of the chapter we will only discuss the case of Dirac dark matter and $\chi\bar{\chi} \to \chi\bar{\chi}$ scattering. All of our results can be straightforwardly generalized to the other cases.

We denote the dark matter field as χ. The consistency of a Dirac effective theory requires a good approximate global symmetry,

$$\chi \to e^{i\alpha}\chi \tag{2.2.1}$$

In the absence of such a symmetry, we could write Majorana mass terms which split the Dirac fermion into two Majorana mass eigenstates.

We now list various cases that we will individually consider in this chapter. The Lagrangian for dark matter coupling with a real scalar φ is,

$$\mathcal{L}_{\text{scalar}} = i\bar{\chi}\gamma^\mu\partial_\mu\chi - m_\chi\bar{\chi}\chi + \frac{1}{2}\partial_\mu\varphi\partial^\mu\varphi - \frac{1}{2}m_\varphi\varphi^2 - \lambda\varphi\bar{\chi}\chi. \tag{2.2.2}$$

If instead we wish to couple to a pseudoscalar φ, we obtain the following,

$$\mathcal{L}_{\text{pseudoscalar}} = i\bar{\chi}\gamma^\mu\partial_\mu\chi - m_\chi\bar{\chi}\chi + \frac{1}{2}\partial_\mu\varphi\partial^\mu\varphi - \frac{1}{2}m_\varphi\varphi^2 - i\lambda\varphi\bar{\chi}\gamma^5\chi. \tag{2.2.3}$$

Note that we have assumed a CP symmetry to a good approximation, so that φ has well-defined CP quantum numbers.

We can also couple the dark matter to a U(1) gauge field φ_μ. If the charge assignments are vectorlike

(i.e. we simply gauge the Dirac U(1) symmetry), then we end up with the vector interaction of the gauge field with the dark matter. In order to generate a mass for the U(1) gauge field, we can couple it to a charged scalar that gets a vev. Imposing a separate global U(1) Dirac symmetry under which the scalar is a singlet forbids a coupling of this scalar to the dark matter.

$$\mathcal{L}_{\text{vector}} = i\bar{\chi}\gamma^{\mu}\partial_{\mu}\chi - m_{\chi}\bar{\chi}\chi - \frac{1}{4}F_{\mu\nu}F^{\mu\nu} + \frac{1}{2}m_{\varphi}^{2}\varphi_{\mu}\varphi^{\mu} - \lambda\varphi^{\mu}\bar{\chi}\gamma_{\mu}\chi\,. \tag{2.2.4}$$

To obtain a purely axial vector interaction of Dirac fermion dark matter is a little intricate. For clarity, we start with two left-handed Weyl fermions, χ_1 and χ_2, with the same charge under the U(1) gauge group. In this case, the Dirac mass term is not invariant under a U(1) gauge transformation, and must arise from the U(1) breaking. This also implies that the coupling of an axial vector mediator to a massive fermion must vanish in the limit that the vector boson mass goes to zero. This distinguishes the axial vector case from the other cases, in which we are free to take the couplings to be order-one numbers. Explicitly, we write an abelian Higgs model with a Higgs boson of charge 2:[1]

$$\begin{aligned}\mathcal{L}_{\text{axial vector}} = &-\frac{1}{4}F_{\mu\nu}F^{\mu\nu} + |(\partial_{\mu} - 2i\lambda\varphi_{\mu})H|^{2} + \frac{\lambda_{q}}{2}(H^{\dagger}H - v^{2})^{2} \\ &+ i\chi_1^{\dagger}\bar{\sigma}^{\mu}\partial_{\mu}\chi_1 + i\chi_2^{\dagger}\bar{\sigma}^{\mu}\partial_{\mu}\chi_2 - \lambda\varphi^{\mu}\chi_1^{\dagger}\bar{\sigma}_{\mu}\chi_1 - \lambda\varphi^{\mu}\chi_2^{\dagger}\bar{\sigma}_{\mu}\chi_2 - [yH\chi_1\chi_2 + \text{h.c.}]\,.\end{aligned} \tag{2.2.5}$$

Again, an additional global U(1) Dirac symmetry needs to be imposed to ensure that terms like $H\psi_1\psi_1$ are absent. After SSB, we can expand the Higgs around its expectation value: $H = v + \frac{1}{\sqrt{2}}(h + i\varphi_2)$.

[1] One could consider other possibilities, e.g., a Higgs boson of charge 1 that couples quadratically to give the fermion a mass through a higher-dimension operator. This would only make the problem of achieving a large coupling for a light mediator more severe.

Keeping the relevant terms, we find in unitary gauge,

$$\begin{aligned}\mathcal{L}_{\text{axial vector}} = &-\frac{1}{4}F_{\mu\nu}F^{\mu\nu} + 4\lambda^2 v^2 \varphi_\mu \varphi^\mu \\ &+ \frac{1}{2}|\partial_\mu h|^2 - \lambda_q v^2 h^2 \\ &+ i\bar{\chi}\gamma^\mu \partial_\mu \chi - y v \bar{\chi}\chi + \lambda \varphi^\mu \bar{\chi}\gamma_\mu \gamma^5 \chi - \frac{y}{\sqrt{2}} h \bar{\chi}\chi \end{aligned} \tag{2.2.6}$$

The masses and couplings of the massive vector, radial Higgs mode, and fermion are given in terms of the fundamental parameters as,

$$m_\varphi^2 = 8\lambda^2 v^2 \qquad m_h^2 = 2\lambda_q v^2 \qquad m_\chi = y v. \tag{2.2.7}$$

In particular, this scenario predicts that the coupling of the axial vector mediator to the dark matter behaves as

$$\lambda = \frac{y}{2\sqrt{2}} \frac{m_\varphi}{m_\chi}, \tag{2.2.8}$$

so light axial-vector mediators are necessarily weakly coupled.

From an effective field theory point of view, all these interactions are equally well motivated to analyze. Furthermore, if we keep an eye towards UV completions, some of these scenarios arise more naturally than others. Light scalars that are not pseudo-Nambu-Goldstone bosons are unnatural. Light vectors are also unnatural, if their mass comes from Higgsing, because the Higgs boson mass must also be protected. On the other hand, pseudoscalars are particularly well motivated because we know examples of underlying dynamics which can generate pseudoscalar couplings with an associated light

boson, such as pions in QCD. So it is much easier to embed a light pseudoscalar into a UV complete theory.

2.3 General Procedure

In this section, we outline the general procedure of obtaining the scattering cross sections, starting from a weakly-coupled Lagrangian. For light mediators, there can be substantial effects from multiple exchanges of the mediator in nonrelativistic scattering processes, so that the tree-level approximation does not reflect the true answer. A convenient way to resum these contributions in this case is to map the problem on to the equivalent quantum mechanical scattering problem. We can then solve the QM problem nonperturbatively and extract the scattering matrix elements. These amplitudes include the putative Sommerfeld enhancement effects.

Before we outline the procedure, it is worth highlighting the validity of the procedure carried out below. At small enough values of the coupling, the scattering amplitude at some fixed velocity is well-approximated by the tree-level amplitude in the QFT. If the relativistic corrections are small, the same amplitude is also well described by the Born approximation in a quantum mechanical system. The scattering potential is calculated by matching a QFT amplitude with the corresponding QM amplitude in the Born approximation. However, a subtlety that we will encounter involves potentials where the higher-order Born terms are "divergent". This is the case for singular potentials that grow faster than $1/r^2$ as $r \to 0$. In such a case, to calculate the higher-order Born terms we would need to regulate and renormalize the quantum mechanical problem, and consistently match with the QFT at loop

level. Indeed, this is true for the potentials we consider, but these potentials do have a well-defined first order Born limit as $r \to 0$ which will be sufficient for us to avoid the issue of divergences.

Our problem neatly factorizes into two pieces. The short-distance $r \to 0$ piece is the part where the potential divergence shows up, but from the QFT point of view this corresponds to high energy scattering, where Sommerfeld enhancement should not play a role and the amplitude should be well approximated by the tree-level diagram, or equivalently the first Born approximation in the QM picture. The potential Sommerfeld enhancement from multiple exchanges of the mediator appears in the larger r region, where the QM potential is well-behaved.

Thus, we use the following procedure, described in further detail below. We match the QFT tree-level amplitude with the QM amplitude in the first Born approximation to calculate the matching condition close to the origin at $r = a$. The nonrelativistic effective theory should not be expected to accurately describe momenta of order m_χ, at which dark matter particles are semirelativistic. As a result, the natural radius at which to match the relativistic theory to the nonrelativistic theory is the Compton radius of the dark matter, $a \simeq 1/m_\chi$. With the boundary condition established by matching, we solve the Schrödinger equation numerically, and thereby derive the scattering amplitude. We illustrate this procedure schematically in Figure 2.1. We then proceed to extract the S-matrix from the QM solution, highlighting the coupled channel case. We will then be in a position to critically evaluate which interactions give rise to a Sommerfeld enhancement.

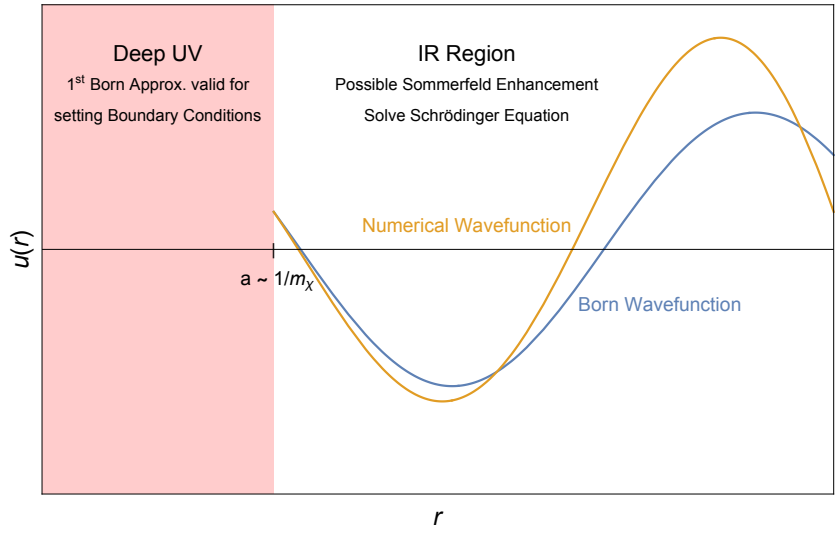

Figure 2.1: A schematic of our matching procedure. In the deep UV, we expect the Born approximation to hold, which we use to set our boundary conditions at $r = a$. Beyond this is the IR of our theory where Sommerfeld enhancement might be important and we need to solve the Schrödinger equation with the appropriate potential.

2.3.1 Computing the Tree Level Potential

To compute the tree level potential, we first compute the tree-level perturbative QFT amplitude for the process we are interested in. To illustrate our procedure, we consider $\chi\bar{\chi} \to \chi\bar{\chi}$. At tree level, this has contributions from an s- and a t-channel Feynman diagram. Next, we take the nonrelativistic limit of this amplitude and keep the leading terms. The scattering amplitude in the Born approximation in nonrelativistic quantum mechanics is given by

$$\langle \vec{p}_f | i\mathcal{T} | \vec{p}_i \rangle = -i\widetilde{V}(\vec{q})(2\pi)\delta(E_{p_f} - E_{p_i}), \qquad \vec{q} = \vec{p}_f - \vec{p}_i. \tag{2.3.1}$$

Comparing this expression to the nonrelativistic limit of our QFT amplitude gives us

$$\widetilde{V}(\vec{q}) = -\frac{1}{4E_{p_f}E_{p_i}}M, \tag{2.3.2}$$

where the extra factors of $2E_p$ come from the difference in the conventional normalizations of relativistic and nonrelativistic single particle states. Finally, to compute the real space potential $V(\vec{r})$, we have to Fourier transform $\widetilde{V}(\vec{q})$ with respect to $\vec{q}$.

We obtain the following potentials

$$V_{\text{scalar}}(r) = -\frac{\lambda^2}{4\pi r}e^{-m_\varphi r} \tag{2.3.3}$$

$$\begin{aligned} V_{\text{pseudoscalar}}(r) = \frac{\lambda^2}{4\pi}\Bigg(&\frac{4\pi\delta^3(\vec{r})}{4m_\chi^2 - m_\varphi^2}\left(\frac{1}{2} - 2S_1\cdot S_2\right) - \frac{4\pi\delta^3(\vec{r})}{3m_\chi^2}e^{-m_\varphi r}S_1\cdot S_2 \\ &+\frac{e^{-m_\varphi r}}{m_\chi^2}\left[\frac{m_\varphi^2}{3r}S_1\cdot S_2 + \frac{3(S_1\cdot\hat{r})(S_2\cdot\hat{r}) - S_1\cdot S_2}{r^3}\left(1 + m_\varphi r + \frac{m_\varphi^2 r^2}{3}\right)\right]\Bigg) \end{aligned} \tag{2.3.4}$$

$$V_{\text{vector}}(r) = \frac{\lambda^2\delta^3(\vec{r})}{4m_\chi^2 - m_\varphi^2}\left(\frac{3}{2} + 2S_1\cdot S_2\right) - \frac{\lambda^2}{4\pi r}e^{-m_\varphi r} \tag{2.3.5}$$

$$V_{\text{axial vector}}(r) = \frac{\lambda^2\delta^3(\vec{r})}{4m_\chi^2 - m_\varphi^2}\left(2S_1\cdot S_2 - \frac{1}{2}\right) - \frac{\lambda^2}{\pi r}e^{-m_\varphi r}S_1\cdot S_2 + \frac{4m_\chi^2}{m_\varphi^2}V_{\text{pseudoscalar}} \tag{2.3.6}$$

The terms in these potentials arising from t-channel contributions have been previously computed (e.g., [330,202,80,158]). To leading order in q^2, our results also agree with those in [200]. The s-channel contributions provide contact terms that we have written in the form of a nonrelativistic potential via Fierz rearrangement (see, e.g., [25]). As detailed in Appendix A.2, the spin matrices for antifermions

come with an additional minus sign.

In the pseudoscalar potential, we observe two delta-function terms. The first term comes from the s-channel, but the second term comes from the t-channel, which can be seen in the following manner:

$$\begin{aligned}\partial_i\partial_j\Big(\frac{e^{-m_\varphi r}}{r}\Big) &= e^{-m_\varphi r}\Big[\frac{1}{3}\nabla^2\delta_{ij}+\partial_i\partial_j\Big]\frac{1}{r}+2\Big[\hat{r}_i\frac{-1}{r^2}\hat{r}_j(-m_\varphi e^{-m_\varphi r})\Big]+\frac{1}{r}\partial_i\Big[-m_\varphi\hat{r}_j e^{-m_\varphi r}\Big]\\ &= e^{-m_\varphi r}\frac{m_\varphi^2}{3r}\left[\Big(3\hat{r}_i\hat{r}_j-\delta_{ij}\Big)\Big(1+\frac{3}{m_\varphi r}+\frac{3}{m_\varphi^2 r^2}\Big)+\delta_{ij}\right]-\frac{4\pi}{3}\delta^3(r)\delta_{ij}e^{-m_\varphi r}.\end{aligned} \tag{2.3.7}$$

2.3.2 The Schrödinger Equation

We solve the Schrödinger equation in the partial wave expansion using the potential derived above. The rotational invariance of the Hamiltonian implies that j is a conserved quantum number. For the $2\to 2$ scattering process involving spin-1/2 particles that we consider, the total spin is $s=0,1$. Consequently, it will be convenient to work in a basis of states $|r,j,\sigma,\ell,s\rangle$, where ℓ and s are the total orbital and spin angular momenta respectively, and σ is the z-component of the total angular momentum. Some of the terms in the potentials we consider mix terms with different ℓ values, so for a given j, we get a 4×4 block diagonal Hamiltonian. The wavefunction $\psi(\vec{r})$ can be separated,

$$\psi(\vec{r})=\sum_{j,\sigma,\ell,s}\frac{u_{j\sigma\ell s}(r)}{r}\langle\hat{n}|j\sigma\ell s\rangle\,. \tag{2.3.8}$$

The potential preserves j, σ, so without loss of generality we can set $\sigma = 0$. The Schrödinger equation for a fixed value of j becomes

$$\frac{1}{2\mu}\left(-\partial_r^2 - k^2 + \frac{\ell(\ell+1)}{r^2}\right) u_{\ell s}(r) + \sum_{\ell' s'} V_{\ell s, \ell' s'}(r) u_{\ell' s'}(r) = 0 \tag{2.3.9}$$

The matrix elements of the potential $V(r)$ are given in Appendix A.1. The subscripts (ℓ, s) take on 4 possible values $\{(j,0), (j-1,1), (j,1), (j+1,1)\}$. We have suppressed the j and σ quantum numbers for notational clarity. Conveniently, the four (ℓ, s) states separate into two states that mix with each other ($|j \pm 1, 1\rangle$) and two that evolve independently ($|j, 0\rangle$ and $|j, 1\rangle$).

Assuming that $rV(r) \to 0$ as $r \to \infty$, the asymptotic wavefunction should be a solution to the free particle equation. The solutions of the radial free particle equation, denoted s_ℓ and c_ℓ, are given in terms of the spherical Bessel functions.

$$s_\ell(kr) \equiv krj_\ell(kr), \qquad c_\ell(kr) \equiv -kry_\ell(kr)\,. \tag{2.3.10}$$

The time-independent solution to the Schrödinger equation can also be interpreted as a solution to a scattering problem. The asymptotic form of the solution is a combination of an incoming wave and a scattered wave. Different choices of boundary conditions correspond to different possible incoming waves – there are as many independent boundary conditions as the number of equations. A convenient choice of basis is to label them by (ℓs) values themselves. The asymptotic solutions to the

Schrödinger equation can be written in terms of the free particle solutions as,

$$u_{\ell s}^{(\ell' s')}(r) \sim \delta_{\ell' s',\ell s} s_\ell(kr) + K_{\ell' s',\ell s}\, c_\ell(kr)\,. \tag{2.3.11}$$

The **K**-matrix is the generalization of the more familiar partial wave phase-shift $\tan\delta_l$. By solving the coupled differential equations numerically, we can extract the **K**-matrix, and then calculate the scattering cross section. We describe these steps in detail next.

2.3.3 Setting Boundary Conditions

The boundary conditions for the Schrödinger equation above are set using the Born approximation in the region $r < a = m_\chi^{-1}$ as outlined in Section 2.3. This region of small radii probe the UV of our effective quantum mechanical description and we expect this to match onto the corresponding QFT. Therefore, we expect the first Born approximation to reproduce the tree level perturbative QFT approximation. We show this matching in Figure 2.2. The **K**-matrix in the Born approximation is simple to calculate,

$$K^a_{\ell s,\ell' s} = -\frac{2\mu}{k}\int_0^a \mathrm{d}r\, s_{\ell'}(kr) s_\ell(kr) V_{\ell s,\ell' s'}(r) \tag{2.3.12}$$

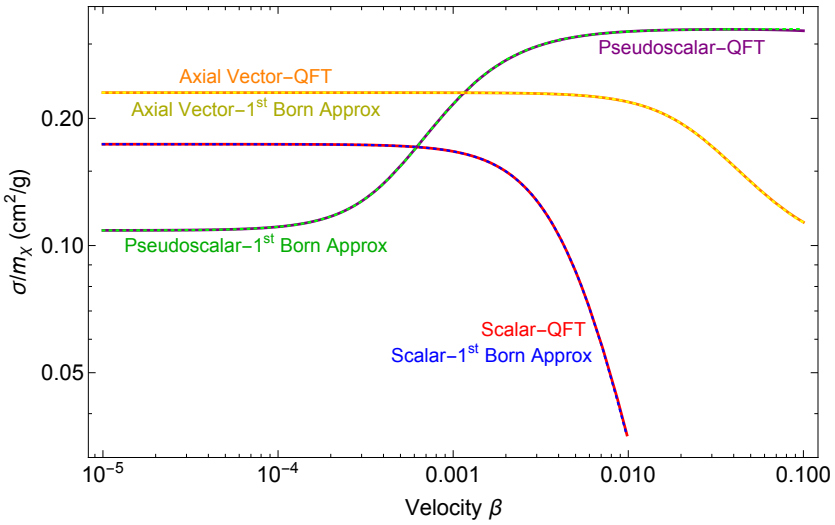

Figure 2.2: Illustration of the validity of the matching procedure via numerical evaluation of the Born cross section compared to the tree-level QFT cross section as a function of velocity for the Yukawa (scalar) potential, pseudoscalar potential and axial vector potential. For the scalar case, we choose $\lambda = 10^{-1}$, $m_\varphi = 10^{-2}$ GeV and $m_\chi = 1$ GeV. For the pseudoscalar case, we choose $\lambda = 10^{-1}$, $m_\varphi = 10^{-3}$ MeV and $m_\chi = 1$ MeV. For the axial vector case, we work in the decoupling limit. We choose the vev $v = 20$ MeV, $\lambda_q = 4\pi$, $\lambda = 10^{-3}$ and $y = 1$. We emphasize that this plot should *not* be taken as an accurate illustration of the full cross section, as the Born approximation receives large corrections in the Yukawa case.

where we have restricted the integral to $r < a$. This gives us our boundary conditions for the numerical solutions

$$u_{\ell s}^{(\ell' s')}(a) \sim \delta_{\ell' s', \ell s} s_\ell(ka) + K^a_{\ell' s', \ell s}\, c_\ell(ka)\,. \tag{2.3.13}$$

which we can use to evaluate the wavefunction and its derivative at $r = a = m_\chi^{-1}$. In our numerical calculations for the various potentials below, we have checked that varying the matching radius has little effect on our results, provided that we choose a of order m_χ^{-1}.

In this whole discussion so far, we have not specified the structure of the potential. In particular, potentials in quantum mechanics can diverge at the origin, and the Born limit may not be well-defined.

A potential is considered non-singular if $r^2 V(r) \to 0$ as $r \to 0$. Since $s_\ell(kr) \sim r^{\ell+1}$ for small r, for such potentials clearly the integral above is convergent. The pseudoscalar potential does not fit this criterion due to the r^{-3} piece and naively looks singular when $\ell = \ell' = 0$. However, as we see from the results in Appendix A.1, these dangerous terms vanish under the action of the operator $\mathcal{O}_T \equiv 3(\vec{S}_1 \cdot \hat{r})(\vec{S}_2 \cdot \hat{r}) - \vec{S}_1 \cdot \vec{S}_2$ appearing in the numerator.

Since we consider all potential terms that are generated from tree-level exchanges, it is interesting to note that the QFT seems to produce highly non-generic potentials which may seem singular, but possess operator structures that remove these divergent pieces at the leading Born approximation.

2.3.4 Extracting the S-Matrix from Numerical Solutions to the Schrödinger Equation

The $\mathbf{K}$-matrix can be extracted from the set of asymptotic solutions $u_{\ell s}^{(\ell' s')}(r)$ at some suitably large value of $r = r_{\max}$. Define the matrix $\mathbf{W}$ in terms of the matrix of solutions $\mathbf{u}$,

$$\mathbf{W} = \left(\mathbf{u}'(r_{\max})\right)^{-1} \cdot \mathbf{u}(r_{\max}) \tag{2.3.14}$$

with the $'$ denoting ∂_r. The $\mathbf{K}$-matrix is

$$\mathbf{K} = \left(\mathbf{s}(kr_{\max}) - \mathbf{W} \cdot \mathbf{s}'(kr_{\max})\right) \cdot \left(\mathbf{c}'(kr_{\max}) \cdot \mathbf{W} - \mathbf{c}(kr_{\max})\right)^{-1} \tag{2.3.15}$$

where we have defined the free-particle solution matrices as

$$\begin{aligned}\mathbf{s}(kr) &= \text{diag}\left[s_j(kr), s_{j-1}(kr), s_j(kr), s_{j+1}(kr)\right], \\ \mathbf{c}(kr) &= \text{diag}\left[c_j(kr), c_{j-1}(kr), c_j(kr), c_{j+1}(kr)\right].\end{aligned} \tag{2.3.16}$$

The $\mathbf{S}$-matrix follows,

$$\mathbf{S} = (1 + \mathrm{i}\mathbf{K}) \cdot (1 - \mathrm{i}\mathbf{K})^{-1}. \tag{2.3.17}$$

We outline the steps involved in obtaining the cross section from the S-matrix in this basis following the notation in Ref. [392]. The differential cross section is given in terms of the scattering amplitude in the familiar way,

$$\frac{d\sigma\left(\hat{k}, \sigma_1, \sigma_2 \to \hat{k}', \sigma_1', \sigma_2'\right)}{d\Omega} = \left|f\left(\hat{k}, \sigma_1, \sigma_2 \to \hat{k}', \sigma_1', \sigma_2'\right)\right|^2. \tag{2.3.18}$$

We can write f in terms of the $(j\sigma\ell s)$ basis S-matrix using the Wigner-Eckart theorem,

$$\begin{aligned}f\left(\hat{k}, \sigma_1, \sigma_2 \to \hat{k}', \sigma_1', \sigma_2'\right) = -\frac{2\pi i}{k} \sum_{j\sigma l' s' p' l s p} & C_{\frac{1}{2}\frac{1}{2}}(s, p; \sigma_1\sigma_2) C_{ls}(j, \sigma; m, p) \\ & \times C_{\frac{1}{2}\frac{1}{2}}(s', p'; \sigma_1'\sigma_2') C_{l's'}(j, \sigma; m', p') \\ & \times Y_l^{m*}(\hat{k}) Y_{l'}^{m'}(\hat{k}') \left(\mathbf{S}^j(E) - 1\right)_{l's';ls},\end{aligned} \tag{2.3.19}$$

where the C's are Clebsch-Gordan coefficients. We have specialized to the case of elastic $2 \to 2$ scattering between spin-1/2 particles. The spin-averaged cross section in this basis is,

$$\sigma = \frac{\pi}{4k^2} \sum_{j,\ell' s',\ell s} (2j+1) \left| \left(\mathbf{S}^j(E) - 1 \right)_{\ell' s',\ell s} \right|^2 . \tag{2.3.20}$$

In SIDM phenomenology, there are other related quantities of interest, such as the momentum transfer cross section or the viscosity cross section. Their utility arises from their well-behaved soft and forward limits, and they have a direct bearing on the evolution of dark matter phase space in halos. They are defined in terms of the differential cross section. The transfer cross section[2] is defined as [210,105,384]

$$\sigma_T = \int \frac{\mathrm{d}\sigma}{\mathrm{d}\Omega} (1 - \cos\theta) \mathrm{d}\Omega \tag{2.3.21}$$

while the viscosity cross section is defined as

$$\sigma_V = \int \frac{\mathrm{d}\sigma}{\mathrm{d}\Omega} (1 - \cos^2\theta) \mathrm{d}\Omega \,. \tag{2.3.22}$$

2.4 Sommerfeld Enhancement

In this section we study the existence of Sommerfeld enhancement for various types of interactions. We begin with a discussion of our results for the Yukawa potential, which has previously been studied extensively [55,105,320,384]. We then present novel results for the pseudoscalar and axial vector cases, which do not show Sommerfeld enhancement. We discuss a diagrammatic argument that reinforces

[2] See [287,26] for further discussion.

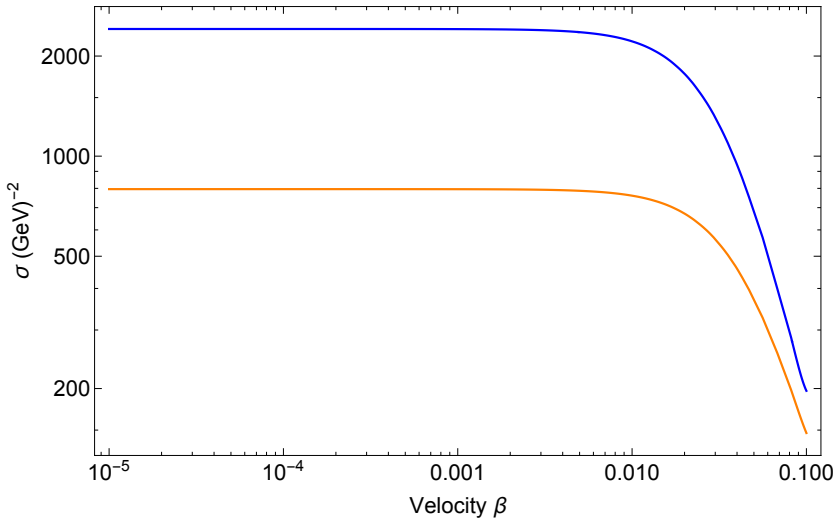

Figure 2.3: Cross section as a function of velocity for dark matter coupled via a scalar mediator. The numerical cross section (solid blue) is compared with the tree-level QFT cross section (solid orange). The numerical cross sections shown here includes the nonperturbative Sommerfeld enhancement and is summed over partial waves (truncated at ℓ_{max} such that $\sigma_{\ell_{\text{max}}} \leq 10^{-4}\sigma_0$). Parameters are $\lambda = 1$, $m_\chi = 1$ GeV and $m_\varphi = 10^{-1}$ GeV. At low velocities, we observe a significant Sommerfeld enhancement but at larger velocities, the numerical cross section becomes well approximated by the Born cross section as expected.

this conclusion, and comment on disagreement with previous work that has found Sommerfeld enhancement in the pseudoscalar case.

2.4.1 Yukawa Potential

In Figure 2.3, we present our results for the Yukawa potential generated via a scalar interaction. The solid orange curve is the tree-level QFT cross section. Using the procedure outlined in Section 2.3.3, we set the boundary conditions and solve the Schrödinger equation. The numerical cross section we obtain is plotted as the solid blue curve. We introduce a dynamical cutoff to compute the numerical cross section. In principle, the total cross section, σ, is given by summing the partial wave cross sections, σ_ℓ, for all the partial waves. In practice, we truncate this sum at ℓ_{max} such that $\sigma_{\ell_{\text{max}}} \leq 10^{-4}\sigma_0$.

It is worth noting here that the Yukawa potential is well-behaved at the origin and does not require the matching procedure. We checked that the cross sections calculated with and without using our matching procedure agree. For consistency with the rest of the results shown in this chapter, we report numerical cross sections for the Yukawa potential computed using the matching procedure. The results in Figure 2.3 show that there is a considerable enhancement in the cross section in the nonrelativistic regime. At higher velocities, the QFT tree-level cross section becomes a better approximation for the cross section. As has been discussed previously in the literature, we expect Sommerfeld enhancement to be a significant effect in the nonrelativistic limit for light mediators and our results are in good agreement with this expectation.

2.4.2 Pseudoscalar Mediator

Previously, in Figure 2.2 we showed the agreement between the first Born approximation and the QFT expectation for the cross section for a pseudoscalar mediator. Having set the boundary conditions, we compute the numerical cross section, shown in blue, and compare it to the tree-level QFT cross section in dashed orange in Figure 2.4. We implement the same dynamical cutoff on the sum over partial waves for the pseudoscalar potential as we did for the Yukawa potential. At large velocities, the two curves deviate by $\mathcal{O}(1\%)$. This discrepancy is saturated by the nonrelativistic corrections which scale as β^2 and we see that there is no additional enhancement. While we might have expected our intuition from the Yukawa potential to apply here, we do not find any significant Sommerfeld enhancement for any values of m_φ.

The absence of enhancements in the small m_φ regime can be understood intuitively. The pseu-

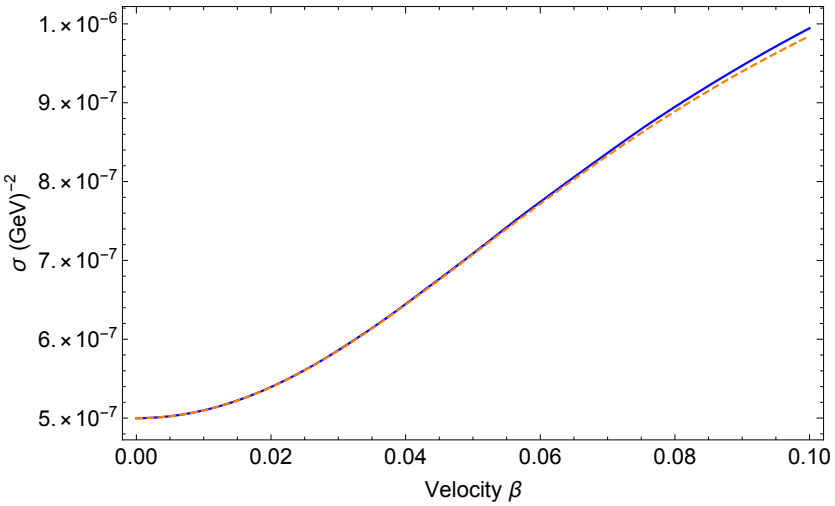

Figure 2.4: Cross section as a function of velocity for dark matter coupled via a pseudoscalar mediator. The numerical cross section (solid blue) computed with the procedure outlined in Section 2.3 is compared with the tree-level QFT cross section (dashed orange). We set $\lambda = 10^{-1}$, $m_\chi = 1$ GeV and $m_\varphi = 10^{-1}$ GeV. At low velocities we do not see any Sommerfeld enhancement. We begin to see deviations at larger velocities, as expected since the tree-level QFT answer is a fully relativistic calculation but the numerical cross section is determined from a nonrelativistic potential.

doscalar potential, in Equation 2.3.4, has two Yukawa like terms which in principle can generate an enhancement, but both of these terms are suppressed by $\frac{m_\varphi^2}{m_\chi^2}$. Therefore, in the limit of small m_φ, the suppression of these terms shuts off possible Sommerfeld enhancement. A similar intuitive argument is provided in [288]. Furthermore, the more divergent terms, such as the r^{-3} term, behave effectively like a short range potential and hence don't generate enhancements. In the large m_φ limit, we don't expect Sommerfeld enhancement in either the Yukawa or pseudoscalar case as the exponential suppression takes over and we have short range potentials.

2.4.2.1 Diagrammatic Argument

Feynman diagrammatic arguments lend further credence to this result. We discuss the general idea and results of this argument for the scalar and pseudoscalar case here and relegate the details to Appendix A.3. Sommerfeld enhancement occurs in a region of phase space where diagrams with two mediator exchanges are comparable or parametrically larger than a tree level diagram with a single mediator exchange. To understand the scaling behavior in this regime, we can analytically compute the resulting box diagram for the cases of scalar and pseudoscalar mediators.

We study the ratio of $\mathcal{M}_{1-\text{loop}}$ to $\mathcal{M}_{\text{tree}}$. For the pseudoscalar case, the leading behavior goes like $\frac{g^2}{16\pi^2}\log\xi$, where we have defined $\xi = m_\chi^2/m_\varphi^2$. On the other hand, for the scalar case the leading behavior goes like $\frac{g^2}{4\pi}\sqrt{\xi}$. The dependence on the coupling g is as expected. As always for a perturbative calculation, if we make the coupling arbitrarily large, then loops will be important. What is relevant for the existence of nonrelativistic enhancement is the scaling with ξ, which is different for the scalar and pseudoscalar cases. At large ξ, the ratio in the scalar case diverges, whereas in the pseudoscalar case, it behaves like a log-enhanced loop factor. This indicates that when we make our mediator light, the box diagram becomes important and dominates over the tree level diagram in the scalar, or more generally the Yukawa case. This is Sommerfeld enhancement. It requires that we resum an infinite family of diagrams, which is accomplished by solving the nonrelativistic Schrödinger equation. On the other hand, in the pseudoscalar case, the box diagram is not enhanced by nonrelativistic effects as the mediator becomes light, which corroborates the numerical results and heuristic arguments we gave above.

Our conclusions deviate from certain claims in the literature. Our analysis of the EFT and its operators largely agrees with that of[80], though they included only t-channel contributions from light mediators and neglected contact terms. Both [80] and [78] correctly explain how pseudoscalar exchange can couple modes with $l = j \pm 1$. However, [80] then argued that scattering should be dominated by a singular $1/r^3$ potential and proceeded to analyze a single-channel equation with such a potential as an idealization of the pseudoscalar exchange potential. We do not believe that this toy single-channel problem has similar physics to pseudoscalar exchange. In particular, our matching procedure works well for the pseudoscalar exchange problem but is not even well-defined for the $l = 0$ mode in a $1/r^3$ potential, because the integral computing the first Born approximation diverges at small r. This reflects the fact that a $1/r^3$ potential is singular whereas, as we have argued, a $[3(S_1\cdot\hat{r})(S_2\cdot\hat{r}) - S_1\cdot S_2]/r^3$ potential is not (at least at leading order in the Born approximation). The authors of [78] studied the coupled-channel problem for $j = 1$ modes and concluded that there can be significant Sommerfeld enhancement. Their approach is similar to ours: they have introduced a short-distance square well regulator, and then solve the full coupled-channel problem at longer distances. However, they have not carried out a detailed matching to perturbative QFT, and as a result they treat the depth of the square well potential and the coupling strength as free parameters to vary. The Sommerfeld enhancement that they observe arises in regions of nonperturbatively large short-distance scattering. We believe that there is no conflict between their numerical results and our claim that Sommerfeld enhancement does not arise within the parameter space one can obtain through perturbative matching to a weakly-coupled quantum field theory.

2.4.3 Axial Vector Mediator

As discussed in Section 2.2, the axial vector interaction is non-trivial. It comes along with a radial Higgs mode that also couples to the fermions. This is a scalar particle coupled to our fermionic dark matter, which in turn will induce a Yukawa potential between them. As we saw already, Yukawa potentials generate a Sommerfeld enhancement. On the other hand, if we want to study just the axial vector type interaction, we need to decouple the Higgs mode by making it heavier. One consistent way of achieving this is by making the square root of the Higgs quartic larger than the Higgs coupling to the dark matter ($\sqrt{2\lambda_q} > y$). Furthermore, to make the axial vector mediator lighter than the dark matter, we need the gauge coupling to be smaller than the Higgs-dark matter coupling ($y > \sqrt{8}\lambda$). By doing so, we can decouple the Higgs and study a pure axial vector theory. Formally, by integrating out the Higgs, we generate a four-Fermi interaction which manifests as a delta function in the potential since it was generated by a contact interaction without any $\vec{q}$ dependence.

Having done so, we can now isolate the potential generated by a purely axial vector type interaction. By inspecting Equation 2.3.6, we see a term proportional to $V_{\text{pseudoscalar}}$. Again, this term does not generate a Sommerfeld enhancement. In addition, there is a Yukawa term in the potential. This term does not generate a Sommerfeld enhancement because in the light mediator regime, the coupling, which is proportional to the mediator mass, is also small. On the other hand, if we want a large coupling, then the mediator mass increases proportionally and Sommerfeld enhancement turns off. The structure of the underlying UV completion restricts the parameter choices we can make. We checked that the results obtained from the QFT match the results obtained from the full quantum mechanical

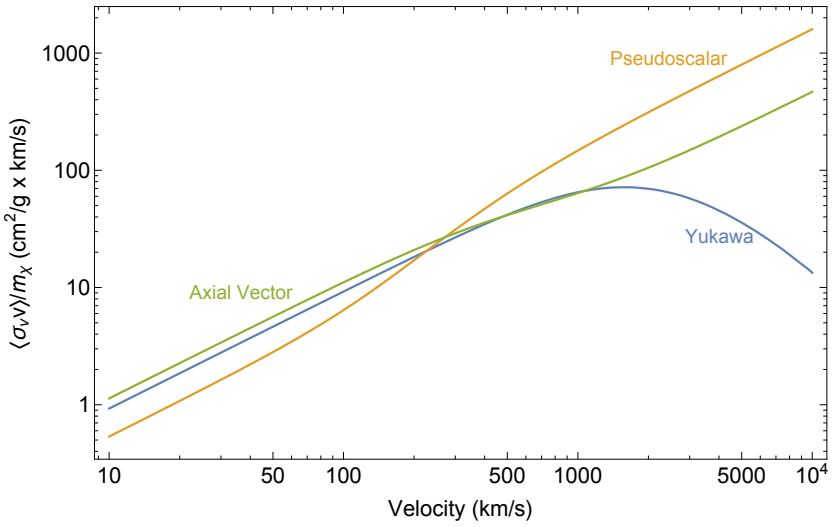

Figure 2.5: Velocity weighted viscosity cross section as a function of average velocity for dark matter coupled via a scalar, pseudoscalar or an axial vector mediator. For the scalar case, we choose $\lambda = 10^{-1}$, $m_\phi = 10^{-2}$ GeV and $m_\chi = 1$ GeV. For the pseudoscalar case, we choose $\lambda = 10^{-1}$, $m_\phi = 10^{-3}$ MeV and $m_\chi = 1$ MeV. For the axial vector case, we work in the decoupling limit. We choose the vev $\langle v\rangle = 20$ MeV, $\lambda_q = 4\pi$, $\lambda = 10^{-3}$ and $y = 1$. We assume the dark matter follows a Maxwell-Boltzmann distribution and use a hard cutoff at the escape velocity. The full numerical cross section for the Yukawa potential includes the nonperturbative Sommerfeld enhancement. On the other hand, as we discuss in the text, the axial vector interaction in the decoupling limit and the pseudoscalar interaction don't induce Sommerfeld enhancement and are therefore computed using tree-level relativistic QFT.

calculation for the axial vector potential when working in the decoupling limit, which supports the heuristic argument we make above. Therefore, when working in this limit, we can also compute $\langle\sigma_V v\rangle$ using the relativistic, perturbative QFT.

2.4.4 Results

In this section, we show the results from the procedure laid out in Section 2.3.3. The quantity of merit is the viscosity cross section σ_V. The angular weighting regulates both forward and backward scattering, which is important since singularities in the forward and backward scattering limit, although physical, do not change the dark matter velocity distribution and hence have no observable effect.

The physical quantity we can extract from measurements is $\langle \sigma_T v \rangle$. The velocity averaging assumes a Maxwell-Boltzmann distribution truncated at an escape velocity $v_{\rm esc} = \sqrt{2} v_{\rm rms}$, as for a virialized halo. The results are shown in Figure 2.5 for the various interactions we considered. The parameters are chosen such that the cross sections are at approximately the correct order of magnitude over the velocity range of interest. A more dedicated exploration of the viable parameter space fitting the self-interaction cross section measurements from astrophysical data in [291] should be performed, but is beyond the scope of this work.

As we discussed in detail above, our numerical results for the pseudoscalar mediator and the axial vector mediator, with a decoupled Higgs, show no Sommerfeld enhancement. So, we can compute $\langle \sigma_T v \rangle$ directly from perturbative, relativistic QFT in both of these cases. For the pseudoscalar mediator, we notice a kink occurring at $v \sim \mathcal{O}(m_\phi / m_\chi)$. The kink exhibits a characteristic factor of 3 increase in the cross section. The cross section plateaus before and after the kink. These are robust predictions for the behavior of the pseudoscalar interaction. The features we highlighted above can be seen more clearly in Figure 2.2, even though it contains only the tree-level QFT results, since these are a good approximation to the answer in the case of pseudoscalar and axial vector interactions.

2.5 Conclusions

In this chapter, we have studied the velocity dependence of interactions between spin-1/2 dark matter particles mediated by a light boson. In particular, we studied the scenario where the boson is a scalar, vector, pseudoscalar or axial vector. We derived the associated potentials including both *s*- and

t-channel contributions to the scattering process. We outlined a new procedure for setting the boundary conditions where we match a tree-level perturbative QFT estimate of short-distance scattering to the Born approximation to short-distance scattering in the effective nonrelativistic quantum mechanical theory. Numerically solving the Schrödinger equation then allows us to capture the effect of Sommerfeld enhancement. While we have only considered simplified models in this work, our procedure generalizes straightforwardly to more complicated models as well.

We presented numerical results for the scalar and pseudoscalar case. The scalar mediator generates significant enhancement for low velocities and light mediators, an effect that has been studied extensively in the literature previously. Our numerical results for the pseudoscalar mediator show an excellent match to the tree-level perturbative QFT approximation. This lack of Sommerfeld enhancement is further supported by a Feynman diagrammatic argument. We also argued that Sommerfeld enhancement is absent for an axial vector mediator. In this scenario, the mediator mass and the gauge coupling are tied together such that as the mass is dialed down, the coupling gets correspondingly weaker. Our results suggest that, if the shape of the cross section discussed in[291] persists with more data and a better understanding of baryonic effects, then pseudoscalar and axial mediators will not fit the data as well as scalar and vector mediators. (These light-mediator models are not the only options, however; see, e.g.,[143,141,142]).

The matching procedure that we have described can be applied beyond the four simple models we have studied. For example, the axial vector model also in general has scattering mediated by the Higgs boson that provides a mass to the axial vector field. One could match to a theory that includes both the Higgs and axial-vector contributions. In general, our matching procedure will be useful in cases

with both long-range Sommerfeld enhanced scattering and short-distance contributions to the amplitude. Once the velocity-dependence of the cross section in a given model is known, it can be fed into simulations or other studies of structure formation, for instance in the ETHOS framework [157,389,172].

Our results also raise a more abstract question: to what extent are singular potentials in quantum mechanics relevant when matching to an underlying perturbative QFT? There is a large literature on singular quantum-mechanical potentials like $1/r^3$. We have observed that when matching to tree-level QFT, such terms are accompanied by spin-dependent factors that eliminate the dangerous terms in the leading-order Born approximation. It would be interesting to better understand the general properties of quantum mechanical models arising from weakly coupled QFTs, which we turn to in the next chapter.

3

The Singularity Structure of Quantum Mechanical Potentials

Quantum mechanical potentials are a low energy non-relativistic description of a scattering process. The space of these potentials is infinite as it contains all possible radial and angular dependences, as well as combinations of operators such as spin and angular momentum. From a bottom-up approach, we

are free to analyze any of these apparently consistent potentials we want in the framework of quantum mechanics. On the other hand, if the eventual goal is to obtain an underlying QFT description of the dynamics we are trying to model, then the space of viable potentials shrinks. This top-down approach relies on theoretical consistency, which serves as a powerful tool to limit the space of effective potentials. Potentials in this subspace can be UV completed into a QFT and as such, have a chance of describing the phenomena we see around us in the non-relativistic and the relativistic regime. In contrast, the potentials which are not a part of this subspace can never be UV completed to a QFT, so regardless of how good of an empirical fit they might be, the underlying microphysics will not be amenable to a QFT description.

Exploring the relationship between quantum mechanical potentials and field theory operators is certainly not new. It was originally studied in the context of Bethe-Salpeter equations in[76]. The authors concluded that super-renormalizable operators yielded regular potentials $V_r(r)$, renormalizable operators yielded transition potentials $V_t(r)$, and non-renormalizable operators yielded singular potentials $V_s(r)$ (see[219] for a review of singular potentials). These potentials satisfied the following conditions at the origin. Here, C is a finite constant.

$$\begin{aligned} \lim_{r\to 0}|r^2 V_r(r)| &= 0 \\ \lim_{r\to 0}|r^2 V_t(r)| &= C \\ \lim_{r\to 0}|r^2 V_s(r)| &= \infty \end{aligned} \tag{3.0.1}$$

Later, Lepage and Caswell developed a non-relativistic effective field theory approach to this prob-

lem in [123,314]. Although they didn't seek to address the relationship between field theory operators and singular potentials, their work simplified the analysis of many non-relativistic phenomena such as low energy scattering due to the new toolkit they introduced which leveraged the non-relativistic nature of the problem. More recently, we developed a novel matching procedure in [27], where we rely on a relativistic field theory description at short distances and a non-relativistic quantum mechanical description at large distances. The matching is performed at the Compton radius of the scattered particle, which is the natural scale where relativistic effects start becoming important. In light of this new approach, it is worth readdressing the question of what classes of field theory operators lead to singular potentials. As we will see, our conclusions about this classification differ from [76].

In [27], we showed that at short distances, there was a match between the tree-level relativistic field theory description and the first Born approximation using the corresponding quantum mechanical potential. This underlying correspondence between QFT and quantum mechanics naturally leads to the following criteria for determining which potentials can be consistently UV completed into a QFT:

> The space of consistent, nonsingular quantum mechanical potentials consists of those arising from a well-defined QFT scattering process. As a consequence of this definition, from the IR perspective, a quantum mechanical potential is inconsistent if it is singular, resulting in a divergent first Born approximation.

The analysis of low energy scattering is ubiquitous in various branches of physics. Non-relativistic nucleon-nucleon scattering [335,194] was a helpful tool in understanding the strong force. Non-relativistic scattering is also of central importance in determining properties of dark matter. Scattering pro-

cesses include dark matter direct detection [25,202,222,215,87] and dark matter scattering and annihilation in galaxies [260,261,262,55,105,320,384,80,291,94,27]. Furthermore, cross sections can be nonperturbatively enhanced via the Sommerfeld effect [373] in the non-relativistic regime. Analysis of the Sommerfeld effect, which was carried out in [27] in the context of self-interacting dark matter models, even showed that the potential generated by pseudoscalar exchange does not lead to any enhancement. This was a new result showing that the matching procedure was sufficient and there was no need to renormalize, as had previously been suggested in the literature. In addition, we also showed that the operator accompanying the potential was critical in reproducing the physics, and it was incorrect to approximate it as a simple $1/r^3$ central potential. With such a wide range of applications, isolating the space of consistent, nonsingular potentials becomes crucial for ensuring that the empirical description of a low energy phenomenon can be consistently completed into a QFT. This classification is also an important tool for effective field theorists tasked with building a theoretical description underlying these low energy processes, since it provides theoretical input on what classes of potentials are viable.

To begin exploring the space of viable potentials, in this chapter we will focus on perturbative QFTs. We will derive the potential experienced by fermions coupled in a variety of ways subject to a tree-level matching between QFT and quantum mechanics. Our focus will be on fermion-fermion scattering because each particle participating in the scattering has intrinsic spin which leads to a larger variety of possible operator structures in the non-relativistic potential. We briefly comment on the scalar-scalar and scalar-fermion scattering cases which work analogously, in Appendix B.1. We will begin by reviewing how to set up the initial conditions for the scattering process of interest in Section 3.1. Then we will start our investigation of potentials. Starting from an underlying QFT, we will study

the potentials generated from tree-level approximations to the field theory scattering process. This can be generated by renormalizable interactions coupling fermions and mediators, which we study in Section 3.2.1, or non-renormalizable interactions, which we study in Section 3.2.2. We relegate some detailed calculations to Appendix B.2. Having derived all of these potentials, we will be in a position to critically address which potentials are truly singular or not. This will conclude our study of tree-level potentials in 3 + 1-dimensions. In Section 3.3, we extend our tree-level results to higher dimensions. We offer concluding remarks in Section 3.4.

3.1 Setting Up the Scattering Calculation

In this section we will begin by discussing the derivation of potentials and then review the procedure we formulated in [27] for setting the boundary conditions. Given a set of interactions in a perturbative QFT, we can write down the tree-level QFT amplitude for a particular scattering process. In non-relativistic quantum mechanics, the Born approximation to the scattering amplitude is given by

$$\langle \vec{p}_f | i\mathcal{T} | \vec{p}_i \rangle = -i\widetilde{V}(\vec{q})(2\pi)\delta(E_{p_f} - E_{p_i}), \qquad \vec{q} = \vec{p}_f - \vec{p}_i. \tag{3.1.1}$$

If the relativistic corrections are small, then we can match the non-relativistic limit of the QFT amplitude to the quantum mechanical amplitude. This gives us the following expression for the Fourier transform of the quantum mechanical potential, $\tilde{V}(\vec{q})$, in terms of the QFT amplitude

$$\tilde{V}(\vec{q}) = -\frac{1}{2E_{p_f}}\frac{1}{2E_{p_i}}\mathcal{M}. \tag{3.1.2}$$

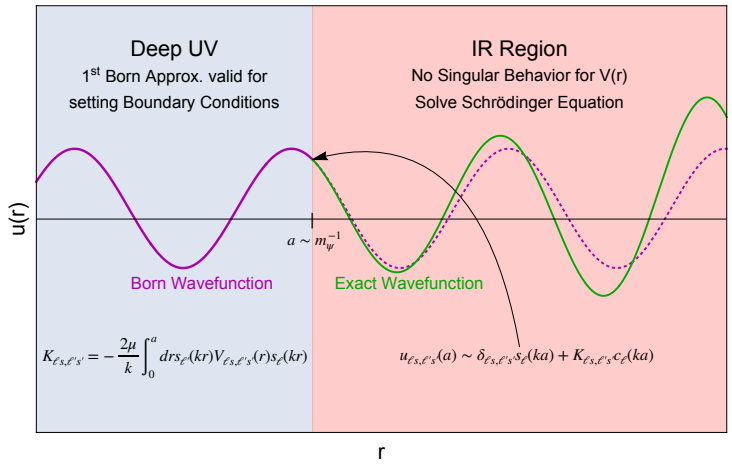

Figure 3.1: A schematic for the matching procedure adapted from [27]. We use the Born approximation to set the boundary conditions since we expect it to approximate the scattering process well in the deep UV. $r > a$ probes the IR of our theory where we expect the quantum mechanical potential to be a good description of our system. Since we have excised the origin, we no longer have to worry about the (potentially) singular nature of the potential while solving the Schrödinger equation. The exact wavefunction, which is the solution to the Schrödinger equation, can deviate from the Born wavefunction and these deformations are of physical significance, as evidenced by the analysis of Sommerfeld enhancement.

Relativistic and non-relativistic single particle states have a relative factor of $2E_p$ in their normalizations which is taken into account by the prefactor. The quantum mechanics calculation occurs in the center-of-mass frame. This effectively reduces it to a single particle problem, and hence provides only a single factor of $2E_p$ for the initial and final state. Once we have $\tilde{V}(\vec{q})$, we can Fourier transform with respect to $\vec{q}$ to compute the potential $V(\vec{r})$ in real space. We follow this procedure to arrive at the results in Section 3.2.

The observable of interest for a low energy scattering process is typically a cross section. In the non-relativistic regime, there can be significant deviations from a tree-level QFT approximation, for example from non-perturbative Sommerfeld enhancement [37 3]. A convenient way of accounting for these effects is to map the problem to an effective quantum mechanical problem, solving the Schrödinger

equation and extracting the scattering matrix elements. To solve the Schrödinger equation, we need to supply appropriate boundary conditions, in addition to the potential. The novel insight from [27] was that the physics occurring on short distance scales influences the wavefunction, which in turn affects the boundary conditions. To achieve this separation of scales, we split the region and match at the Compton radius of the scattered particle which is given by $a \sim \mathcal{O}(m_\psi^{-1})$. The Compton radius is the natural matching scale because for $r < a$, the particles start becoming relativistic with momenta of $\mathcal{O}(m_\psi)$. The quantum mechanical potential is a non-relativistic effective description of the scattering process, so at these scales, we should not expect this description to hold and must resort to the underlying relativistic QFT description. In [27], it was shown numerically that the QFT tree-level amplitude matched with the first Born approximation in quantum mechanics for $r < a$. We showed this for a variety of potentials, and also showed that this matching was robust to variations in the matching scale as long as it was $\mathcal{O}(m_\psi^{-1})$. Establishing this correspondence allows us to compute the boundary conditions at $r = a$, accounting for the effects of the short distance physics. For $r > a$, we are in the non-relativistic regime where quantum mechanics is an appropriate description of the physics. In this region, we can solve the Schrödinger equation and extract scattering matrix elements which incorporate long distance non-perturbative effects. This procedure ensures a separation of scales and that the appropriate description is used in the respective regimes. We show this schematically in Figure 3.1 and proceed to discuss how to implement this procedure in more detail.

If we assume $rV(r) \to 0$ as $r \to \infty$, then asymptotically, the wavefunction is a solution of the free

particle Schrödinger equation. s_ℓ and c_ℓ are solutions to the radial equation. They are given by

$$s_\ell(kr) \equiv krj_\ell(kr) \qquad c_\ell(kr) \equiv -kry_\ell(kr) \tag{3.1.3}$$

where the $j_\ell(kr)$ and $y_\ell(kr)$ are spherical Bessel functions and ℓ is the angular momentum of the corresponding partial wave. These solutions form a basis that the asymptotic solution to the full Schrödinger equation can be decomposed on. The decomposition is given by

$$u_{\ell s,\ell' s'}(r) \sim \delta_{\ell s,\ell' s'} s_\ell(kr) + K_{\ell s,\ell' s'} c_\ell(kr) \tag{3.1.4}$$

$u_{\ell s,\ell' s'}$ is the reduced radial wavefunction. $K_{\ell s,\ell' s'}$ is a matrix which generalizes partial wave phase shifts to account for interactions coupling various partial waves. As we will see shortly, this will be relevant for potentials such as those induced by pseudoscalar exchange. In this case, the differential equations are coupled, so that the potential $V(r)$ is now a matrix $V_{\ell s,\ell' s'}(r)$.

For a perturbative QFT, the tree-level QFT approximation of a particular matrix element will be faithfully reproduced by the first Born approximation which is given by

$$K_{\ell s,\ell' s'} = \frac{-2\mu}{k} \int_0^a dr s_{\ell'}(kr) V_{\ell s,\ell' s'}(r) s_\ell(kr) \tag{3.1.5}$$

In an operator language, the integrand of Equation 3.1.5 can be understood as

$$s_{\ell'}(kr) V_{\ell s,\ell' s'}(r) s_\ell(kr) \propto \langle \ell' | \hat{V}_{\ell s,\ell' s'} | \ell \rangle \tag{3.1.6}$$

where $\hat{V}_{\ell s,\ell' s'}$ is now an operator and $|\ell\rangle$ are states with angular momentum ℓ. The boundary conditions at $r = a$ are then given by

$$u_{\ell s,\ell' s'}(a) \sim \delta_{\ell s,\ell' s'} s_\ell(ka) + K_{\ell s,\ell' s'} c_\ell(ka) \tag{3.1.7}$$

Using the method we described above, we now have a clear analytical diagnostic for evaluating whether a potential is singular or not:

> **Diagnostic:** If the integral in Equation 3.1.5 diverges for *any* combination of incoming and outgoing states, then the potential is singular.

Since we are working in the non-relativistic regime, the argument kr is always small over the interval of integration. For small arguments, we expand the spherical Bessel function and find that $s_\ell(kr) \sim (kr)^{\ell+1}$. Setting $\ell = \ell' = 0$ in Equation 3.1.5 and using the small argument expansion of s_ℓ, we recover the familiar fact that if a potential diverges faster than r^{-2} as $r \to 0$, the potential might be singular. We now derive tree-level potentials for various interactions and analyze whether they are singular or not using the analytic diagnostic discussed above.

3.2 Tree-Level Potentials

In this section, we will compute the tree-level potentials experienced by fermions coupled via various interactions. By tree-level potential here we mean that the amplitude in the QFT is the tree-level am-

plitude. For concreteness, we will study the process $\psi_1\psi_2 \to \psi_1\psi_2$ where ψ_i are spin-1/2 fermions. We will consider cases with and without a mediator.

3.2.1 Renormalizable Interactions

We begin by considering potentials generated by renormalizable operators in the QFT. For concreteness we will consider the following operators

$$\mathcal{L}_{\mathbf{s}} = \lambda\varphi\bar{\psi}\psi \quad \mathcal{L}_{\mathbf{ps}} = i\lambda\varphi\bar{\psi}\gamma^5\psi \quad \mathcal{L}_{\mathbf{v}} = \lambda\varphi^\mu\bar{\psi}\gamma_\mu\psi \quad \mathcal{L}_{\mathbf{av}} = \lambda\varphi^\mu\bar{\psi}\gamma_\mu\gamma^5\psi \tag{3.2.1}$$

Here the subscripts $\mathbf{s}$, $\mathbf{ps}$, $\mathbf{v}$, and $\mathbf{av}$ denote scalar, pseudoscalar, vector and axial vector respectively. To encompass all possible pairings of interactions, we consider two fermion species ψ_1 and ψ_2 each of which is independently subject to one of the interactions in Equation 3.2.1. At tree-level, the process $\psi_1\psi_2 \to \psi_1\psi_2$ only has a t-channel Feynman diagram contributing to it.[1] From the tree-level amplitude, we obtain the following potentials

$$V_{\mathbf{s},\mathbf{s}}(r) = -\frac{\lambda_1\lambda_2}{4\pi r}e^{-m_\varphi r} \tag{3.2.2}$$

$$V_{\mathbf{ps},\mathbf{ps}}(r) = \frac{\lambda_1\lambda_2}{4\pi m_1 m_2}e^{-m_\varphi r}\left[\left(\frac{m_\varphi^2}{3r} - \frac{4\pi\delta^3(\vec{r})}{3}\right)\vec{S}_1\cdot\vec{S}_2 + \frac{\mathcal{O}_T}{r^3}\left(1 + m_\varphi r + \frac{m_\varphi^2 r^2}{3}\right)\right] \tag{3.2.3}$$

[1] Processes like $\psi\bar{\psi} \to \psi\bar{\psi}$ also have a contribution from an s-channel Feynman diagram. This gives rise to a $\delta^3(\vec{r})$ contact interaction in the non-relativistic limit. It can explicitly be shown, by computing Equation 3.1.5, that $\delta^3(\vec{r})$ gives a finite nonsingular result for all possible values of ℓ and ℓ'.

$$V_{\mathbf{v,v}}(r) = \frac{\lambda_1\lambda_2}{4\pi r}e^{-m_\varphi r} \tag{3.2.4}$$

$$V_{\mathbf{av,av}}(r) = -\frac{\lambda_1\lambda_2}{\pi r}e^{-m_\varphi r}\vec{S}_1\cdot\vec{S}_2 + \frac{4m_1m_2}{m_\varphi^2}V_{\mathbf{ps,ps}} \tag{3.2.5}$$

$$V_{\mathbf{s,ps}}(r) = \frac{\lambda_1\lambda_2}{4\pi m_2}\frac{1+m_\varphi r}{r^2}e^{-m_\varphi r}\vec{S}_2\cdot\hat{r} \tag{3.2.6}$$

$$V_{\mathbf{v,av}}(r) = \frac{\lambda_1\lambda_2}{2\pi}\frac{e^{-m_\varphi r}}{r}\left[\frac{1+m_\varphi r}{m_1 r}(\vec{S}_1\times\vec{S}_2)\cdot\hat{r} + \vec{S}_2\cdot\left(\frac{\vec{p}_2}{m_2}-\frac{\vec{p}_1}{m_1}\right) + \frac{i(m_1+m_2)}{2m_1m_2}\frac{1+m_\varphi r}{r}\vec{S}_2\cdot\hat{r}\right] \tag{3.2.7}$$

The potentials we derive above agree with previous results [330,176,202,215,80,158,200][2]. The subscripts for V indicate the type of interaction vertices present in the Feynman diagram. The first subscript denotes the ψ_1 coupling and the second subscript denotes the ψ_2 coupling. Here, m_i denotes the mass of fermion ψ_i and $\vec{S}_i$ its spin. We also define the operator $\mathcal{O}_T$ as

$$\mathcal{O}_T = 3(\vec{S}_1 \cdot \hat{r})(\vec{S}_2 \cdot \hat{r}) - \vec{S}_1 \cdot \vec{S}_2 \tag{3.2.8}$$

We note that the only potential which has terms diverging faster than r^{-2} near the origin is $V_{\mathbf{ps,ps}}$ (and in turn $V_{\mathbf{av,av}}$). The $\mathcal{O}_T$ term is potentially problematic since it has a piece diverging as r^{-3}. In particular, the first Born approximation is well-behaved for every combination of states besides potentially the $\ell = \ell' = 0$ case. While this scenario could be divergent, in [27] we showed that $\langle \ell' = 0 | \mathcal{O}_T | \ell = 0 \rangle = 0$. So, the operator structure in the potential prevents the divergence from arising and $V_{\mathbf{ps,ps}}$ is not singular. Therefore, all of the potentials we consider in this section are non-singular.

3.2.2 Non-Renormalizable Interactions

The case of potentials arising from non-renormalizable interactions factors into two scenarios: ones with a mediator and ones without. Examples of the former include the fermions coupled to a field strength tensor or derivatively coupled to a Goldstone while examples of the latter include four-fermion

[2] $V_{\mathbf{s,ps}}(r)$ and $V_{\mathbf{v,av}}(r)$ differ by an overall sign relative to the results in [200]. This discrepancy arises because we choose ψ_1 to have a scalar (or vector) interaction and ψ_2 to have a pseudoscalar (or axial vector) interaction while they consider the opposite scenario.

operators.

We begin by analyzing the Goldstone and tensor couplings

$$\mathcal{L}_{\text{Goldstone}} = \frac{1}{\Lambda}\overline{\psi}\gamma^{\mu}\gamma^{5}\psi\partial_{\mu}\varphi \qquad \mathcal{L}_{\text{tensor}} = \frac{1}{2\Lambda}\overline{\psi}\sigma^{\mu\nu}\psi F_{\mu\nu} \tag{3.2.9}$$

These couplings are examples of scenarios where we have a scalar or vector mediator but the coupling is non-renormalizable. Here we define $\sigma^{\mu\nu} = \frac{i}{4}[\gamma^{\mu}, \gamma^{\nu}]$ and $F_{\mu\nu} = \partial_{\mu}\varphi_{\nu} - \partial_{\nu}\varphi_{\mu}$.

From the tree-level amplitude, we obtain the following potentials

$$V_{\text{Goldstone}}(r) = \frac{e^{-m_{\varphi}r}}{\pi\Lambda^{2}}\left[\left(\frac{m_{\varphi}^{2}}{3r} - \frac{4\pi\delta^{3}(\vec{r})}{3}\right)\vec{S}_{1}\cdot\vec{S}_{2} + \frac{\mathcal{O}_{T}}{r^{3}}\left(1 + m_{\varphi}r + \frac{m_{\varphi}^{2}r^{2}}{3}\right)\right] \tag{3.2.10}$$

$$V_{\text{tensor}}(r) = \frac{e^{-m_{\varphi}r}}{4\pi\Lambda^{2}}\left[\frac{\mathcal{O}_{T}}{r^{3}}\left(1 + m_{\varphi}r + \frac{m_{\varphi}^{2}r^{2}}{3}\right) - \left(\frac{2m_{\varphi}^{2}}{3r} + \frac{4\pi\delta^{3}(\vec{r})}{3}\right)\vec{S}_{1}\cdot\vec{S}_{2}\right] + \frac{\delta^{3}(\vec{r})}{\Lambda^{2}}\vec{S}_{1}\cdot\vec{S}_{2} \tag{3.2.11}$$

We can also consider tensor couplings of the form $i\overline{\psi}\sigma^{\mu\nu}\gamma^{5}\psi F_{\mu\nu}$. Together, these two tensor couplings are the magnetic and electric dipole interactions, respectively. These two interactions are related via $2i\sigma^{\sigma\rho} = \varepsilon^{\mu\nu\sigma\rho}\sigma_{\mu\nu}\gamma^{5}$. The potential generated by this interaction has an additional ε tensor inserted at each vertex, but this does not change the overall radial dependence of the potential. The difference between these two interactions manifests when we consider monopole-dipole type couplings. Particles with an intrinsic electric dipole moment experience enhancements in the non-relativistic regime when scattering off a charged particle, whereas particles with intrinsic magnetic dipole moments do

not. Understanding the nature of this enhancement warrants solving the Schrödinger equation with the appropriate potential. For the purpose of our study, we are only interested in the structure of the potential and whether it gives rise to a finite first Born approximation. It can be shown that this is the case for both tensor potentials and the Goldstone potential, so all these potentials are consistent and nonsingular.

Next, we consider the scenario where we don't have a mediator. Scenarios like this arise when a heavy mediator has been integrated out leaving effective four fermion operators. The most general four fermion operator we can write down has the form

$$\frac{\lambda}{\Lambda^2}\overline{\psi}_1\Gamma_1\psi_1\overline{\psi}_2\Gamma_2\psi_2 \tag{3.2.12}$$

In Table 3.1, we tabulate the leading non-relativistic potentials in position space for various four fermion operators, which agree with the results in [202].

The Goldstone and tensor potentials both have potentially problematic terms which are accompanied by $\mathcal{O}_T$ preventing the singularity from arising. The potentials from four fermion operators are all accompanied by $\delta^3(\vec{r})$, as seen in Table 3.1. For a simple delta function, the integrand of Equation 3.1.5 scales as $\delta(r)r^{\ell+\ell'}$ which is finite for $\ell = \ell' = 0$ and zero otherwise. Potentials with derivatives might seem problematic at first, but we show in detail in Appendix B.2 that they also produce finite well-behaved first Born approximations. So we see that any tree-level potential arising from a QFT is nonsingular. In the next section, we consider generalizations to arbitrary spatial dimensions.

Table 3.1: Leading non-relativistic potentials generated for various effective four fermion operators.

Effective Operator	Position Space Potential
$\frac{\lambda}{\Lambda^2}\overline{\psi}_1\psi_1\overline{\psi}_2\psi_2$	$\frac{\lambda}{\Lambda^2}\delta^3(\vec{r})$
$\frac{\lambda}{\Lambda^2}\overline{\psi}_1\gamma^5\psi_1\overline{\psi}_2\gamma^5\psi_2$	$\frac{\lambda}{m_1m_2\Lambda^2}(\vec{S}_1\cdot\vec{\nabla})(\vec{S}_2\cdot\vec{\nabla})\delta^3(\vec{r})$
$\frac{i\lambda}{\Lambda^2}\overline{\psi}_1\psi_1\overline{\psi}_2\gamma^5\psi_2$	$\frac{\lambda}{m_2\Lambda^2}(\vec{S}_2\cdot\vec{\nabla})\delta^3(\vec{r})$
$\frac{\lambda}{\Lambda^2}\overline{\psi}_1\gamma^\mu\psi_1\overline{\psi}_2\gamma_\mu\psi_2$	$\frac{\lambda}{\Lambda^2}\delta^3(\vec{r})$
$\frac{\lambda}{\Lambda^2}\overline{\psi}_1\gamma^5\gamma^\mu\psi_1\overline{\psi}_2\gamma^5\gamma_\mu\psi_2$	$-\frac{4\lambda}{\Lambda^2}\vec{S}_1\cdot\vec{S}_2\delta^3(\vec{r})$
$\frac{\lambda}{\Lambda^2}\overline{\psi}_1\gamma^\mu\psi_1\overline{\psi}_2\gamma^5\gamma_\mu\psi_2$	$\frac{\lambda}{\Lambda^2}\left(2\vec{S}_2\cdot\left(\frac{\vec{p}_2}{m_2}-\frac{\vec{p}_1}{m_1}\right)-i\frac{m_1+m_2}{m_1m_2}(\vec{S}_2\cdot\vec{\nabla})+\frac{2}{m_1}(\vec{S}_2\times\vec{S}_1)\cdot\vec{\nabla}\right)\delta^3(\vec{r})$

3.3 Extension to Arbitrary Dimensions

We begin by considering the Schrödinger equation for a particle that is not subject to any potential, in d spatial dimensions [196,177,237,120]. This is given by

$$-\frac{1}{2\mu}\nabla_d^2\Psi(r)=E\Psi(r)\qquad\nabla_d^2=\partial_r^2+\frac{d-1}{r}\partial_r+\frac{1}{r^2}\Omega^2 \tag{3.3.1}$$

∂_r represents derivatives with respect to the radial coordinate, Ω^2 is the Laplacian on the $(d-1)$-sphere and μ is the reduced mass. We can decompose $\Psi(r)$ into the product of a radial function $R(r)$ and Gegenbauer polynomials, which are eigenfunctions of Ω^2. The Gegenbauer polynomials are a generalization of the spherical harmonics to higher dimensions. We notice that for $d=3$, we recover the familiar eigenvalue of $\ell(\ell+1)$ for the angular momentum term. Analogous to the 3 + 1-dimensional

case, we obtain a radial equation for every harmonic.

$$\partial_r^2 R + \frac{d-1}{r}\partial_r R - \frac{\ell(\ell+d-2)}{r^2}R = -k^2 R \tag{3.3.2}$$

To cancel the term with the first derivative of $R(r)$, we can set $u(r) = r^{(d-1)/2}R(r)$. This simplifies the radial equation to

$$\partial_r^2 u + \left[k^2 - \frac{j(j+1)}{r^2}\right]u = 0 \qquad j = \ell + \frac{d-3}{2} \tag{3.3.3}$$

The radial free particle solutions are denoted s_j and c_j and are given in terms of spherical Bessel functions as before, with the only difference being that the order is now dimension dependent.

$$s_j(kr) = krj_j(kr) \qquad c_j = -kry_j(kr) \tag{3.3.4}$$

As a test case, we will consider the Coulomb potential which in d spatial dimensions is given by $V(r) = \alpha/r^{d-2}$. For $d > 4$, this potential diverges faster than r^{-2} and there is no accompanying operator structure that can give vanishing matrix elements between potentially problematic states. Naively, this potential appears to be problematic. To test whether this potential is singular, we compute the

first Born approximation using Equation 3.1.5

$$\begin{aligned} K_{js,j's'} &= \frac{-2\mu}{k}\int_0^a dr s_{j'}(kr)V_{js,j's'}(r)s_j(kr) \\ &\approx \frac{-2\alpha\mu}{k}\int_0^a dr r^{j'+1}r^{2-d}r^{j+1} \\ &\approx \frac{-2\alpha\mu}{k}\int_0^a dr r^{\ell'+\ell+1} \end{aligned} \tag{3.3.5}$$

The most divergent case corresponds to $\ell = \ell' = 0$, which we explicitly see is finite and nonsingular. This is a clear indication that potentials diverging faster than r^{-2} should not be the sole diagnostic for evaluating whether they are singular or not. Furthermore, the dependence on dimension drops out. This indicates that Coulomb potentials, which have well-defined QFT descriptions in any number of dimensions, are always nonsingular, and our proposed diagnostic for testing this works. By extending our analysis to an arbitrary number of dimensions, we see that our earlier results were not just an artifact of working in 3 + 1-dimensions. It also indicates that there exists a deeper connection between QFT and quantum mechanics, where a tree-level perturbative QFT will always produce a nonsingular potential. These results clearly support our refined definition of what a singular potential is as well as our criteria for determining if a potential is singular or not.

3.4 Conclusions

In this chapter, we have studied the non-relativistic potentials generated for a variety of interactions between spin-1/2 particles. These include interactions mediated by scalars or vectors as well as four fermion operators. We reviewed the procedure laid out in [27] for setting boundary conditions. In ad-

dition to setting the boundary conditions for the Schrödinger equation, this procedure also provided us with an analytic cross-check for determining whether a potential is singular or not. Using this diagnostic, we showed that all of the potentials generated from tree-level QFT descriptions of scattering processes give rise to nonsingular well-behaved quantum mechanical potentials. In many cases, this nonsingular behavior is preserved by nontrivial cancellations that arise due to the accompanying operators. Furthermore, we extended this analysis to higher dimensions and showed that Coulomb potentials in an arbitrary number of dimensions are also nonsingular. These results lend credence to the notion of a subspace of consistent, effective quantum mechanical potentials and indicate that subject to our matching procedure, singular potentials in quantum mechanics are irrelevant when considering a matching to an underlying perturbative tree-level QFT.

We emphasize that all of the evidence presented so far is from tree-level examples. This motivates various different avenues to follow up on our results. In particular, it would be interesting to understand how to extend the matching procedure beyond tree-level. This extension will be relevant for computing loop-level corrections to these potentials as well as processes where the leading order scattering occurs at 1-loop in QFT [122,212,208,274,209,270,214,245,211,89,213,100,376,305,152,229,369,151,96]. QFTs that spontaneously break Lorentz invariance also yield long-range potentials and it will be interesting to explore the structure of these potentials in more detail [53]. Nonperturbative QFT, such as coupling to CFT sectors [152], presents an additional class of nontrivial examples and at present, it is not clear whether this can give rise to singular potentials from the quantum mechanics viewpoint. As such, it is worth exploring the types of potentials which can arise in these theories. These various investigations will help further refine the boundary between quantum mechanical potentials which can be UV

completed to a QFT and those which cannot.

4

A Closer Look at CP-Violating Higgs Portal Dark Matter as a Candidate for the GCE

4.1 Introduction

Over the years, there have been tantalizing hints in various experiments of potential dark matter signatures; while many of these signals have vanished due to increased statistics or a better understanding

of systematic uncertainties, some signals, such as the Galactic Center Excess (GCE), have persisted for over a decade.

In astrophysical settings, the Galactic Center is expected to have some of the largest dark matter densities, and is therefore one of the most promising targets for indirect searches. The GCE is a statistically significant excess of gamma rays at energies of $\sim 2-3$ GeV observed in the Galactic Center by the Fermi Gamma Ray Space Telescope[29]. As pointed out by[238,267,269,241,13,161,114], the GCE could be explained by a thermal WIMP annihilating to Standard Model particles. To truly confirm such a hypothesis, it is crucial to observe a signal in other indirect channels. In fact, it is possible that AMS-02 is observing an antiproton excess[28] at a concordant energy range[156,155,138,268], though the existence of this excess is not as well established[97,258]. While promising, it has also been suggested that the GCE signal could be generated by millisecond pulsars[136,137]. In recent years, the debate surrounding the origin of the GCE has intensified[311,73,312,322,251,74,323,306,397,307,308,109,14,318,329,293]. New measurements in the coming decade and a better theoretical understanding of Galactic diffuse emission models will help settle this debate, but until then, the origin of the GCE remains unknown and dark matter annihilation remains a viable explanation.

As discussed in[161,114], the GCE can be well described by dark matter annihilations, particularly to $b\bar{b}$. This has fostered the development of many dark matter models with WIMP-like annihilation mechanisms, which are too numerous to review here (see[50] for a review). Of these, models with pseudoscalar s-channel mediators are particularly well-motivated because they are neutral and can evade direct detection constraints. In particular, if the dark matter lives close to resonance, the annihilation cross section can be boosted enough to explain the GCE[271,95,128,250,116,84,227,182]. While much of

the previous work relies on the introduction of a new pseudoscalar mediator, the authors of [119] proposed an interesting alternative. In their setup, the dark sector is connected to the visible sector via a CP-violating coupling to the Higgs, which allows annihilation and spin-independent scattering to be governed by different parameters. In principle, the CP-violating coupling can generate a viable thermal relic candidate even away from the resonance, by suppressing the scattering rather than enhancing the annihilation. However, in [119], the authors consider specific model realizations within the context of supersymmetry where the benchmark best fit model still has the dark matter mass very close to half the Higgs mass.

In this work, we extract the key ingredients of their model, namely a Majorana dark matter candidate with CP-violating coupling to the Higgs, and explore the extent of freedom away from the mass resonance that can be achieved with larger CP-violating couplings. We see that for large enough coupling in the dark matter EFT, there is $\mathcal{O}(10)$ GeV flexibility for the dark matter mass when the phase is approximately $\pi/2$.

We also consider and explore the phenomenology of two different minimal UV realizations of this scenario: singlet-doublet dark matter [325,170,192,149,129,17,113,221,68,111,321] and doublet-triplet dark matter [164,17,221,321]. We study both how these models translate to EFT parameters, and constraints governing these UV realizations, including contributions to the electron electric dipole moment (EDM), the Peskin-Takeuchi parameters, as well as possible collider signatures. We find that while the dark matter mass and CP-violating phase are independent parameters in the EFT, their dependence in the UV completion is quite nonlinear since the Yukawa coupling directly affects the dark matter mass. Specifically, it is difficult to achieve the phase tuning scenario without also tuning the mass in the UV

completion, because the large couplings that are required to generate the annihilation cross section when away from resonance also change the dark matter mass. Additionally, we find that the amount of CP-violation in the UV may not be reflective of that observed in the EFT. In the singlet-doublet case, we find two different types of viable parameter space. When the UV couplings are small, both the singlet mass in the UV and the dark matter mass must be very close to $m_h/2$, but the phase is flexible. When the UV couplings are larger, parameters must be chosen such that both the phase of the dark matter-Higgs coupling and the dark matter mass must be somewhat tuned, but there is more flexibility in the dark matter and singlet masses than in the small coupling case. In the doublet-triplet model, we find that EDM, spin-independent direct detection, and charged fermion collider search constraints are sufficient to rule out any WIMP-scale annihilation signal.

The rest of this chapter is organized as follows. In Section 4.2, we discuss the effective field theory of Majorana dark matter interacting with the Standard Model through a CP-violating Higgs coupling. The EFT parameters dictate the annihilation and scattering cross sections which are broadly applicable independent of specific UV completions. In Section 4.3, we UV complete the EFT by introducing a singlet Majorana fermion and a doublet Dirac fermion. In Section 4.4, we consider another UV completion by introducing a doublet Dirac fermion and a triplet Majorana fermion. We discuss the strong constraints placed on each of these models by a variety of complementary experimental probes such as the electron EDM, precision electroweak parameters, and collider searches. Finally, we offer concluding remarks in Section 4.5.

4.2 Model Independent Constraints in the Effective Theory

In this section we take an effective field theory approach and focus on the phenomenology of a single species of Majorana dark matter which couples to the visible sector via a CP-violating Higgs portal. After spontaneous symmetry breaking (SSB), the corresponding terms in the Lagrangian are given by

$$\mathcal{L} \ni \frac{y_{h\chi}}{2\sqrt{2}} h\bar{\chi}P_L\chi + \frac{y^*_{h\chi}}{2\sqrt{2}} h\bar{\chi}P_R\chi + \frac{g_{Z\chi}}{2} Z_\mu \bar{\chi}\gamma^\mu\gamma^5\chi \tag{4.2.1}$$

where the CP-violation manifests in the complex nature of dark matter-Higgs coupling $y_{h\chi}$. Furthermore, we have also allowed for a coupling $g_{Z\chi}$ to the Z boson.[1]

As in all WIMP-type solutions to the GCE, the burden of the model is to reconcile the $\mathcal{O}(1)$ pb annihilation cross section necessary to achieve both the observed gamma-ray excess and the dark matter relic density, with the $\mathcal{O}(10^{-10})$ pb bounds on spin-independent scattering with nucleons from direct detection experiments. Traditionally, this is achieved for Higgs-portal dark matter by tuning the dark matter mass to the s-channel resonance $2m_\chi \sim m_h$, but an additional avenue is available in the case of our model.

In the non-relativistic limit, two Majorana fermions form a CP-odd state, so annihilation into the CP-even Higgs through a CP-conserving coupling is p-wave suppressed. It then follows that if the coupling is complex, the annihilation in this limit is dominantly set by the imaginary part of $y_{h\chi}$, which is reflected in the result we obtain in Equation 4.2.4. Conversely, the dark matter scattering off of the nucleon (or quark) does not require any CP-violation since the initial and final states have the same

[1] χ does not have a vector current coupling because $\bar{\chi}\gamma^\mu\chi$ vanishes identically for Majorana fermions.

CP properties, and thus we expect the spin-independent scattering cross section to be proportional to the real part of $y_{h\chi}$. This is reflected in the result we obtain in Equation 4.2.13. Therefore, the phase of the Higgs coupling can also contribute to a large hierarchy between the scattering and annihilation cross sections. With this intuition, we describe the details and corresponding phenomenology of this theory in the remainder of this section.

4.2.1 Annihilation

Annihilation is mediated by both the Higgs and the Z boson through an s-channel diagram. The dark sector couplings contributing to dark matter annihilation into SM fermions are given in Equation 4.2.1, and the visible sector couplings have the form

$$\mathcal{L} \ni \sum_f \frac{y_{hf}}{\sqrt{2}} h\bar{f}f + g_{Zf} Z_\mu \bar{f}\gamma^\mu (v_f - a_f\gamma^5) f. \tag{4.2.2}$$

The couplings are given by their SM values

$$y_{hf} = -\frac{\sqrt{2}m_f}{v}, \quad g_{Zf} = \frac{e}{2\cos\theta_w \sin\theta_w}, \quad v_f = I_3 - 2Q\sin^2\theta_w, \quad a_f = I_3, \tag{4.2.3}$$

where v is the Higgs vev, θ_w is the Weinberg angle, and m_f, I_3, and Q are the mass, weak isospin, and electric charge of the fermion respectively. In the non-relativistic limit, the total spin-averaged amplitude squared for annihilation can be written as

$$|\mathcal{M}|^2_{\chi\chi\to f\bar{f}} = 4m_\chi^2 \left[\frac{m_f^2}{m_Z^4} g_{Zf}^2 g_{Z\chi}^2 a_f^2 + y_{hf}^2 \mathrm{Im}[y_{h\chi}]^2 \frac{(m_\chi^2 - m_f^2)}{(m_h^2 - 4m_\chi^2)^2 + m_h^2 \Gamma_h^2} \right], \tag{4.2.4}$$

where Γ_h denotes the width of the Higgs. The Higgs mediated piece depends only on the imaginary part of the coupling as expected. The cross section is correspondingly given by

$$\langle \sigma v \rangle = \sum_{m_f \leq m_\chi} \frac{N_c \sqrt{m_\chi^2 - m_f^2}}{64\pi m_\chi^3} |\mathcal{M}|^2_{\chi\chi\to f\bar{f}}. \tag{4.2.5}$$

If the dark matter is a thermal relic, then the present-day dark matter abundance, $\Omega_\chi h^2 = 0.11$, sets the annihilation cross section at the time of freeze-out, which is the well-known $\mathcal{O}(1)$ pb weak-scale cross section [396,131,310,272,394,380,368,85,375,244,236,381]. Recent work [86,15] has shown that for models with a hierarchy between annihilation and scattering strengths, early kinetic decoupling before freeze-out alters this number, requiring a larger cross section to achieve the observed abundance. At most extreme, a $\sim$ 20 pb annihilation cross section may be needed for a $\sim$ 57 GeV dark matter with purely imaginary couplings, though this is quite sensitive to the details of the QCD phase transition. However, this effect is significantly weaker for masses $\gtrsim m_h/2$, so we do not take our annihilation cross section to be this large.

At present, dark matter annihilation is expected to produce a distribution of gamma-rays whose flux is given by

$$\frac{d^2\Phi_\gamma}{d\Omega dE_\gamma} = \frac{1}{2}\langle \sigma v \rangle \left(\sum_f \frac{dN_\gamma}{dE\gamma} \mathrm{Br}_{\chi\chi\to f\bar{f}} \right) \int_{\mathrm{los}} \frac{\rho_\chi^2(r) d\ell}{4\pi m_\chi^2}, \tag{4.2.6}$$

where $\mathrm{Br}_{\chi\chi\to f\bar{f}}$ denotes the branching ratio to the $f\bar{f}$ final state, and dN_γ/dE_γ its corresponding injec-

tion spectrum. $\rho_\chi(r)$ denotes the dark matter halo profile and is integrated over the line-of-sight to the Galactic Center. It has been shown that the Fermi GCE data is well-modeled by a Higgs portal dark matter with a cross section $\langle\sigma v\rangle \sim 3$ pb, assuming a modified NFW profile[267]. As the precise best fit depends on many details, including the galactic profile and background modeling[171], in conjunction with the modeling uncertainties of the thermal relic argument, we will consider here a range of cross sections $\langle\sigma v\rangle$ from 1 to 10 pb to be in concordance with both the GCE and the relic abundance.

4.2.2 Direct Detection

In contrast with annihilation, processes relevant for direct detection occur below the weak scale and should be considered in terms of effective interactions with target nuclei. Much of the subsequent discussion follows[317]. At momentum transfers $t \ll m_Z^2$, the interactions in Equations 4.2.1 – 4.2.2 are rewritten as the following dimension-6 operators

$$\mathcal{L} \ni \frac{C_S}{m_h^2}\bar{\chi}\chi\bar{f}f + \frac{C_{PS}}{m_h^2}\bar{\chi}\gamma^5\chi\bar{f}f + \frac{C_V}{m_Z^2}\bar{\chi}\gamma^\mu\gamma^5\chi\bar{f}\gamma_\mu f + \frac{C_{PV}}{m_Z^2}\bar{\chi}\gamma^\mu\gamma^5\chi\bar{f}\gamma_\mu\gamma^5 f \tag{4.2.7}$$

with C_S, C_{PS}, C_V, and C_{PV} denoting the scalar, pseudo-scalar, vector, and pseudo-vector pieces of the quark-gauge couplings respectively. The contributions governed by C_{PS} and C_V are velocity-suppressed and we neglect them in the following. After matching to the UV theory, the coefficients are given by

$$C_S = \frac{1}{2}\mathrm{Re}[y_{h\chi}]y_{hf} \qquad C_{PV} = g_{Z\chi}g_{Zf}a_f. \tag{4.2.8}$$

In the zero momentum transfer limit, the nucleon-level operators are matched to the quark-level ones via form factors

$$\langle N(p)|\bar{f}\gamma^{\mu}\gamma^{5}f|N(p')\rangle = \bar{u}_N(p)\left[\Delta_1^{f,N}(q^2)\gamma^{\mu}\gamma^{5}\right]u_N(p') \tag{4.2.9}$$

$$\langle N(p)|\bar{f}f|N(p')\rangle = \frac{m_N}{m_f}f_f^N\bar{u}_N(p)u_N(p') \tag{4.2.10}$$

where N represents a nucleon (a proton or neutron), $q = p' - p$ denotes the momentum transfer, and the form factors are listed in Table 4.1. We have neglected higher order terms in q^2. For the scalar term specifically, the heavy quarks also contribute via a gluon loop. After integrating out heavy quarks, the relevant operator for each flavor appears as

$$-\frac{C_S}{m_b^2}\frac{\alpha_s}{12\pi m_f}\bar{\chi}\chi G^{\mu\nu}G_{\mu\nu}. \tag{4.2.11}$$

To match to the nucleon-level picture the following matrix element is taken into account

$$\langle N(p)|G^{\mu\nu}G_{\mu\nu}|N(p')\rangle = -\frac{8\pi}{9\alpha_s}m_N f_g^N\bar{u}_N(p)u_N(p'). \tag{4.2.12}$$

In terms of the quark-level couplings, the nucleon-level spin-independent cross section is given by

$$\sigma_{SI} = \frac{m_N^2 m_\chi^2}{4\pi(m_\chi + m_N)^2}\left[\frac{\mathrm{Re}[y_{b\chi}]}{m_b^2}\left[\sum_{f\in u,d,s} y_{bf}\frac{m_N}{m_f}f_f^N + \sum_{f\in c,b,t} y_{bf}\frac{2}{27}\frac{m_N}{m_f}f_g^N\right]\right]^2. \tag{4.2.13}$$

	$\Delta_1^{N,u}$	$\Delta_1^{N,d}$	$\Delta_1^{N,s}$	f_u^N	f_d^N	f_s^N	f_g^N
Protons	0.80	-0.46	-0.12	0.018	0.027	0.037	0.917
Neutrons	-0.46	0.80	-0.12	0.013	0.040	0.037	0.910

Table 4.1: Here we show the light quark and gluon form factors for the proton and neutron. These values come from [146,259,88,188] and are summarized in [317].

As discussed earlier, the cross section only depends on the real part of the Higgs coupling. Furthermore, the dependence on the coupling to the Z boson vanishes in the $q \to 0$ limit. Likewise the spin-dependent cross section is given by

$$\sigma_{SD} = \frac{3m_N^2 m_\chi^2}{\pi(m_\chi + m_N)^2} \left[\frac{g_{Z\chi}}{4m_Z^2} \sum_{f \in u,d,s} g_{Zf} a_f \Delta_1^{N,f} \right]^2 . \tag{4.2.14}$$

4.2.3 Results and Discussion

In this subsection we examine the phenomenology of the effective theory, and discuss the regions of parameter space where a high annihilation and low scattering cross section can be achieved – specifically we are interested in an annihilation cross section between approximately 1 and 10 pb to fit the GCE and a scattering cross section consistent with direct detection experiments. For spin-independent scattering, the strongest limits come from XENON1T[46,47], while for spin-dependent scattering, the strongest limits come from both XENON1T[48] and PICO[42,43]. LZ[32] and XENONnT[49] are projected to improve on current limits within the parameter space of interest. The projected limits are comparable, so we show only one in our figures for clarity. We omit limits from IceCube[12], LUX[30,31]

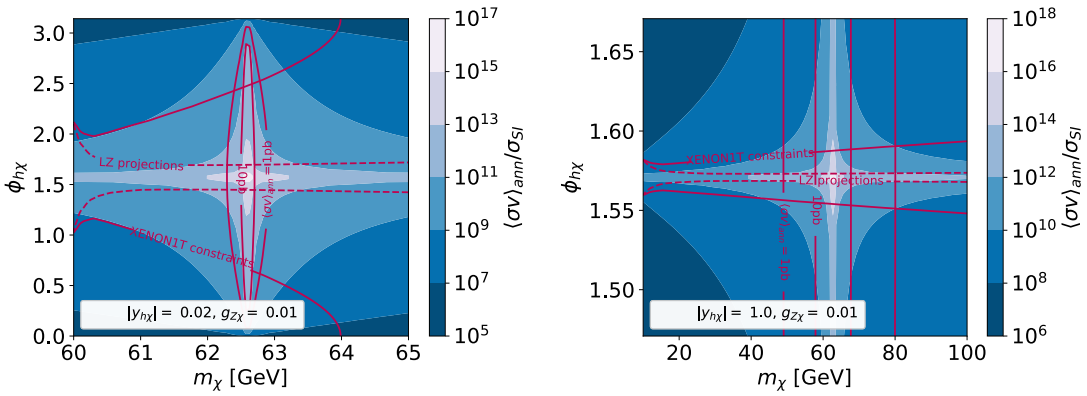

Figure 4.1: The ratio between annihilation and spin-independent direct detection cross sections on the $m_\chi - \varphi_{h\chi}$ plane for different values of $|y_{h\chi}|$. The region allowed by direct detection is inside the solid XENON1T[46,47] constraint line, while the region allowed by annihilation is between the solid 1 pb and 10 pb lines. We also show projected limits from LZ[32] as dashed lines. Note that the axis scales on the two plots are different. We assume $m_h = 125.2$ GeV here and throughout this chapter. The left plot shows the mass resonance with small $y_{h\chi}$, for which the dark matter mass must be tuned to within less than a GeV of the pole, but there is some flexibility in the phase. The right plot shows the phase tuning: away from $m_h = 2m_\chi$ a large coupling is required to achieve a sufficient annihilation cross section, but tuning the phase near $\pi/2$ avoids direct detection limits despite the large coupling. In this case, the flexibility of the allowed mass range changes to $\mathcal{O}(10)$ GeV. Both of these plots include a small non-zero Z coupling that is consistent with spin-dependent direct detection constraints. The limits are similar for vanishing Z coupling.

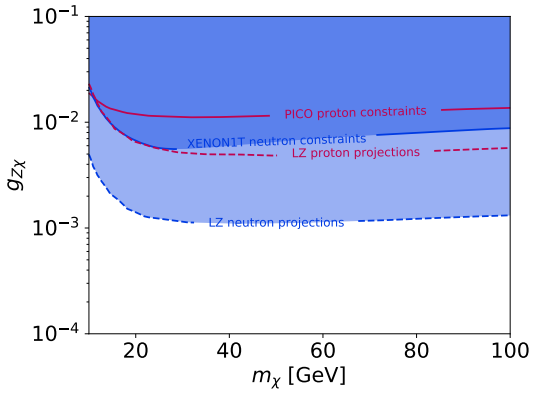

Figure 4.2: Spin-dependent direct detection limits as a function of dark matter mass and dark matter-Z coupling. Constraints are close to horizontal because the spin-dependent cross section depends on the reduced mass. For neutrons, XENON1T[48] is the strongest model independent constraint. For protons, PICO[42,43] provides a slightly stronger constraint. Additionally, we show projected limits from LZ[32].

and PandaX-II [154] because they are slightly weaker than those we've shown for $\mathcal{O}(60)$ GeV dark matter. For the spin-independent constraints, we consider only dark matter-proton scattering because in this case the difference between proton and neutron cross sections is negligible.

First we review which masses and coupling magnitudes are in general concordance with scattering constraints and annihilation requirements. Typical couplings that can generate an annihilation cross section of ~ 1 pb are shown in Equation 4.2.15 for two different dark matter masses. In Equation 4.2.16, we show approximate couplings and masses that are consistent with direct detection constraints.

$$\begin{aligned}\left[\frac{\langle\sigma v\rangle}{1\,\text{pb}}\right] &= \left[\frac{m_\chi}{80\,\text{GeV}}\right]^2 \left[\frac{4m_\chi^2 - m_h^2}{10^4\,\text{GeV}^2}\right]^{-2} \left[\frac{y_{h\chi}\sin\varphi_{h\chi}}{1.0}\right]^2 \\ &= \left[\frac{m_\chi}{62.5\,\text{GeV}}\right]^2 \left[\frac{4m_\chi^2 - m_h^2}{50\,\text{GeV}^2}\right]^{-2} \left[\frac{y_{h\chi}\sin\varphi_{h\chi}}{0.007}\right]^2\end{aligned} \tag{4.2.15}$$

$$\begin{aligned}\left[\frac{\sigma_{SI}}{10^{-10}\,\text{pb}}\right] &= \left[\frac{y_{h\chi}\cos\varphi_{h\chi}}{0.02}\right]^2 \\ \left[\frac{\sigma_{SD}}{10^{-5}\,\text{pb}}\right] &= \left[\frac{g_{Z\chi}}{0.01}\right]^2\end{aligned} \tag{4.2.16}$$

We remind the reader that the free parameters of the theory are $m_\chi, g_{Z\chi}$, and the complex coupling $y_{h\chi}$ with phase $\varphi_{h\chi}$. While $g_{Z\chi}$ and $\text{Im}[y_{h\chi}]$ set the annihilation cross section, only $\text{Re}[y_{h\chi}]$ sets the magnitude of scattering. In order to generate a large enough annihilation cross section while avoiding direct detection constraints, Higgs portal dark matter models typically tune the dark matter mass close to half the Higgs mass [271,95,128,250,116,84,227,118,119]. While tuning the mass is one way to generate the

correct ratio in this model, we emphasize that in the EFT, the correct ratio can also be obtained for a wider mass range by increasing the magnitude of the Higgs coupling while tuning the phase, $\varphi_{h\chi}$, of the Higgs coupling close to $\pi/2$ to suppress direct detection constraints. This is illustrated in Figure 4.1, which plots annihilation and spin independent direct detection constraints in the $m_\chi - \varphi_{h\chi}$ plane for different magnitudes of the Higgs couplings. We can see that near the mass resonance, a small Higgs coupling (~ 0.02) is sufficient to generate the annihilation cross section and the phase does not need to be near $\pi/2$ to avoid direct detection constraints. However, with phase tuning, the larger Higgs coupling required to generate the correct annihilation cross section away from resonance is allowed because direct detection only constrains the real part of $y_{h\chi}$. This widens the mass range considerably to $\mathcal{O}(10)$ GeV. Even for the mass resonance, the coupling cannot be purely real, because the leading velocity dependent term is not large enough to generate the required annihilation cross section given the finite Higgs width. See Appendix C.1 for more details. Note that while in principle a large pseudo-vector Z coupling could also generate a sufficient annihilation cross section, this is constrained by spin-dependent direct detection constraints, as shown in Figure 4.2. Within the range of Z couplings allowed by direct detection, the effect on the allowed annihilation signal is negligible.

4.3 Singlet-Doublet Model

A well-motivated way to UV complete the dark matter EFT provided in Section 4.2 in a gauge invariant manner is to introduce additional particles charged under G_{SM}. In this section, we discuss a simple potential UV completion, where the only additional particles we introduce to the Standard Model are

a singlet Majorana fermion and a doublet Dirac fermion. This model has previously been discussed in other contexts in [325,170,192,149,129,17,113,221,68,111,321].

4.3.1 Model in the UV

We start by establishing notation and describing the model. The model contains a singlet Majorana fermion ψ_1 and an additional SU(2) doublet Dirac fermion with hypercharge 1/2. We describe the SU(2) doublet with two left handed Weyl fermions ψ_2 (with neutral component ψ_2^0 and charged component ψ_2^1) and $\tilde{\psi}_2$ (with neutral component $\tilde{\psi}_2^0$ and charged component $\tilde{\psi}_2^{-1}$). All new fermions are SU(3) singlets. The Lagrangian for this model is

$$\mathcal{L} = \mathcal{L}_{SM} + \mathcal{L}_{\text{kinetic}} - m_2 \psi_2 \cdot \tilde{\psi}_2 - \frac{m_1}{2}\psi_1\psi_1 + Y\psi_1 H^\dagger \psi_2 - \tilde{Y}\psi_1 H \cdot \tilde{\psi}_2 + \text{h.c.} \tag{4.3.1}$$

As we introduce three new fields and four free parameters, there is one remaining physical phase. We make the choice to fix each of the Yukawa terms to the same phase, which carries the CP-violation,

$$Y \equiv y\, e^{i\delta_{CP}/2}, \qquad \tilde{Y} \equiv \tilde{y}\, e^{i\delta_{CP}/2}. \tag{4.3.2}$$

After SSB, the mass terms are written as

$$\mathcal{L}_{\text{mass}} = -m_2\left(\tilde{\psi}_2^{-1}\psi_2^1 - \tilde{\psi}_2^0\psi_2^0\right) - \frac{m_1}{2}\psi_1\psi_1 + \frac{v}{2}y\, e^{i\delta_{CP}/2}\psi_1\psi_2^0 + \frac{v}{2}\tilde{y}\, e^{i\delta_{CP}/2}\psi_1\tilde{\psi}_2^0 + \text{h.c.} \tag{4.3.3}$$

Let us define $\psi_2^s \equiv \frac{1}{\sqrt{2}}(\psi_2^0 + \tilde{\psi}_2^0)$ and $\psi_2^d \equiv \frac{1}{\sqrt{2}}(\psi_2^0 - \tilde{\psi}_2^0)$ to be the two Majorana fermions that constitute the neutral Dirac fermion $\{\psi_2^0, \tilde{\psi}_2^0\}$. The mass eigenstates thus result from the mixing of the doublet and singlet Majorana fermions, $\psi_i = (\psi_2^s, \psi_2^d, \psi_1)_i$. We will denote the mass eigenstates $\chi_i = (\chi, \chi_1, \chi_2)_i$, the lightest of which, χ, is the dark matter candidate. Then

$$\mathcal{L}_{\text{mass}} = -m_2 \tilde{\psi}_2^{-1} \psi_2^1 - \frac{1}{2} \psi_i M_{ij} \psi_j, \tag{4.3.4}$$

where M is the mass matrix. This basis change is governed by J, the matrix of eigenvectors that diagonalizes both $M^\dagger M$ and M, phase rotated such that $J^T M J$ has real eigenvalues. After diagonalizing, the Higgs Yukawa couplings are

$$\mathcal{L}_{\text{Higgs}} = \frac{1}{2} h \chi_i [J^T U_h J]_{ij} \chi_j + \text{h.c.} \tag{4.3.5}$$

where

$$U_h = \begin{pmatrix} 0 & 0 & \frac{(Y+\tilde{Y})}{2} \\ 0 & 0 & \frac{(Y-\tilde{Y})}{2} \\ \frac{(Y+\tilde{Y})}{2} & \frac{(Y-\tilde{Y})}{2} & 0 \end{pmatrix}. \tag{4.3.6}$$

Since one of the new fermions is an SU(2) doublet, the new fermions also couple to the electroweak gauge bosons. The Z couplings are

$$\mathcal{L}_Z = \chi_i^\dagger [J^\dagger U_Z J]_{ij} Z \bar{\sigma} \chi_j + g_Z (\cos^2 \theta_W - \sin^2 \theta_W)(\psi_2^{1\dagger} Z \bar{\sigma} \psi_2^1 - \tilde{\psi}_2^{-1\dagger} Z \bar{\sigma} \tilde{\psi}_2^{-1}) \tag{4.3.7}$$

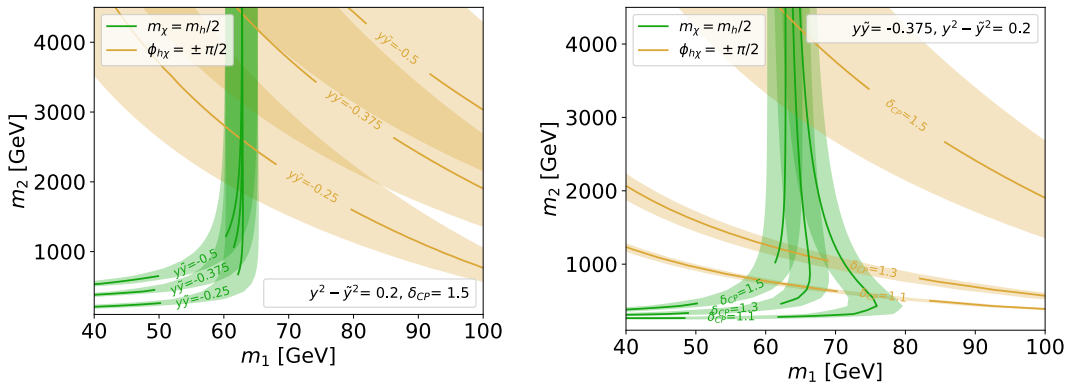

Figure 4.3: Plots show EFT coupling phase and dark matter mass as a function of m_1 and m_2 for different values of $y, \tilde{y}$, and δ_{CP}. Left: δ_{CP} is fixed to 1.5 while $y\tilde{y}$ is varied. Right: $y\tilde{y}$ is fixed to -0.375 while δ_{CP} is varied. The shaded regions give a sense of the width of the regions of interest: $60\,\text{GeV} \leq m_\chi \leq 65\,\text{GeV}$ and $1.55 \leq \varphi_{h\chi} \leq 1.60$. We can see that changing $y\tilde{y}$ has a minimal effect on m_χ at large m_2 but strongly affects which masses correspond to the central value of $\varphi_{h\chi} = \pi/2$. $y\tilde{y}$ also affects the smallest value of m_2 that can lead to a mass resonance. Changing δ_{CP} has a larger effect on which m_1 is required to get the mass resonance, and also affects the width of the $\varphi_{h\chi} = \pi/2$ band in addition to the position of its central value.

while the W couplings are

$$\mathcal{L}_W = \chi_i^\dagger [bJ^*]_i W^+ \bar{\sigma} \tilde{\psi}_2^{-1} + \psi_2^{1\dagger} W^+ \bar{\sigma} [aJ]_j \psi_j + \text{h.c.} \tag{4.3.8}$$

where g is the SU(2) gauge coupling, g' is the U(1) hypercharge gauge coupling, θ_W is the Weinberg angle, and $g_Z \equiv \sqrt{g^2 + g'^2}/2$. Here, $a_i = (g/2, g/2, 0)_i$, $b_i = (g/2, -g/2, 0)_i$ and

$$U_Z = \begin{pmatrix} 0 & -g_Z & 0 \\ -g_Z & 0 & 0 \\ 0 & 0 & 0 \end{pmatrix}. \tag{4.3.9}$$

The dark matter candidate χ obtains the couplings seen in the EFT via mixing between the singlet

and doublet. The strength of these couplings can be adjusted by altering the makeup of the lightest Majorana fermion. The theory at this level is fully specified by five degrees of freedom: the singlet mass m_1, the doublet mass m_2, the doublet Yukawa coupling magnitudes $\{y, \tilde{y}\}$ and the associated CP-violating phase δ_{CP}.

4.3.2 Translating to the EFT

Now we discuss how the EFT parameters $g_{Z\chi}$, m_χ, and $y_{h\chi}$ depend on the UV parameters $y, \tilde{y}, m_1, m_2$, and δ_{CP}. We focus mostly on the region where m_2 is large, but also comment on the more general case.[2] Since the theory has a charged fermion with mass m_2, parameter space with small m_2 will generically be ruled out by collider constraints [1,2]. EDM and electroweak constraints are likewise more stringent in this regime.

Figure 4.3 shows the EFT mass and phase as a function of m_1 and m_2 for different values of the UV coupling magnitudes and phase. On the left we show multiple values of $y\tilde{y}$ for fixed δ_{CP} while on the right we show multiple values of δ_{CP} for fixed $y\tilde{y}$. In both cases, we can see that only a narrow range in m_1 translates to dark matter with mass near the mass resonance. When m_2 is large, the lightest fermion is mostly m_1. In this limit, mixing is small, so to have the dark matter mass near the mass resonance, m_1 must be fairly close to half the Higgs mass. We can see that changing $y\tilde{y}$ changes where $\varphi_{h\chi} = \pi/2$ is located but only has a minimal effect on which m_1 value translates to the mass resonance. We can also see that for the same m_1, smaller $y\tilde{y}$ requires a correspondingly smaller m_2 to get dark matter with

[2] We also omit the case where both m_1 and m_2 are large. In this case, extremely large couplings are required in order to get dark matter with mass near $m_h/2$. This means the δ_{CP} must be small to avoid EDM constraints, which leaves us with $\varphi_{h\chi}$ mostly real and prevents us from simultaneously evading spin-independent constraints.

$m_\chi \approx m_h/2$. Changing δ_{CP} also changes the location of $\varphi_{h\chi} = \pi/2$ contour, but additionally affects the m_1 required to get the mass resonance and the width of the $\varphi_{h\chi} \approx \pi/2$ band.

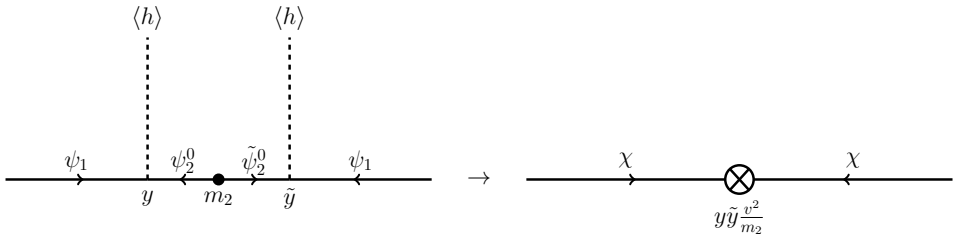

Figure 4.4: Diagram generating dark matter mass in the limit where m_2 is large.

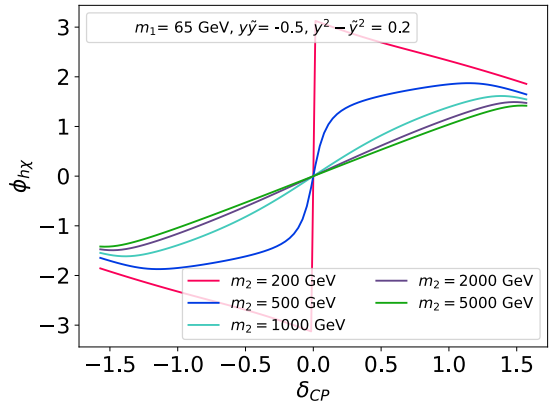

Figure 4.5: Plot of $\varphi_{h\chi}$ as a function of δ_{CP} for different values of m_2. We note that as m_2 increases, the IR phase maps directly to the UV phase and $\varphi_{h\chi} \sim \delta_{CP}$.

Figure 4.4 shows that the corrections to the mass scale as $y\tilde{y}v^2/m_2$.[3] This diagram also tells us that $\varphi_{h\chi} = \delta_{CP}$ in the large m_2 limit, as long as mixing is small and the dark matter mass comes mostly from m_1 rather than the Higgs vev. This can also be seen in Figure 4.5. When the dark matter mass gets a large contribution from the Higgs vev the story is more complicated: when $y\tilde{y}$ and m_1 have opposite signs, the Higgs contribution can cancel with m_1 at $y\tilde{y} = -m_2 m_1/v^2$ to get a massless state. There is a

[3] Although we need to phase rotate ψ_2^s, the phase rotations in the couplings and mass insertion cancel out.

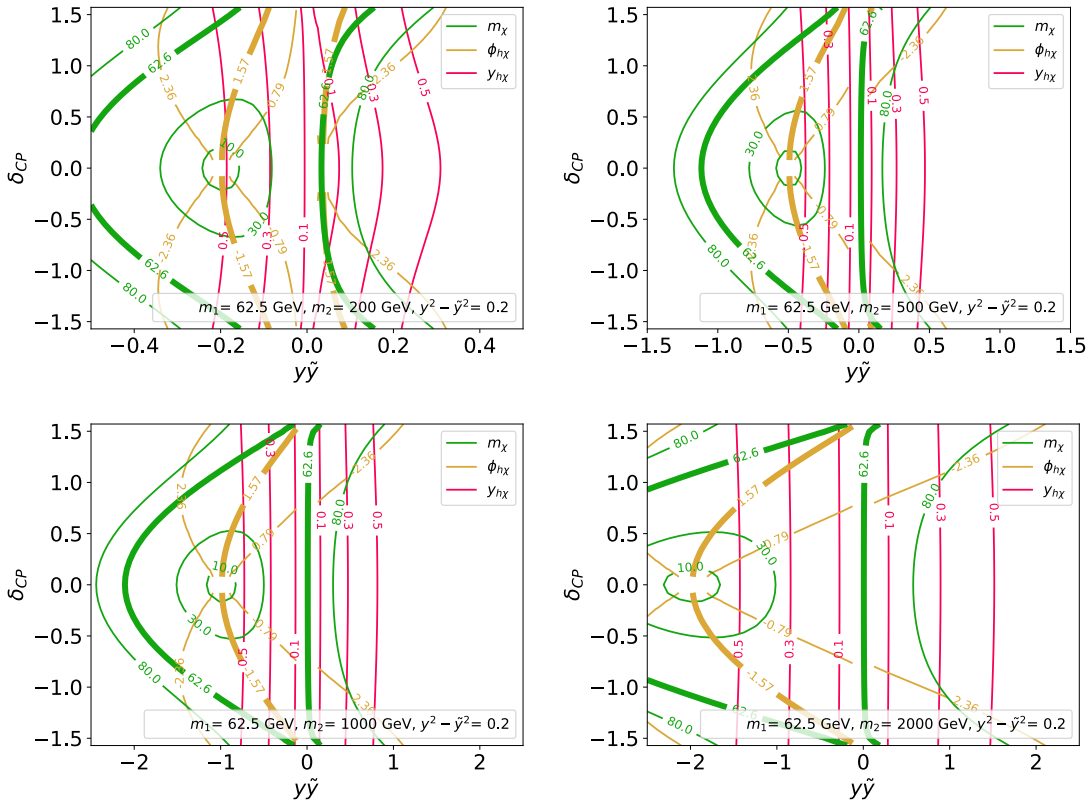

Figure 4.6: Dark matter mass, EFT phase, and dark matter-Higgs Yukawa coupling as a function of the UV parameters $y\tilde{y}$ and δ_{CP} for different values of m_2. In each plot we see a similar mass structure: we see a massless state when $y\tilde{y}$ and m_1 have opposite signs, and have a lightest fermion near 60 GeV for both larger and smaller $y\tilde{y}$ than this value. We can also see the scaling of both the EFT mass and Higgs coupling with $y\tilde{y}$ and m_2. Note the different values on the $y\tilde{y}$ axis in each of the plots.

mass resonance contour for $y\tilde{y}$ both larger and smaller than this value, which can be seen in Figure 4.6. We might also ask whether a small δ_{CP} in the UV can translate to $\varphi_{h\chi} \approx \pi/2$ in the IR and produce an annihilation signal that evades both direct detection and EDM constraints. However, from the same figure, we can see that although there is a point where small δ_{CP} translates to $\varphi_{h\chi} \approx \pi/2$, it corresponds precisely to the massless state mentioned above and cannot generate our annihilation signal. This is evidenced by all the phase contours converging at the massless point, because when m_χ is zero, we can

freely rotate m_1 to absorb the phase in y since the phase is no longer physical.

In the small mixing and large m_2 limit, there are two contributions to the Higgs coupling: one where ψ_1 mixes into ψ_2^s and one where it mixes into ψ_2^d, as shown in Figure 4.7. Each of these contributes $(y \pm \tilde{y})^2 v/m_2$, with a relative minus sign between the two contributions because we need to phase rotate ψ_2^s to have positive mass. This means the Higgs coupling scales as $y\tilde{y}v/m_2$, which determines the scaling of the annihilation signal. This can also be seen from the pink lines in Figure 4.6. Note that this scaling breaks down once the Yukawa contributions become the dominant contribution to the mass.

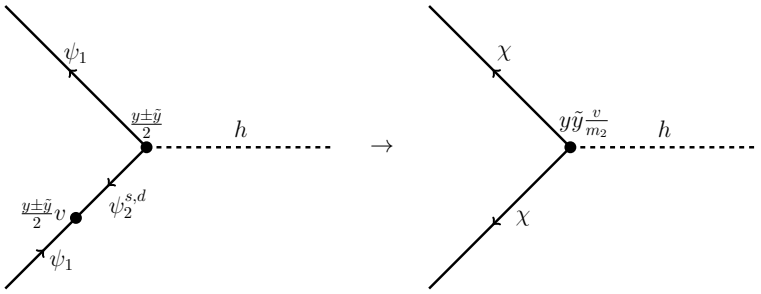

Figure 4.7: Diagram that generates the dark matter-Higgs coupling in the limit where m_2 is large.

In the same limit, the dominant contribution to the Z coupling comes from Figure 4.8, which scales as $g_Z(y^2 - \tilde{y}^2)v^2/m_2^2$. Even away from this limit, we still get a vanishing Z coupling for $y = \tilde{y}$, because only one of the doublet states mixes with the singlet when $y = \tilde{y}$. For small m_2, spin-dependent direct detection constraints require $y \approx \tilde{y}$, but for $m_2 \gtrsim 500$ GeV this constraint becomes irrelevant, since the Higgs coupling (which determines the annihilation signal) scales as m_2^{-1} while the Z coupling scales as m_2^{-2}. This can be seen in Figure 4.9.

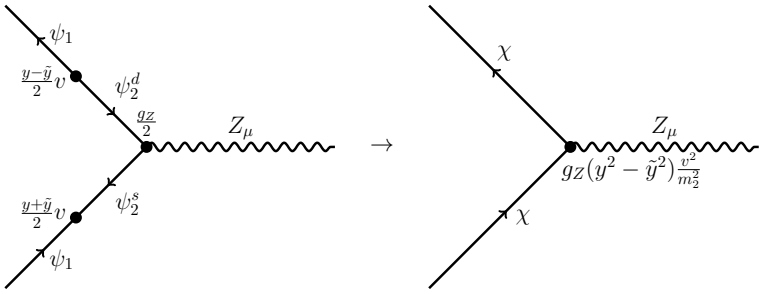

Figure 4.8: Diagram that generates the dark matter-Z coupling in the limit where m_2 is large.

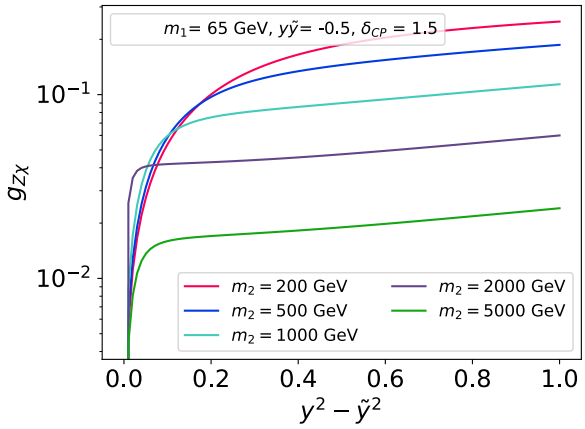

Figure 4.9: Plot of $g_{Z\chi}$ as a function of $y^2 - \tilde{y}^2$ for different values of m_2. $g_{Z\chi}$ increases with increasing $y^2 - \tilde{y}^2$ and decreases with increasing m_2, corroborating the scaling derived from the diagrams in Figure 4.8.

4.3.3 Constraints

In this section, we discuss the experimental constraints that apply to the singlet-doublet model. We focus on constraints that apply directly to the parameters in the UV theory, including discussing their scaling in the large m_2 limit.

4.3.3.1 Electric Dipole Moment

Any new source of CP-violation in a given model can lead to additional contributions to electric dipole moments. Since our model contains new CP-violating couplings to the Higgs, we expect electron EDM constraints to be relevant for our model. For small m_2, the EDM limit will be one of the strongest on our model, since the EDM is precisely constrained to be below $1.1 \times 10^{-29}\, e\,\text{cm}$[44].

For the singlet-doublet model above, the only relevant diagram is the Barr-Zee diagram with W bosons in the outer loop[72], displayed in Figure 4.10. There are no other Barr-Zee diagrams with Higgs or Z legs; since CP-violation is only in the neutral sector of this model and a charged particle is necessary to radiate a photon, the inner loop must contain both a neutral and charged particle. Additionally, there are no other non-Barr-Zee diagrams that contribute to the EDM at 2 or fewer loops. For any non-Barr-Zee diagrams to contribute, there would have to be a CP-odd correction to a gauge boson or Higgs propagator. With only a single external momentum, it is impossible to contract with an epsilon tensor and make a non-vanishing CP-odd Lorentz invariant.

To compute the value of the relevant Barr-Zee diagram, we use a simplified version of Equation 21 in[61], where we have neglected the neutrino mass, approximated lepton couplings as flavor diagonal, and used the fact that one of the fermions in the loop is neutral:

$$\frac{d_e}{e} = -\frac{g^2}{(4\pi)^4} \sum_i \text{Im}([af]_i^* [bf^*]_i) \left(\frac{m_c m_{n,i} m_e}{M_W^4}\right) G(x_c, x_i, 0). \tag{4.3.10}$$

Here, $x_\alpha = m_\alpha^2/M_W^2$ and $G(a,b,c)$ is defined as

$$G(a,b,c) = \frac{1}{1-c}\int_0^1 \frac{dx}{1-x}\left(\frac{c}{z-c}\log\left(\frac{c}{z}\right) + \frac{1}{1-z}\log\left(\frac{1}{z}\right)\right) \tag{4.3.11}$$

with

$$z(x,a,b) = \frac{b}{x} + \frac{a}{1-x}. \tag{4.3.12}$$

Recall from Section 4.3.1 that couplings a_i and b_i parameterize the W boson couplings to the inner loop fermions in the gauge basis, which are given in Equation 4.3.8, and J is the change of basis matrix.

When m_2 is large enough that we can integrate out the doublet and mixing is small, the dominant contribution to the EDM comes from Figure 4.10, since each helicity of charged fermion couples to a different neutral doublet component and mixing with the singlet is necessary to generate CP-violation. This contribution scales as $y\tilde{y}v^2/m_2^2$. The m_2 scaling follows from dimensional analysis: three factors of m_2 from the integral measure cancel with three of the five factors of m_2 from the propagators.[4]

4.3.3.2 Electroweak parameters

Here we consider constraints from electroweak precision measurements, where deviations from the SM are parametrized by oblique parameters S, T, U, W, and Y[349,110], defined in Equations 4.3.13-4.3.17.

[4] The ψ_1 propagator also scales as m_2^{-1} since $p = m_2 \gg m_1$.

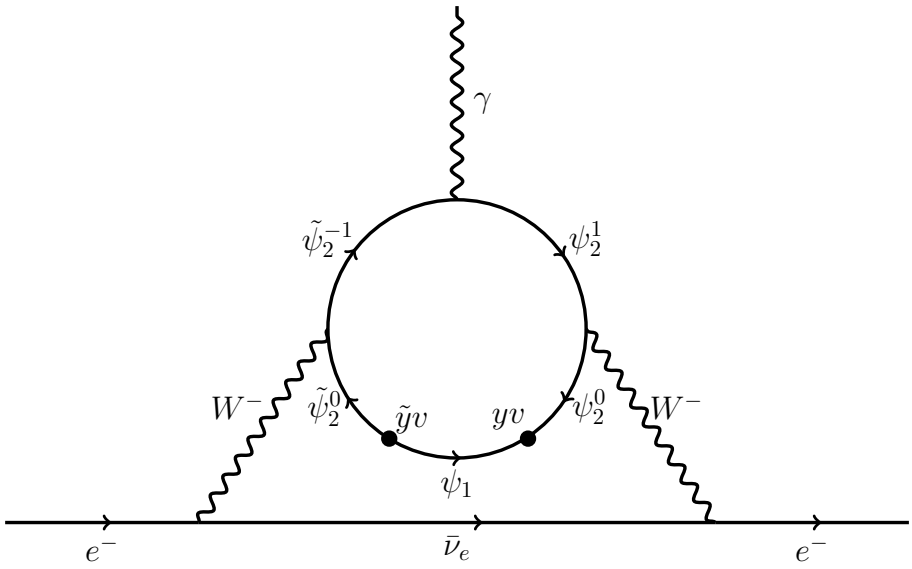

Figure 4.10: Leading contribution to the non-zero Barr-Zee diagram in the large m_2 limit. In this limit, we can work perturbatively in the gauge basis. The relevant W couplings are the coefficients of $\chi_{21}^\dagger \frac{\sqrt{g}}{2} W^- \chi_{20}$ and $\tilde{\chi}_{20}^\dagger \frac{\sqrt{g}}{2} W^+ \tilde{\chi}_{2-1}$.

$$S \equiv \frac{4c^2 s^2}{\alpha_e}\left[\Pi'_{ZZ}(0) - \frac{c^2-s^2}{cs}\Pi'_{Z\gamma}(0) - \Pi'_{\gamma\gamma}(0)\right] \tag{4.3.13}$$

$$T \equiv \frac{1}{\alpha_e}\left[\frac{\Pi_{WW}(0)}{m_W^2} - \frac{\Pi_{ZZ}(0)}{m_Z^2}\right] \tag{4.3.14}$$

$$U \equiv \frac{4s^2}{\alpha_e}\left[\Pi'_{WW}(0) - \frac{c}{s}\Pi'_{Z\gamma}(0) - \Pi'_{\gamma\gamma}(0)\right] - S \tag{4.3.15}$$

$$W \equiv \frac{m_W^2 s^2 c^2}{8\pi\alpha_e}\left[\Pi''_{ZZ}(0) + \frac{2s}{c}\Pi''_{Z\gamma}(0) + \frac{s^2}{c^2}\Pi''_{\gamma\gamma}(0)\right] \tag{4.3.16}$$

$$Y = \frac{m_W^2 s^2}{8\pi\alpha_e}\left[c^2\Pi''_{\gamma\gamma}(0) + s^2\Pi''_{ZZ}(0) - 2sc\Pi''_{\gamma Z}(0)\right] \tag{4.3.17}$$

The masses and couplings are evaluated at m_Z^2 and c and s are $\cos\theta_W$ and $\sin\theta_W$ respectively. Π_{XX} represents the new particles' contribution to the vacuum polarization of the gauge boson X at 1-loop,

computed in $\overline{\text{MS}}$ scheme under the convention shown in Figure 6.4.

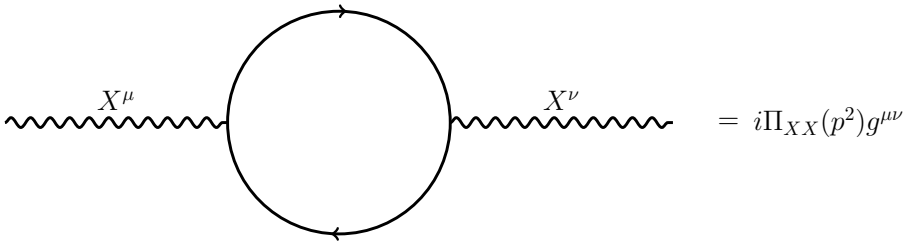

Figure 4.11: New particles that couple to the Standard Model gauge bosons contribute to the vacuum polarization at 1-loop through this diagram. The X^μ represents an electroweak gauge boson. We ignore the $p^\mu p^\nu$ terms since they aren't relevant for Equations 4.3.13 - 4.3.17.

To lend intuition, we note that T parametrizes custodial SU(2) breaking inherent in the asymmetry within the doublet terms; in our theory this manifests in the difference in Yukawa couplings y and $\tilde{y}$. U is the derivative of T, and thus is typically smaller. All these parameters fall off with increasing m_2.

The most recent constraints, at 95% CL, from the LHC yield

$$S = -0.01 \pm 0.10 \qquad T = 0.03 \pm 0.12 \qquad U = -0.01 \pm 0.10 \tag{4.3.18}$$

with correlations +0.92 between S and T, -0.80 between S and U, and -0.93 between T and U[399]. W and Y are measured to be

$$W = (-2.7 \pm 2.0) \times 10^{-3} \qquad Y = (4.2 \pm 4.9) \times 10^{-3} \tag{4.3.19}$$

with correlation -0.96[70], though we find these to be subdominantly constraining for this theory.

4.3.3.3 Collider Experiments

Constraints from many collider searches (in particular SUSY searches) can be applied to this model. Specifically, we consider those searches included in the database of the publicly available SModelS version 1.2.4 software [298,40,184,41,303,60,372,37,104]. To generate the necessary input, we use SARAH 4.14.3 [377,378,379] to create modified versions of SPheno [352,353] and Madgraph [38,39] which include the singlet and doublet. Then we use this version of SPheno at tree level to compute the spectrum and branching ratios for SModelS and the run card for Madgraph, which was used to obtain the production cross sections that SModelS also needs as input. These constraints are combined into a single exclusion limit labeled LHC when included in our plots. In addition to this constraint, we also show the constraint from invisible Higgs decay. We do not include the constraint from invisible Z decay, since it is not kinematically allowed in the parameter space of interest.

4.3.4 Full Exclusion Limits and Discussion

Finally, combining all of these constraints, we examine the remaining parameter space for singlet-doublet dark matter that has the desired amount of annihilation. Our results are shown in Figures 4.12 and 4.13. We find that in all cases, some tuning of the parameters is required, but that there is flexibility in which UV parameters we need to tune.

As in the EFT, in order to achieve a pure mass resonance (and not have to tune the EFT phase) we need small couplings. This can be seen in Figures 4.12a and 4.12b. The spin-independent constraints are weak for small couplings, regardless of δ_{CP} or the EFT phase. Other constraints are even less re-

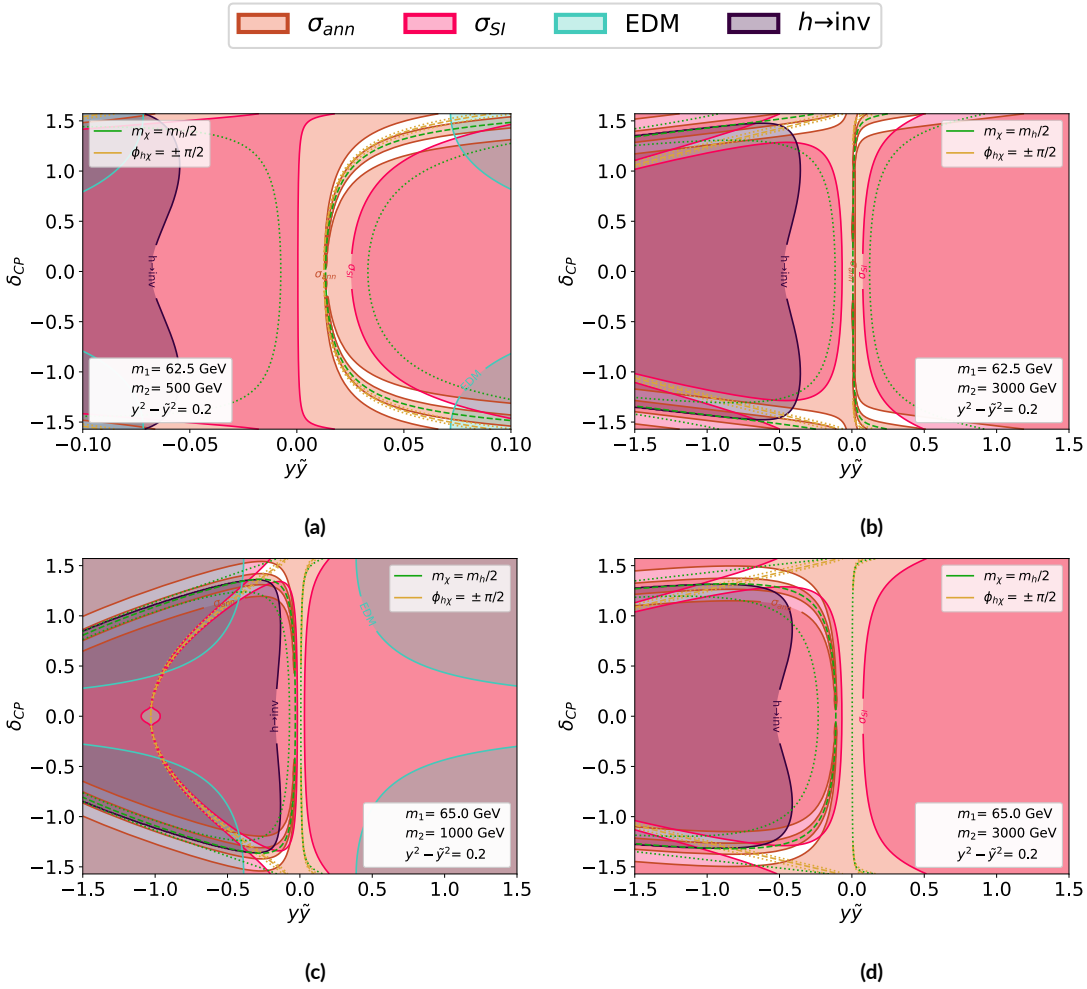

Figure 4.12: Full constraints on the model parameter space in the $y\tilde{y} - \delta_{CP}$ plane, for different values of m_1 and m_2. In this and subsequent plots the shaded regions denote parameter space ruled out by experimental bounds[44,371,46,47]. For annihilation, we include both an upper and lower bound. Other constraints are not relevant for these slices of parameter space. Spin-dependent direct detection constraints in particular are weak since $y^2 - \tilde{y}^2$ is small. Dotted lines indicate proximity to mass resonance and pure imaginary EFT coupling: the green dotted lines bound a region with dark matter mass $60\ \text{GeV} \leq m_\chi \leq 65\ \text{GeV}$, the yellow with EFT phase $1.55 \leq \varphi_{h\chi} \leq 1.6$. In Figures (a) and (b) we show that viable parameter space can be found at small couplings, corresponding to a pure mass resonance with flexibility in $\varphi_{h\chi}$. In this case, smaller values of m_2 are allowed but m_1 must be close to $m_h/2$. Figures (b) - (d) also show allowed parameter space for larger couplings: (b) shows $m_1 \approx m_h/2$; (c) and (d) show m_1 further away from $m_h/2$ for two different values of m_2. In all of (b) - (d), viable parameter space requires $m_1 \approx 60 - 70$ GeV, $\delta_{CP} \gtrsim 1$, and $\varphi_{h\chi} \approx \pi/2$.

strictive, except for the EDM at very large δ_{CP}. Since the couplings are small, m_1 must be tuned near $m_b/2$ in order to achieve a sufficient annihilation signal, but there is flexibility in the value of m_2, as can be seen in Figure 4.13a. This is the region of parameter space that is relevant for the best fit in [119].

If instead we choose our parameters so that we allow the EFT phase to be tuned near $\pi/2$, there is other viable parameter space with larger couplings. Here, we have slightly more flexibility in m_1 (which still needs to be roughly $60-70$ GeV), but m_2 must be large ($m_2 \gtrsim \mathcal{O}(1)$ TeV) to avoid EDM, electroweak, and collider constraints. This can be seen in Figure 4.13b. Additionally, to achieve an EFT phase near $\pi/2$ and avoid spin-independent constraints, generally $\delta_{CP} \gtrsim 1$. Note that limits from spin-dependent scattering can be avoided, since they vanish when $y = \pm\tilde{y}$. This part of parameter space generally requires proximity to both the mass resonance and the phase $\pi/2$ line. However, there is still some flexibility in both values; masses $m_\chi > 65$ GeV and phases $\varphi_{b\chi} < 1.5$ are allowed in these intersections, albeit not simultaneously. Unlike in the case of the EFT, it is very difficult to tune only the phase because we cannot make couplings arbitrarily large without affecting the mass spectrum, as we saw in Section 4.3.2.

Figures 4.12b - 4.12d shows several examples of this. In Figure 4.12b, we can see the case where we still choose m_1 to be near $m_b/2$ but allow larger couplings. If instead we choose m_1 further away from $m_b/2$, the only viable parameter space requires large couplings in order to get the dark matter mass sufficiently close to resonance. This is shown in Figures 4.12c and 4.12d. Comparing these two plots, we can see that there is more flexibility in δ_{CP} and larger required coupling values for higher m_2, because higher m_2 changes the shape of the EFT phase $\pi/2$ contour. Specifically, there is more overlap between $\varphi_{b\chi}$ near $\pi/2$ and the annihilation signal in the large m_2 case since the condition $\varphi_{b\chi} = \pi/2$

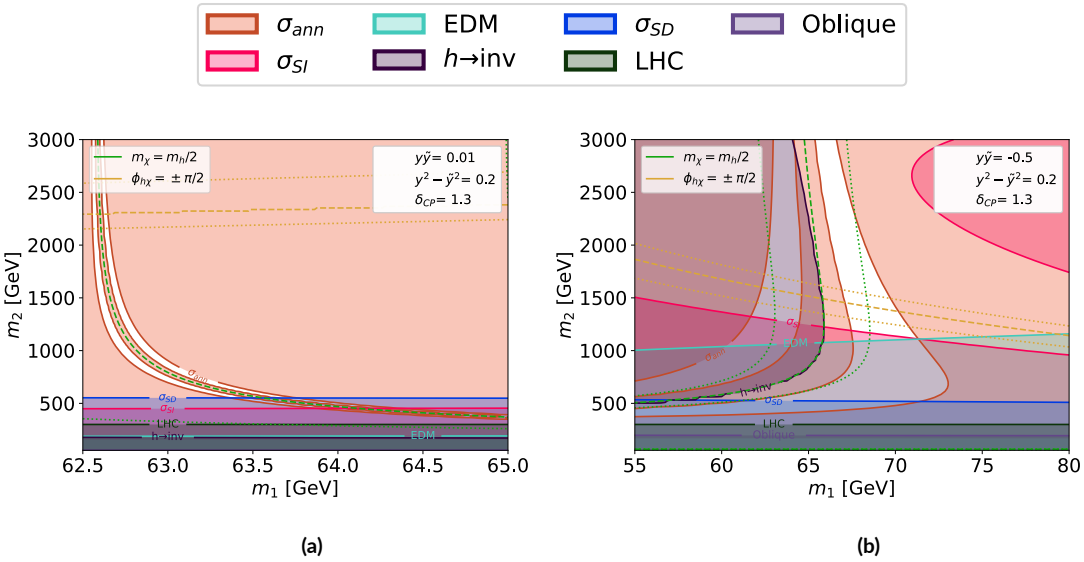

Figure 4.13: Similar to Figure 4.12, in slices of the $m_1 - m_2$ plane and for different values of $y\tilde{y}$ and δ_{CP}. We show constraints from[399,70,48,42,43,298,40,184,41,303,60,372,37,104] in addition to the constraints shown in Figure 4.12. Dotted lines around the critical mass and phase values give a guide towards the proximity of any viable space to mass resonance and pure imaginary EFT coupling: the green dotted lines bound a region with dark matter mass $60\text{ GeV} \leq m_\chi \leq 65\text{ GeV}$, the yellow with EFT phase $1.55 \leq \varphi_{h\chi} \leq 1.6$. The left shows the case of a mass resonance with small couplings, where m_2 down to ~ 500 GeV is allowed. The right shows the case of larger couplings, where we need $m_2 \gtrsim \mathcal{O}(1)$ TeV. We omit light charged fermion constraints since small m_2 is already ruled out.

becomes less dependent on $y\tilde{y}$ at larger m_2.[5]

4.4 Doublet-Triplet Model

In this section, we describe another potential UV completion, doublet-triplet dark matter. This model includes the addition of a doublet Dirac fermion and a triplet Majorana fermion to the Standard Model. This model has been previously discussed in other contexts in [164,17,221,321].

[5] This is because the $\varphi_{h\chi} = \pi/2$ contour always goes through the massless state that exists for negative $y\tilde{y}$, which occurs at larger couplings for larger m_2. All phase contours go through this point since the phase becomes unphysical when the lightest state is massless.

4.4.1 Model in the UV

We begin by describing our model and establishing the notation. This model contains a Dirac doublet of two left handed Weyl fermions with hypercharge 1/2 (denoted by ψ_2 and $\tilde{\psi}_2$ as in the singlet-doublet case) and a triplet of Majorana fermions (with components ψ_3^{-1}, ψ_3^0, ψ_3^1), all of which are SU(3) singlets. The Lagrangian is given by

$$\mathcal{L} = \mathcal{L}_{\text{SM}} + \mathcal{L}_{\text{kinetic}} - \frac{1}{2} m_3 \psi_3 \psi_3 - m_2 \psi_2 \cdot \tilde{\psi}_2 - Y H^\dagger \psi_3 \psi_2 - \tilde{Y} (\varepsilon H^*)^\dagger \psi_3 \tilde{\psi}_2 + \text{h.c.} \tag{4.4.1}$$

As in the singlet-doublet case, this theory also has a single physical phase, and we can choose the same convention as the previous section to localize CP-violation to the Yukawa couplings, where

$$Y \equiv y\, e^{i\partial_{CP}/2}, \qquad \tilde{Y} \equiv \tilde{y}\, e^{i\partial_{CP}/2}. \tag{4.4.2}$$

Next we describe our notation after SSB. We denote the gauge basis neutral particles by $\psi_n = \{\psi_3^0, \psi_2^s, \tilde{\psi}_2^d\}$ and the gauge basis charged particles by $\psi_c^+ = \{\psi_3^{+1}, \psi_2^{+1}\}$ and $\psi_c^- = \{\psi_3^{-1}, \tilde{\psi}_2^{-1}\}$. We label the neutral mass eigenstates $\chi_n = \{\chi, \chi_1, \chi_2\}$ and the charged mass eigenstates $\chi_c^+ = \{\chi_1^{+1}, \chi_2^{+1}\}$, and $\chi_c^- = \{\chi_1^{-1}, \chi_2^{-1}\}$. Each is ordered from least to most massive, and χ again denotes the dark matter. We call the basis change matrices J_n and $J_c^\pm$, which are defined by $\psi_n = J_n \chi_n$, $\psi_c^\pm = J_c^\pm \chi_c^\pm$. The phases of the eigenvectors are chosen such that the mass eigenvalues are real. Then the mass terms are given by

$$\mathcal{L}_{mass} = -\frac{1}{2}\chi_n[J_n^T M_n J_n]\chi_n - \chi_c^-[J_-^T M_c J_+]\chi_c^+ + \text{h.c.} \tag{4.4.3}$$

with

$$M_n \equiv \begin{pmatrix} m_3 & (y-\tilde{y})v/2\sqrt{2} & (y+\tilde{y})v/2\sqrt{2} \\ (y-\tilde{y})v/2\sqrt{2} & -m_2 & 0 \\ (y+\tilde{y})v/2\sqrt{2} & 0 & m_2 \end{pmatrix}, \qquad M_c \equiv \begin{pmatrix} m_3 & -yv/\sqrt{2} \\ -\tilde{y}v/\sqrt{2} & m_2 \end{pmatrix}. \tag{4.4.4}$$

The Higgs Yukawa couplings are

$$\mathcal{L}_{\text{Higgs}} = \frac{1}{2}h\chi_n[J_n^T Y_n J_n]\chi_n + h\chi_c^-[J_-^T Y_c J_+]\chi_c^+ + \text{h.c.} \tag{4.4.5}$$

with

$$Y_n \equiv \begin{pmatrix} 0 & -(y-\tilde{y})/2\sqrt{2} & -(y+\tilde{y})/2\sqrt{2} \\ -(y-\tilde{y})/2\sqrt{2} & 0 & 0 \\ -(y+\tilde{y})/2\sqrt{2} & 0 & 0 \end{pmatrix}, \qquad Y_c \equiv \begin{pmatrix} 0 & y/\sqrt{2} \\ \tilde{y}/\sqrt{2} & 0 \end{pmatrix}. \tag{4.4.6}$$

The Z couplings are

$$\mathcal{L}_Z = \frac{1}{2}Z^\mu \bar{\sigma}_\mu \chi_n[J_n^\dagger U_n J_n]\chi_n + Z^\mu \chi_c^+ \bar{\sigma}_\mu[J_+^\dagger U_+ J_+]\chi_c^+ + Z^\mu \chi_c^- \bar{\sigma}_\mu[J_-^\dagger U_- J_-]\chi_c^-, \tag{4.4.7}$$

with

$$U_n \equiv \begin{pmatrix} 0 & 0 & 0 \\ 0 & 0 & -\sqrt{g^2+g'^2} \\ 0 & -\sqrt{g^2+g'^2} & 0 \end{pmatrix}, \tag{4.4.8}$$

$$U_+ \equiv \begin{pmatrix} \frac{g^2}{\sqrt{g^2+g'^2}} & \\ 0 & \frac{(g^2-g'^2)}{2\sqrt{g^2+g'^2}} \end{pmatrix}, \quad U_- \equiv \begin{pmatrix} -\frac{g^2}{\sqrt{g^2+g'^2}} & 0 \\ 0 & -\frac{(g^2-g'^2)}{2\sqrt{g^2+g'^2}} \end{pmatrix},$$

while the W couplings are

$$\mathcal{L}_W = W^{\mu+}\chi_n\bar{\sigma}_\mu[J_n^\dagger D_- J_-]\chi_c^- + W^{\mu-}\chi_n\bar{\sigma}_\mu[J_n^\dagger D_+ J_+]\chi_c^+ + \text{h.c.} \tag{4.4.9}$$

with

$$D_- \equiv \begin{pmatrix} g & 0 \\ 0 & g/2 \\ 0 & -g/2 \end{pmatrix}, \qquad D_+ \equiv \begin{pmatrix} -g & 0 \\ 0 & g/2 \\ 0 & g/2 \end{pmatrix}. \tag{4.4.10}$$

The charged fermions also couple to the photon with charge ± 1.

4.4.2 Constraints

We treat most of the constraints in the doublet-triplet model similarly to those in the singlet-doublet model. There are two exceptions that we discuss in more detail: the EDM and collider constraints.

The EDM calculation differs from the singlet-doublet case because there are additional diagrams. Like in the singlet-doublet case, the relevant contributing diagrams are all Barr-Zee diagrams[72]. The

diagram with charged W legs, shown in Figure 4.10, that contributed in the singlet-doublet case is still relevant, but for the doublet-triplet model there are two additional relevant Barr-Zee diagrams: Zh and γh, shown in Figure 4.14. There is still no γZ contribution because in that case the same charged fermion runs through the entire loop, leaving no place for CP-violation to enter since the diagonal Z coupling is real. We also neglect the hh diagram since it is suppressed by two factors of the electron Yukawa. We use the general forms of the Zh and γh contributions from [336],

$$d_e^{bV} = \frac{1}{16\pi^2 m_b^2}\int_0^1 dx \frac{1}{x(1-x)} j\left(\frac{m_V^2}{m_b^2}, \frac{\tilde{\Delta}^V}{m_b^2}\right) g_e^V c_O^V \frac{m_e}{v}, \tag{4.4.11}$$

where g_e^V is the electron coupling to Z or γ, v is the Higgs vev, and we define

$$j(r,s) = \frac{1}{r-s}\left(\frac{r\log r}{r-1} - \frac{s\log s}{s-1}\right). \tag{4.4.12}$$

c_O^V and $\tilde{\Delta}^V$ are determined by the inner fermion loop which only contains charged fermions for both γh and γZ. They are given by

$$\begin{aligned} c_O^Z &= -\frac{e}{2\pi^2}\mathrm{Re}\Big(m_c^i x^2(1-x)(g_{ij}^S g_{ji}^{V*} + i g_{ij}^P g_{ji}^{A*}) + (1-x)^3 m_c^j (g_{ij}^S g_{ji}^{V*} - i g_{ij}^P g_{ji}^{A*})\Big), \\ \tilde{\Delta}^Z &= \frac{x m_c^i + (1-x) m_c^j}{x(1-x)}, \qquad c_O^\gamma = -\frac{e^2 g_{jj}^P}{2\pi^2}(1-x) m_c^j, \qquad \tilde{\Delta}^\gamma = \frac{(m_c^j)^2}{x(1-x)}, \end{aligned} \tag{4.4.13}$$

where

$$
\begin{aligned}
g^S &= \frac{1}{2}(J_-^T Y_c J_+ + J_+^\dagger Y_c^\dagger J_-^*), \qquad & g^P &= \frac{i}{2}(J_-^T Y_c J_+ - J_+^\dagger Y_c^\dagger J_-^*), \\
g^V &= J_-^T U_+ J_-^* + J_+^\dagger U_+ J_+, & g^A &= J_-^T U_+ J_-^* - J_+^\dagger U_+ J_+
\end{aligned}
\tag{4.4.14}
$$

are given in terms of the matrices defined in Section 4.4.1. By definition, χ_j is the fermion which radiates the on-shell external photon, and $g_{ij}^* = (g_{ji})^*$.

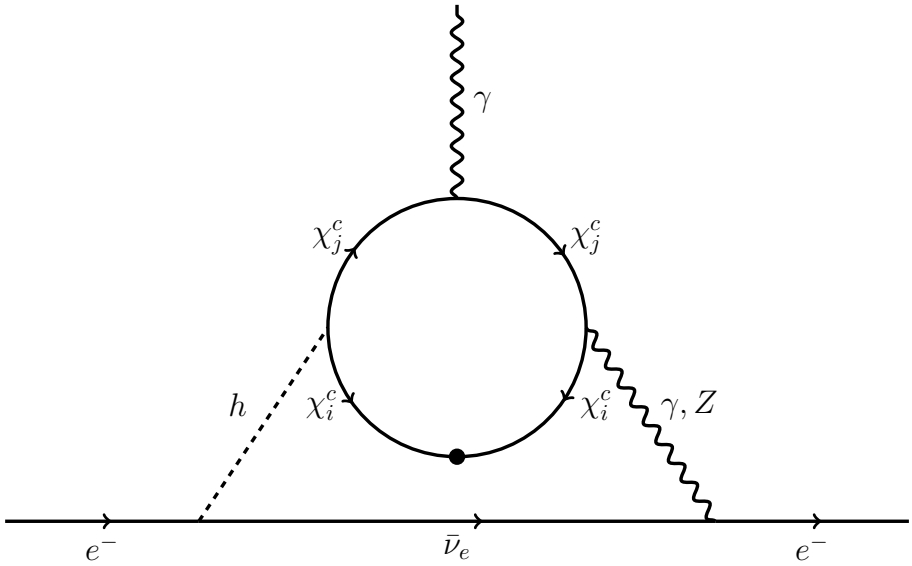

Figure 4.14: Additional class of Barr-Zee diagrams contributing to the electron EDM. χ_c is the tuple of charged fermions in the mass basis. For the γh diagram, $i = j$, whereas for the Zh diagram, we also have contributions where $i \neq j$.

A key difference between the singlet-doublet and doublet-triplet cases is that in the latter the mass of the lightest charged fermion is set by similar scales as those that set the mass of the dark matter, and thus generically the lightest charged fermion mass is $\mathcal{O}(100)$ GeV for the doublet-triplet model. This allows us to treat collider constraints differently here than in the singlet-doublet case; we apply generic LEP constraints on charged fermions rather than running the full collider pipeline we considered pre-

viously. Specifically, charged fermions lighter than 92.4 GeV are ruled out as long as the mass splitting between the lightest neutral and lightest charged particle is ≥ 100 MeV[1,2].[6]

4.4.3 Full Exclusion Limits and Discussion

Unlike in the singlet-doublet case, there is no viable parameter space in this model. In order to show this, we consider three different cases. First, we discuss the case where the magnitude of the couplings is small, for any phase. Then we discuss the case of large coupling and large phase. Finally we discuss the case of large coupling but very small phase.

In the first case, parameter space is entirely ruled out by charged fermion constraints, as we can see from Figure 4.15. On the left, this figure shows the values of several EFT parameters for fixed y, $\tilde{y}$, and δ_{CP} and various values of m_2 and m_3. On the right, we show the annihilation signal and a subset of constraints that are sufficient to rule out this region of parameter space.[7] From these plots, we can see that since the couplings are small, in order to get a sufficient annihilation signal one of m_2 or m_3 must be $\gtrsim m_h/2$, with the other UV mass larger. Since the magnitude of the couplings is small while the UV masses are large, in this region there will only be a very small splitting between charged and neutral fermions. Therefore, the parameter space here will be entirely ruled out by charged fermion constraints from LEP. This occurs regardless of phase, though EDM constraints are also strong enough to rule this out for larger phases.

[6] If the lightest charged state is more than 3 GeV heavier than the lightest neutral state, then there is a stronger bound ruling out charged fermions up to mass 103.5 GeV[2]. We use the smaller of the two values for simplicity since it is sufficient for our purposes.

[7] The other constraints from the singlet-doublet case still apply here, but we omit them from these plots for clarity.

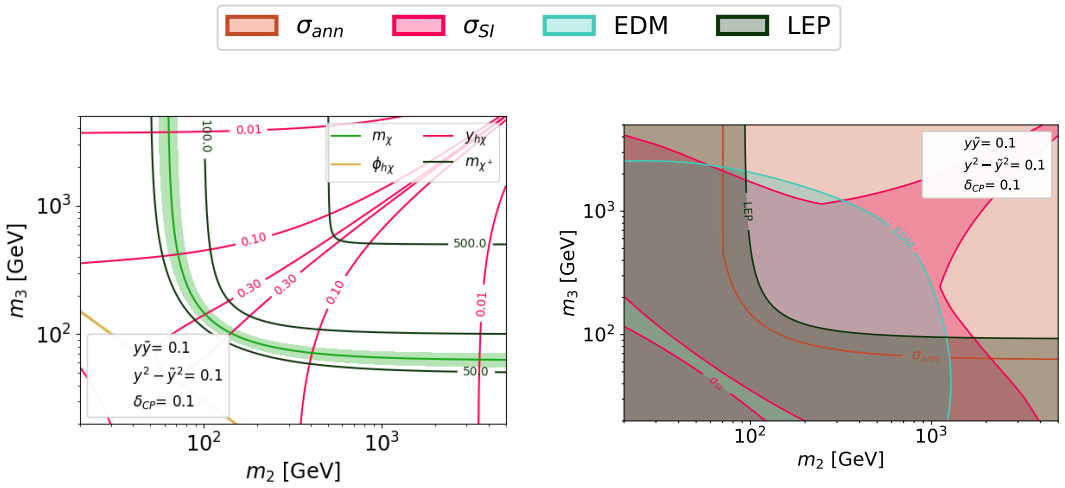

Figure 4.15: Example where the magnitude of couplings y and $\tilde{y}$ are small, for different values of m_2 and m_3. The left plot shows the values of the EFT parameters: dark matter mass, dark matter-Higgs coupling phase, dark matter-Higgs coupling magnitude, and lightest charged fermion mass. Regions around the mass and phase points of interest are shaded: 55 GeV $\leq m_\chi \leq$ 70 GeV and $1.3 \leq \varphi_{h\chi} \leq 1.85$. The right shows the annihilation signal and a subset of relevant constraints including EDM[44], spin-independent direct detection[46,47], and charged fermion constraints from LEP[1,2]. The annihilation signal appears as a single brown line because a viable annihilation signal is only achievable in a tuned region of parameter space.

In the second case of large coupling and large phase, EDM constraints are typically very strong. The only exceptions are if both m_2 and m_3 are very large (which can't generate the necessary annihilation signal) or if one of m_2 or m_3 is very small. This is because in the limit where one of m_2 or m_3 is exactly zero, the phase becomes unphysical since we can rotate it away. In the limit where m_2 is small, the lightest state will have mass even less than m_2 and the DM mass won't be in the right mass range to generate the necessary annihilation signal. But in the limit where m_3 is small, if the couplings are large enough we can potentially generate the right annihilation signal. However, since the physical phase is small, the EFT phase will also be small, and spin-independent direct detection constraints will always

rule out any part of the annihilation signal that isn't constrained by the EDM. This can be seen in Figure 4.16, which again shows various values of EFT parameters for fixed $y, \tilde{y}$, and δ_{CP} and different m_2 and m_3 values on the left, and the annihilation signal and a subset of constraints on the right.

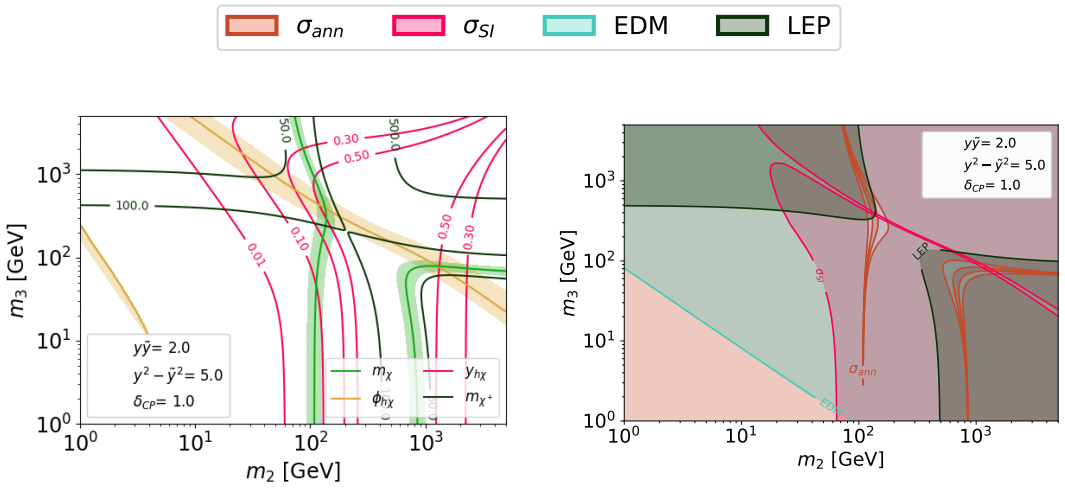

Figure 4.16: Here we show plots where the magnitude of couplings y and $\tilde{y}$ are large and δ_{CP} is also large, for different values of m_2 and m_3. The left plot shows the values of EFT parameters: dark matter mass, dark matter-Higgs coupling phase, dark matter-Higgs coupling magnitude, and lightest charged fermion mass. Regions around the mass and phase points of interest are shaded: 55 GeV $\leq m_\chi \leq$ 70 GeV and $1.3 \leq \varphi_{h\chi} \leq 1.85$. The right shows the annihilation signal and a subset of relevant constraints, and from here we can see that the combination of EDM constraints and spin-independent constraints entirely rule out the parameter space generating a viable annihilation signal.

The third case of large magnitude coupling but very small phase is shown in Figure 4.17. The top plots show the case where y and $\tilde{y}$ are similar in magnitude, while the bottom plots show a large splitting between y and $\tilde{y}$. In both, the EFT coupling is mostly real since the phase is small. There are two different trends depending on the magnitude of the coupling. In both plots, we see regions where the magnitude of the EFT coupling is large, and the annihilation signal is ruled out by spin-independent constraints. In the case of small splitting, we also see a region where the EFT coupling is

small (because the lightest state doesn't mix), which is unable to generate the necessary annihilation signal.

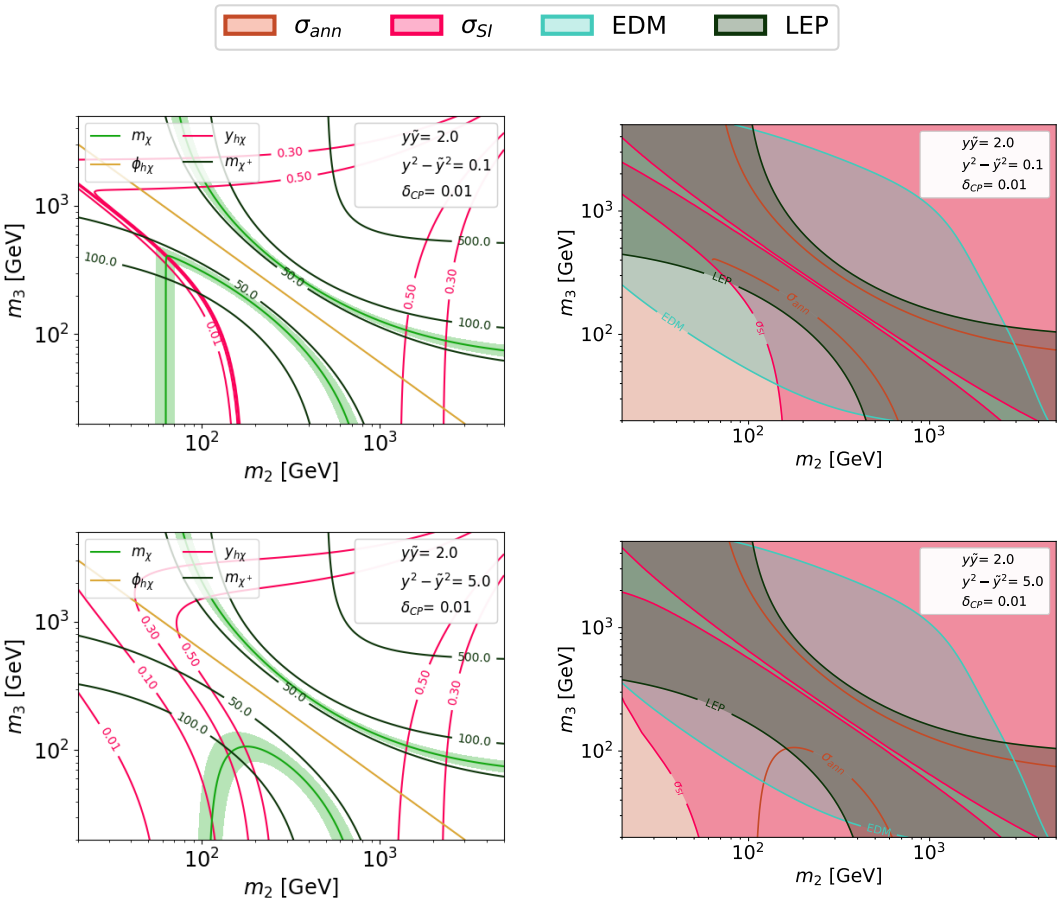

Figure 4.17: Two examples where the magnitude of couplings y and $\tilde{y}$ are large and δ_{CP} is small, for different values of m_2 and m_3. The top plots show the case where y and $\tilde{y}$ have similar magnitudes; the bottom plots show the case where their magnitudes are very different. As in the other doublet-triplet plots, the left plots show the values of various EFT parameters with shaded regions of interest and the right plots show the annihilation signal and a subset of relevant constraints. The annihilation signal appears as two brown lines on each plot, since the region of allowed masses is so narrow. In both cases, spin-independent constraints rule out the signal. In the case where the couplings are nearly equal, there is also a region where the lightest neutral state decouples, and the dark matter-Higgs coupling is insufficient to generate the annihilation signal despite the dark matter mass being close to $m_h/2$.

4.5 Conclusion

Given that the GCE is one of the most persistent signals of potential new physics, it is worth cataloging and understanding what could generate it. While there is still substantial debate over the source of the GCE, one promising and well explored possibility is dark matter annihilating to $b\bar{b}$. In this chapter, we revisit the particular case where dark matter is a Majorana fermion with a CP-violating Higgs coupling, which allows annihilation and spin-independent scattering to be governed by different parameters. Specifically, the leading contribution to annihilation is determined by the imaginary part of the coupling to the Higgs, while spin-independent scattering constraints depend primarily on the real part of the coupling to the Higgs in the mass ranges we are interested in. We study the EFT of this dark matter model for the GCE in detail, and find that while tuning the dark matter mass very close to half the Higgs mass is one potential way to obtain a large enough signal, tuning the phase of the Higgs coupling to make it near imaginary loosens this restriction in the context of the EFT.

We also explore two potential UV completions: singlet-doublet dark matter and doublet-triplet dark matter. In both, the story is more complicated than the EFT because the UV phase and mass are not independent parameters. Although more elaborate supersymmetric realizations of a CP-violating Higgs portal have been discussed in [119], our goal throughout this work has been to gain a more detailed qualitative understanding of the mechanism through simpler models. In particular, we have discussed the scaling of the signal and various constraints with the different parameters in the simplified models, as well as quantified how much tuning is necessary to explain the signal without running into constraints. The singlet-doublet dark matter case is particularly interesting because it is a minimal

working example of how Majorana dark matter could explain the GCE through the Higgs portal.

We find that in the minimal singlet-doublet case, there is still viable parameter space when the doublet mass is much larger than the singlet mass. There are two viable regions of parameter space for the singlet-doublet model. In the case where the UV couplings are small, the tuning of the dark matter mass manifests as a tuning of the singlet mass, but the restriction on both UV and EFT phase is loose. When the couplings are larger, the doublet mass is required to be $\gtrsim \mathcal{O}(1)$ TeV. The EFT phase, and often the UV phase as well, must be close to pure imaginary to avoid spin-independent constraints, and the dark matter and singlet masses also must still be relatively close to $m_h/2$ to generate a sufficient annihilation signal (though the allowed region is comparatively much wider).

Upcoming direct detection and EDM experiments, such as LZ, XENONnT and ACME, will search through significant portions of the remaining parameter space. These two types of probes combine to explore both the limits of minimal and maximal CP-violation, and we expect to definitively rule out doublet masses below the TeV scale in the small coupling case. In the more optimistic case of larger coupling, new experiments will be able to probe doublet masses up to $\mathcal{O}(15)$ TeV or larger for some phases. In either case, this type of model offers a range of complementary detection avenues that may combine to elucidate the nature of annihilating dark matter.

In the doublet-triplet case, we do not find any viable parameter space. Spin-independent and EDM constraints restrict the size of the real and imaginary parts of the Higgs coupling, respectively. When the coupling is small in overall magnitude, the annihilation signal requires a dark matter mass near the $m_h/2$ resonance, and the small splitting between the lightest charged and neutral states results in a prohibitively light charged fermion. Hence, the remaining parameter space is ruled out by LEP.

While our results are framed in the context of the GCE, models which include a CP-violating Higgs portal interaction coupling the dark and visible sectors are also compelling for other reasons. These types of interactions could be the key to some of the biggest mysteries of particle physics, including the particle nature of dark matter and also various problems that CP-violation is necessary to solve, such as the matter/antimatter asymmetry of the universe and the strong CP problem. For example, for some models the addition of a CP phase around the weak scale could increase the viability of electroweak baryogenesis. While new Higgs boson couplings have the potential to make the hierarchy problem worse, the minimal models we studied can also be realized within the larger framework of SUSY[119] which can ameliorate this issue. These connections could be potential avenues for further exploration, if it turns out that dark matter communicates with the Standard Model through a CP-violating Higgs portal.

5

Interpreting the Electron EDM Constraint

5.1 Introduction

The ACME collaboration has used ThO molecules to constrain the electron electric dipole moment (EDM) to be[44]

$$|d_e| < 1.1 \times 10^{-29}\, e\,\text{cm}. \tag{5.1.1}$$

This is about an order of magnitude improvement on the previous bound from ACME[71] and from studies of HfF^+ at JILA[112]. A nonzero electron EDM would establish physics beyond the Standard Model. The electron EDM violates CP (or equivalently, T) symmetry. In the Standard Model, this symmetry is violated by a handful of parameters: the CKM phase, which generates an electron EDM only at four loops with $|d_e| \sim 10^{-44}\, e\,\mathrm{cm}$ but also a CP-odd electron-nucleon interaction that can mimic an EDM of size $|d_e| \sim 10^{-38}\, e\,\mathrm{cm}$[355] (see[266,356] for earlier work); the strong phase $\bar{\theta}$, which generates an electron EDM $|d_e| \lesssim 10^{-37}\, e\,\mathrm{cm}$[134,228]; and phases associated with the lepton sector, which give contributions at two loops suppressed by neutrino masses[337] with an expectation that $|d_e| \lesssim 10^{-43}\, e\,\mathrm{cm}$ or, in the presence of severe fine-tuning, at most $|d_e| \lesssim 10^{-33}\, e\,\mathrm{cm}$[51]. As a result, it is of great interest to continue searching for a smaller electron EDM consistent with (5.1.1) but inconsistent with the Standard Model.

The recent progress in EDM searches comes at a key time in the field of particle physics. The discovery of the Higgs boson at the LHC filled in the last missing piece of the Standard Model. While there are many motivations for searching for physics beyond the Standard Model, three of the most important are the matter-antimatter asymmetry of our universe, the existence of dark matter, and the fine-tuning puzzle of the Higgs boson mass. The matter-antimatter asymmetry clearly indicates a need for new CP-violating physics, which could first be detected through its indirect effect on the electron EDM. As we will discuss below, EDMs also have interesting connections with WIMP dark matter (in specific models) and with the fine-tuning problem.

The possibility of testing heavy new physics through electric dipole moment measurements has been studied extensively; reviews include[354,193,365,144]. Here we attempt to briefly summarize some

of the important history of the topic, with apologies for inevitable omissions. Some early theoretical studies of lepton EDMs appeared already in the 1970s[343,178]. Many of the early studies of CP violation in supersymmetric theories focused on the neutron EDM[189,130,351], but studies of the electron EDM in supersymmetry commenced[166] shortly after a suggestion of Gavela and Georgi that lepton EDMs could be effective probes of new physics[225]. Subsequently, a variety of additional sources of EDMs were studied, such as 3-gluon operators[391] or two-loop diagrams mediated by electroweak bosons[72,313]. A variety of new physics scenarios have been shown to predict interesting EDMs, including: stops in SUSY[124]; electroweakinos in SUSY[315] and specifically split SUSY[54,232]; two Higgs doublet models[313,125,284,16]; SUSY beyond the MSSM[93,35]; and fermionic top partners[345].

Our goal in this chapter is to give a brief survey of how theories of new physics are constrained by the ACME result, including a range of novel possibilities where an EDM is mediated by the charm or top quark. We begin in §5.2 by giving a general argument, based on effective field theory, for the range of mass scales that are probed by the EDM. In scenarios with two-loop EDMs where the electron Yukawa coupling appears explicitly in the new physics couplings—which includes many SUSY scenarios—the ACME constraint probes masses of a few TeV. Other scenarios, where loop effects generate both the EDM and the electron Yukawa coupling, potentially probe scales of hundreds of TeV. We also discuss the case where the dominant effect on ThO is not the electron EDM at all but the CP-odd electron-nucleon coupling (as discussed in e.g.[309,169,354,283,145]). Next we turn to a discussion of EDM constraints on supersymmetric scenarios: one-loop SUSY in §5.3; two-loop split SUSY in §5.4; and two-loop natural SUSY in §5.5. Our calculations in the two loop cases follow[336], which can be consulted for more details. Our discussion of split SUSY includes a comparison of the reach of

EDMs and of recent dark matter direct detection results from Xenon1T[47]. Most of our discussion of SUSY draws heavily on earlier literature, but updates it in light of the new experimental result. In the context of one-loop effects, if sleptons and squarks are at a comparable mass scale then we show that there is an interesting complementarity between the requirement of consistency with a 125 GeV Higgs (which prevents making the scalar mass too large, for any given $\tan\beta$) and the EDM constraint (which prevents the scalars from being too light, for a given CP-violating phase). This interesting qualitative point is shown in Figure 5.4, which provides a novel way to visualize how EDM experiments are encroaching on the viable SUSY parameter space. In §5.6 we discuss the possibility that the EDM is induced by the QULE operator $(q_f\bar{\sigma}^{\mu\nu}\bar{u}_f)\cdot(\ell\bar{\sigma}_{\mu\nu}\bar{e})$. In this case new physics need not couple to the Higgs boson at all to generate an EDM. Instead, new physics couples quarks and leptons, and then the quark Yukawa coupling supplies the necessary interaction with the Higgs. The most plausible version of this scenario has the top quark inducing the EDM, though the charm quark could also play this role. (If the up quark is the leading coupling, then the CP-odd electron-nucleon coupling plays a more important role in the ThO measurement than the electron EDM itself.) The QULE operator could be induced by scalar leptoquark exchange at tree level, as previously discussed in [58,224,165]. It could also arise from a box diagram, a case that we discuss for the first time. We classify a number of possibilities for the quantum numbers of the particles appearing in the loop, which could have a variety of distinctive collider signals. In some of these models, the QULE-generated EDM is the leading contribution, as couplings allowing for other EDM contributions (e.g. of Barr-Zee type) are absent. We conclude in §5.7 with a few remarks on the implications of future improvements in EDM searches. If no EDM is detected, then the CP-violating phases associated with any new physics near the TeV scale will be

constrained to be very small. We believe that it is timely to further investigate how naturally small CP-violating phases might be explained. Conversely, if a nonzero EDM is detected, then either it arises from TeV-scale particles that may be detected at future colliders, or from even heavier particles, out of reach of currently feasible experiments. We argue that in the latter case, these new particles would lead to a very concrete form of the hierarchy problem, motivating the construction of new colliders even if the particles directly contributing to the EDM are out of reach.

5.2 Interpreting the EDM constraint: the big picture

In this section, we present a general argument for the range of mass scales probed by the EDM experiments. The cases where the dominant effect on ThO comes from the CP-odd electron-nucleon coupling as well as the electron EDM are discussed.

5.2.1 The electron EDM

Dipole moment interactions flip the chirality of a fermion. In the Standard Model, since left- and right-handed fermion fields carry different charges, gauge invariance requires that the EDM is a dimension-six operator involving the Higgs boson: either $ih^\dagger \ell \bar{\sigma}^{\mu\nu} \bar{e} B_{\mu\nu}$ or $ih^\dagger \ell \sigma^i \bar{\sigma}^{\mu\nu} \bar{e} W^i_{\mu\nu}$. Hence, an EDM generated by new physics at a mass scale M is always proportional to v/M^2 times a product of couplings and loop factors. Physics that produces the EDM operators can also produce corrections to the electron Yukawa interaction $h^\dagger \ell \bar{e}$, simply by removing the gauge interaction vertex from the Feynman diagrams that appear in the EDM calculation. As a result, we expect the size of the EDM to be bounded in terms of the size of the electron Yukawa in typical scenarios without fine-tuning.

We can consider three scenarios for how to treat the relationship between the EDM and the electron Yukawa:

- **Spurion approach.** Here we assume that the couplings generating the EDM are directly proportional to y_e. If the EDM is generated at k loops, we expect:

$$d_e \sim \delta_{\text{CPV}} \left(\frac{y^2}{16\pi^2}\right)^k \frac{m_e}{M^2}, \tag{5.2.1}$$

  with y standing in for whatever coupling arises in the loop, generally presumed to be an order-one number, and δ_{CPV} the size of the CP-violating phase.

- **Radiative stability approach.** Here we make the weaker assumption that the interactions generating the EDM make no more than an order-one change to the size of the electron Yukawa coupling. This could be the case, for example, if the electron Yukawa coupling is radiatively generated by the same interactions. We have:

$$d_e \sim \delta_{\text{CPV}} \frac{m_e}{M^2}. \tag{5.2.2}$$

  In this case the estimate matches the 0-loop spurion estimate, as we assume that the same loop factors are shared by y_e and d_e.

- **Tuning approach.** In this case, we allow for the interactions generating the EDM to generate a contribution to the electron Yukawa much larger than the Yukawa itself, so that the final Yukawa is tuned to be small via a cancellation. This is the least aesthetically appealing case, but is a logical possibility. The EDM can arise from a k-loop diagram containing $2k+1$ Yukawa couplings, each in principle as large as $y \lesssim 4\pi$, the value estimated by Naive Dimensional Analysis (NDA). Hence we estimate a maximum EDM consistent with NDA:

$$d_e \sim \delta_{\text{CPV}}\, y \left(\frac{y^2}{16\pi^2}\right)^k \frac{v}{M^2} \lesssim \delta_{\text{CPV}} \frac{4\pi v}{M^2}. \tag{5.2.3}$$

  The tuning approach allows for the largest mass scale for new physics.

Following these simple estimates and taking, for concreteness, $y = g$ with $g \approx 0.65$ the weak coupling constant, we obtain the following rough estimates of the mass scales of new physics probed

Table 5.1: Mass Scale of New Physics Necessary for $|d_e| \lesssim 1.1 \times 10^{-29}\, e\,\mathrm{cm}$

	0-loop	1-loop	2-loop
Spurion	1000 TeV	50 TeV	3 TeV
Radiative	1000 TeV	1000 TeV	1000 TeV
Tuned	2×10^9 TeV	2×10^9 TeV	2×10^9 TeV

by the EDM measurement (5.1.1):

We see that with fine tuning to cancel large corrections to the electron Yukawa, the EDM measurement can in principle probe physics far above that being studied at colliders. However, for more theoretically plausible models, the mass scale probed is below 1000 TeV and, in a wide range of models that lead to EDMs at two loops, is of order 1 TeV.

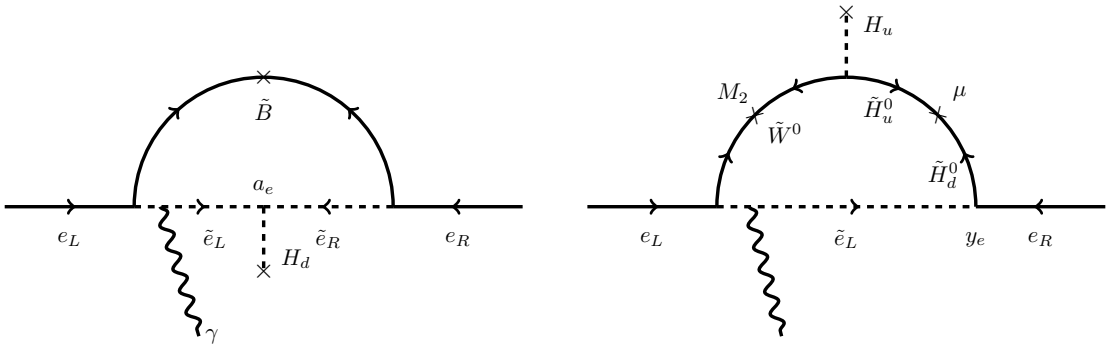

Figure 5.1: One-loop EDMs in supersymmetric theories.

In later sections, we will see the simple estimates in the table substantiated in a variety of concrete models of new physics, but let us briefly summarize the models we expect in each category of the table. First, we look at tree-level contributions to the electron EDM. If the lepton sector couples to some new strongly-coupled sector with CP violation, we do not expect any loop suppression factor in the expression of the EDM. In the case where the physics giving the electron chirality flip is still proportional to

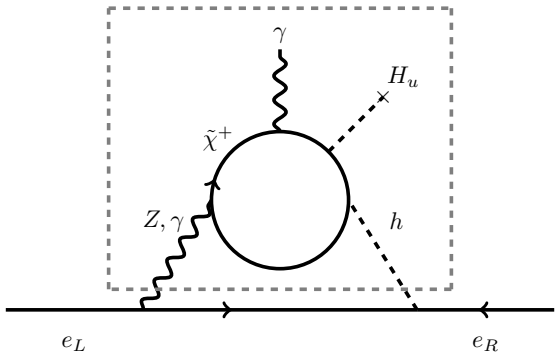

Figure 5.2: Two-loop EDMs in supersymmetric theories. The one-loop diagram in the dashed box is a CP-violating analogue of familiar "electroweak precision" corrections.

the electron Yukawa, this corresponds to the tree-level spurion approach. On the other hand, in the scenario of partial compositeness where the lepton sector linearly couples to a new strongly-coupled sector giving a composite Higgs[289], the electron EDM is generated by the same interactions realizing the electron Yukawa coupling, which is the tree-level radiative stability approach.

An example of a one-loop EDM in SUSY theories is shown in Figure 5.1. The right diagram is explicitly proportional to the electron Yukawa while the left diagram is not. However, depending on the proportionality of the A-term to y_e, this contribution is classified into the spurion scenario or the other scenarios. These diagrams illustrate an important general point: one-loop diagrams for the EDM will generally contain *some new particle with lepton quantum numbers*, like the electron superpartner appearing in this diagram. If all new particles with lepton quantum numbers are heavy, there may be no important one-loop diagrams contributing to the EDM, and the most important contributions may arise at two loops.

A two-loop electron EDM can arise from the Barr-Zee type diagrams[72], from similar diagrams

induced by the W boson EDM[61], or from rainbow diagrams[395]. They are all proportional to the electron Yukawa coupling and classified into the spurion approach. The two-loop EDM can also arise from RGE running induced by $q\bar{u}\ell\bar{e}$-type operators arising from a one-loop box diagram[34] which provides an example of the radiative stability approach as we will study in detail later. An example of a two-loop EDM in SUSY theories is shown in Figure 5.2.

5.2.2 An alternative: the CP-odd electron-nucleon coupling

We should consider the possibility that the electron EDM inferred from ThO is not really the electron EDM at all, but instead evidence of a CP-odd electron-nucleon interaction $-iC_S\bar{e}\gamma_5 e\bar{N}N$. Indeed, in the Standard Model this is expected to be a larger effect[355], though we will argue that the opposite is true for many models of new physics. The coupling C_S contributes to the effective EDM as[145]

$$\begin{aligned} d_{\mathrm{ThO}} &\approx d_e + kC_S, \\ k &\approx 1.6 \times 10^{-15}\ \mathrm{GeV}^2\, e\,\mathrm{cm}. \end{aligned} \tag{5.2.4}$$

The size of k depends in a somewhat nontrivial way on factors including the ratio of atomic and nuclear radii and the value of $Z\alpha$ for the atoms involved; we refer readers to the appendix of[185] for details. The microscopic origin of such a four-fermion interaction is in similar interactions with quarks in place of nucleons:

$$\mathcal{L}_{\mathrm{Four-Fermi}} \supset \sum_q C_{qe}\,(\bar{q}q)\,\left(\bar{e}\,i\gamma_5 e\right), \tag{5.2.5}$$

where q denotes any flavor of quarks. These four-fermion interactions lead to

$$\begin{aligned} C_S &\approx C_{de}\langle N|\bar{d}d|N\rangle + C_{se}\langle N|\bar{s}s|N\rangle + C_{be}\langle N|\bar{b}b|N\rangle \\ &\quad + C_{ue}\langle N|\bar{u}u|N\rangle + C_{ce}\langle N|\bar{c}c|N\rangle + C_{te}\langle N|\bar{t}t|N\rangle \\ &\approx C_{de}\frac{29\,\mathrm{MeV}}{m_d} + C_{se}\frac{49\,\mathrm{MeV}}{m_s} + C_{be}\frac{74\,\mathrm{MeV}}{m_b} \\ &\quad + C_{ue}\frac{16\,\mathrm{MeV}}{m_u} + C_{ce}\frac{76\,\mathrm{MeV}}{m_c} + C_{te}\frac{77\,\mathrm{MeV}}{m_t}. \end{aligned} \tag{5.2.6}$$

Here, we have used the matrix elements [190,285],

$$\begin{aligned} &(m_u + m_d)\langle N|\bar{u}u + \bar{d}d|N\rangle \simeq 90\,\mathrm{MeV}, \qquad \langle N|\bar{u}u - \bar{d}d|N\rangle \simeq 0, \\ &m_s\langle N|\bar{s}s|N\rangle \simeq 49\,\mathrm{MeV}, \qquad m_b\langle N|\bar{b}b|N\rangle \simeq 74\,\mathrm{MeV}, \\ &m_c\langle N|\bar{c}c|N\rangle \simeq 76\,\mathrm{MeV}, \qquad m_t\langle N|\bar{t}t|N\rangle \simeq 77\,\mathrm{MeV}. \end{aligned} \tag{5.2.7}$$

and $m_u/m_d = 0.55$.

As in the case of the electron EDM, physics generating the C_S coupling can also produce corrections to the electron mass by connecting two quark legs of (5.2.5) with an insertion of the quark mass, and we can consider three scenarios in the relationship between the C_S coupling and the Yukawa couplings:

- **Spurion approach.** We assume that the couplings generating the four-fermion interactions are directly proportional to the electron and quark Yukawa couplings. If the four-fermion interactions are generated at k loops, we expect:

$$C_{qe} \sim \delta_{\mathrm{CPV}} \left(\frac{y^2}{16\pi^2}\right)^k \frac{m_q m_e}{v^2 M^2}. \tag{5.2.8}$$

In this scenario, the quark mass suppression in (5.2.6) is cancelled by the quark mass dependence in C_{qe}. If we take this ansatz for all of the quarks, the top quark gives the most important contribution.

- **Radiative stability approach.** As in the case of the electron EDM, we make the weaker assumption that the generated four-fermion interactions do not lead to more than an order-one change to the size of the electron Yukawa coupling, which gives a constraint on the size of the coupling in an underlying theory to generate the four-fermion interactions. Then, we expect:

$$C_{qe} \sim \delta_{\text{CPV}} \frac{16\pi^2 m_e}{m_q} \frac{1}{M^2}. \tag{5.2.9}$$

  Due to the quark mass suppression in this expression as well as in (5.2.6), the up quark gives the most important contribution (assuming that we take this ansatz for all of the quarks). Since $m_q > m_e$, the requirement that the four-fermion interactions do not lead to more than an order-one change to the size of quark Yukawa couplings does not lead to a further constraint on the size of C_{qe}.

  Notice that because the operator breaks both quark and lepton chiral symmetries, if it has a large coefficient one can think of it as leaving invariant only a combined chiral rotation of both quarks and leptons.

- **Tuning approach.** In this scenario, we allow for underlying interactions generating the four-fermion interactions to generate a contribution to the electron Yukawa much larger than the correct size, so that the final electron Yukawa is tuned to be small. If the four-fermion interactions are generated at k loops, we expect from NDA:

$$C_{qe} \sim \delta_{\text{CPV}}\, y^2 \left(\frac{y^2}{16\pi^2}\right)^k \frac{1}{M^2} \lesssim \delta_{\text{CPV}} \frac{16\pi^2}{M^2}. \tag{5.2.10}$$

  The quark mass suppression in (5.2.6) makes the top quark contribution naively very small and the up quark gives the most important contribution.

Following these simple estimates and taking $y = g$, we obtain the following rough estimates of the mass scales of new physics probed by the EDM measurement (the parenthesis denotes the dominant contribution in each category):

Table 5.2: Mass Scale of New Physics Necessary for $|d_{\mathrm{ThO}}| \lesssim 1.1 \times 10^{-29}\, e\,\mathrm{cm}$

	0-loop	1-loop	2-loop
Spurion	300 GeV (C_{te})	20 GeV (C_{te})	0.8 GeV (C_{te})
Radiative	1×10^5 TeV (C_{ue})	1×10^5 TeV (C_{ue})	1×10^5 TeV (C_{ue})
Tuned	4×10^5 TeV (C_{ue})	4×10^5 TeV (C_{ue})	4×10^5 TeV (C_{ue})

In listing the dominant contribution we assume the same ansatz applies for all quarks; of course, a more general flavor structure, including the possibility of off-diagonal couplings, is also possible, but the simple ansatz gives a qualitative sense of the range of mass scales of interest. The tuned and radiative stability approaches probe large energy scales. On the other hand, in the spurion approach, the mass scale is below 1 TeV even in the 0-loop case and has been already explored at colliders.

5.3 The EDM constraint on one-loop SUSY

In this section we discuss constraints on supersymmetry arising from 1-loop EDMs. The relevant formulas are well-known in the literature (e.g. [273]), but it is useful to update the bounds in light of new data. Furthermore, by comparing the parameter space ruled out by EDMs with the parameter space in which the MSSM cannot accommodate the measured Higgs mass, we provide a novel visualization of the power of EDM searches (see Figure 5.4).

We showed examples of one-loop SUSY EDMs above in Figure 5.1. To unpack the diagrams a bit more: the electron splits into a virtual pair of its superpartner (the selectron) and a neutralino (the superpartner of the photon, Z, or Higgs boson). The diagram at right contains a selectron–electron–Higgsino interaction, which depends on the electron Yukawa coupling $y_e = m_e/v$. Then, it is proportional to m_e. The diagram at *left*, on the other hand, transforms the left-handed selectron to the

right-handed selectron using the A-term trilinear coupling, $a_e H_d \tilde{e}_L \tilde{e}_R$. In a general supersymmetric theory, a_e is formally independent of the Yukawa coupling y_e, although in many models they are proportional: $a_e \approx y_e M_{\text{SUSY}}$, where M_{SUSY} is some measure of the SUSY-breaking scale. Since attempting to break this proportionality would lead to large corrections to m_e, it is reasonable to assume the proportionality. In this section, we concentrate on flavor-diagonal contributions to the EDM, which exist even in the absence of flavor violation in soft scalar masses generating dangerous FCNCs. If there are large off-diagonal scalar mass terms, different diagrams with insertion of scalar mass mixing become important [328,36].

In the diagram at left, the invariant phase that would contribute to CP violation is $\arg(a_e^* M_{1,2})$. In many particular models of SUSY breaking, like gauge mediation (for reviews, [231,299]), this CP phase is zero, and the contribution is absent. In more general models, like gravity mediation, it is unclear whether we should expect this phase to be small. The diagram at right is sensitive to the phase $\arg(\mu M_2 b_\mu^*)$.[1] Generation of μ, the Higgsino mass parameter, is typically one of the thorniest problems in building a supersymmetric model, and it seems very plausible that it could have a CP phase different from other SUSY-breaking parameters.

Let us summarize a general one-loop formula of the fermion EDM induced by a fermion ψ_i with mass m_i and electric charge Q_i and a complex scalar φ_j with mass m_j and electric charge Q_j. Their interactions with the SM fermion f are:

$$\mathcal{L}_{\psi f \varphi} = L_{ij} \left(\bar{\psi}_i P_L f\right) \varphi_j^* + R_{ij} \left(\bar{\psi}_i P_R f\right) \varphi_j^* + \text{h.c.}, \tag{5.3.1}$$

[1] Much of the literature performs a field redefinition to remove the phase of b_μ and refers to this simply as $\arg(\mu M_2)$, which we will sometimes write below.

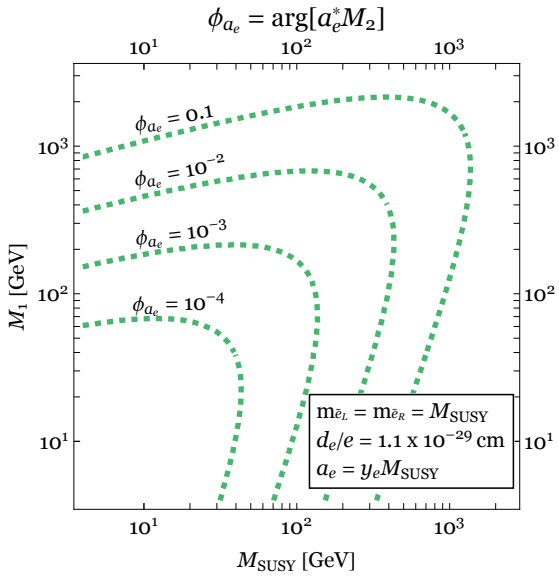

Figure 5.3: The ACME II constraint on the selectron mass scale $M_{\rm SUSY}$ and the Bino mass M_1. The left region of each contour is excluded. We plot four cases of the phase $\varphi \equiv \arg[a_e^* M_2] = 0.1, 10^{-2}, 10^{-3}, 10^{-4}$. We assume the left-handed and right-handed selectron soft masses are the same, $m_{\tilde{e}_L} = m_{\tilde{e}_R} = M_{\rm SUSY}$.

where $P_{R,L} = \frac{1}{2}\left(1 \pm \gamma^5\right)$ and L_{ij} and R_{ij} are coupling constants. With these interaction terms, the one-loop calculation gives[273]

$$\frac{d_f}{e} = \left(\frac{m_i}{16\pi^2 m_j^2}\right) \mathrm{Im}[(R_{ij})^* L_{ij}] \left[Q_i \frac{1}{2(1-r)^2}\left(\frac{2\log r}{1-r} + 3 - r\right) + Q_j \left(\frac{1 + r + \frac{2r\log(r)}{1-r}}{2(1-r)^2}\right)\right]. \tag{5.3.2}$$

Here, $r = m_i^2/m_j^2$.

We now look at the contribution to the electron EDM from the diagram at the left of Figure 5.1. The mass terms of the selectrons and the Bino and their interaction terms (in two-component spinor

notation) are

$$\begin{aligned}\mathcal{L} \supset & -m_{\tilde{e}_L}^2|\tilde{e}_L|^2 - m_{\tilde{e}_R}^2|\tilde{e}_R|^2 - \left(\frac{1}{2}M_1\tilde{B}\tilde{B} + \text{h.c.}\right) \\ & - a_e H_d\, \tilde{e}_L\tilde{e}_R^* - g' Y_L \tilde{B} e_L \tilde{e}_L^* - g' Y_R \tilde{B} e_R^\dagger \tilde{e}_R + \text{h.c.},\end{aligned} \tag{5.3.3}$$

where g' is the $U(1)_Y$ coupling constant and Y_L and Y_R are the hypercharges of the left-handed and right-handed electrons respectively. With a nonzero vev of H_d, the A-term gives an off-diagonal component in the selectron mass matrix. We first diagonalize the mass matrix and rewrite the interactions in terms of the mass-eigenstate basis. Then, using the above general formula (5.3.2), we can obtain the expression for the electron EDM d_e. There are also contributions from the other neutralinos in the similar loops, but they are subdominant when the gaugino masses are large enough compared to the electroweak breaking scale and ignored. Figure 5.3 shows the ACME II constraint on the selectron mass scale M_{SUSY} and the Bino mass M_1. The left region of each contour is excluded. We plot four cases of the phase $\varphi \equiv \arg[a_e^* M_2] = 0.1, 10^{-2}, 10^{-3}, 10^{-4}$. We assume that the left-handed and right-handed selectron soft masses are the same, $m_{\tilde{e}_L} = m_{\tilde{e}_R} = M_{\text{SUSY}}$. Since the diagram contains an insertion of the vev v_d and $a_e = y_e M_{\text{SUSY}}$ is assumed, the contribution to the EDM is proportional to $a_e v_d = m_e M_{\text{SUSY}}$ and does not depend on $\tan\beta$.[2] Taking into account the size of the $U(1)_Y$ coupling $(g'/g)^2 \approx 0.3$, the obtained lower bound on the mass is consistent with our general argument presented in Section 5.2.1.

[2] Choosing a/y of the same order as the soft masses can, in the stop sector, lead to color- and charge-breaking vacua [148,121]. For $a_t/y_t = m_{\tilde{Q}_3} = m_{\tilde{u}_3} = M_{\text{SUSY}}$ there is no vacuum stability problem, but for a_t/y_t an order-one factor larger there could be [140,91].

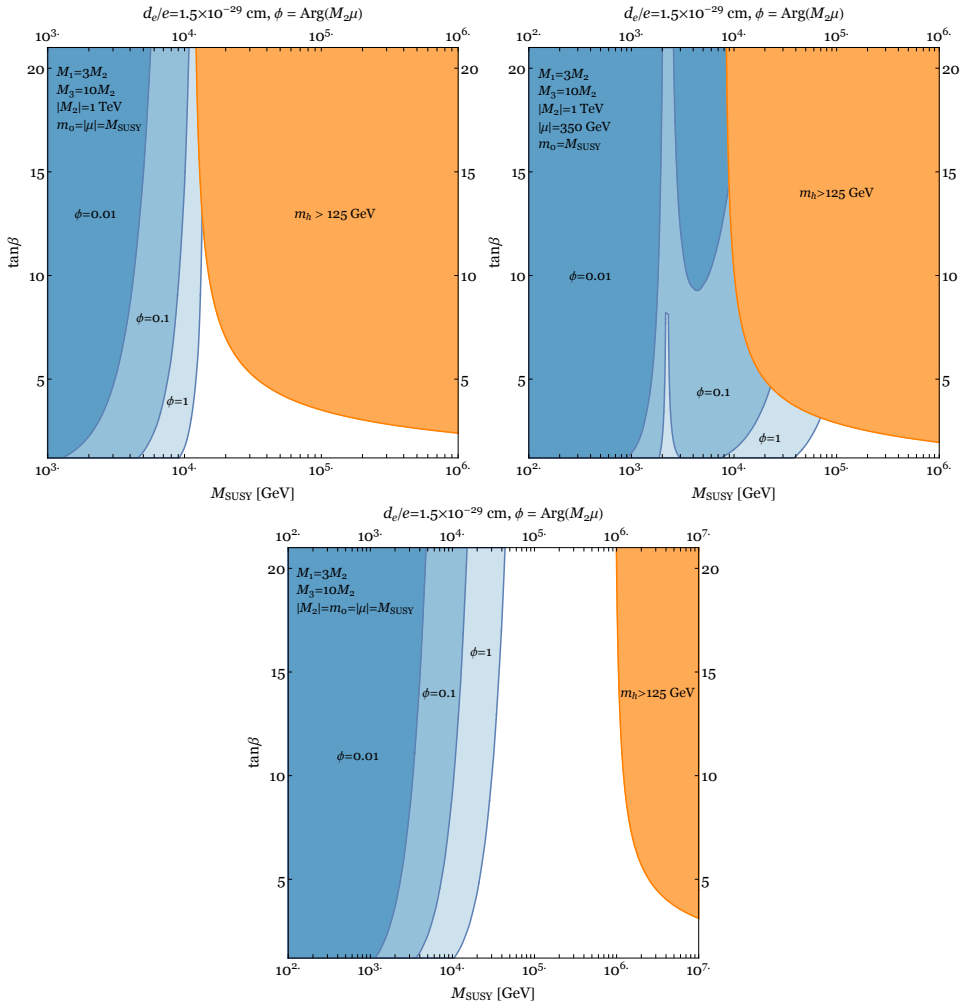

Figure 5.4: The ACME II constraint on $M_{\rm SUSY}$ and $\tan\beta$. The electron EDM is generated by the right diagram of Figure 5.1. The orange region is excluded from $m_h > 125$ GeV. The upper left and right panels correspond to the case of split SUSY, $M_{1,2,3} \ll m_0 = M_{\rm SUSY}$. We take $|\mu| = M_{\rm SUSY}$ and $|\mu| = 350$ GeV in the left and right panels respectively. The lower panel corresponds to the case of high-scale SUSY, $M_{1,2,3} \sim m_0 = M_{\rm SUSY}$. In all cases, we assume a gaugino mass ratio, $M_1 : M_2 : M_3 = 3 : 1 : 10$. In each panel, we plot three cases of the phase $\varphi \equiv \arg(M_2\mu) = 1, 0.1, 0.01$.

We next consider the diagram at the right of Figure 5.1. As above, the contribution to the electron EDM can be calculated by applying the general formula (5.3.2). The relevant interaction terms should be given in terms of the basis of the neutralino and chargino eigenstates. With the resulting expression

of the electron EDM, the ACME II gives a direct constraint on slepton masses. However, most scenarios of SUSY breaking, including gauge mediation and anomaly mediation [360,230], generate squark and slepton soft masses at the same order of magnitude. In addition, a large splitting between slepton and squark masses inside each generation induces a large one-loop effect of the hypercharge D-term, which may drive light scalars tachyonic. Then, it is reasonable to assume squark and slepton masses at the same order and the null result of the EDM experiment implies a lower bound on squark masses as well as slepton masses. Since top/stop loops give a significant radiative correction to the Higgs mass, too-large stop masses may lead to a Higgs mass larger than 125 GeV, which sets an upper bound on the mass scale of squarks and sleptons.

In Figure 5.4, we show constraints on the parameter space for EDMs from mixed electroweakinos and left-handed sleptons. We compute the Higgs mass using SusyHD [346] assuming universal scalar masses m_0. The orange region is excluded from $m_h > 125\,\mathrm{GeV}$. The upper left and right panels correspond to the case of split SUSY, $M_{1,2,3} \ll m_0 = M_{\mathrm{SUSY}}$. We take $|\mu| = M_{\mathrm{SUSY}}$ and $|\mu| =$ 350 GeV in the left and right panels respectively. The lower panel corresponds to the case of high-scale SUSY, $M_{1,2,3} \sim m_0 = M_{\mathrm{SUSY}}$. In all cases, we assume a gaugino mass ratio, $M_1 : M_2 : M_3 = 3 : 1 : 10$. In each panel, we plot three cases of the phase $\varphi \equiv \arg(M_2 \mu) = 1, 0.1, 0.01$. In the upper two cases of split-SUSY, the EDM bound has already hit the excluded region of a too-large Higgs mass (provided $\tan\beta$ is not too small) while there is still room between the EDM bound and the Higgs mass bound in the case of high-scale SUSY.

5.4 The EDM constraint on two-loop split SUSY

In this and the following section, we will examine how the new experimental result allows us to update earlier conclusions about EDM constraints from 2-loop SUSY contributions. In split supersymmetry, if we decouple the squarks, sleptons, and heavy Higgs bosons (working at relatively low $\tan\beta$), the dominant EDMs will arise from loops of charginos and neutralinos [54,232]. These are Barr-Zee type diagrams with an inner loop connected to the electron with γh, Zh, or WW propagators. The dominant diagram is γh; WW is not negligible, but Zh is subleading since $\frac{1}{4} - \sin^2\theta_W$ happens to be small. If we integrate out charginos at one loop we obtain the effective operator

$$\frac{e^2}{16\pi^2}(\arg\det \mathcal{M}_{\widetilde{C}})F_{\mu\nu}\widetilde{F}^{\mu\nu} = \frac{e^2}{8\pi^2}\frac{\mathrm{Im}(g^2 M_2 \mu H_u \cdot H_d)}{|M_2\mu - g^2 H_u \cdot H_d|^2}F_{\mu\nu}\widetilde{F}^{\mu\nu} \tag{5.4.1}$$

where $\mathcal{M}_{\widetilde{C}}$ is the chargino mass matrix. This operator mixes into the EDM at one loop, allowing us to easily understand the leading-log contribution to the two-loop calculation. Because the numerator involves $H_u \cdot H_d$, the EDM becomes smaller at large $\tan\beta$ when the light Higgs boson has little overlap with H_d.

The EDM requires a coupling to the Higgs boson, meaning that it vanishes if we send either the gaugino masses $M_{1,2}$ or the higgsino mass μ to infinity. As a result, the size of the EDM is highly correlated with a variety of other observables, including the dark matter direct detection cross section if the lightest neutralino is dark matter (see e.g. [334,302] for further discussion of the EDM/DM interplay). Majorana neutralinos have a dominant spin-independent scattering rate through their coupling to the

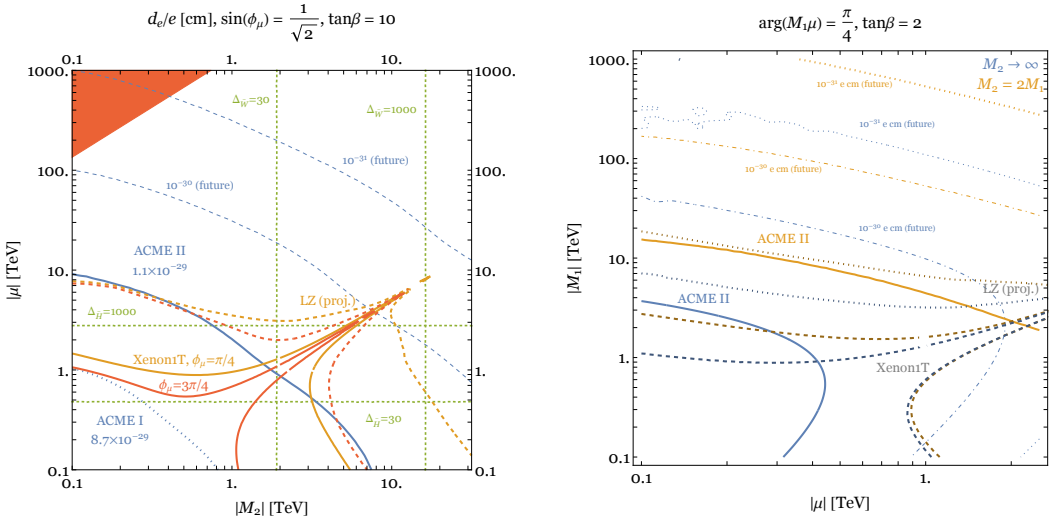

Figure 5.5: Constraints on electroweakinos from EDMs and from dark matter direct detection in the case of a large CP-violating phase, $\sin(\varphi_\mu) = 1/\sqrt{2}$. Left-hand panel: bounds as a function of $|M_2|$ and $|\mu|$, assuming $M_1 = M_2/2$. We have fixed $\tan\beta = 10$ for relatively weak EDM constraints. The orange Xenon1T and LZ curves are for $\varphi_\mu = \pi/4$ while the red curves are for $\varphi_\mu = 3\pi/4$, where the direct detection constraints are weaker. We see that the EDM constraint is generally stronger except near the diagonal. The green dashed curves are fine-tuning contours and the upper-left triangular region requires tuning away a threshold correction to M_2; see [336] §6.1 for further discussion. The dashed "future" curves represent hypothetical future improvements, possibly arising from experiments with polyatomic molecules [301]. Right panel: bounds as a function of $|\mu|$ and $|M_1|$ with $\tan\beta = 2$. Here we present two scenarios, one with $M_2 = 2M_1$ and one where winos are decoupled ($M_2 \to \infty$, see [218]). Decoupling the winos removes the dominant (γh) Barr-Zee contributions to the EDM and leaves a much weaker constraint from the W boson EDM. Dark matter experiments more strongly constrain the parameter space in this case.

Higgs boson [69], which is highly constrained by xenon-based dark matter experiments like Xenon1T [47] and PandaX II [154]. Of course, dark matter direct detection experiments can only constrain new physics if the particles in question actually constitute dark matter. In the discussion here we will consider only neutralinos that saturate the observed dark matter relic abundance. (In particular, we do not assume that neutralinos are thermal relics; nonthermal mechanisms for populating dark matter are ubiquitous in SUSY theories.) Neutralinos making up a subdominant fraction of dark matter are more weakly constrained.

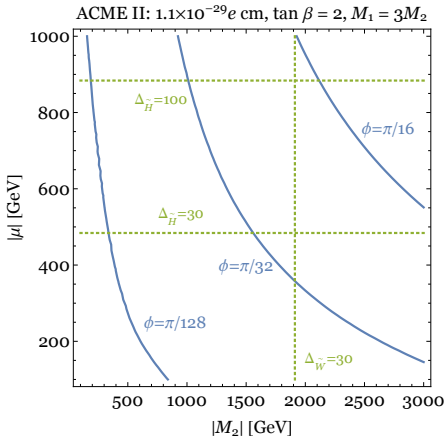

Figure 5.6: Constraints on electroweakinos from EDMs: the case of small phases. Here we have fixed $M_1 = 3M_2$, as in anomaly mediated SUSY breaking, and $\tan\beta = 2$. We see that the ACME result is compatible with light electroweakinos only for percent-level phases.

In Figure 5.5 we show comparisons of the electron EDM constraint on electroweakino parameter space with the dark matter direct detection constraint from Xenon1T[47] and a projected future constraint corresponding to the goal of the LZ experiment[333]. (For the nucleon matrix elements used in the direct detection calculation we follow[75], which in turn uses[79].) We see that both experiments are powerful probes of electroweakino masses, reaching into regions of multi-TeV mass. In all curves we have taken the phase appearing in the EDM to be $\varphi_\mu \equiv \arg(\mu M_2 b_\mu^*) = \pi/4$ and assumed the phases of M_1 and M_2 to be equal. In the left-hand panel, we fix $M_1 = M_2/2$ and $\tan\beta = 10$. The right panel of Figure 5.5 gives a different look at the constraints, focusing on the bino/higgsino sector. The orange curves assume $M_1 = \frac{1}{2}M_2$ as in the left panel, but the light blue curves correspond to the case of a completely decoupled wino ($M_2 \to \infty$), as in the Hypercharge Impure model of Split Dirac SUSY[218]. This case is of interest for the possibility of nearly pure Dirac higgsino dark matter; we see from the figure that ACME's constraint is relatively weak, though for weak-scale higgsino masses it

still probes multi-TeV bino masses. Finally, in Figure 5.6 we zoom in on the low-mass region of electroweakino parameter space, showing that compatibility with the ACME bound requires small (10% or lower) phases in the region with a chargino below 1 TeV.

Although we have focused in this section on charginos and neutralinos in the SUSY context, so that the Yukawa couplings are pinned to the size of Standard Model gauge interactions, much of the discussion would carry over to a more general scenario with new fermions with electroweak quantum numbers and Yukawa couplings to the Higgs boson. These are often discussed in the dark matter context as singlet-doublet and doublet-triplet models[325,149,164]. The interplay between EDM constraints and other probes of such fermions as dark matter has been discussed in[201]. If new fermions with large Yukawa couplings are added to the Standard Model without additional bosons (such as their supersymmetric partners), radiative corrections can destabilize the Higgs potential and lead to rapid vacuum decay[281,52,92]. As a result such particles are often discussed in the context of supersymmetry[282], and are interesting for explaining the 125 GeV Higgs mass[75]. In the presence of CP violation, these models also provide an appealing fermionic scenario for electroweak baryogenesis[186,117].

5.5 The EDM constraint on natural SUSY

In this section, we explore implications of the EDM constraint from the ACME II experiment on the framework of natural SUSY where the only particles that play a key role in naturalness of the electroweak breaking are relatively light. That is, only higgsinos, stops, the left-handed sbottom and gauginos are light and the other superpartners such as the first and second generations of squarks and

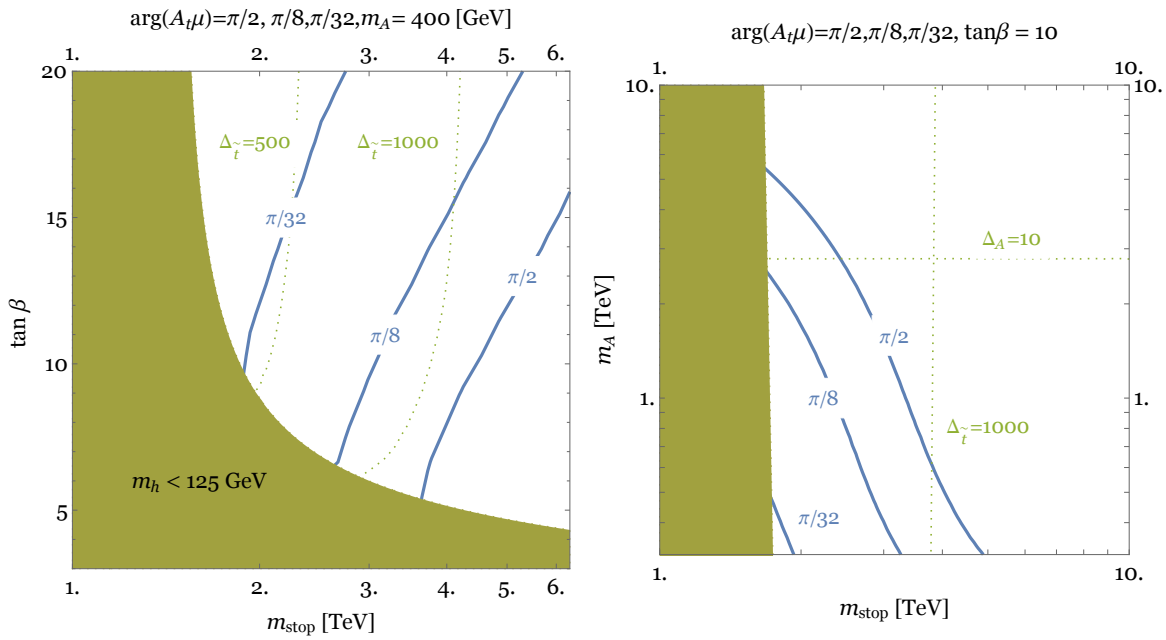

Figure 5.7: The implication of the EDM bound in the ACME II experiment on the stop parameter space in the MSSM where the 125 GeV Higgs mass is realized by stop loops with a large A-term. The horizontal axis is the common stop mass $m_{\rm stop} = m_{\widetilde{Q}_3} = m_{\widetilde{u}_3}$. The vertical axes show $\tan\beta$ and m_A in the left and right panels respectively. We fix $m_A = 400$ GeV in the left panel and $\tan\beta = 10$ in the right panel. The phase is taken to be $\arg(A_t\mu) = \pi/2, \pi/8, \pi/32$. The parameter $|\mu|$ is 350 GeV. The green region is excluded by the small Higgs mass with any values of the A-term. The blue curves denote the ACME II constraint. The green dotted curve describes the degree of fine-tuning defined in (5.5.1).

sleptons can be very heavy. While the squarks and sleptons contribute to sizable FCNCs and 1-loop EDMs, these contributions are suppressed in natural SUSY. In this framework, the two-loop Barr-Zee-type diagram, with an inner stop loop connected to the electron with a photon and a pseudoscalar Higgs, gives the dominant contribution to the electron EDM. This scenario gives a minimum size of the EDM in TeV-scale SUSY with CP-violation whether or not 1-loop contributions from the squarks or sleptons exist or not.

The MSSM predicts a small Higgs mass because the tree-level Higgs quartic coupling is related to the electroweak gauge couplings. Then, a sizable radiative correction is needed to explain the 125 GeV

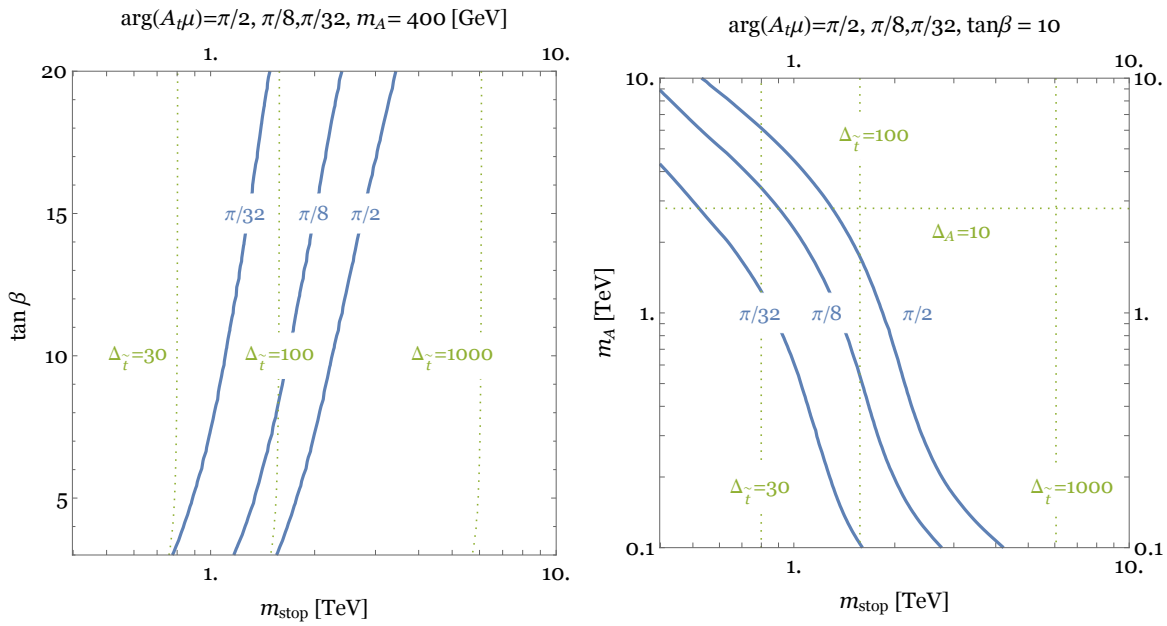

Figure 5.8: The implication of the EDM bound in the ACME II experiment on the stop parameter space assuming some other interactions to explain the correct Higgs mass. The A-term is still radiatively generated from the gluino mass. The parameters are taken to be the same values as those of figure 5.7. The blue curves denote the ACME II constraint with phases $\arg(A_t\mu) = \pi/2, \pi/8, \pi/32$.

Higgs mass. In general, stop masses must be around 10 TeV, which leads to a serious fine-tuning. However, if we consider a near-maximal stop mixing, the correct Higgs mass can be realized with light stops by a large A-term. The two-loop EDM induced by stops is proportional to the A-term and we obtain a detectably large EDM with a nonzero phase of the A-term, $\arg(A_t\mu)$. Another direction to realize light stops and reduce the tuning is to extend the Higgs sector of the MSSM and provide a new interaction to lift up the Higgs mass. In this case, we do not need a large A-term (and heavy stops), but the A-term is still radiatively generated from the gluino mass, which can lead to a nonzero EDM.

Let us now investigate implications on the natural SUSY parameter space from the ACME II experiment. We consider two scenarios to raise the Higgs mass described above. Figure 5.7 shows the

stop parameter space in the MSSM where the 125 GeV Higgs mass is realized by stop loops with a large A-term. We use the SusyHD code[346] for the Higgs mass calculation. We assume the same left and right-handed stop masses $m_{\text{stop}} = m_{\tilde{Q}_3} = m_{\tilde{u}_3}$ for simplicity. The parameter $|\mu|$ is taken to be 350 GeV. The green region is excluded by the small Higgs mass with any values of the A-term. The blue curves denote the ACME II constraint. We estimate the degree of tuning by using the following measures (for a more detailed discussion, see[294,336]),

$$\Delta_A \equiv \frac{2m_A^2}{m_h^2 \tan^2\beta}, \qquad \Delta_{\tilde{t}} \equiv \left| \frac{2\delta m_{H_u}^2}{m_h^2} \right|, \tag{5.5.1}$$

where m_A is the pseudoscalar Higgs mass and $\delta m_{H_u}^2$ denotes the stop radiative correction to the up-type Higgs soft mass squared. The degree of fine-tuning from the stop radiative correction is worse than one percent in this scenario.

Figure 5.8 shows the EDM constraint on the stop parameter space assuming some other interactions to explain the correct Higgs mass. As described above, the A-term is still radiatively generated from the gluino mass. The parameters are taken to be the same values as those of figure 5.7. The blue curves denote the ACME II constraint. In the viable parameter region, at least one percent tuning is needed.

5.6 QULE-induced EDMs

5.6.1 The RGE of the electron EDM

The electron EDM could be induced from various other dimension-six operators in the Standard Model through renormalization group equations. The relevant RGE has been given in [34] (which together with [278,279] constructs the RGEs for all of the SM dimension-six operators [249]). In a standard chosen basis of dimension six operators, the subset which are of interest for the measurement of CP violation through leptons is:

$$\begin{aligned}\mathcal{L}_{\dim 6} \supset\ & C_{h\widetilde{W}B} h^\dagger \sigma^i h \widetilde{W}^i_{\mu\nu} B^{\mu\nu} + C_{h\widetilde{W}} h^\dagger h \widetilde{W}^i_{\mu\nu} W^{i\mu\nu} + C_{h\widetilde{B}} h^\dagger h \widetilde{B}_{\mu\nu} B^{\mu\nu} \\ & + \left[C_{eW} (\bar{\ell} \sigma^{\mu\nu} e) \sigma^i h W^i_{\mu\nu} + C_{eB} (\bar{\ell} \sigma^{\mu\nu} e) h B_{\mu\nu} + \text{h.c.} \right] \\ & + \left[C_{ledq;f} (\bar{\ell} e) \cdot (\bar{d}_f q_f) + C^{(1)}_{lequ;f} (\bar{\ell} e) \cdot (\bar{q}_f u_f) + C^{(3)}_{lequ;f} (\bar{\ell} \sigma_{\mu\nu} e) \cdot (\bar{q}_f \sigma^{\mu\nu} u_f) + \text{h.c.} \right] . \end{aligned} \tag{5.6.1}$$

We see several four-fermion operators in the last line. Only one of them, the operator $(q_f \bar{\sigma}^{\mu\nu} \bar{u}_f) \cdot (\ell \bar{\sigma}_{\mu\nu} \bar{e})$, which we will refer to as the "QULE operator," feeds into the electron EDM through the 1-loop RGE. On the other hand, the first two types of operators, whose coefficients are $C_{ledq;f}$ and $C^{(1)}_{lequ;f}$, contribute to the CP-odd electron-nucleon coupling C_S that we discussed in §5.2.2. We can easily extract the coefficients C_{qe} in (5.2.5) from these operators.

The RGE in [34] is given for a quantity $\widetilde{C}_{e\gamma}$ which is, in our conventions, $-\sqrt{2} d_e/(ev)$. The one-loop RGE shows that the EDM can be generated from:

- The electron EDM $\widetilde{C}_{e\gamma}$ or the related $\widetilde{C}_{eZ}$ which replaces the photon coupling with a coupling

to the Z-boson. When these contributions appear, we just have a one-loop renormalization of a pre-existing EDM.

- The Wilson coefficients $C_{h\widetilde{W}B}$, $C_{h\widetilde{W}}$, and $C_{h\widetilde{B}}$. If these arise at one loop, then the two-loop EDM they generate is of the well-studied Barr-Zee type.
- The Wilson coefficient Im $C^{(3)}_{lequ;f}$, i.e. the "QULE operator."

It is the last of these contributions, which has received relatively little attention in the literature, that we turn our attention to now. The EDM arises diagramatically by closing up the quark loop with a Higgs insertion and attaching a photon line. (We make the simplifying assumption that quarks appear in a flavor-diagonal manner.) The leading-log estimate of the EDM induced by the quark flavor f is given by

$$d_e = -e\frac{m_f}{\pi^2}\log\frac{M}{m_f}\,\mathrm{Im}\,C^{(3)}_{lequ;f}, \tag{5.6.2}$$

with m_f the mass of the quark flavor appearing in the loop and M the scale at which the QULE operator is generated.

Some models of new physics will generate four-fermion operators that are not expressed in the chosen basis, so we must make use of identities to reduce to this basis to determine if the QULE Wilson coefficient Im $C^{(3)}_{lequ;f}$ is nonzero. By Fierz rearrangement, we see that the four-fermi operators $(\bar{\ell}u)\cdot(\bar{q}e)$ and $(\bar{\ell}\cdot\bar{q})(ue)$ generate an EDM although the operator $(\bar{\ell}e)\cdot(\bar{q}u)$ does not (though it does contribute to the CP-odd electron-nucleon term C_S discussed in §5.2.2). Specifically, we have

$$\begin{aligned}(q\bar{e})\cdot(\ell\bar{u}) &= -\frac{1}{2}\left[(q\bar{\sigma}^{\mu\nu}\bar{u})\cdot(\ell\bar{\sigma}_{\mu\nu}\bar{e}) + (q\bar{u})\cdot(\ell\bar{e})\right],\\ (q\cdot\ell)(\bar{u}\bar{e}) &= +\frac{1}{2}\left[(q\bar{\sigma}^{\mu\nu}\bar{u})\cdot(\ell\bar{\sigma}_{\mu\nu}\bar{e}) - (q\bar{u})\cdot(\ell\bar{e})\right].\end{aligned} \tag{5.6.3}$$

Thus, models that generate $(q\bar{e}) \cdot (\ell\bar{u})$ or $(q \cdot \ell)(\bar{u}\bar{e})$ will, when rewritten in the operator basis of [34], have a QULE contribution. In this section we will survey models of QULE-induced EDMs. The first case is a one-loop EDM arising from a tree-level QULE operator. The second case is a two-loop EDM arising when a QULE operator is generated through a one-loop box diagram.

The two 4-fermi operators in (5.6.3) generate both $C^{(3)}_{lequ;f}$ (and hence, at one higher loop order, an EDM) as well as $C^{(1)}_{lequ;f}$, which contributes to C_S as discussed in §5.2.2. Since ACME constrains the linear combination d_{ThO} in (5.2.4), we can ask whether the constraint on these operators is dominantly from d_e or from C_S. The ratio of the two contributions is

$$\left|\frac{d_{\mathrm{ThO;EDM}}}{d_{\mathrm{ThO};C_S}}\right| \approx \frac{m_q \log(M/m_q)}{\pi^2 \times 1.6 \times 10^{-15}\ \mathrm{GeV}^2\ \mathrm{cm}\ \langle N|\bar{q}q|N\rangle} \approx \begin{cases} 6 \times 10^{-3}, & q = u, \\ 2 \times 10^{2}, & q = c, \\ 2 \times 10^{6}, & q = t. \end{cases} \tag{5.6.4}$$

In the numerical estimate we have plugged in $M = 10$ TeV for the mass scale running in the loop, though the result depends only logarithmically on this choice. The upshot is that if new physics couples dominantly to a heavier up-type quark, the constraint is primarily on the electron EDM, while if new physics couples dominantly to the up quark, the constraint is primarily on the CP-odd electron-nucleon interaction C_S. This is consistent with results in [224]. Of course, new physics might couple to all of the quarks, in which case the flavor structure of the interaction will determine which quark gives

the largest contribution.

5.6.2 One loop EDM from tree level QULE

A nonzero Wilson coefficient $C^{(3)}_{lequ;f}$ (after reducing to the appropriate basis) can be generated at tree level by integrating out a scalar with leptoquark-type couplings. In such a model, there is a one-loop electron EDM [58,179,224,165]. There are two possible charge assignments for the scalar that will generate a QULE operator that induces an EDM:

$$\varphi \in (3,1)_{-1/3}, \quad \mathcal{L} \supset \left(y_{1f}\varphi^\dagger q_f \cdot \ell + y_{2f}\varphi \bar{u}_f \bar{e} + \text{h.c.}\right) - m_\varphi^2 \varphi^\dagger \varphi, \tag{5.6.5}$$

$$\text{generates :} \quad C^{(3)*}_{lequ;f} = -C^{(1)*}_{lequ;f} = \frac{y_{1f}y_{2f}}{2m_\varphi^2}, \tag{5.6.6}$$

$$\varphi \in (3,2)_{+7/6}, \quad \mathcal{L} \supset \left(y_{1f}\varphi^\dagger q_f \bar{e} + y_{2f}\varphi \cdot \ell \bar{u}_f + \text{h.c.}\right) - m_\varphi^2 \varphi^\dagger \varphi, \tag{5.6.7}$$

$$\text{generates :} \quad C^{(3)*}_{lequ;f} = C^{(1)*}_{lequ;f} = -\frac{y_{1f}y_{2f}}{2m_\varphi^2}. \tag{5.6.8}$$

The case $(3,1)_{-1/3}$ (the quantum numbers of a down-type squark) allows for diquark-like couplings $\varphi q_f \cdot q_g$ and $\varphi^\dagger \bar{u}_f \bar{d}_g$, which together with the couplings above violate baryon number and can lead to proton decay. Hence, this case requires some mechanism (or an extreme accident) to suppress these dangerous couplings. However, the case of $(3,2)_{+7/6}$ does not share this problem. Both models generate a contribution to C_S and to d_e (our result appears to differ from [224], which claims that only the case $(3,2)_{+7/6}$ generates both operators). In the case where the scalar φ couples to the top quark, the constraint that loop corrections do not generate a large correction to the electron Yukawa coupling is $|y_{1t}y_{2t}| \lesssim \mathcal{O}(10^{-6})$. A variety of assumptions about the flavor structure of the model are possible:

in some models φ may couple most strongly to the third generation, while in others it may couple to all generations of quarks. In any case, the electron mass naturalness constraint prevents the couplings from being too large. In the case where the scalar φ couples to the up quark, the CP-odd electron-nucleon coupling C_S leads to the strongest constraint on the model. The scalar particle in this model must be very heavy and far out of reach for collider searches unless it has small couplings.

5.6.3 Two loop EDM from one loop QULE

We could also consider theories in which a QULE-type operator is generated, not at tree level, but at one loop. In this case the corresponding EDM will arise from a 2-loop diagram, as depicted in Figure 5.9. These diagrams are topologically distinct from Barr-Zee diagrams in that they do not contain a closed internal fermion loop; rather, a single fermion line runs continuously through the diagram. (The diagrams are also different from previously discussed rainbow diagrams which have Standard Model fermions on some internal lines[395].) As shown in the figure, such diagrams can arise if we introduce new vectorlike fermions $\psi_{1,2}, \bar{\psi}_{1,2}$ and complex scalars φ_1, φ_2 with appropriate Yukawa couplings. A variety of choices of quantum numbers for the particles are possible. For simplicity, we make the simplifying assumption that a single $SU(3)$ color index and $SU(2)$ weak isospin index run continuously through the diagram, e.g. in Figure 5.9 we might take φ_1 to be a color singlet and $\psi_1, \varphi_2, \bar{\psi}_2$ to be color triplets. With such an assumption, it is a straightforward (but lengthy) task to enumerate all of the possibilities. We provide these results in Appendix D.1.

In some cases, models with these contributions also allow couplings that generate contributions of more well-studied types. For example, from Figure 5.9 we see that the quantum numbers allow for a

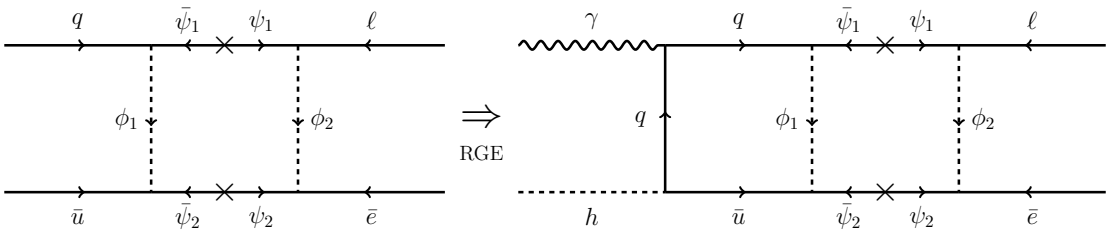

Figure 5.9: Feynman diagrams for an EDM arising at two loops from a one-loop QULE operator. Similar diagrams exist that generate the operator $(q\bar{e}) \cdot (\bar{u}\ell)$ instead of $(q \cdot \ell)(\bar{u}\bar{e})$.

vertex connecting ψ_1 and ψ_2 to a Higgs boson, which would allow a 1-loop electron EDM. If this coupling to the Higgs is present, then the 1-loop EDM could dominate over the QULE contribution we study. We could *assume* the Higgs coupling to be small, so that the QULE contribution is dominant, but this assumption is not obviously well-motivated. On the other hand, if we exchanged the position of $\bar{u}$ and $\bar{e}$ in the lower line of Figure 5.9, then in general the quantum numbers of the new particles would not allow any direct couplings to the Higgs boson. In that case both 1-loop EDMs and 2-loop Barr-Zee EDMs would be absent, and the QULE contribution would be dominant.

Rather than directly computing a 2-loop diagram as in the right panel of Figure 5.9, we consider the leading-log approximation given by feeding the box diagram in the left panel into the RGE estimate (5.6.2). The coefficient of the four-fermion operator generated by this box diagram is given by

$$C_{\mathrm{g}} \cdot y_1 y_2 y_3 y_4 \int \frac{d^4p}{(2\pi)^4} \frac{1}{p^2 - m_{\varphi_1}^2} \frac{m_{\psi_1}}{p^2 - m_{\psi_1}^2} \frac{1}{p^2 - m_{\varphi_2}^2} \frac{m_{\psi_2}}{p^2 - m_{\psi_2}^2}, \tag{5.6.9}$$

with C_{g} a group-theory factor depending on the $SU(3)_C$ and $SU(2)_L$ representations of the particles running in the loop. With our simplifying assumption about representations above, the group theory

factor is 1. Evaluating the loop integral, we obtain

$$\frac{C_g y_1 y_2 y_3 y_4 m_{\psi_1} m_{\psi_2}}{16\pi^2 (m_{\psi_1}^2 - m_{\psi_2}^2)(m_{\psi_1}^2 - m_{\varphi_2}^2)(m_{\psi_2}^2 - m_{\varphi_2}^2)(m_{\psi_1}^2 - m_{\varphi_1}^2)(m_{\psi_2}^2 - m_{\varphi_1}^2)(m_{\varphi_1}^2 - m_{\varphi_2}^2)} \times$$
$$\left\{ m_{\varphi_1}^2 m_{\psi_1}^2 (m_{\psi_2}^4 - m_{\varphi_2}^4) \log \frac{m_{\varphi_1}^2}{m_{\psi_1}^2} + m_{\varphi_1}^2 m_{\varphi_2}^2 (m_{\psi_1}^4 - m_{\psi_2}^4) \log \frac{m_{\varphi_1}^2}{m_{\varphi_2}^2} + m_{\varphi_1}^2 m_{\psi_2}^2 (m_{\varphi_2}^4 - m_{\psi_1}^4) \log \frac{m_{\varphi_1}^2}{m_{\psi_2}^2} \right.$$
$$\left. + m_{\psi_1}^2 m_{\psi_2}^2 (m_{\varphi_2}^4 - m_{\varphi_1}^4) \log \frac{m_{\psi_2}^2}{m_{\psi_1}^2} + m_{\varphi_2}^2 m_{\psi_1}^2 (m_{\psi_2}^4 - m_{\varphi_1}^4) \log \frac{m_{\psi_1}^2}{m_{\varphi_2}^2} + m_{\varphi_2}^2 m_{\psi_2}^2 (m_{\varphi_1}^4 - m_{\psi_1}^4) \log \frac{m_{\psi_2}^2}{m_{\varphi_2}^2} \right\}. \tag{5.6.10}$$

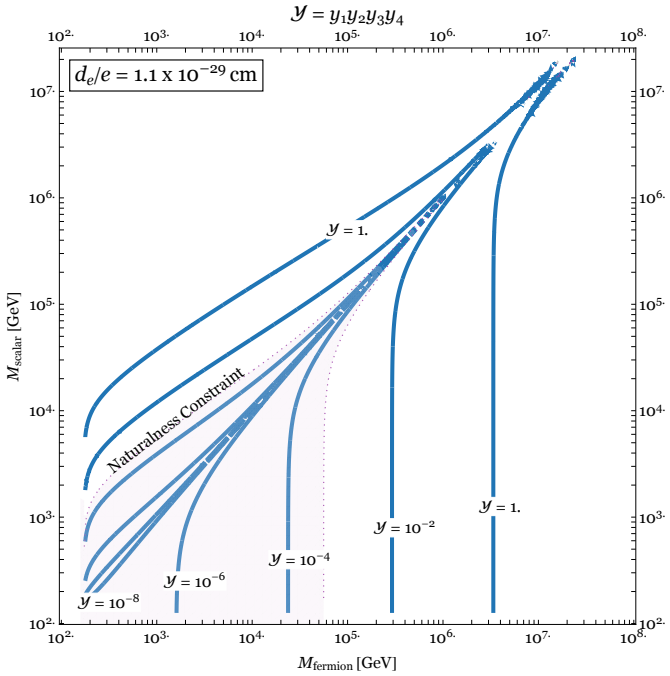

Figure 5.10: The constraint of the electron EDM arising at two loops from a one-loop QULE operator. Contours show the largest allowed imaginary part of the product of Yukawa couplings appearing in the box diagram, as a function of the masses of the fermions and scalars in the loop. The shaded region shows the case where the constrained value of $\mathcal{Y}$ is small enough that it does not generate an unnaturally large correction to the electron Yukawa coupling. We see that new physics as heavy as a few hundred TeV can be constrained, consistent with the estimate in the radiative scenario in §5.2.

While we reserve the detailed discussion of possible quantum numbers for the appendix D.1, let us

highlight some example scenarios here.

- **SUSY:** in Figure 5.9, we could take $\varphi_1 = \widetilde{u}$; $\bar{\psi}_1 = \widetilde{H}_u$; $\psi_1 = \widetilde{H}_d$; $\varphi_2 = \widetilde{e}$; and $\bar{\psi}_2 = \psi_2 = \widetilde{B}^0$. Then the diagram gives rise to a 2-loop SUSY EDM, distinct from the Barr-Zee type diagram, and scaling approximately as $\sim g_1^2 y_e y_t^2 \mu M_1 / \left[(16\pi^2)^2 m_{\tilde{t}}^2 m_{\tilde{e}}^2\right] \log(m_\varphi / m_t)$. Such a contribution is generally expected to be smaller than the one-loop diagrams considered in §5.3.

- **New physics parities:** some possibilities resemble SUSY in having an analogue of R-parity, with all of the new physics particles in the loop charged under a parity symmetry so that they can cascade decay to a neutral parity-odd particle (which could serve as a dark matter candidate). For example, consider this scenario (the $Y = \frac{1}{6}$ row of table D.1.1.1)

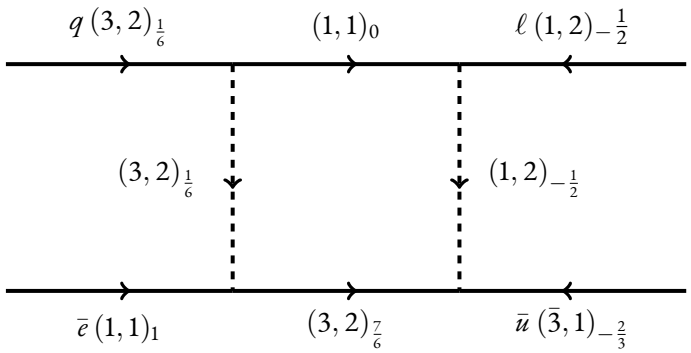

(5.6.11)

  This case includes an exotic vectorlike doublet quark X of hypercharge $7/6$, corresponding to electric charges $5/3$ and $2/3$. This particle can decay as, for example, $X_{+5/3} \to te^+\psi^0$ with ψ^0 a neutral stable fermion. Thus we see that the collider signals for some scenarios resemble SUSY in having missing momentum, but resemble leptoquarks in having decay chains with both quarks and leptons. The final state for X pair production is $t\bar{t}e^+e^- + p_T^{\text{miss}}$. Because two different decay chains with the same final state are open (moving clockwise or counterclockwise from the $(3,2)_{7/6}$ particle to the $(1,1)_0$ particle in the diagram), reconstructing masses of the intermediate scalars could be an interesting challenge.

  Notice that this is an example in which the two-loop QULE contribution is the leading possible EDM, because no couplings permitting a one-loop EDM or Barr-Zee diagram exist.

- **Leptoquarks:** In some cases, the quantum numbers permit one of the particles running in the loop to decay to one Standard Model quark and one lepton. For example, consider the $Y = 0$

row of D.1.4.1:

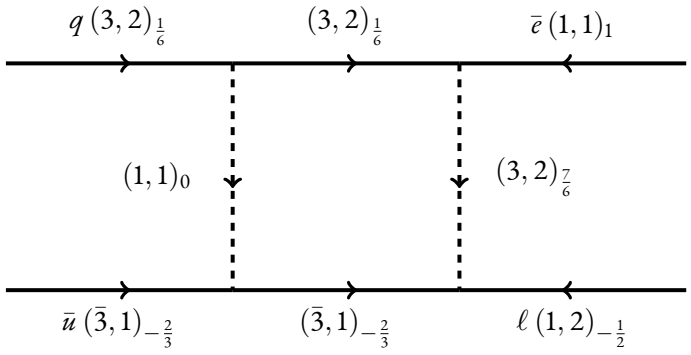

(5.6.12)

In this case, the scalar φ_2 with quantum numbers $(3,2)_{7/6}$ can decay to one quark and one lepton if appropriate Yukawa couplings exist to $q\bar{e}$ or to $(\ell\bar{u})^\dagger$. The other particles could cascade down to it, for instance,

$$\varphi_1 \to u\psi_2, \quad \psi_2 \to \bar{\ell}\varphi_2^*, \quad \varphi_2^* \to \ell\bar{u}, \tag{5.6.13}$$

so that the final states could involve several quarks and leptons. An alternative phenomenological scenario for this choice of quantum numbers is that ψ_1 or ψ_2, a vectorlike quark, is the lightest of the new particles; these could then decay through a Yukawa coupling with a SM quark and the Higgs boson.

This is an example of a case where couplings leading to a 1-loop EDM are allowed to exist, and so the 2-loop contribution considered here may be subdominant.

Scalar leptoquarks are of phenomenological interest for many reasons. For example, a leptoquark with the quantum numbers of a right-handed down squark has been suggested as an explanation for the $B \to D^{(*)}\tau\bar{\nu}$ anomaly[223] and could even fit other flavor anomalies through loop effects[77].

In Figure 5.10 we plot the experimental constraints on these models. The product of Yukawa couplings $\mathcal{Y} \equiv y_1y_2y_3y_3$ in the one-loop QULE are constrained such that it does not generate an unnaturally large correction to the electron Yukawa coupling. The maximum value of $\mathcal{Y}$ allowed by naturalness is weakly dependent on the masses of the scalars and fermions in the loop, and coincides

roughly with $\mathcal{Y} \sim 10^{-4}$. Contours of fixed $\mathcal{Y} \lesssim 10^{-4}$ lay neatly in the shaded region and are allowed. We see that new physics up to several hundred TeV are consistent with this constraint.

5.7 Conclusions

We have studied implications of the new ACME constraint on a variety of theories of new physics with CP violation. The general argument based on effective field theory has revealed the range of mass scales probed by the EDM constraint. In scenarios with two-loop EDMs where the electron Yukawa coupling appears explicitly in the new physics couplings, including many SUSY scenarios, the new ACME constraint probes masses of a few TeV. Other scenarios, where loop effects generate both the EDM and the electron Yukawa coupling, potentially probe scales of hundreds of TeV. We have also discussed the case where the dominant effect on ThO comes from the CP-odd electron-nucleon coupling. Then, we have interpreted the bound in the context of different scenarios for SUSY. For 1-loop SUSY, the constraint probes sleptons above 10 TeV. Assuming the universal mass for squarks and sleptons, the mass bound start to hit the excluded region giving a too-large Higgs mass. For 2-loop SUSY, multi-TeV charginos in split SUSY or stops in natural SUSY are constrained from the new EDM result, which is consistent with the general argument.

Although there has been extensive study of scenarios where an electron EDM is induced at two loops by new electroweak physics coupling to the Higgs boson, an equally viable possibility is that the electron EDM arises at two loops from physics that is decoupled from the Higgs boson. Such physics, instead, would couple to the charm or (perhaps more plausibly) the top quark. This possibility is real-

ized through the QULE operator which generates the EDM through RG evolution. We have classified scenarios in which the QULE operator is generated at one loop through a box diagram, which include SUSY and leptoquark models. The electron EDM bound gives the leading constraint in most viable models. If a nonzero electron EDM is measured in the future, it will be of paramount importance for colliders to search for the particles responsible for the effect. We have seen that a variety of models with distinctive phenomenology could be the source of the EDM through the QULE operator. In particular, searches for scalar leptoquarks or heavy vectorlike fermions that decay to Standard Model fermions could play a role in pinning down the origin of the EDM if it is measured to be nonzero.

The rest of this section is devoted to a brief discussion on the implications of future improvements in EDM searches. We will discuss first the possibility that null results persist, and then the possibility that a nonzero EDM is measured. We argue that both cases indicate a variety of interesting directions in the exploration of physics beyond the Standard Model with CP violation.

5.7.1 Null results and new physics: spontaneously broken CP?

If EDM experiments continue producing null results even as they attain orders of magnitude more sensitivity than ACME (proposals include e.g. [301,390,316]), theorists must decide whether to doubt that *any* new physics near the TeV scale interacts with the Standard Model. Our naive expectation is that anywhere a CP phase is allowed, it should be order one. The CKM phase is order one; the QCD theta angle is not, but we know a simple dynamical mechanism for relaxing it to zero (the axion), unlike generic phases. Furthermore, there are tentative indications from neutrino experiments (so far at low statistical significance) that the CP violating phase in the PMNS matrix is large as well (see e.g. [198]).

Is our intuition that new physics should come with order-one CP violating phases robust, or could there be fundamental reasons (apart from fine tuning) why the CP phases associated with new physics could all be small? One possible explanation for small phases lies in spontaneously broken CP. It is likely that, at a fundamental level, CP is a gauge symmetry; in this case, the CP violation that we see in nature is a result of spontaneous breaking by the VEVs of various scalar fields [174,135]. If the fields spontaneously violating CP also violate other symmetries, then their contributions may generically be suppressed by small symmetry-breaking order parameters [339]. For instance, if only flavon VEVs have CP-violating phases, they can effectively contribute a large phase in the CKM matrix when added to other VEVs violating the same flavor symmetries, but they will have subleading contributions to parameters that do not violate flavor. Since [339] focused on the quark sector, it could be interesting to revisit such models given that the neutrino Jarlskog invariant appears to be ~ 0.03, much larger than 3×10^{-5} in the quark sector [198].

More generally, UV complete theories could have additional structure suppressing some CP violating effects. It has been observed that "mirror mediation" of SUSY breaking, with flavor structure arising from complex structure moduli and SUSY breaking from Kähler moduli (or vice versa), suppresses CP phases in soft SUSY breaking terms [150]. The structure appears somewhat ad hoc in low energy effective field theory, but arises from a higher dimensional theory with extended SUSY. Relatively little exploration has been carried out of the sizes of small CP-violating phases arising from corrections to this picture. (For a different moduli mediation scenario, see [191], which predicts an electron EDM of about $5 \times 10^{-30}\, e$ cm—not far below the current bound!)

Detailed model building of the origin of the CKM matrix and complex phases in supersymmetric

theories, and their correlation with the predicted size of EDMs, has somewhat fallen out of fashion. We believe that the current rapid improvement in experimental results makes it very timely to revisit these questions: the answer could have major implications for the plausibility of scenarios like mini-split SUSY in light of data.

5.7.2 An EDM would reify the hierarchy problem

If a nonzero electron EDM is detected in the foreseeable future, it will necessarily indicate physics beyond the Standard Model. As we have seen, this physics could arise over a wide range of mass scales. In some models, the particles generating the EDM would likely lie within reach, if not of the LHC, at least of a conceivable future collider. In other cases, they would not. For instance, in §5.3 we have seen that EDMs arising at one loop in a SUSY theory could come from sleptons with masses approaching 10 TeV, well out of reach of any proposed collider. Scenarios where the electron Yukawa coupling is generated radiatively could come from even higher energy physics, as discussed in §5.2. While an EDM discovery would be a solid indicator that there is physics beyond the Standard Model at energies far below the GUT scale, it would not immediately give rise to a "no-lose" theorem for technologically feasible colliders.

Despite the lack of a clean no-lose theorem, an electron EDM would clearly motivate renewed enthusiasm for searching for heavy particles. In particular, new CP phases need not be order one, and as we have just discussed, in some models there could be compelling reasons for phases to be small and for the associated EDM-generating particles to be lighter. However, there is another argument for searching for new physics at colliders if EDMs are generated by heavy particles: the Higgs mass

fine-tuning problem, which would assume a new and very concrete form.

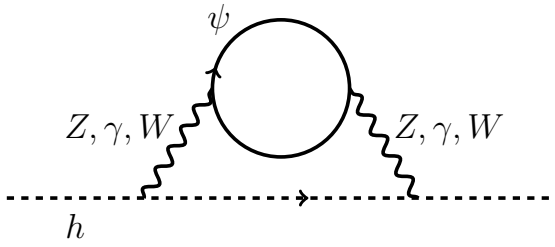

Figure 5.11: Two-loop correction to the Higgs boson mass-squared parameter proportional to the mass squared of any heavy field ψ (here depicted as a fermion for concreteness) with electroweak quantum numbers. Such contributions produce a very concrete, calculable variation on the Higgs fine-tuning problem if the particles generating an EDM are much heavier than the TeV scale.

Discussions of fine-tuning of the Higgs mass are often phrased in terms of quadratic divergences: if we cut off loops of Standard Model particles at a scale Λ, we obtain corrections to the Higgs mass squared parameter proportional to Λ^2. However, as is often pointed out by skeptics, UV cutoffs are theorists' conventions; what we really should mean by a hierarchy problem is sensitivity to *physical* mass scales, such as masses of heavy particles beyond the Standard Model. To be confident that the hierarchy problem is a problem, we must know that there *is* new physics at energies above the weak scale. While there is a compelling argument to be made that the existence of gravity necessitates such physics, one can (and many do) question this logic. However, if we have actual evidence of new physics at high energies from the measurement of a small coefficient for a higher dimension operator like an EDM, it becomes much harder to dismiss the hierarchy problem.

If heavy particles with electroweak quantum numbers exist, the hierarchy problem can assume a concrete, calculable form in which the Higgs boson mass parameter receives corrections proportional to the physical masses of those new particles. Such dependence always arises from two-loop diagrams

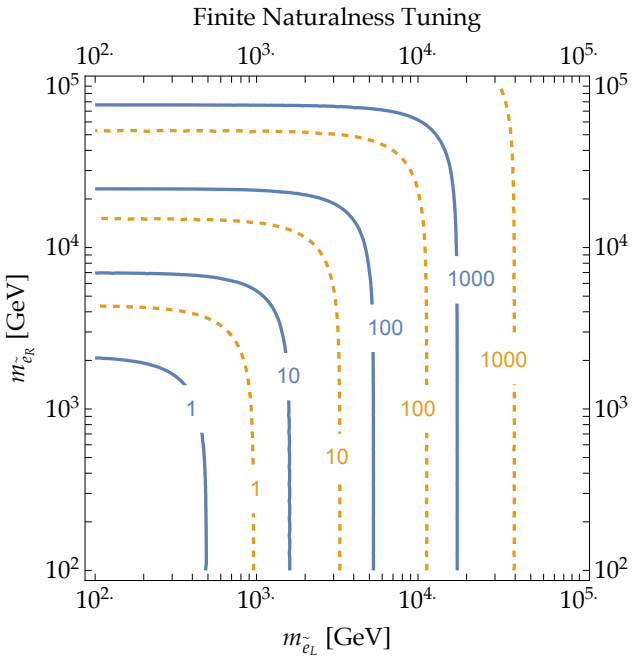

Figure 5.12: "Finite naturalness" tuning measure for a model consisting of a bino and left- and right-handed selectrons. Contours correspond to $\Delta = |\delta m^2_{\rm loop}/m^2_{\rm higgs}|$ for two different choices of UV cutoff, $\Lambda = 2 \times 10^{16}$ GeV (blue) and 10^{10} GeV (orange), with log divergences included but no power divergences.

as shown in Figure 5.11. The size of this loop correction relative to the measured Higgs boson mass, $\Delta \equiv |\delta m^2_{\rm loop}/m^2_{\rm higgs}|$, is a very conservative measure of fine tuning (see e.g. [386,207,163] for related discussions). The two-loop Higgs mass squared corrections proportional to the mass squared of new fermions or scalars transforming in any representation of the electroweak gauge group have been given in [207]. (These have logarithmic sensitivity to the UV cutoff, but no power law sensitivity.) Using these expressions, we have plotted the corresponding "finite naturalness" tuning contours in Figure 5.12 for a model with an EDM generated by particles with the quantum numbers of a bino, left-handed selectron, and right-handed selectron. We see that as the masses approach the 10 TeV scale, the theory is tuned at worse than a percent level. We emphasize that we are *not* assuming that the underlying theory

is SUSY or that any new particles exist except for the ones that produce the EDM. Already, this minimal model for EDM generation would imply a sharp form of the hierarchy problem, which would be much more difficult for skeptics to dismiss than the usual formulation of the problem. Nonetheless, this problem could only be solved by invoking the same types of physics that solve the usual hierarchy problem, such as supersymmetry or compositeness of the Higgs boson. These in turn imply new particles (such as top partners) whose masses the Higgs is sensitive to, and all of the usual arguments for expecting such particles near the TeV scale would go through—but resting on a firmer foundation.

In summary, we believe that any future nonzero electron EDM measurement would have profound and exciting implications for particle physics. It would immediately provide a much stronger case for pursuing new high energy colliders, and would guarantee that we have more to learn about the fundamental laws of nature. In the meantime, null results of EDM experiments like the recent ACME result provide stringent constraints on theories of new physics and motivate further work to assess what principles could lead to small CP-violating phases if new TeV-scale physics exists. We eagerly await further results from precision measurements.

6

Oblique Lessons from the *W* Mass Measurement at CDF II

6.1 Introduction

The Standard Model of particle physics (SM) has been remarkably successful in explaining various experimental results. The discovery of the Higgs boson [4,127] at the Large Hadron Collider (LHC) was

imperative to confirming the pattern of spontaneous symmetry breaking in the electroweak sector of the SM. However, as we continue to collect data and improve analysis techniques, we have seen a proliferation of precision measurements that deviate from SM predictions, such as the muon magnetic moment [33,21,82] and the R_K/R_K^* anomalies [5,6,8]. The most recent anomalous measurement reported is the mass of the W boson M_W [9]. A discrepant measurement of M_W could be an indication of supersymmetry (SUSY), composite Higgs, or other phenomena beyond the Standard Model (BSM) at potentially very high energy scales. It is therefore essential that we explore the phenomenological implications of this new M_W measurement.

Measuring the W mass with high precision requires a global fit of the SM, known as the electroweak fit. This method involves fitting over a set of well-measured SM observables, and minimizing the χ^2 value over both the fitted ('free') observables as well as derived observables, see Refs. [216,65,64]. The electroweak fit leverages the small uncertainties of the fitted observables to produce precise predictions of the derived observables. Additionally, since this fit is an exceptional probe of precision measurements, it is also highly sensitive to BSM effects.

We can parameterize the effects of new physics phenomena on the electroweak sector using oblique parameters S, T, and U [349,348] (see also Refs. [296,265,235]). These parameters capture the effects of higher-dimension operators [254,253] that can arise in a variety of UV completions. In most models, S and T are the dominant corrections since they arise from dimension 6 operators, whereas U is dimension 8 and therefore suppressed by a factor of $v^2/\Lambda_{\text{UV}}^2$.

The power of the electroweak fit is dependent on precision of experimental measurements of SM observables, and improves along with collider technology and luminosity. The leading measurements

are made at the Large Electron-Positron Collider (LEP), Stanford Linear Collider (SLC), Tevatron, and LHC. The discovery of the Higgs greatly improved the electroweak fit as it provided the final measured value to span the free parameters of the SM [400,147,162].

The most recent update to the SM values used in the fit comes from the CDF collaboration at the Tevatron [9]. Their analysis was completed with a four-fold increase of data, reduced uncertainty in PDFs and track reconstruction, and updated measurements compared to their previous result [11]. They report

$$M_{W,\text{CDF II}} = 80.4335 \pm 0.0094\ \text{GeV}, \tag{6.1.1}$$

which, without averaging with other experimental results, shows a 7σ deviation from the SM prediction. This value is notably higher than the previous measurement averaged from the Tevatron and LEP experiments ($M_W = 80.385 \pm 0.015$ GeV) [10], as well as ATLAS ($M_W = 80.370 \pm 0.019$ MeV) [3] and LHCb[1] ($M_W = 80.354 \pm 0.032$ GeV) [7].

In this chapter we explore how new physics contributions, parameterized by the values of the oblique parameters, can adjust the electroweak fit such that M_W is consistent with the updated CDF measurement. We first perform our fits scanning over values of S and T with U fixed to zero (since U is suppressed) and identify the range of these variables that can resolve the observed anomaly in M_W. We then study how the fit changes if we allow U to float. Large values of U can easily accommodate the observed increase in M_W; however, it is difficult to construct models with the primary new physics contributions affecting only U while leaving S and T unchanged.

[1] This total error is calculated assuming all errors are uncorrelated and can be added in quadrature. The LHCb collaboration reports $M_W = 80.354 \pm 0.023_{\text{stat}} \pm 0.01_{\text{exp}} \pm 0.017_{\text{th}} \pm 0.009_{\text{PDF}}$.

Next we consider several well-motivated simple extensions of SM that can produce nonzero S and T values. The models discussed in this chapter include a generic dark photon with kinetic mixing, a two Higgs doublet model (2HDM), a neutral scalar $\mathrm{SU}(2)_L$ triplet (that can be referred to correctly as a *swino*), and various singlet-doublet fermion scenarios. For each model we check if there is available parameter space that corresponds to the fitted values of T and S. We find that a dark photon or a scalar singlet/doublet extension of SM can not explain the observed anomaly in M_W measurements, while singlet-doublet fermion extension are strongly constrained by various experimental bounds. A $\mathcal{O}(\mathrm{TeV})$ swino, on the other hand, can explain the observed anomaly while evading current bounds and provides a well-motivated target for future high energy colliders.

The remainder of the chapter is organized as follows. In Section 6.2, we define the parameters and methodology of our electroweak fit. Section 6.3 discusses the results and the implications of the oblique parameters on fitting the measured observables. In Section 6.4 we map the values of the fitted oblique parameters to the parameters of various models, and comment on the viability of this space. We conclude in Section 6.5.

6.2 Electroweak Fit

To assess the impact of the new measurements of M_W, and the implications for potential new physics, we perform an electroweak fit to a representative set of observables, following the strategy of the GFitter group [216,65,64,252][2] with a modified version of the code used in Refs. [203,204]. A set of five core ob-

[2] With respect to the GFitter results in [252], we consider an updated value of the Higgs mass and the revised values of Γ_Z and σ^0_{had} from [277].

servables are free to vary in the fit: the Z boson mass M_Z, the top mass M_t, the Higgs mass M_h, the Z-pole value of the strong coupling constant $\alpha_s(M_Z)$, and the hadronic contribution to the running of α, denoted $\Delta\alpha^{(5)}_{\text{had}}(M_Z^2)$.

These five predicted values and other observables derived from them are compared to their measured values (see Table 6.1). In addition to measurements of these five parameters, the observables considered include the W mass and a host of other electroweak precision measurements performed at SLC, LEP, the Tevatron, and the LHC, which are listed with their measured values below the horizontal line in Table 6.1. These other observables can be determined in the SM as functions of the five core observables, the Fermi constant G_F, and the fine structure constant $\alpha(q^2 = 0)$. In the electroweak fit, $G_F = 1.1663787 \times 10^{-5}\,\text{GeV}^{-2}$ and $\alpha = 1/137.03599084$ are treated as fixed values since they are determined with much higher precision than the rest of the observables[400].

For the W mass, we will consider several different values to assess the impact of the recent CDF measurement on the overall state of the global EW fit. These are,

$$\begin{aligned} M_W &= 80.4335 \pm 0.0094\,\text{GeV} \qquad \text{(CDF II)}, \\ M_W &= 80.4112 \pm 0.0076\,\text{GeV} \qquad \text{(LHC + LEP + Tevatron)}, \\ M_W &= 80.379 \pm 0.012\,\text{GeV} \qquad \text{(PDG 2020)}, \end{aligned} \tag{6.2.1}$$

where the uncertainties quoted above include the statistical, systematic and modeling uncertainties used in each experiment. The second scenario is our estimate for the global average of different M_W mea-

Observable	Measured Value
M_Z [GeV]	91.1876 ± 0.0021
M_h [GeV]	125.25 ± 0.17
M_t [GeV]	172.89 ± 0.59
$\alpha_s(M_Z^2)$	0.1181 ± 0.0011
$\Delta\alpha^{(5)}_{\rm had}(M_Z^2)$	0.02766 ± 0.00007
Γ_Z [GeV]	2.4955 ± 0.0023
Γ_W [GeV]	2.085 ± 0.042
$\sigma^0_{\rm had}$ [nb]	41.481 ± 0.033
R^0_ℓ	20.767 ± 0.025
$A^{0,\ell}_{\rm FB}$	0.0171 ± 0.0010
A_ℓ	0.1499 ± 0.0018
$\sin^2\theta^\ell_{\rm eff}(Q_{\rm FB})$	0.2324 ± 0.0012
$\sin^2\theta^\ell_{\rm eff}$(Tevt.)	0.23148 ± 0.00033
A_b	0.923 ± 0.020
A_c	0.670 ± 0.027
$A^{0,b}_{\rm FB}$	0.0992 ± 0.0016
$A^{0,c}_{\rm FB}$	0.0707 ± 0.0035
$R^{0,b}$	0.21629 ± 0.00066
$R^{0,c}$	0.1721 ± 0.0030

Table 6.1: Summary of the observables included in the fit, and their experimental values. The five observables above the horizontal line are allowed to float in the fit, while the SM values of the remaining observables are determined from these five values, as discussed in the main text. The values of M_Z, M_t, M_h, $\alpha_s(M_Z^2)$, $\Delta\alpha^{(5)}_{\rm had}(M_Z^2)$, and Γ_W are taken from the most recent PDG average [400]. For Γ_Z and $\sigma^0_{\rm had}$ we use the updated values computed in Ref. [277]. The remaining Z-pole observables are taken from the LEP and SLC measurements [367]. For A_ℓ we use the average of the LEP and SLC values, following [252].

surements, assuming zero correlations between experimental result to first approximation.[3] In addition, to assess the particular impact of the new, high precision measurement from CDF II, we will also perform the fit with M_W taken to be the CDF II value with the systematic uncertainty artificially inflated by a factor of 2, $M_W = 80.4335 \pm 0.0157$, to better understand the compatibility of the CDF measurement with the SM prediction. This scenario is referred to as the CDF II (2x Syst.) throughout the chapter.

The SM values of the other observables are determined from the free parameters using the full two-loop electroweak results available in the literature. The running of α is computed using the floating value of $\Delta\alpha^{(5)}_{\text{had}}$ as well as the leptonic piece, $\Delta\alpha_{\text{lep}} = 0.031497686$[382], which is kept fixed in the fit. The W mass is determined using the parameterization in[63], which also includes corrections up to $\mathcal{O}(\alpha\alpha_s^3)$ for the radiative correction (referred to as Δr in the literature). The expression for the width of the W is taken from the parameterization in[132]. For the Z width Γ_Z, hadronic peak cross section σ^0_{had}, and width ratios R^0_ℓ, R^0_b, R^0_c, we use the parameterizations in[181]. For the effective weak mixing angle, $\sin^2\theta^\ell_{\text{eff}}$, we use the results in[62]. The value of $\sin^2\theta^\ell_{\text{eff}}$ is used as a proxy for the weak mixing angle to determine the left- and right-handed couplings of the Z, allowing us to compute the asymmetries:

$$\mathcal{A}_f = \frac{g^2_{Lf} - g^2_{Rf}}{g^2_{Lf} + g^2_{Rf}} \tag{6.2.2}$$

for $f = \ell, c, b$. The value of $\sin^2\theta^\ell_{\text{eff}}$ is also used to compute the forward-backward asymmetry $A^{0,\ell}_{\text{FB}}$.

[3] While there are sources of uncertainty such as parton distribution functions that might introduce some correlation between these results, when we repeated the world average M_W scenario (Tevatron + LEP + LHC) with a few different values for the correlations, we arrived at similar qualitative results. A comprehensive global averaging of these experimental results considering all correlations is left for future work.

Finally, for the other forward-backward asymmetries, we compute the effective weak mixing angles $\sin^2\theta^b_{\rm eff}$ and $\sin^2\theta^c_{\rm eff}$ using the parameterizations in Refs.[62,180], respectively. These are then translated to $A^{0,b,c}_{\rm FB}$ using the standard relations summarized e.g., in [180]. See also Ref. [195] for a recent review of the status of relevant theoretical calculations.

We parameterize potential effects of BSM physics in the electroweak fit in terms of the oblique parameters, S, T and U[349,348]:

$$\begin{aligned} S &\equiv \frac{4c_W^2 s_W^2}{\alpha}\left[\Pi'_{ZZ}(0) - \frac{c_W^2 - s_W^2}{c_W s_W}\Pi'_{Z\gamma}(0) - \Pi'_{\gamma\gamma}(0)\right], \\ T &\equiv \frac{1}{\alpha}\left[\frac{\Pi_{WW}(0)}{m_W^2} - \frac{\Pi_{ZZ}(0)}{m_Z^2}\right], \\ U &\equiv \frac{4s_W^2}{\alpha}\left[\Pi'_{WW}(0) - \frac{c_W}{s_W}\Pi'_{Z\gamma}(0) - \Pi'_{\gamma\gamma}(0)\right] - S, \end{aligned} \tag{6.2.3}$$

where Π_{XX} denotes the vacuum polarization for $X = W, Z, \gamma$, and c_W, s_W are $\cos\theta_W$, $\sin\theta_W$ with θ_W denoting the Weinberg mixing angle. (Note that S, T and U do not completely characterize potential BSM effects in the electroweak precision data—a larger set of oblique parameters was developed in Refs.[70,110]. We will not consider their effects here, as they are typically smaller in perturbative theories[203,133].) The new physics contributions to the electroweak observables can be expressed as linear functions of S, T and U[349,348,326,106,107], which are are summarized in Appendix A of [147].

For a class of universal effective theories, both S and T are related to the Wilson coefficients[254,253,249]

of dimension-6 operators[4]:

$$\mathcal{L}_{\text{oblique}} = S\left(\frac{\alpha}{s_W c_W v^2}\right) H^\dagger W_a^{\mu\nu} \sigma^a H B_{\mu\nu} - T\left(\frac{2\alpha}{v^2}\right) |H^\dagger D_\mu H|^2. \tag{6.2.4}$$

The U parameter is often fixed to zero in electroweak fits, as it corresponds to a dimension-8 operator from an effective field theory point of view, and its effects are therefore subleading compared to S and T. We will frequently set $U = 0$ in our fits, but consider its effect in more details in Section 6.3.2. We will discuss new physics interpretations of S and T following the results of the fit with $U = 0$ in Section 6.4.

With all of these inputs, we perform the electroweak fit by minimizing a χ^2 function,

$$\chi^2 = \sum_j \left(\frac{M_j - O_j}{\sigma_j}\right)^2, \tag{6.2.5}$$

where the sum runs over all the observables in Table 6.1, in addition to the W mass. Here, M_j is the experimentally measured value of the observable, O_j is the predicted value in terms of the five free parameters and S, T, U, and σ_j is the measured uncertainty on the observable. We repeat this calculation for all the four scenarios for M_W measurements defined around Equation 6.2.1.

[4]See Ref. [393] for a detailed discussion of the relationship between the oblique parameters and effective theories.

6.3 Results of the Fit

6.3.1 Fitting S and T

We first consider the fit results where U is fixed to zero. The results of our electroweak fit with different values of M_W are summarized in Table 6.2. The first row indicates the χ^2 per degree of freedom (d.o.f.) for the SM for the fit with each value of M_W. We observe that, prior to the CDF measurement, the Standard Model provides a good fit to the data using the PDG 2020 value of M_W, with $\chi^2/(n_{\text{d.o.f.}} = 15) = 1\,(p = 0.45)$. Taking instead the recent CDF II measurement of M_W, however, the p-value for the SM drops to 2.52×10^{-7}, exemplifying the tension discussed in [9]. This is somewhat ameliorated when considering the smaller world average value of M_W ($p = 1.06 \times 10^{-4}$), but notable tension remains.

In the middle rows of Table 6.2 we summarize the results of the fit when we allow S and T to float in addition to the five free observables. We report the best fit values of S and T, and then the χ^2 per degree of freedom. We find a good fit to the data with the PDG average value of M_W, prior to the CDF measurement ($p = 0.53$), where the fit prefers small values of S and T at 0.05 and 0.08, respectively. This is consistent with the electroweak fit presented in [400]. For all of the fits accounting for the new measurement of M_W from CDF II, the fit instead prefers much larger values of S and T. Despite this, we still find a good fit to the data, with p values ranging from 0.26 when using the CDF measurement alone to 0.41 using the combination of measurements at LHC, Tevatron, and LEP.

The results of the fit for the oblique parameters S and T are illustrated in Figure 6.1. Here we

		CDF-II	CDF-II ($2\times$ syst.)	World Average	PDG 2020
SM	$\chi^2/(n_{\text{d.o.f.}} = 15)$	4.00	2.30	2.94	1.00
Best Fit ($U = 0$)	(S, T)	$(0.17, 0.27)$	$(0.15, 0.24)$	$(0.12, 0.20)$	$(0.05, 0.08)$
	$\chi^2/(n_{\text{d.o.f}} = 13)$	1.21	1.17	1.04	0.92
Best Fit (U floating)	(S, T, U)	$(0.03, 0.05, 0.19)$	$(0.03, 0.05, 0.19)$	$(0.03, 0.05, 0.12)$	$(0.03, 0.05, 0.03)$
	$\chi^2/(n_{\text{d.o.f}} = 12)$	0.99	0.99	0.99	0.99

Table 6.2: Fit results including the oblique parameters and χ^2 per degree of freedom. Different columns correspond to different input M_W measurement scenarios around Equation 6.2.1.The first row shows the χ^2 per degree of freedom for SM in each M_W scenario. Results of the fit including (excluding) U in the list of floating parameters are included in the middle (bottom) row.

show ellipses indicating the $2\,\sigma$ contours around the best-fit values of S and T. These are computed by computing the χ^2 at each point in the $S - T$ plane, marginalizing over the free observables, and requiring $\Delta\chi^2 \equiv \chi^2(S, T) - \chi^2_{\text{min}} < 6.18$, where χ^2_{min} is the minimum value of the χ^2 as a function of all the free parameters as well as S and T.

The 2σ contours of the fit with the PDG average value of M_W (excluding the recent CDF II measurement) are shown in blue and agree with the results of[252]. This fit slightly prefers $T > 0$, though the correlation between S and T leaves some parameter space with $S, T < 0$ as well. Once the new measurement of M_W from CDF II is included, however, the preferred region in the $S - T$ plane shifts dramatically. The correlation between S and T remains, but values of $T < 0$ are no longer allowed, even when the systematic error on the CDF measurement is artificially inflated. In all, we find a strong preference for BSM contributions in the electroweak fit, particularly for positive, nonzero values of T.

For each fit, we also find the best fit value of each individual observable both for the SM (with S and T fixed to zero) and for the best-fit value of S and T. The results are shown in Table 6.3. Each entry

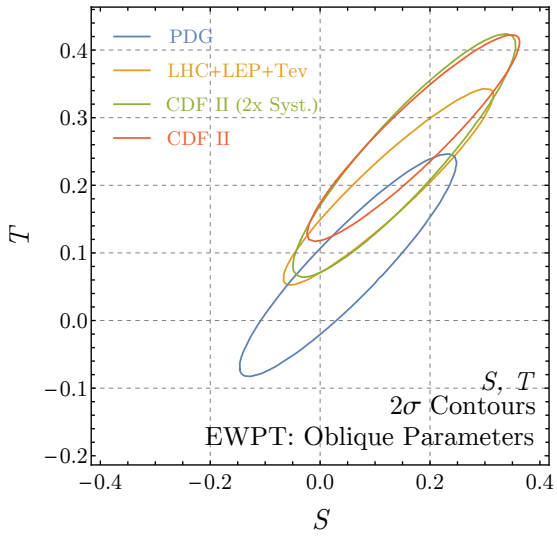

Figure 6.1: The 2σ preferred regions in the S and T plane from the electroweak fit, marginalizing over the five input parameters and for various experimental values of M_W (see the discussion around Equation 6.2.1). We do not include U in these fits. The blue curve is in good agreement with results of GFitter group[216,65,64,252]. Including the recent CDF II measurement of M_W[9] moves the best-fit region to larger positive values of S and T. The SM (with $(S,\ T) = (0,\ 0)$) is strongly disfavored when the new CDF II M_W measurement is included in the fit.

indicates the best-fit value of the observable, along with the pull (calculated as the fit value minus the measured value, divided by the experimental uncertainty) shown in parentheses. For all three values of M_W including the new CDF measurement, we see a significant pull (ranging from -4.5 to -6.3) on the fit value of M_W in the Standard Model. This is entirely ameliorated at the best fit values of S and T, at the cost of a small tension in the values of Γ_Z, which are fit to be larger than the experimental value when S and T are allowed to float. All of the other observables have quite similar values at their best-fit point and at the SM, regardless of the experimental value of M_W used in the fit. Note also that the previously existing tension in the forward-backward asymmetry, $A_{\rm FB}^{0,b}$ measured at LEP is unaffected by the floated values of S and T and is roughly the same for any value of M_W.

	Fit Value (Pull) at SM / Best Fit (S,T)							
	CDF-II		CDF-II (2× syst.)		World Average		PDG 2020	
(S, T)	(0,0)	(0.17, 0.27)	(0,0)	(0.15, 0.24)	(0,0)	(0.12, 0.20)	(0,0)	(0.05, 0.08)
M_Z [GeV]	91.1910 (+1.6)	91.1875 (0.0)	91.1893 (+0.8)	91.1876 (0.0)	91.1908 (+1.5)	91.1876 (0.0)	91.1884 (+0.4)	91.1876 (0.0)
M_h [GeV]	125.24 (-0.1)	125.26 (+0.1)	125.25 (0.0)	125.25 (0.0)	125.24 (-0.1)	125.26 (+0.1)	125.25 (0.0)	125.25 (0.0)
M_t [GeV]	174.14 (+2.1)	172.93 (+0.1)	173.49 (+1.0)	172.90 (0.0)	174.07 (+2.0)	172.91 (0.0)	173.16 (+0.46)	172.93 (+0.1)
$\alpha_s(M_Z^2)$	0.1179 (-0.2)	0.1179 (-0.2)	0.1182 (+0.1)	0.1179 (-0.2)	0.1180 (-0.1)	0.1180 (-0.1)	0.1183 (+0.2)	0.1183 (+0.2)
$\Delta\alpha^{(5)}_{\rm had}(M_Z^2)$	0.02761 (-0.7)	0.02766 (0.0)	0.02764 (-0.3)	0.02766 (0.0)	0.02761 (-0.7)	0.02766 (0.0)	0.02764 (-0.3)	0.02766 (0.0)
M_W [GeV]	80.3690 (-6.3)	80.4272 (-0.6)	80.3622 (-4.5)	80.4204 (-0.8)	80.3682 (-5.0)	80.4082 (-0.3)	80.3587 (-1.6)	80.3776 (-0.1)
Γ_Z [GeV]	2.4950 (-0.2)	2.4995 (+1.7)	2.4948 (-0.3)	2.4990 (+1.5)	2.4950 (-0.2)	2.4982 (+1.2)	2.4946 (-0.4)	2.4961 (+0.3)
Γ_W [GeV]	2.091 (+0.1)	2.096 (+0.3)	2.091 (+0.1)	2.095 (+0.2)	2.091 (+0.1)	2.094 (+0.2)	2.090 (+0.1)	2.092 (+0.2)
$\sigma^0_{\rm had.}$ [nb]	41.489 (+0.2)	41.492 (+0.3)	41.489 (+0.2)	41.492 (+0.3)	41.489 (+0.2)	41.491 (+0.3)	41.489 (+0.2)	41.490 (+0.3)
R^0_ℓ	20.748 (-0.8)	20.749 (-0.7)	20.750 (-0.7)	20.749 (-0.7)	20.748 (-0.8)	20.749 (-0.7)	20.750 (-0.7)	20.750 (-0.7)
$A^{0,\ell}_{\rm FB}$	0.0163 (-0.8)	0.0163 (-0.8)	0.0162 (-0.9)	0.0163 (-0.8)	0.0163 (-0.8)	0.0163 (-0.8)	0.0162 (-0.9)	0.0162 (-0.9)
A_ℓ	0.1474 (-1.4)	0.1474 (-1.4)	0.1471 (-1.6)	0.1473 (-1.4)	0.1474 (-1.4)	0.1472 (-1.5)	0.1469 (-1.7)	0.1470 (-1.6)
$\sin^2\theta^\ell_{\rm eff}(Q_{\rm FB})$	0.2315 (-0.8)	0.2315 (-0.8)	0.2315 (-0.8)	0.2315 (-0.8)	0.2315 (-0.8)	0.2315 (-0.8)	0.2315 (-0.8)	0.2315 (-0.8)
$\sin^2\theta^\ell_{\rm eff}$(Tevt.)	0.23147 (0.0)	0.23148 (0.0)	0.23152 (+0.1)	0.23148 (0.0)	0.23148 (0.0)	0.23150 (+0.1)	0.23154 (+0.2)	0.23153 (+0.2)
A_b	0.936 (+0.7)	0.936 (+0.7)	0.936 (+0.7)	0.936 (+0.7)	0.936 (+0.7)	0.936 (+0.7)	0.936 (+0.7)	0.936 (+0.7)
A_c	0.668 (-0.1)	0.668 (-0.1)	0.668 (-0.1)	0.668 (-0.1)	0.668 (-0.1)	0.668 (-0.1)	0.667 (-0.1)	0.667 (-0.1)
$A^{0,b}_{\rm FB}$	0.1033 (+2.6)	0.1033 (+2.6)	0.1031 (+2.4)	0.1033 (+2.6)	0.1033 (+2.6)	0.1032 (+2.5)	0.1030 (+2.4)	0.1030 (+2.4)
$A^{0,c}_{\rm FB}$	0.0739 (+0.9)	0.0739 (+0.9)	0.0737 (+0.9)	0.0738 (+0.9)	0.0738 (+0.9)	0.0738 (+0.9)	0.0736 (+0.8)	0.0736 (+0.8)
$R^{0,b}$	0.21582 (-0.7)	0.21586 (-0.7)	0.21584 (-0.7)	0.21586 (-0.7)	0.21583 (-0.7)	0.21586 (-0.7)	0.21585 (-0.7)	0.21586 (-0.7)
$R^{0,c}$	0.1722 (0.0)	0.1722 (0.0)	0.1722 (0.0)	0.1722 (0.0)	0.1722 (0.0)	0.1722 (0.0)	0.1722 (0.0)	0.1722 (0.0)

Table 6.3: The best fit values of the observables, and their pulls (calculated as the fit value minus the measured value, divided by the experimental uncertainty).

6.3.2 The U Parameter

In the fits described above, we have fixed $U = 0$. As discussed in Section 6.2, this is motivated by the fact that the U-parameter is dimension 8, and is typically suppressed relative to S and T in concrete models.

Nevertheless, in light of the large value of M_W measured at CDF II, it is worth examining the effects of the U-parameter on the electroweak fits in more detail. This is because, of all the electroweak precision observables we consider, the U parameter affects only two: the W mass and width [326,106,147]:[5]

$$\begin{aligned} M_W &= M_{W,\mathrm{SM}}\left(1 - \frac{\alpha(M_Z^2)}{4(c_W^2 - s_W^2)}(S - 2c_W^2 T) + \frac{\alpha(M_Z^2)}{8s_W^2}U\right), \\ \Gamma_W &= \Gamma_{W,\mathrm{SM}}\left(1 - \frac{3\alpha(M_Z^2)}{4(c_W^2 - s_W^2)}(S - 2c_W^2 T) + \frac{3\alpha(M_Z^2)}{8s_W^2}U\right). \end{aligned} \tag{6.3.1}$$

The W decay width is not measured to nearly as high precision as M_W, so the observed discrepancy in the W mass at CDF II[9] can be accommodated in the SM electroweak fit by setting $U \approx 0.11$, without affecting any of the other observables.

To illustrate this in more detail, we perform the fits to the S and T parameters as described above again, except that we now marginalize over the value of U in addition to the free observables, rather than fixing it to zero. The results are shown in Figure 6.2. We see that, when marginalizing over U, the 2σ-preferred range of S and T with the new CDF measurement of M_W is quite similar to the allowed region using the smaller value of M_W. Instead, the U parameter is inflated to account for the shift in mass.

[5] We thank Ayres Freitas for emphasizing this point to us.

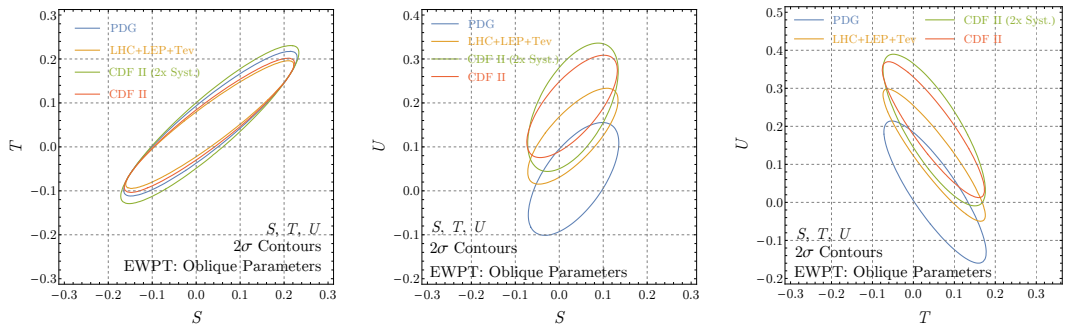

Figure 6.2: Similar to Figure 6.1, but now also marginalizing over U in the global fit. We show the 2σ preferred region of all oblique parameters in the $S - T$ plane (left), $S - U$ plane (center), and $U - T$ plane (right). We find that when we include U in the fit, S and T remain nearly centered about 0, whereas U has a notable positive shift. Getting such large values of U are quite challenging in perturbative models.

The difficulty in this interpretation is that a large value of U is challenging to generate in perturbative models, because, as mentioned in Section 6.2, U corresponds to a dimension-8 operator[248], and a value of $\mathcal{O}(0.1)$ indicates scales of order few 100 GeV for tree-level models, and $\ll 100$ GeV for particles contributing in loops. As the U parameter violates custodial symmetry, it is difficult to imagine a model that generates a large, nonzero value of U without also generating large values of T. We therefore do not attempt to construct models generating large values of U. In the concrete BSM models we consider in the next section, we will ignore the (subleading) U-dependence altogether.

6.4 Implications for BSM Models

From the results of our electroweak fit shown in Section 6.3, we see that the value of M_W can dramatically change the preferred values of the oblique parameters. While the 95% CL region fitting with PDG measurements is nearly centered around the predicted SM values of $(S, T, U) = (0, 0, 0)$, the updated value of M_W shifts this region to positive $\mathcal{O}(0.1)$ values of oblique parameters (see Figures 6.1

and 6.2).

In this section we explore various tree-level and loop-level contributions to the oblique parameters from simple models, and assess their viability. For clarity, we focus on the scenario of M_W equal to the world average from Tevatron, LEP, and LHC measurements (second scenario in Equation 6.2.1).

It is first worthwhile to estimate the scale of new physics implied by $\mathcal{O}(0.1)$ values of S and T. Comparing to the dimension-6 operators defined in Equation 6.2.4, we see that for tree-level matching with perturbative couplings, these operators can be generated by new physics at a scale $\Lambda \sim$ TeV. If the new physics arises in loops, on the other hand, the loop factor suppression implies a scale closer to $\mathcal{O}(100\,\text{GeV})$. We will examine this matching in both scenarios, first considering minimal extensions to the SM that can be integrated out at tree-level, such as an additional gauge boson or scalar, then consider a one-loop example with new singlet-doublet fermion pairs. Note that, as indicated in Figure 6.1, it is important for these models to shift T to positive values to be consistent with our electroweak fit.

6.4.1 Tree-Level Models

Here we consider models that lead to corrections to the oblique parameters at tree level. Given the results of the fits shown in Figure 6.1, we are particularly interested in models that can accommodate large positive values of S and T.

The simplest examples of models leading to oblique parameter corrections are new vectors that acquire couplings to the Higgs. As an example, consider a Z' from a spontaneously broken additional U(1) gauge symmetry. The oblique corrections from a new gauge boson have been worked out in the most general case in [264]. Focusing on the simplest example, where the gauge boson has only kinetic

mixing with SM hypercharge gauge boson, $\mathcal{L} \supset -\frac{1}{2}\varepsilon B^{\mu\nu} Z'_{\mu\nu}$, the corrections to the oblique parameters are given by

$$S = \frac{4 s_W^2 c_W^2}{\alpha} \varepsilon^2 \frac{1}{1-r}\left(1 - s_W^2 \frac{1}{1-r}\right), \qquad T = -\frac{s_W^2}{\alpha}\varepsilon^2 \frac{r}{(1-r)^2} \tag{6.4.1}$$

where $r \equiv (m_{Z'}/M_Z)^2$, with m'_Z the mass of the new gauge boson. While S can change sign depending on whether the new gauge boson is heavier or lighter than M_Z, the T parameter in this model is always negative, and therefore cannot resolve the tension in the electroweak fit.

In the more general case with mass mixing, the simple relations above no longer hold, and different values of S and T may be possible, but generating the necessary mixing terms would require strong dynamics involved in electroweak symmetry breaking, which are likely tightly constrained and beyond the scope of this work.

Instead, we are led to consider new scalars affecting the oblique parameters. An $\mathrm{SU}(2)_L$ singlet scalar leads only to an overall rescaling of the Higgs couplings that do not affect S and T or shifts in the Higgs self-coupling. Models with extra $\mathrm{SU}(2)_L$ doublet scalars, such as a 2HDM [99], can affect the Higgs couplings to the gauge bosons, but these deviations are proportional to $\cos^2(\beta - \alpha)$, the square of the alignment parameter, which from an effective field theory perspective is dimension 8, and therefore cannot affect the oblique parameters S and T, which are dimension 6.

An $\mathrm{SU}(2)_L$ triplet scalar ϕ^a, however, leads to more interesting possibilities [90].[6] Such a triplet can have interactions with the SM Higgs $\sim \phi^a H^\dagger \sigma^a H$. After electroweak symmetry breaking, this inter-

[6] We thank Matthew Strassler for bringing this model to our attention.

action leads to a small vacuum expectation value for the scalar triplet, which shifts the mass of the W bosons without changing the mass of the Z, therefore offering a possibility of resolving the tension between the CDF measurement of M_W and the SM expectation.

For concreteness, we will consider a real scalar $\mathrm{SU}(2)_L$ triplet ϕ^a with $Y = 0$ which we will refer to as a swino. The Lagrangian takes the form

$$\mathcal{L} \supset \frac{1}{2} D_\mu \phi^a D^\mu \phi^a - \frac{1}{2} M_T^2 \phi^a \phi^a + \kappa \phi^a H^\dagger \sigma^a H - \eta H^\dagger H \phi^a \phi^a . \tag{6.4.2}$$

The constraints on $\mathrm{SU}(2)_L$ triplet scalars, including the oblique parameters, have been worked out in [297], where they include the matching up to one-loop order. At tree-level, the contribution to S from scalar triplets vanishes. The $Y = 0$ swino does, on the other hand, lead to a contribution to the T parameter given by

$$T = \frac{v^2}{\alpha} \frac{\kappa^2}{M_T^4} \tag{6.4.3}$$

Importantly, unlike the dark photon model, this contribution is *positive* for any value of κ and can naturally explain the observed discrepancy in M_W measurement.

One can also consider scalar triplets with $Y = 1$, but these lead to the wrong sign for T at tree level. At one loop, both $Y = 0$ and $Y = 1$ triplets lead to additional corrections to both S and T, which can be potentially large and positive, depending on the quartic couplings to the Higgs. We leave a more detailed study of these possibilities to future works.

In Figure 6.3, we show the band of values of κ and M_T that are compatible with the electroweak

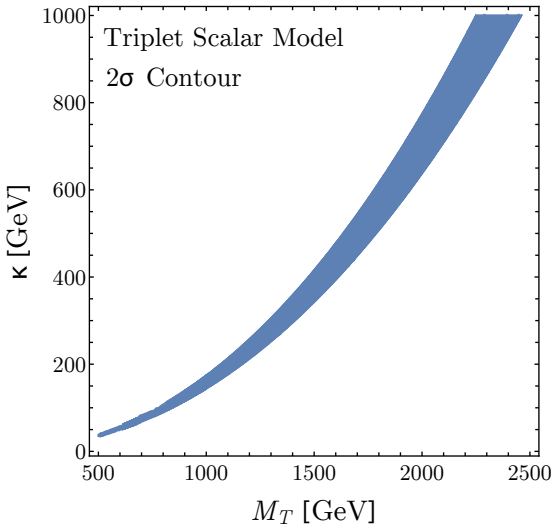

Figure 6.3: The 2σ band in the $M_T - \kappa$ plane of the triplet scalar model. We find viable parameter space for $\mathcal{O}(\text{TeV})$ swino masses that can potentially be probed with future high-energy colliders.

fit with the combined value of M_W at 2σ. As is clear from the scaling in Equation 6.4.3, the necessary large value of T can be achieved even for large triplet masses. Requiring $\kappa/M_T \lesssim 1$, the triplet mass can be up to $\mathcal{O}(\sim \text{TeV})$, evading any potential collider bounds.

6.4.2 Singlet-Doublet Model

We now shift our attention to another simple extension of the SM, the $\text{SU}(2)_L$ singlet-doublet fermion model. Unlike the previous discussion, the contribution of this model to electroweak precision measurements first occurs at loop level. The model includes N_f families of a singlet Majorana and doublet Dirac fermion charged under the electroweak sector [325,170,192,149,129,17,113,221,68,111,321,220].[7] Such a setup can be embedded inside supersymmetric extensions of the SM. The $\text{SU}(2)_L$ doublet has hyper-

[7] For simplicity, we consider the scenario where these fermions do not mix with each other, but in principle mixing could lead to richer phenomenology.

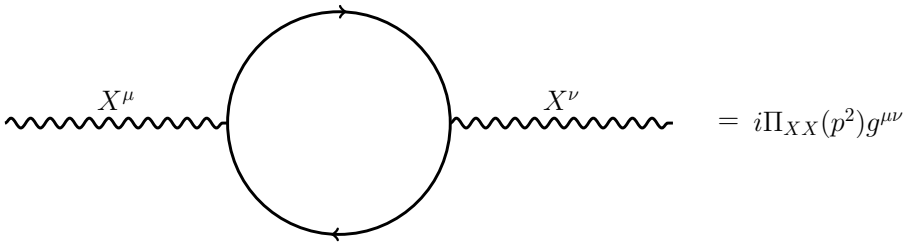

Figure 6.4: The 1-loop contribution to the vacuum polarization of SM gauge bosons. X^μ here stands for any electroweak gauge boson $X = W, Z, \gamma$.

charge 1/2 and is composed of two left-handed Weyl fermions ψ_2 and $\tilde{\psi}_2$. The Lagrangian is

$$\mathcal{L} = \mathcal{L}_{SM} + \mathcal{L}_{\text{kinetic}} - m_2\psi_2 \cdot \tilde{\psi}_2 - \frac{m_1}{2}\psi_1\psi_1 + y\, e^{i\delta_{\text{CP}}/2}\psi_1 H^\dagger \psi_2 - \tilde{y}\, e^{i\delta_{\text{CP}}/2}\psi_1 H \cdot \tilde{\psi}_2 + \text{h.c.} \quad (6.4.4)$$

This Lagrangian has a physical CP-violating phase, as we have four new parameters and three new fields. Since S and T are CP-even observables, we set $\delta_{\text{CP}} = 0$ in this analysis for simplicity. However, this model is also interesting with nonzero values of δ_{CP} as it can potentially explain the Galactic Center Excess (see [220] for details). Additionally, because of the Yukawa terms, there is mass mixing between the fermions and the ψ_i fields are not the propagating degrees of freedom. We call attention to this point because the mass of the lightest propagating fermion is relevant for Higgs (and Z) decay constraints, which require $M_\chi > M_h/2$.

The singlet-doublet model contributes to the S and T parameters at loop-level with the new fermions running in the loop. While more details of the calculation are given in [220], we provide a quick summary here. We write a generic coupling between gauge bosons i and fermions j as $i\gamma^\mu(C_{ij}^V - C_{ij}^A\gamma^5)$

where C_{ij}^V and C_{ij}^A are the vector and axial vector couplings respectively. In $\overline{\text{MS}}$, we find

$$\begin{aligned} i\Pi(p^2)g^{\mu\nu} = \frac{-ig^{\mu\nu}}{4\pi^2}\int_0^1 dx \left(\left(|C_{Vij}|^2+|C_{Aij}|^2\right)p^2x(1-x)\right. \\ \left. + \left(|C_{Vij}|^2-|C_{Aij}|^2\right)m_im_j - \left(|C_{Vij}|^2+|C_{Aij}|^2\right)\Delta\right)\log\frac{\mu^2}{\Delta}, \end{aligned} \tag{6.4.5}$$

where $\Delta = m_i^2 + x(m_j^2 - m_i^2) - x(1-x)p^2$. The other relevant expression is $\Pi'(p^2)$, which is given by

$$\begin{aligned} i\Pi'(p^2)g^{\mu\nu} = \frac{-ig^{\mu\nu}}{4\pi^2}\int_0^1 dx\Bigg\{2\left(|C_{Vij}|^2+|C_{Aij}|^2\right)x(1-x)\log\frac{\mu^2}{\Delta} \\ +\Big[(|C_{Vij}|^2+|C_{Aij}|^2)p^2x(1-x) + \left(|C_{Vij}|^2-|C_{Aij}|^2\right)m_im_j \\ -\left(|C_{Vij}|^2+|C_{Aij}|^2\right)\Delta\Big]\frac{x(1-x)}{\Delta}\Bigg\}. \end{aligned} \tag{6.4.6}$$

The diagram topology contributing to S and T in this model is shown in Figure 6.4 and scales linearly with the number of new fermion generations, N_f. We can only get a nonzero T value when the custodial symmetry is broken, i.e. $y \neq \tilde{y}$. Furthermore, S and T both decrease as m_2 or m_1 increase, making it difficult to reach values consistent with both the updated electroweak fit and existing experimental constraints.

In Figure 6.5 we plot the dependence of S and T on the new fermion mass parameters m_1 and m_2 to get a benchmark value of the couplings. Lower values of m_1 and m_2 are strongly constrained by a host of different measurements (including LEP bounds on charged fermions, Higgs and invisible Z decays, and direct searches for light fermions carrying electroweak charge). In the left panel of the figure we consider the model with only one generation of new fermions. We find that the contribution to S and

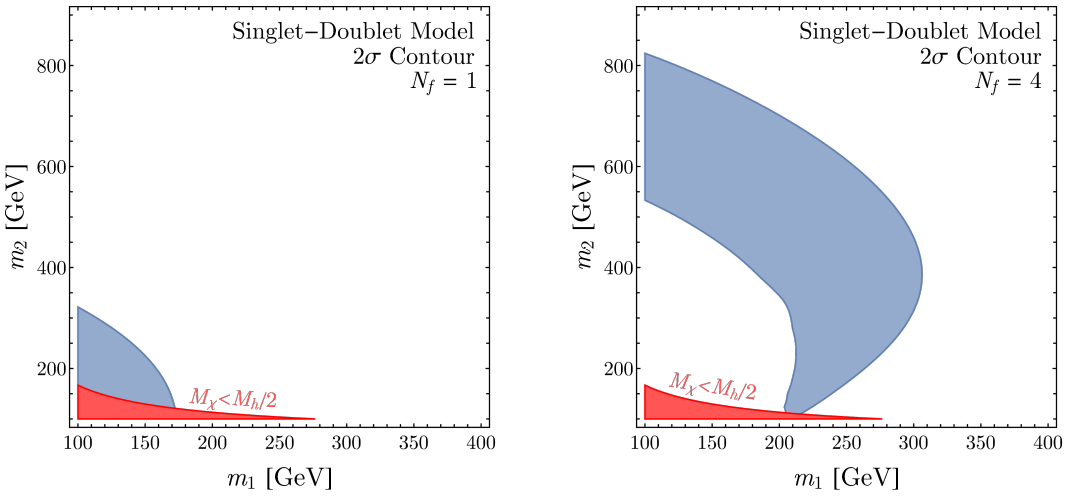

Figure 6.5: Contribution to the S and T parameters from singlet-doublet fermions for benchmark values of the couplings ($y = 0.1$, $\tilde{y} = 1$, $\delta_{\rm CP} = 0$) and N_f generations of new fermions, where $N_f = 1$ ($N_f = 4$) on the left (right). In the blue band the model can give rise to large enough S and T to explain the world average M_W measurement within 2σ. Relevant constraints on the model are briefly discussed in the text; in particular, direct LHC searches can potentially rule out most of the blue band for $N_f = 1$ and probe much of the $N_f = 4$ allowed region.

T is only large enough to explain the CDF II anomaly in a small corner of the parameter space; direct searches at LHC strongly constrain this range of masses.

In the right panel of Figure 6.5 we show the contribution of the model to the oblique parameters with $N_f = 4$. We now find a larger range of masses that give rise to M_W values within 2σ of the global average measurement. Direct LHC searches can again rule out some of this parameter space, but there is still viable parameter space in the range of masses shown in the figure, specifically in the limit of degenerate masses or at high values of m_2. A more thorough exploration of the viable parameter space (with other values of y and $\tilde{y}$) is left for future work.

6.5 Conclusion

In this chapter we studied the effect of recent M_W measurement at CDF II on global fits of electroweak precision observables and the implications for physics beyond the SM. By performing a standard χ^2 fit over SM parameters as well as the oblique parameters S, T, and U, we explored the efficacy of a variety of models for generating an upward shift in the M_W mass. After combining all M_W measurements at the Tevatron, LEP, and the LHC, there exists a significant discrepancy with SM predictions.

The results of our fit suggest that new physics models that contribute to S and, more substantially, a positive T are potential candidates to explain the anomaly. While we considered a global fit also including U, the results did not have a natural model-building interpretation. Of the models we consider, we find that a generic dark photon mixing with SM photon, a singlet scalar extension of SM, and a 2HDM model fail to yield S and T contributions consistent with our fit. However, the swino model was markedly successful since it generated positive $\mathcal{O}(0.1)$ values of T in unconstrained regions of parameter space. Viable triplet mass values were found to be near or above the TeV scale, which can evade current experimental bounds while giving rise to interesting signatures in future high energy colliders such as FCC-hh or muon colliders. We leave a detailed study of such signals to future work. Additionally, we found some success with a singlet-doublet fermion model when considering multiple generations.

As previously mentioned, there are other anomalies in the SM that could arise from discrepant electroweak precision measurements, such as the anomalous magnetic moment of the muon $g-2$. It was pointed out in Ref.[153] that the existing discrepancy between the theoretical and measured values of

$(g-2)_\mu$ can be absorbed in a shift to the hadronic vacuum polarization contribution by changing $\Delta\alpha^{(5)}_{\text{had}}$, at the cost of increasing the tension in the SM electroweak fit, particularly by *decreasing* the preferred value of M_W. It is of high importance to explore if the necessary change in the fit to ameliorate the $(g-2)_\mu$ discrepancy can be accommodated by the BSM effects of interest for the W mass measurement, or if something much more exotic is required.

Finally, we would like to call attention to the fact that a tension arising from the global SM electroweak fit is not unique to the W boson mass. For example, significant deviations from the SM have been evident the forward-backward asymmetry observable at LEP for many years [367], and numerous attempts at explaining this with BSM physics (e.g. [139], among others). This further motivates future study of how potential new physics affects electroweak precision observables.

These results can be interpreted as new *oblique* signs of BSM appearing around the TeV scale. In light of this new measurement, further experimental results, including improvement to measurement of M_W at LHC or future colliders, are strongly motivated.

7

A Tale of Two $U(1)$'s: Kinetic Mixing from Lattice WGC States

7.1 Motivation and Introduction

One generic feature of string compactifications is the presence of hidden sectors containing additional matter that is possibly charged under extensions of the Standard Model (SM) gauge group G_{SM}. This

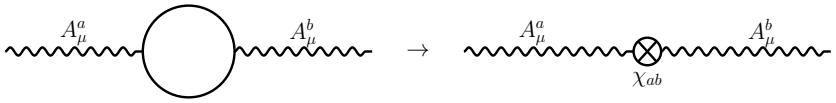

Figure 7.1: If bi-charged matter exists in the UV model, integrating it out can generate a 1-loop kinetic mixing in the IR via this diagram.

expectation is borne out in our universe through the existence of a dark sector. In fact, cosmological observations have shown that about 95% of the energy density in the universe resides within such a dark sector, with 25% as dark matter and 70% as dark energy[23]. Despite this abundance of dark matter, it has proven difficult to detect any non-gravitational interactions between our sector and the dark sector. It is a logical possibility that dark matter is not charged under any gauge group or that interactions between the two sectors are only mediated by operators suppressed by a large mass scale. In these cases, directly observing any hidden sector physics would require high energy experiments beyond the reach of current technology. However, if dark matter is charged under an additional $U(1)_X$, there is a dimension four kinetic mixing operator between $U(1)_X$ and the SM hypercharge $U(1)_Y$ that is not suppressed by a large mass scale:

$$\mathcal{L} \supset -\frac{1}{4}F^2_{(Y)} - \frac{1}{4}F^2_{(X)} + \frac{\chi}{2}F^{\mu\nu}_{(Y)}F_{(X)\mu\nu}$$

This operator can be generated by integrating out massive particles in a UV theory that are charged under both Abelian groups[263] (see also[199] for a review), as shown schematically in Figure 7.1. Each scalar bi-charged state, with mass m and charges Q_a and Q_b under the respective U(1)'s, contributes

an amount χ to the kinetic mixing given by[1]

$$\frac{\chi}{g_a g_b} = -\frac{Q_a Q_b}{48\pi^2} \ln \frac{m^2}{\mu^2} \tag{7.1.1}$$

The effect is similar to that of a threshold correction to the gauge coupling. If the low-energy theory does not contain any more particles charged under $U(1)_X$, one is free to define a rotation in field space $A'_Y \equiv A_Y - \chi A_X$ along with a new gauge coupling $g'_Y \equiv g_Y/\sqrt{1-\chi^2}$ that removes all effects of the kinetic mixing operator. But in the presence of light charged hidden matter, the effect of a kinetic mixing operator is to give certain dark matter species a 'minicharge' under the visible $U(1)_Y$ and in turn $U(1)_{\text{EM}}$. This can be seen by a similar field redefinition as above which causes a dark matter particle of charge $g_X Q$ under $U(1)_X$ to acquire a charge $\chi Q g_X/g_Y$ under $U(1)_Y$. So far, we have assumed that the $U(1)_X$ gauge boson is also massless, which provides the freedom to rotate the mixing into either sector. An interesting alternative is to consider a massive dark photon. In this scenario, diagonalizing to the mass basis fixes the eigenstates and uniquely determines the coupling of the photon and dark photon to both the Standard Model and dark currents. The standard mechanism for generating a mass for the dark photon is by spontaneously breaking the symmetry with a Higgs or by providing a Stueckelberg mass, which is a special case of the Higgs mechanism where the Higgs has been decoupled. In either case, above the symmetry breaking scale, we have a massless Abelian field, so for the purposes of our analysis, we will restrict our attention to this case, with the expectation that our results will also apply to the massive case as well. The phenomenological implications of the massive dark photon have been

[1] The numerical prefactor changes if we integrate out fermions or chiral supermultiplets in a supersymmetric theory, but the dependence on charges and masses remains.

extensively explored in recent years, so we will, of necessity, refer the readers to an excellent recent review article and the references therein [199].

Numerous current and near-future experimental efforts (see for example [199] for a recent review) are directed at detecting minicharged particles. These have phenomenological signatures that vary with the mass of the dark matter particle and the strength of the kinetic mixing parameter χ. For masses below $\sim$ 0.1 MeV, the most constraining effect is due to stellar energy loss. This has been investigated using data from the Sun [385], white dwarves, red giants and horizontal branch stars [388]. SN1987a also provides constraints extending to $\sim$ 1 MeV [126]. At higher masses, cosmological observations (for $\chi \lesssim 10^{-3}$) and laboratory searches (for larger χ) are more relevant. The former rely on N_{eff} constraints from BBN and the CMB [388] as well as effects of minicharged particles on acoustic oscillations during recombination [108]. The latter involve collider searches [276,160], beam-dump experiments [357], ortho-positronium decays [66], light shining through a wall experiments [187] and neutrino experiments [324]. Future experiments will further explore this parameter space [361,358,359,67,295,234,233].

Given the vast parameter space, it is important to provide theoretical input on the expected magnitude of the coefficient χ. Since the value of χ in any effective field theory (EFT) is very model-dependent, one may hope that turning to a UV complete theory (with a more rigid framework) would provide a better picture of generic expectations. Indeed, several such investigations have been carried out in the literature giving predictions for the value of χ ranging over many orders of magnitude with some models having a seemingly vanishing mixing parameter.[2]

[2] Although the expectation is that mixing is present anyways from low-energy effects such as SUSY breaking, GUT symmetry breaking or Dine-Seiberg-Witten vacuum shifts.

One of the pioneering studies is due to [173] where contributions to χ from massive string states were computed in semi-realistic orbifold compactifications of the heterotic string in the fermionic formulation. The surprising result was that massive string states do not contribute to mixing in the low-energy theory. Later works [240] outlined the requirements for kinetic mixing to be present in heterotic orbifolds by extending early results about threshold corrections [292,175]. When present, the kinetic mixing effect is considerable with $\chi \gtrsim 10^{-4}$. In the context of Type II theories with D-branes, kinetic mixing has been found in Calabi-Yau orientifolds with D7-branes [280], D6-branes [18], D5-branes [247] and in the LARGE volume scenario [239]. Additionally, kinetic mixing can occur in non-SUSY set-ups with anti-branes in the extra dimensions [20,19] such as $\overline{\text{D3}}$-branes in Klebanov-Strassler throats. Finally, kinetic mixing has also been shown to arise at strong coupling in F-theory constructions [168].

As such, different limits of the string landscape have been investigated but no overall picture is currently available. Here we revisit some of these arguments in light of the Sublattice Weak Gravity Conjecture (sLWGC) which is expected to hold in the entire landscape [256,257]. As we review in the next section, the sLWGC requires massive states charged under all Abelian symmetries. When integrated out, these can generate the kinetic mixing operator in the low-energy EFT. Of course, explicit constructions include these states but the highly symmetric set-ups required for computational control can possibly lead to large cancellations and thus biases estimates of χ towards lower values. In this chapter, we point out that the sLWGC, in addition to an assumption about the mass spectrum of relevant states, also leads to an estimate of χ, extending the analysis of [81]. This approach is complementary to the available constructions in the sense that it is more general but inevitably less precise. The question of computing kinetic mixing effects is replaced by an estimate of the mass spectrum of

states charged under the various $U(1)$ symmetries.

This chapter is organized as follows. In Section 7.2, we begin with a review of the relevant Swampland conjectures. Next, we discuss a statistical approach to estimating the kinetic mixing arising from a generic spectrum of sLWGC states in Section 7.3. We discuss specific constructions in Section 7.4. This includes a QFT construction in Section 7.4.1, heterotic orbifold constructions in Section 7.4.2, and Type II on a Calabi-Yau in Section 7.4.3. Section 7.5 discusses various potential known loopholes. Finally, we offer concluding remarks in Section 7.6.

7.2 Swampland/Quantum Gravity Preliminaries

The Swampland conjectures are a set of conjectures which impose constraints on low-energy effective theories. These constraints arise from the fact that seemingly innocuous effective field theories in the IR run into pathologies when we try to UV complete them into a theory of quantum gravity. Theories satisfying these constraints are said to be in the Landscape, while theories violating these constraints live in the Swampland. Taking these conjectures as a theoretical input, we can make predictions for the size of certain parameters in our effective field theory, such as the kinetic mixing parameter χ. These predictions allow us to bring quantum gravity into contact with our rich experimental program. In this section, we will review the relevant Swampland conjectures. See the reviews [101,344] for more details.

7.2.1 Review of sLWGC

The Weak Gravity Conjecture (WGC)[56] is one of the oldest conjectures in the Swampland program. The WGC states that if we have a U(1) gauge theory coupled to gravity, then there exists a (superextremal) particle whose charge to mass ratio is larger than that of a large, non-rotating, extremal black hole[56].

The conjecture was originally proposed to avoid the existence of stable black holes. If there is a particle in the spectrum of states satisfying the WGC, then an extremal black hole can decay away from extremality by emitting a superextremal particle. Although appealing, a priori there isn't any fundamental obstruction in having a stable extremal black hole charged under a gauge symmetry in the same way that there is for a global symmetry. On the other hand, we know the WGC holds in a large class of string theory constructions. Furthermore, simple toy examples such as Kaluza-Klein (KK) reductions also generate towers of states satisfying the WGC.

The authors of[256,257] further refined this conjecture. They generalized the Weak Gravity Conjecture to state that an Abelian p-form gauge field with gauge coupling $e_{p;d}$ in d dimensions with varying dilaton couplings α, necessitates the existence of a $(p-1)$-brane of tension T_p and charge q satisfying

$$\left[\frac{\alpha^2}{2}+\frac{p(d-p-2)}{d-2}\right]T_p^2 \leq e_{p;d}^2 q^2 M_d^{d-2} \tag{7.2.1}$$

They also proposed the Sublattice Weak Gravity Conjecture. The sLWGC states that if we have a charge lattice Γ in a given theory, then there exists a sublattice $\Gamma_{\text{sup}} \subseteq \Gamma$ such that all $\vec{q} \in \Gamma_{\text{sup}}$ corre-

spond to a superextremal state. The coarseness of the sublattice, defined as the smallest integer N such that $N\vec{q} \in \Gamma_{\text{sup}}, \forall \vec{q} \in \Gamma$, is finite. Therefore, Γ_{sup} and Γ have the same dimensionality. Crucially, in a U(1)×U(1) gauge theory, the sLWGC implies the existence of a sublattice of superextremal states charged under both gauge groups. The existence of these states is an important starting point for generating kinetic mixing. A toy model illustrating this feature is the KK compactification of 6D pure gravity on T^2. This dimensional reduction generates two graviphotons, giving us a U(1)×U(1) gauge theory in 4D. The masses of the KK modes are given by

$$m^2 = \frac{\varphi^{ij} n_i n_j}{R^2} \qquad Q_i = n_i \tag{7.2.2}$$

φ denotes the metric on moduli space and R^2 is the overall compactification scale. The extremality bound, which was also derived in [256], is given by

$$M^2 \geq \frac{\varphi^{ij} Q_i Q_j}{R^2} \tag{7.2.3}$$

The KK modes saturate this bound. Furthermore, we have a state for each choice of Q_i. So, we immediately see that the sLWGC is satisfied with $\Gamma_{\text{sup}} = \Gamma$.[3]

[3] This was intended as an illustrative example. If we compactify on other manifolds, such as toroidal orbifolds, we are only guaranteed a sublattice of superextremal states.

7.2.2 Species Scale

The QFT we analyze is an effective lower dimensional theory with gravity propagating in higher dimensions. This effective theory is valid up to a cutoff scale which is set by the species scale Λ_s. Above the species scale, gravity becomes strongly coupled in the higher dimensional theory. The species scale conjecture states that if we consider a d-dimensional gravitational theory having N single particle states, with Planck mass $M_p^{(d)}$, then requiring gravity to remain weakly coupled necessitates a cutoff scale Λ below the species scale given by

$$\Lambda_s = \frac{M_p^d}{N^{\frac{1}{d-2}}}. \tag{7.2.4}$$

This conjecture can be derived by counting KK modes, but is expected to hold more generally. For computing kinetic mixing, this implies that every light state we integrate out, lowers the cutoff of our theory. States with masses below Λ_s contribute to kinetic mixing, while states with masses above are not part of our effective description and hence are excluded.

7.3 Estimating χ from sLWGC states

In this section, we carry out a phenomenological estimate of χ by assuming that the sLWGC holds in a high energy theory and integrating out string-scale states to obtain the low-energy kinetic mixing coefficient. This also allows us to investigate the dependence of the mixing on the mass distribution of superextremal particles on the charge lattice. To isolate the effect of these particles, we assume that the $U(1)$'s under consideration do not kinetically mix in the full theory. In addition, we assume that this

mixing cannot be rotated away by redefining the $U(1)$ generators. This could be due to the existence of a light particle carrying either $U(1)$ charge for example, as mentioned in Section 7.1, or other effects such as the possibility of measuring the coupling constant of a GUT. The χ estimates obtained here should be viewed as lower bounds since we are only considering superextremal states whereas any string construction typically includes a large number of subextremal states as well.

More precisely, we consider the charge lattice of a $U(1)_a \times U(1)_b$ theory with superextremal particles of mass:

$$\frac{m}{M_{\rm Pl}} = c \times q \qquad\qquad q \equiv \sqrt{(g_a Q_a)^2 + (g_b Q_b)^2} \tag{7.3.1}$$

at position (Q_a, Q_b) on the lattice. The expression for q in Equation 7.3.1 is a good approximation when the mixing is small. However when the mixing is $\mathcal{O}(1)$, the off-diagonal elements of the metric on field space contribute to this formula. We will ignore this subtlety for our estimate. The c's are random coefficients drawn from a distribution that depends on the charge site and are strictly less than unity to ensure superextremality. In principle, the probability density function of c is calculable from Landscape constructions but this is prohibitively difficult in practice except perhaps within the context of a limited class of models.[4] For our estimate, we choose the following distribution:

$$P(c; q, q_0) = \alpha(q^2 - q_0^2)\frac{e^{\alpha(q^2-q_0^2)c}}{e^{\alpha(q^2-q_0^2)} - 1} \tag{7.3.2}$$

[4]Assigning a probability distribution to c is akin to assigning a probability measure on theory space and we are certainly not claiming that we have access to that measure. Instead one may think of this probability distribution as an area weight over moduli space.

where we define

$$q_0 \equiv \sqrt{g_a^2 + g_b^2}. \tag{7.3.3}$$

This choice of probability distribution makes it exponentially difficult for states far out on the lattice to be light. This aligns with WGC intuition, according to which very massive string states should be viewed as black holes and, since we are modeling superextremal states only, their mass-to-charge ratio must therefore match the black hole extremality bound. In addition, for $\alpha = 1$ and large q, the mean of the above distribution is $1 - 1/q^2$ which lines up with the mass-to-charge ratio of superextremal states of the heterotic string. The width of the distribution and the parameter α can then be thought of as resulting from symmetry breaking effects that contribute to particle masses. These effects are certainly less prominent for heavy states and this is captured by the decreasing width of the distribution as q^2 increases.

Our choice of probability distribution is invariant under a $\mathbb{Z}_2$ symmetry where $Q_{a,b} \to -Q_{a,b}$ and this will result in a distribution of χ that is centered at 0, as illustrated in the right panel of Figure 7.2. In order to facilitate comparisons with string constructions in Section 7.4.2, we consider a particle spectrum which includes states with charges $(Q_a, \pm|Q_b|)$. As above, the masses of these states are different and are drawn at random from the distribution in Equation 7.3.2. The contribution of any such pair of states is μ-independent and given by:

$$\chi_{ij} = -\frac{g_a Q_a g_b |Q_b|}{48\pi^2} \ln \frac{m_+}{m_-} = -\frac{g_a Q_a g_b |Q_b|}{48\pi^2} \ln \frac{c_+}{c_-} \tag{7.3.4}$$

where the subscripts on $c_\pm$ indicate the sign of the charge under $U(1)_b$ and we use the (i,j) subscripts (with $j > 0$, say) as a reminder that this is the contribution from one pair of lattice sites[5]. We can now derive an expression for probability distribution of χ_{ij} using the distribution we assumed for $P(c)$. We leave the details to Appendix E.1 and quote the result here:

$$P(\chi_{ij}) = \left|\frac{48\pi^2}{g_a Q_a g_b Q_b}\right| \times \begin{cases} \dfrac{e^{\beta(1+r)}(1-\beta(1+r))-1}{(1-e^{\beta})^2(1+r)(1+r^{-1})} & \text{for } r<1 \\ \dfrac{e^{\beta(1+r^{-1})}(1-\beta(1+r^{-1}))-1}{(1-e^{\beta})^2(1+r)(1+r^{-1})} & \text{for } r>1 \end{cases} \tag{7.3.5}$$

where we have defined

$$r \equiv \frac{c_+}{c_-} = \exp\left\{-\frac{48\pi^2\chi_{ij}}{g_a Q_a g_b |Q_b|}\right\} \quad \text{and} \quad \beta \equiv \alpha(q^2 - q_0^2).$$

Note that under $\chi_{ij} \to -\chi_{ij}$, we have $r \to 1/r$ and the distribution is invariant implying $P(\chi_{ij}) = P(-\chi_{ij})$. The mean of χ then vanishes as a result of the vanishing of $\langle\chi_{ij}\rangle$ in agreement with the expectation outlined above. It is difficult to use $P(\chi_{ij})$ to determine the distribution of $\chi = \sum\chi_{ij}$ since the latter sum requires knowledge of which lattice sites represent states with masses below the species scale, as discussed in Section 7.2.2. This question can only be answered by considering the full lattice realization at once. Thus, determining whether a particular (pair of) lattice sites contributes to the kinetic mixing is a complicated problem that depends on the probability distributions of all other lattice sites. For this reason, we approach this problem numerically and use the above analytic distribution

[5] Of course we can label the lattice by the coordinates (Q_a, Q_b) but we use the notation χ_{ij} since it is simpler than χ_{Q_a,Q_b}. The reader can always take $Q_a^{(i,j)} = i$ and $Q_b^{(i,j)} = j$.

to compute χ in the limit where the relevant lattice sites form a dense subset of the full charge lattice.

The numerical estimate of χ is carried out by creating an ensemble of lattice realizations and estimating the kinetic mixing by summing contributions of the form shown in Equation 7.3.4. We show the $Q_b > 0$ region of a sample charge lattice in the left panel of Figure 7.2. The red and blue lattice sites correspond to states with masses below the species scale which are relevant for the estimate of kinetic mixing. The right panel of the same figure shows the distribution of χ in an ensemble of 2500 lattices. As explained above, the distribution is centered at $\chi = 0$ but we generically expect a value of the mixing of order the standard deviation which is $\sigma \sim 10^{-3}$ in this case.

We now briefly comment on the dependence of χ on parameters of the distribution in Equation 7.3.2. First, the parameter α controls how quickly the exponential rises. For larger α, states approach the extremality bound at smaller charge and are on average more massive than the corresponding states with the same charge for a lower value of α. As such, increasing α has the effect of discarding some states with large charges since these would now have masses that exceed the species scale. In turn, this decreases the value of the mixing on average and suppresses the tails of the χ distribution. We show this effect in Figure 7.3. Second, the coupling constants roughly control the eccentricity of the ellipse containing the relevant states. As such, increasing one of the couplings, say g_a, from a small value while holding the other fixed, again removes the contribution of some states with large charge and the kinetic mixing decreases. This continues until we have $g_a^2 \sim g_b^2 + \alpha^{-1}$ when the variance begins to increase again. This increase in variance can be attributed to the fact that we are limited by small numbers. For such large couplings, the lattice is populated by only a few superextremal states. Now if we make g_a large, the most common configuration for these states is to lie on the Q_a axis. The next most common

configuration is when one state has a nonzero charge Q_a. This generates a larger contribution to the kinetic mixing compared to when two states have nonzero Q_a charge, but partially cancel. As g_a gets larger, having multiple states with nonzero Q_a charge is exceedingly difficult and as a result the kinetic mixing, and its variance, both increase. We show this behavior in Figure 7.4. Finally, we note that in the regime $g_a \gg g_b$, we found that most of the states have $Q_a = 0$. In the context of the Swampland, this amounts to lifting the $U(1)_a$ WGC towers above the species bound cutoff of $U(1)_b$. This effect is ubiquitous and we will see it again in Section 7.4.1.

We now turn to a limit where we can use the analytical form of $P(\chi_{ij})$ to get an estimate of the kinetic mixing. Note that the probability distribution of $c = m/(qM_p)$ is controlled by the single parameter β. As such, in regions of the lattice where $\beta \ll 1$, we typically have a large number of light states below the species scale. By taking the limit of large α and small couplings $g_a, g_b \ll 1$ we can arrange for $\beta \ll 1$ in a region on the lattice that spans a large number of sites. In this limit, the relevant states for kinetic mixing can be approximated by a continuum inside the region $\beta \lesssim 1$. We can then calculate the variance of $\chi = \sum \chi_{ij}$ by noting that the χ_{ij} are independent variables (i.e. with a vanishing covariance). This allows us to first compute the variance of χ_{ij} and integrate the result over the ellipse defined by $\beta < 1$ to get the variance of χ. Evaluating the integral numerically, we get:

$$\langle \chi_{ij}^2 \rangle = 1.49 \times \left(\frac{g_a g_b Q_a Q_b}{48\pi^2} \right)^2 \approx \frac{3}{2} \left(\frac{g_a g_b Q_a Q_b}{48\pi^2} \right)^2 . \tag{7.3.6}$$

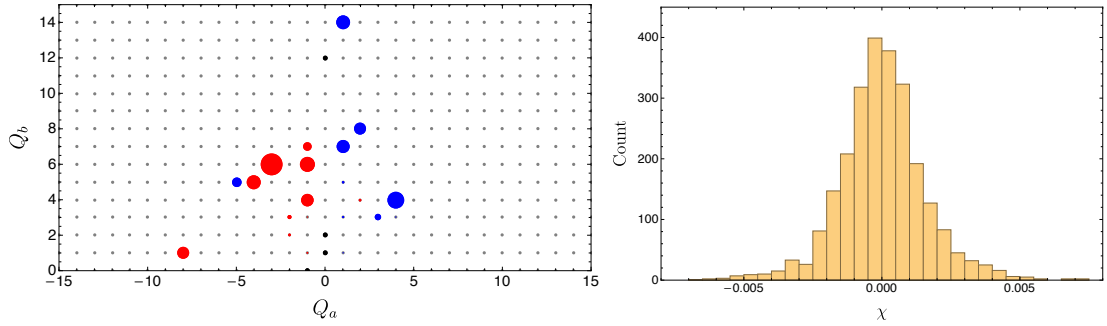

Figure 7.2: We show a sample charge lattice on the left. The relevant states are indicated by black (zero contribution), red (negative) and blue (positive) circles with the size of the circle being proportional to the magnitude. The right panel shows the distribution of kinetic mixing results. Due to our choice of PDF for the c_{ij}, we expect this distribution to be centered around $\chi_{ab} = 0$. Here we set g_a = 0.1, g_b = 0.2 and α = 6 and take $N = 2500$ lattice realizations.

Finally, summing the contributions from the $\beta < 1$ half-ellipse, we get:

$$\langle \chi^2 \rangle = \frac{(1 + \alpha(g_a^2 + g_b^2))^3}{73728\pi^3\alpha^3 g_a g_b}. \tag{7.3.7}$$

In its regime of applicability, this is a decreasing function of each of its three parameters as expected from the explanation above. For example, for $\alpha = 10^3$ and $g_a = g_b = 10^{-3}$, we get $\chi \sim 10^{-5}$. Surprisingly, this also gives a good estimate for the benchmark values of couplings and α shown in Figure 7.2.

7.4 Computing χ in Explicit Examples

In this section we consider explicit QFT and string theory examples and compute the kinetic mixing parameter in these constructions. We aim to support the above arguments based on the sLWGC by showing that generic backgrounds typically lead to mixing between Abelian gauge groups in the low-energy theory. First we consider a 5D $U(1)$ gauge theory compactified on a circle. The associated

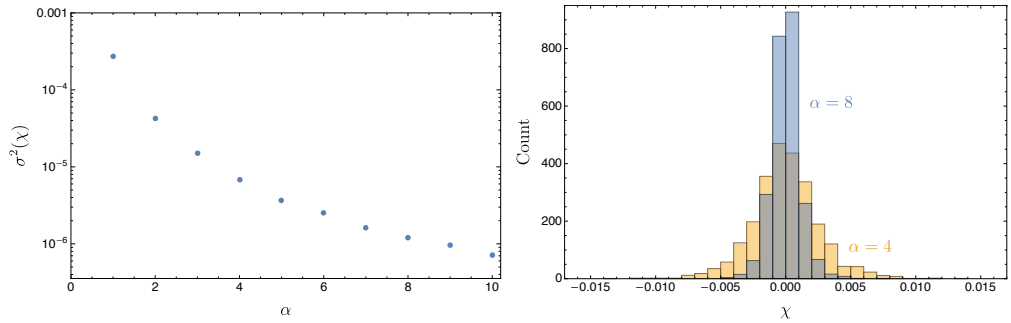

Figure 7.3: In the left panel, we show the variance as a function of α. We fix g_a = 0.1 and g_b = 0.2. We notice that as α increases, the variance decreases. In the right panel, we show the distributions for χ_{ab} for α = 4 (yellow) and α = 8 (blue) and $N = 2500$ lattice realizations.

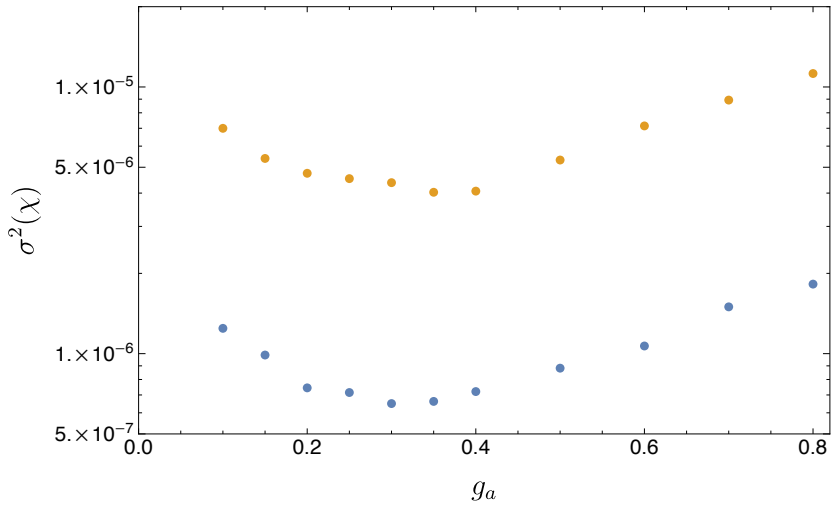

Figure 7.4: Here we show the dependence of the variance on the coupling. We fix α = 8. The blue curve shows $g_b = 0.2$ and the orange curve shows $g_b = 0.02$. We take $N = 2500$ lattice realizations.

graviphoton provides us with the second $U(1)$. We further consider scalars in this 5D theory which satisfy the LWGC. Upon compactification on S^1, we get a 4D theory with associated KK towers for each scalar that are charged under both gauge groups. These states generate kinetic mixing at 1-loop provided we turn on a background Wilson line. The next class of examples we consider are toroidal orbifold compactifications of the $E_8 \times E_8$ heterotic string. In particular, we consider the ensemble of $\mathbb{Z}_{6-\mathrm{II}}$ orbifolds of[338] and compute the kinetic mixing distribution of these 1858 MSSM-like models. Finally, we work out the kinetic mixing in Type IIB supergravity compactified on the mirror quintic manifold. Here we perform an area average over the complex structure moduli space to produce an estimate of the kinetic mixing.

7.4.1 5D $U(1)$ Example

We start with the simplest example that illustrates mixing from a lattice by considering a 5D Abelian gauge theory coupled to gravity. The LWGC implies that each site on the charge lattice Γ is populated with a state.[6] We will take these states to be represented by complex scalars φ_i of mass m_i and charge q_i. This is given by the following action:

$$S = \int d^5x\sqrt{-g}\left[\frac{1}{2\kappa_{5\mathrm{D}}^2}\mathcal{R} - \frac{1}{4e_{5\mathrm{D}}^2}F_{MN}F^{MN} - \sum_{i\in\Gamma}(D_M\varphi_i)^\dagger(D^M\varphi_i) - m_i^2|\varphi_i|^2\right]. \tag{7.4.1}$$

[6] Assuming a sublattice won't qualitatively change the results and is similar to rescaling the charges of the states by an $\mathcal{O}(1)$ number.

For the following discussion, we turn off the dilaton coupling (i.e. $\alpha = 0$ in Equation 7.2.1). For a 1-form gauge field in 5D, this implies that a state of charge q has a mass satisfying

$$\frac{2}{3} m_{5\mathrm{D}}^2 \leq e_{5\mathrm{D}}^2 q^2 M_{5\mathrm{D}}^3 \quad \rightarrow \quad m_{5\mathrm{D}}^2 \leq \frac{3}{2} e_{4\mathrm{D}}^2 q^2 M_{4\mathrm{D}}^2 \tag{7.4.2}$$

We will take each of our scalars to have a mass saturating the bound in Equation 7.4.2. This is conservative because of two effects. The first is that the contribution of states with $\pm n$ is proportional to $\log(m_+/m_-)$ and the fractional difference in the masses decreases as $m_{5\mathrm{D}}$ increases. The second effect is a reduction in the number of contributing particles since the masses of heavy states saturate the species bound for a smaller total number of states. We compactify on a circle of radius R yielding a $U(1)_{\mathrm{F}} \times U(1)_{\mathrm{KK}}$ gauge theory where $U(1)_{\mathrm{F}}$ descends from 5D with coupling $e_{4\mathrm{D}}$ in 4D and $U(1)_{\mathrm{KK}}$ arises from the graviphoton with coupling $e_{\mathrm{KK}}^2 R^2 = 16\pi G$.[7] A KK tower is generated for each scalar. Furthermore, under the assumption of genericity, there can exist a nonzero Wilson line $\theta = \int dy A^5$ along the compact direction which shifts the mass of each state. The 4D theory then contains a full lattice of states. Each lattice site is labelled by (q, n) and is populated by a state with mass given by

$$m_{4\mathrm{D}}^2 = m_{5\mathrm{D}}^2 + \frac{1}{R^2}\left(n - \frac{q\theta}{2\pi}\right)^2 \tag{7.4.3}$$

The charge under $U(1)_{\mathrm{F}}$ is denoted by q and $n \in \mathbb{Z}$ denotes the charge under $U(1)_{\mathrm{KK}}$. In addition to the scalars, the KK compactification generates a tower for the graviton as well as the photon. These

[7] The 5D and 4D gauge coupling and Planck mass M_d are related via $e_d^2 = 2\pi R e_{d-1}^2$ and $M_{d-1}^{d-3} = 2\pi R M_d^{d-2}$.

states are charged under $U(1)_{\text{KK}}$, but uncharged under $U(1)_{\text{F}}$. Their masses are given by setting $q = 0$ in Equation 7.4.3. Although these states don't contribute to the mixing, they are important because they are light states included in our effective theory which determine the species scale. We show our results in Figure 7.5. We fix the 4D gauge coupling to $e_{4\text{D}} = 10^{-3}$. This leaves the compactification radius R and the Wilson line θ as the two free parameters.

The parameter R controls the size of the extra dimension, and in turn also controls the size of e_{KK}. Increasing R decreases the KK gauge coupling. As we begin to develop a hierarchy between the two gauge couplings in our 4D theory, we also begin to lift the tower of one of our U(1)s above the species bound cutoff of the other U(1). This means that the species bound of our theory is saturated by states which are uncharged under one of the U(1) gauge groups. This can be seen in Figure 7.5, where increasing R leads to a decreased magnitude of kinetic mixing.

The parameter θ controls the breaking of an exact $\mathbb{Z}_2$ symmetry.[8] When $\theta = 0$, states with charge $(\pm q, n)$ are exactly degenerate as can be seen from Equation 7.4.3. In this limit, the contribution to the kinetic mixing, as shown in Equation 7.1.1, from both of these states exactly cancels. As we increase θ, we increase the mass splitting between these oppositely charged states. This allows for a nonzero contribution to the mixing. This is reflected in Figure 7.5, where larger values of θ correspond to an increased magnitude of kinetic mixing. We note that the mixing increases until $\theta = \pi$ and then decreases. In particular, the mixing is symmetric about $\theta = \pi$. We can consider the symmetries of our theory to better understand this behavior. The theory is invariant under $\theta \to \theta + 2\pi$ due to large

[8] This is a global symmetry which we expect to either be broken or gauged. When $\theta \neq 0 \bmod 2\pi$, it is broken. We relegate discussion of the gauged case to Section 7.5.

gauge transformations in the compact dimension. This is consistent with the fact that the mixing vanishes at $\theta = 0$ and $\theta = 2\pi$. Furthermore, parity in the fifth dimension implies that $\theta \to -\theta$ also leaves the theory invariant. Combining these two symmetries, we find that the theory is identical at $\theta = \pi \pm \alpha$, and hence the mixing contours are symmetric about $\theta = \pi$. Since our theory is endowed with an integer charge lattice, these symmetries can also be understood using GL(2,$\mathbb{Z}$) transformations. Suppose we define the generators of GL(2,$\mathbb{Z}$) as follows

$$S = \begin{pmatrix} 0 & -1 \\ 1 & 0 \end{pmatrix} \qquad T = \begin{pmatrix} 1 & -1 \\ 0 & 1 \end{pmatrix} \qquad P = \begin{pmatrix} 1 & 0 \\ 0 & -1 \end{pmatrix} \tag{7.4.4}$$

According to these definitions, $\theta \to \theta + 2\pi$ is given by $\mathcal{L}_\theta(T\vec{a}) = \mathcal{L}_{\theta+2\pi}(\vec{a})$ and $\theta \to -\theta$ is given by $\mathcal{L}_\theta(P\vec{a}) = \mathcal{L}_{-\theta}(\vec{a})$, where $\vec{a}$ is a vector containing our two gauge fields. As an example, suppose we consider our theory at $\theta_1 = \pi/2$ and $\theta_2 = 3\pi/2$. For a state with $q = 1$ under $U(1)_F$, the lightest state, given by Equation 7.4.3, corresponds to $n = 0$ for θ_1 and $n = 1$ for θ_2. We can either fix the gauge eigenbasis, in which case the lightest mass eigenstate has different charges at the two values of θ, or we can fix the charges of the lightest mass eigenstate, and redefine our gauge eigenbasis. We choose to do the latter. Performing this gauge basis change, we find that the spectrum of the theory is identical at θ_1 and θ_2 producing identical mixings, consistent with our discussion of the symmetries above.

7.4.2 Heterotic string theory on orbifolds

Kinetic mixing has been studied in the three popular settings for string phenomenology: heterotic string compactifications, brane-world scenarios for the Type II string and F-theory. The earliest inves-

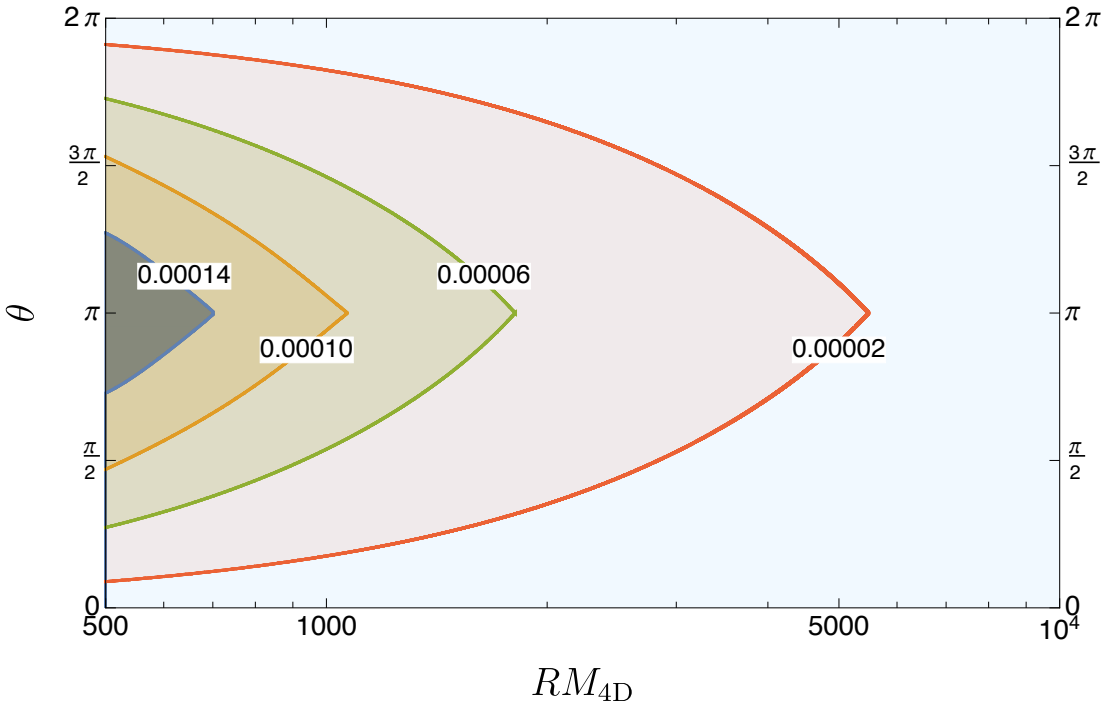

Figure 7.5: Here we show the one-loop χ generated from integrating out the KK modes of the graviton, photon and scalars as a function of the compactification radius R and the Wilson line θ. We fix $e_{4D} = 10^{-3}$. θ induces a mass splitting between oppositely charged states leading to the increase in χ_{ab} as a function of θ. The symmetries of the theory, namely parity and large gauge transformations in the compact dimension, imply that the theory is identical at $\theta = \pi \pm \alpha$. We discuss this in more detail in the text. Increasing R decreases e_{KK} which eventually lifts all states charged under both U(1)s above the species scale, thereby decreasing χ.

tigations were based on the heterotic string but later studies also found mixing in Type II constructions [18] as well as F-theory compactifications [168]. In this section, we will focus on orbifold compactifications of the heterotic string as an example where the generic expectation for kinetic mixing can be estimated. We will study the statistics of the mixing parameter in a large sample of semi-realistic heterotic orbifold models. Our aim is to compare these estimates with the phenomenological ones derived above.

In heterotic orbifolds, being exact CFT constructions, the full spectrum of states is known which allows for an explicit calculation of threshold corrections to kinetic mixing. This is similar to the computation of threshold corrections to gauge coupling constants which have been studied in [292]. The latter formalism was extended to compute kinetic mixing between the gauge bosons of two different U(1)'s in [173] and we now review the relevant details. If we take $\chi = 0$ at the string scale, then the low-energy kinetic mixing between $U(1)_a$ and $U(1)_b$ at one loop is given by:

$$\left\{\frac{\chi}{g_a g_b}\right\}(\mu) = \frac{b_{ab}}{16\pi^2}\ln\frac{M_{\rm st}^2}{\mu^2} + \frac{1}{16\pi^2}\Delta_{ab} \tag{7.4.5}$$

where $M_{\rm st}$ is the string scale. In the above expression, the first term describes the running of the mixing parameter due to the presence of light bi-charged matter and the second term gives the string threshold correction to kinetic mixing due to the presence of massive states above the string scale. We are mainly interested in estimating the magnitude of the kinetic mixing parameter and so we will focus on the value of the threshold correction Δ_{ab} and will ignore contributions of the first term. That said, the

threshold correction is computed by:

$$\Delta_{ab} = \int_F \frac{\mathrm{d}^2\tau}{\tau_2} \left(B_{ab}(\tau, \bar{\tau}) - b_{ab} \right) \tag{7.4.6}$$

where we have ignored a universal term proportional to k_{ab}, the coefficient of the $1/z^2$ pole in the OPE $J_a(z)J_b(0)$ between the $U(1)$ worldsheet currents. This is justified since we have chosen the two $U(1)$ generators to be orthogonal in the UV theory implying the vanishing of the $1/z^2$ pole in the OPE of their worldsheet currents. What remains then is an integral over the $PSL(2,\mathbb{Z})$ fundamental domain of

$$B_{ab}(\tau, \bar{\tau}) \equiv |\eta(\tau)|^{-4} \sum_{\text{even } \mathbf{s}} (-1)^{s_1+s_2} \frac{\mathrm{d}Z_\Psi(\mathbf{s}, \bar{\tau})}{2\pi i \mathrm{d}\bar{\tau}} \mathrm{Tr}_{s_1} \left(Q_a Q_b (-1)^{s_2 F} q^H \bar{q}^{\bar{H}} \right) \tag{7.4.7}$$

from which we have subtracted the contribution of the massless states, b_{ab}. In the above expression, $\eta(\tau)$ is the Dedekind eta function and $Z_\Psi(\mathbf{s}, \bar{\tau})$ is the partition function of the right-moving non-compact complex fermion with spin structure $\mathbf{s}$. The threshold correction Δ_{ab} then calculates the effect of integrating out massive string states above the string threshold.

After developing the above formalism, [173] applied it to three standard-like models [45,205,206] as an example. The kinetic mixing in all these models surprisingly vanishes but this result is not robust to *any* correction to the mass spectrum and the expectation is that kinetic mixing is still present from other low-energy effects. Subsequently, [240] investigated mixing in symmetric Abelian factorizable orbifolds arguing, along the lines of [292,175], that models with non-zero mixing are ones that have an $\mathcal{N} = 2$ subsector. For this class of models, the existence of an $\mathcal{N} = 2$ subsector requires an orbifold point

group of non-prime order so that certain twists fix one of the compact tori leaving additional unbroken SUSY charges.

We will focus on these $\mathcal{N}=2$ subsectors but briefly comment on the other sectors. The orbifold models we are considering also have $\mathcal{N}=1$ (e.g. the first twisted sector) and $\mathcal{N}=4$ (the untwisted sector) subsectors but these do not provide moduli-dependent contributions to the kinetic mixing and can be ignored for our purposes as we now briefly explain. We begin by considering the untwisted sector. In this sector it is easy to see that the spin structure dependent part of B_{ab} becomes:

$$\sum_{\text{even } \mathbf{s}} (-1)^{s_1+s_2} \frac{\mathrm{d}Z_\Psi}{\mathrm{d}\bar{\tau}} \times Z_\Psi^3 = \frac{1}{4}\frac{\mathrm{d}}{\mathrm{d}\bar{\tau}} \sum_{\text{even } \mathbf{s}} (-1)^{s_1+s_2} Z_\Psi^4, \tag{7.4.8}$$

which vanishes due to Jacobi's abstruse identity. Turning to the $\mathcal{N}=1$ subsectors it is easy to see that any contribution they provide cannot depend on the Kähler and complex structure moduli T_i and U_i describing the compact torus since such states reside at fixed points and cannot probe the torus geometry. Any contribution to Δ_{ab} must then be an additive constant. However, since the contribution from the $\mathcal{N}=2$ sector is moduli dependent and we will choose rough $\mathcal{O}(1)$ numbers for these moduli, computing the $\mathcal{N}=1$ contributions is of little value for our estimate.[9]

The focus is then on $\mathcal{N}=2$ subsectors which are twisted sectors whose twist fixes one of the three directions of the compact torus. String states in these sectors are not localized along the fixed direction and can probe the torus geometry allowing for dependence of the threshold correction on the torus moduli. The form of the moduli dependence was first calculated in [292,175] for threshold corrections

[9] For a more accurate calculation, one could average over moduli space and produce an area weighted probability distribution but we leave this for future work.

to gauge couplings and then adapted to the kinetic mixing scenario in [240]. The exact dependence will not be important for our estimates. Instead, with $\mathcal{O}(1)$ values for the moduli vevs, we have:

$$\Delta_{ab} = \mathcal{O}(1) \times \sum_i \frac{b^i_{ab}|G^i|}{16\pi^2|G|} \tag{7.4.9}$$

where b^i_{ab} is evaluated from the massless states in the $\mathcal{N} = 2$ subsector that fixes the i-th torus, $|G|$ is the order of the orbifold group and $|G^i|$ is the order of its subgroup fixing the i-th torus.

Using this expression for the mixing, we evaluate $\chi/g_a g_b$ for models from the mini-Landscape [338] which contains a large number of inequivalent heterotic orbifold models. The results are shown in Figure 7.6. This is similar to what we saw in our phenomenological estimate: the distribution again has zero mean and a variance that is comparable in magnitude to the distributions of Section 7.3. This gives us confidence that the phenomenological estimate carried out above reproduces the generic expectation in the string Landscape. In addition, it shows that modeling the superextremal states is sufficient for our estimate given the agreement with the string computation which takes into account all charged states.

7.4.3 Type II on a Calabi-Yau Manifold

In the previous section we considered models based on the heterotic string on orbifolds (CFT constructions) but we can also estimate the mixing using supergravity, i.e. using the low energy effective description of string theory. For concreteness we will take an example based on Type IIB supergravity compactified to four dimensions on the mirror quintic where the mixing is determined in terms of the

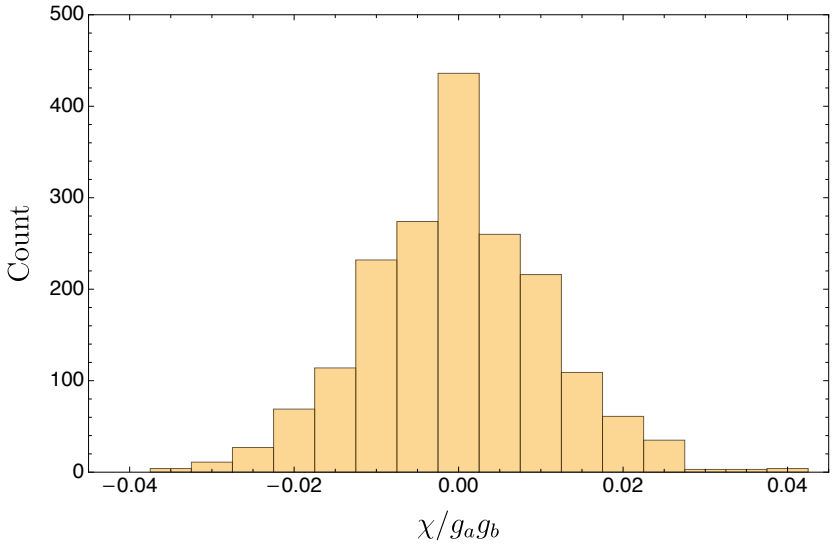

Figure 7.6: We show the distribution of the kinetic mixing coefficient in a sample of 1858 MSSM-like $\mathbb{Z}_{6-\mathrm{II}}$ orbifolds.

one-dimensional complex structure moduli space and thus receives no α' corrections. In addition, we imagine we are at a fixed point in Kähler moduli space at large volume so that the supergravity approximation is valid. The supergravity approach can be used to estimate the kinetic mixing distribution on backgrounds more general than orbifolds, such as flux compactifications (see for example [18]).

We begin by recalling the bosonic terms in the Type IIB low-energy action in Einstein frame (see for example [350]):

$$2\kappa_{10}^2 S_{10D}^{\mathrm{IIB}} = \int \mathrm{d}^{10}x\sqrt{-G}\left(R - \frac{1}{2}\partial_\mu\varphi\partial^\mu\varphi - \frac{1}{2}e^{-\varphi}|H_3|^2 - \frac{1}{2}e^{2\varphi}|F_1|^2 - \frac{1}{2}e^{\varphi}|F_3|^2 - \frac{1}{4}|F_5|^2\right) \tag{7.4.10}$$

where

$$H_3 = \mathrm{d}B_2, \qquad F_1 = \mathrm{d}C_0, \qquad F_3 = \mathrm{d}C_2 - C_0 \wedge H_3 \tag{7.4.11}$$

$$F_5 = \mathrm{d}(C_4 - \frac{1}{2} C_2 \wedge B_2) \equiv \mathrm{d}\tilde{C}_4 \quad \text{with} \quad F_5 = \star F_5. \tag{7.4.12}$$

Dimensional reduction of the above action on a CY threefold leads to an effective action in 4D whose field content is determined by topological data (namely Hodge numbers $h^{p,q}$) of the compact space. In particular, the RR potentials decompose into a sum over a basis of harmonic forms on the CY where the coefficients are 4D massless fields. Of relevance to the gauge kinetic function is the real symplectic basis of 3-forms (α_i, β^j) with $i = 0, \ldots, h^{2,1}$. The expansion of $\tilde{C}_4$ thus includes $2(h^{2,1}+1)$ 1-forms in 4D (i.e. gauge potentials which are the coefficients of (α_i, β_j)). However, the self-duality condition imposed on F_5 halves the number of 4D gauge fields. In total we therefore get $h^{2,1}+1$ gauge fields, one of which resides in the 4D $\mathcal{N}=2$ gravity multiplet and the remaining $h^{2,1}$ are part of the vector multiplets. In 4D, the terms relevant for our study of these gauge potentials are given by:

$$S_{4D}^{\mathrm{IIB}} \supset \int \mathrm{d}^4x \sqrt{-g} \left(\frac{1}{8\pi} \mathrm{Im}\mathcal{M}_{ij} F^i_{\mu\nu} F^{j\mu\nu} + \frac{1}{8\pi} \mathrm{Re}\mathcal{M}_{ij} F^i_{\mu\nu} \tilde{F}^{j\mu\nu} \right) \tag{7.4.13}$$

where the gauge kinetic function can be derived from the periods of the holomorphic 3-form Ω on

the CY and depends on the complex structure parameters. Explicitly, we have:

$$z^i = \int_{\text{CY}} \Omega \wedge \beta^i, \qquad \mathcal{G}_i = \int_{\text{CY}} \Omega \wedge \alpha_i, \tag{7.4.14}$$

$$\mathcal{M}_{ij} = \overline{\mathcal{G}}_{ij} + 2i \frac{\text{Im}\mathcal{G}_{im} z^m \text{Im}\mathcal{G}_{jn} z^n}{\text{Im}\mathcal{G}_{kl} z^k z^l} \tag{7.4.15}$$

where $\mathcal{G}_{ij} \equiv \partial_{z^i} \mathcal{G}_j$, recalling that the periods are not independent and that one may regard $\mathcal{G}_i(z)$ as functions of z^i which are homogeneous coordinates on the complex structure moduli space. More details on the effective theory of Type II supergravity can be found in [246].

As an example CY_3, we consider the mirror of the quintic hypersurface in $\mathbb{CP}^4$ which has $h^{2,1} = 1$ and is thus characterized by a single complex structure parameter we call ψ. The periods and the geometry of the moduli space have been studied long ago in [115] and the results can be expressed analytically in terms of hypergeometric functions. These periods can be used to determine the mixing between the two photons in the 4D theory according to the gauge kinetic function described above - the two photons being the graviphoton and the additional one in the vector multiplet. We show the metric and the kinetic mixing in the ψ-plane in the left panel of Figure 7.7.

At this point, it is necessary to make a few comments. First, the choice of basis 3-forms (α_i, β^j) is not unique and any other basis related to the one chosen by a symplectic transformation is equally valid. In the 4D theory, this corresponds to a choice of electric-magnetic duality frame. While all these choices are physically equivalent, they do not always allow for a weakly coupled description and one must be careful when extracting information about kinetic mixing. In addition, the kinetic mixing, like the couplings, depends on the choice of duality frame but one ideally wants a basis-independent

prediction for the mixing. In order to deal with these issues, we adopt a specific basis choice given by placing all $\mathcal{M}_{ij}$ matrices in the so-called genus 2 Siegel's fundamental domain[10]. We describe Siegel's fundamental domain and the procedure we follow in Appendix E.2. Despite these duality transformations, there remain parts of moduli space (colored gray in Figure 7.7), where there is no weakly coupled description and we excise this region before carrying out our statistical estimate. Finally, since the $\text{Arg}[\psi] = \{0, 2\pi/5\}$ rays are identified, we see a monodromy effect like that discussed in Section 7.4.1.

In order to estimate the generic expectation for kinetic mixing, we calculate an area weighted distribution using the metric and $\mathcal{M}_{ij}(\psi)$ on the ψ-plane taking:

$$P(\chi)\mathrm{d}\chi \propto \mathrm{d}A(\chi,\chi+\mathrm{d}\chi) \tag{7.4.16}$$

where $\mathrm{d}A(\chi,\chi+\mathrm{d}\chi)$ is the area on the ψ-plane with χ values in the range $(\chi,\chi+\mathrm{d}\chi)$. The resulting distribution is shown in the right panel of Figure 7.7. We find that the distribution's variance is 6×10^{-3} which is in rough agreement with the phenomenological, orbifold, and KK estimates. One might worry whether contributions to $P(\chi)$ from regions of large $|\psi|$ diverge or skew the distribution making our estimate unreliable. However, it is easy to check that the large $|\psi|$ region only contributes to $\chi < \chi_{\text{max}} = \sqrt{3}\pi/5\log|\psi|$. As χ_{max} is a decreasing function of $|\psi|$, one can conclude that the variance does not diverge. In addition, the contribution to $P(\chi)$ close to $\chi \approx 0$ is proportional to $\log(\sqrt{3}\pi/5\chi)$ which changes the variance negligibly since it has to be integrated against χ or χ^2. We also check this numerically by ensuring that our estimate is stable against removing points from our

[10] Technically, we work with $\mathcal{M}^*_{ij}$ since this has positive definite imaginary part but this distinction does not affect the results.

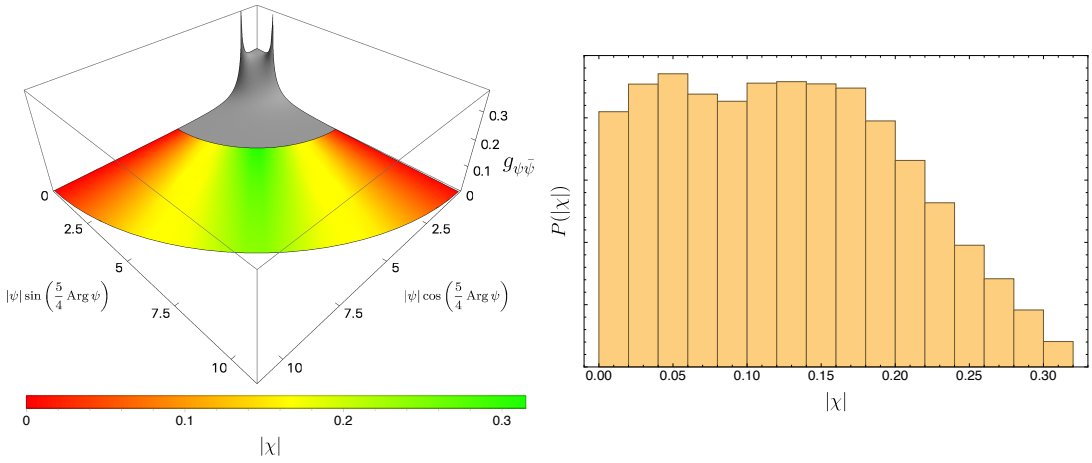

Figure 7.7: We show the moduli space metric $g_{\psi\bar{\psi}}$ as a function of the complex parameter ψ in the range $0 \leq \mathrm{Arg}[\psi] < 2\pi/5$. The color coding corresponds to the size of the kinetic mixing coefficient at that point.

sample. This then provides an example where the χ distribution has a nonzero mean and shows that the phenomenology of kinetic mixing could be much richer than one might expect from the simplest estimates of the previous sections.

7.5 Loopholes

In this section we review potential loopholes that could obstruct the above genericity arguments and lead to vanishing kinetic mixing between low energy $U(1)$'s. These loopholes typically correspond to finely tuned regions of parameter space and/or enjoy an enhanced symmetry.

- **Non-Abelian unification:** The simplest loophole to the above genericity arguments is the presence of a symmetry between charged particles running in the loop that leads to cancellations when evaluating the total kinetic mixing from all available species. These symmetries are easy to come by since one can consider, for instance, a non-Abelian $SU(N)$ gauge group that is Higgsed down to a product of $U(1)$ factors by going on the Coulomb branch. Since the generators of $SU(N)$ are traceless, each $SU(N)$ representation decomposes into $U(1)$ representations where particles have charges with a vanishing sum under each $U(1)$. It is then easy to see that

kinetic mixing from such a spectrum would vanish (e.g. by considering all the particles with charge q_* under the first $U(1)$). In this scenario, however, Higgs insertions can still allow for a kinetic mixing effect (albeit a mass suppressed one). Estimates of this effect have been carried out in the context of GUT models (see for example [226] for a recent discussion).

- **Charge conjugation in the dark sector:** This is similar to the unification scenario discussed above and implements a symmetry in the spectrum that leads to cancellations preventing loop corrections from generating kinetic mixing. We saw this explicitly in the example in Section 7.4.1, where $\theta = 0$ corresponds precisely to the case where the 4D particle spectrum has a charge conjugation symmetry. Alternatively, one can note that the operator $F^{(a)}_{\mu\nu} F^{(b)\mu\nu}$ is not invariant under separate charge conjugations and is thus forbidden if the symmetry is left intact. In a theory of quantum gravity, this charge conjugation must be a discrete gauge symmetry such as the one obtained by Higgsing $SO(3)$ with a Higgs in the 5-dimensional irreducible representation to $U(1) \rtimes \mathbb{Z}_2 \simeq O(2)$. We see then that in a theory with strict $U(1)$ (rather than $O(2)$) gauge groups, this charge conjugation is absent. In addition, in cases where it is present, there are additional physical effects that could potentially distinguish the two gauge groups such as 'Alice' strings.

- **Fine-tuned loci in moduli space:** In theories with supersymmetry, there could be a moduli space of vacua parametrized by the vev of scalar fields. In these cases, it might be possible to tune the moduli to a value that leads to vanishing kinetic mixing. However, such loci are typically lower dimensional submanifolds of the moduli space and would thus be missed by generic field vevs. An example is an $\mathcal{N} = 2$ $SU(N)$ gauge theory where one can give a vev to the scalar in the vector multiplet to Higgs $SU(N) \to U(1)^{N-1}$. The low-energy Lagrangian then contains a gauge coupling matrix that depends on the particular vev configuration; $\mathcal{L} \supset \int d^2\theta \tau^{ij}(\varphi) W_i W_j$. However, the mixing in the case would vanish only on a lower dimensional subspace of the full moduli space and is non-zero at a generic point.

- **Prime orbifolds:** This scenario is similar to the previous case since orbifolds are special points in moduli space. In particular, prime orbifolds provide many examples where kinetic mixing vanishes. In this case, generic points on moduli space describe orbifolds where the singularities have been blown up by giving vevs to twisted moduli. This alters the spectrum of states and is expected to generate kinetic mixing. In addition, these prime orbifold examples typically include massless bi-charged matter which must be lifted for the model to become phenomenologically viable. Giving these states mass would again generically induce a kinetic mixing signal.

- **Braneworld Scenarios:** In this case, the two $U(1)$ gauge groups can be localized on separate branes and the kinetic mixing between them could be exponentially suppressed if it relies only on the overlap between the two wavefunctions localized on each brane. In the presence of light bi-charged bulk modes, kinetic mixing can still be appreciable. An example is considered in [18], where a bulk $B_{\mu\nu}$ field mediates the interaction and leads to a wide range of values for the mixing parameter depending on the relation between the B-field mass and the radius of the extra dimension. In string theory, it might not be possible to engineer exponentially sequestered sectors (e.g. [286,83,255]) as in phenomenological RS setups and as such these light modes may always be present in quantum gravity constructions.
- **Large lattice index:** It has been shown that the lattice WGC does not hold in full generality but that a sublattice version holds in all known examples. If the index of the sublattice could be made arbitrarily large then the kinetic mixing signal estimated here could be suppressed. However, it is believed that there is a universal upper bound on the index and indeed in all known examples, it is an $\mathcal{O}(1)$ number.

7.6 Conclusion and Outlook

String theory provides a natural framework for exploring generic expectations at low energies since it provides us with a large number of consistent vacua. It is important to quantify these expectations by studying Landscape constructions, however these constructions tend to be limited to highly symmetric scenarios and can sometimes lead to biased results. A complementary approach is to appeal to a feature believed to hold in quantum gravity generally and directly derive estimates from it. In this work, we performed such an estimate by considering the connection between the WGC and kinetic mixing. Ideally, both approaches should give comparable results and we verify this by also computing the kinetic mixing in a large number of heterotic orbifolds and Type IIB supergravity on a Calabi-Yau

manifold.

In this work, we focused on the massless dark photon, but our results are equally applicable to the case of massive light $U(1)$ gauge bosons as well. We generically expect the WGC to apply to light gauge bosons. In particular, since these bosons get masses from either Higgsing or the Stueckelberg mechanism, there is some UV scale where they are effectively massless. Above this scale, the theory contains a massless dark photon and the analysis we carried out holds. To connect these results to experiment, we require knowledge of the dynamics governing the mass generation mechanism, which are model-dependent, but calculable.

A clear future direction that would allow for further explorations of this type is to better understand the distribution of massive states. On the one hand, some of these states could reside in the dark sector of our universe. Alternatively, they could contribute threshold effects to the low energy theory when integrated out. For instance, in the example of kinetic mixing we consider here, we saw that there is a minimum variance to kinetic mixing as a function of the gauge coupling. It would be interesting to see if this effect is verified in more rigorous constructions or seen using mass distributions derived from string theory. Genericity studies of this type could also help in isolating a few 'loophole' scenarios for focused exploration if experiment happens to rule out all generic expectations.

A

Appendices to Chapter 2

A.1 Angular Momentum Basis Conversions

The potentials we are looking at are spherically symmetric potentials. For the case of scalar and vector interactions, the following decomposition is unnecessary, but for the potentials generated by pseudoscalar and axial vector interactions, we have to evaluate the matrix elements of operators such as $S_1 \cdot S_2$ and $3(S_1 \cdot \hat{r})(S_2 \cdot \hat{r}) - S_1 \cdot S_2$. These operators can change spin and orbital angular momentum

but, due to the overall spherical symmetry, won't change total angular momentum J^2 or J_z. So, we can consider our states to be labeled by the eigenvalues of J^2, L^2, S^2, and J_z and look at the decomposition of one of these states into the basis of states labelled by L^2, L_z, S^2, S_z.

Consider a state with eigenvalues $j(j+1)$ and σ for J^2 and J_z respectively. For spin-1/2 fermions the total spin can either be 0 or 1, as we saw above. The state with the spin singlet configuration looks like

$$|j,\sigma,j,0\rangle_{j,m_j,l,s} = |j,\sigma\rangle_{l,m_l} \otimes |0,0\rangle_{s,m_s} \tag{A.1.1}$$

The states with the spin triplet configurations look like

$$\begin{aligned} |j,\sigma,j+1,1\rangle_{j,m_j,l,s} =& \sqrt{\frac{(j-\sigma+1)(j-\sigma+2)}{2(j+1)(2j+3)}}|j+1,\sigma-1\rangle_{l,m_l} \otimes |1,1\rangle_{s,m_s} \\ &- \sqrt{\frac{(j-\sigma+1)(j+\sigma+1)}{(j+1)(2j+3)}}|j+1,\sigma\rangle_{l,m_l} \otimes |1,0\rangle_{s,m_s} \\ &+ \sqrt{\frac{(j+\sigma+1)(j+\sigma+2)}{2(j+1)(2j+3)}}|j+1,\sigma+1\rangle_{l,m_l} \otimes |1,-1\rangle_{s,m_s} \end{aligned} \tag{A.1.2}$$

$$\begin{aligned} |j,\sigma,j,1\rangle_{j,m_j,l,s} =& -\sqrt{\frac{(j-\sigma+1)(j+\sigma)}{2j(j+1)}}|j,\sigma-1\rangle_{l,m_l} \otimes |1,1\rangle_{s,m_s} \\ &+ \sqrt{\frac{\sigma^2}{j(j+1)}}|j,\sigma\rangle_{l,m_l} \otimes |1,0\rangle_{s,m_s} \\ &+ \sqrt{\frac{(j-\sigma)(j+\sigma+1)}{2j(j+1)}}|j,\sigma+1\rangle_{l,m_l} \otimes |1,-1\rangle_{s,m_s} \end{aligned} \tag{A.1.3}$$

$$
\begin{aligned}
|j,\sigma,j-1,1\rangle_{j,m_j,l,s} =& \sqrt{\frac{(j+\sigma-1)(j+\sigma)}{2j(2j-1)}}|j-1,\sigma-1\rangle_{l,m_l}\otimes|1,1\rangle_{s,m_s} \\
&+\sqrt{\frac{(j-\sigma)(j+\sigma)}{j(2j-1)}}|j-1,\sigma\rangle_{l,m_l}\otimes|1,0\rangle_{s,m_s} \\
&+\sqrt{\frac{(j-\sigma-1)(j-\sigma)}{2j(2j-1)}}|j-1,\sigma+1\rangle_{l,m_l}\otimes|1,-1\rangle_{s,m_s}
\end{aligned}
\tag{A.1.4}
$$

A.1.1 $\vec{S}\cdot\hat{r}$ Operator

A useful decomposition of $\vec{S}\cdot\hat{r}$ is given by

$$
\vec{S}\cdot\hat{r} = S_x\sin\theta\cos\varphi + S_y\sin\theta\sin\varphi + S_z\cos\theta = \frac{1}{2}[S_+e^{-i\varphi}\sin\theta + S_-e^{i\varphi}\sin\theta] + S_z\cos\theta \tag{A.1.5}
$$

The action of the angular operators is given by

$$
(\cos\theta)\cdot Y_\ell^m(\theta,\varphi) = \sqrt{\frac{(\ell+1+m)(\ell+1-m)}{(2\ell+1)(2\ell+3)}}Y_{\ell+1}^m(\theta,\varphi) + \sqrt{\frac{(\ell+m)(\ell-m)}{(2\ell+1)(2\ell-1)}}Y_{\ell-1}^m(\theta,\varphi) \tag{A.1.6}
$$

$$
(e^{i\varphi}\sin\theta)\cdot Y_\ell^m(\theta,\varphi) = -\sqrt{\frac{(\ell+m+2)(\ell+m+1)}{(2\ell+1)(2\ell+3)}}Y_{\ell+1}^{m+1}(\theta,\varphi) + \sqrt{\frac{(\ell-m)(\ell-m-1)}{(2\ell+1)(2\ell-1)}}Y_{\ell-1}^{m+1}(\theta,\varphi) \tag{A.1.7}
$$

$$(e^{-i\varphi}\sin\theta)\cdot Y_\ell^m(\theta,\varphi) = \sqrt{\frac{(\ell-m+2)(\ell-m+1)}{(2\ell+1)(2\ell+3)}}\,Y_{\ell+1}^{m-1}(\theta,\varphi) - \sqrt{\frac{(\ell+m)(\ell+m-1)}{(2\ell+1)(2\ell-1)}}\,Y_{\ell-1}^{m-1}(\theta,\varphi) \tag{A.1.8}$$

The action of $\mathcal{O}_T \equiv 3(\vec{S_1}\cdot\hat{r})(\vec{S_2}\cdot\hat{r}) - \vec{S_1}\cdot\vec{S_2}$ on our states is

$$\mathcal{O}_T|j,\sigma,j,0\rangle_{j,m_j,l,s} = 0 \tag{A.1.9}$$

$$\mathcal{O}_T|j,\sigma,j,1\rangle_{j,m_j,l,s} = \frac{1}{2}|j,\sigma,j,1\rangle_{j,m_j,l,s} \tag{A.1.10}$$

$$\mathcal{O}_T|j,\sigma,j+1,1\rangle_{j,m_j,l,s} = \frac{-(j+2)}{2(2j+1)}|j,\sigma,j+1,1\rangle_{j,m_j,l,s} + \frac{3\sqrt{j(j+1)}}{2(2j+1)}|j,\sigma,j-1,1\rangle_{j,m_j,l,s} \tag{A.1.11}$$

$$\mathcal{O}_T|j,\sigma,j-1,1\rangle_{j,m_j,l,s} = \frac{-(j-1)}{2(2j+1)}|j,\sigma,j-1,1\rangle_{j,m_j,l,s} + \frac{3\sqrt{j(j+1)}}{2(2j+1)}|j,\sigma,j+1,1\rangle_{j,m_j,l,s} \tag{A.1.12}$$

So we see that the states with angular momentum $j+1$ and $j-1$ mix with each under the action of the operator $\mathcal{O}_T$.

$$\mathcal{O}_T \begin{pmatrix} |j,\sigma,j+1,1\rangle_{j,m_j,l,s} \\ \\ |j,\sigma,j-1,1\rangle_{j,m_j,l,s} \end{pmatrix} = \begin{pmatrix} \frac{-(j+2)}{2(2j+1)} & \frac{3\sqrt{j(j+1)}}{2(2j+1)} \\ \\ \frac{3\sqrt{j(j+1)}}{2(2j+1)} & \frac{-(j-1)}{2(2j+1)} \end{pmatrix} \begin{pmatrix} |j,\sigma,j+1,1\rangle_{j,m_j,l,s} \\ \\ |j,\sigma,j-1,1\rangle_{j,m_j,l,s} \end{pmatrix} \tag{A.1.13}$$

A.2 Fermion/Antifermion Spin Matrices and Minus Signs

Following the conventions of[347], we have the following definitions:

$$J_z a_0^{s\dagger}|0\rangle = \pm\frac{1}{2}a_0^{s\dagger}|0\rangle \qquad J_z b_0^{s\dagger}|0\rangle = \mp\frac{1}{2}b_0^{s\dagger}|0\rangle \tag{A.2.1}$$

$$\text{Upper Sign} \quad \xi^s = \begin{pmatrix} 1 \\ \\ 0 \end{pmatrix} \qquad \text{Lower Sign} \quad \xi^s = \begin{pmatrix} 0 \\ \\ 1 \end{pmatrix} \tag{A.2.2}$$

This means that for a particle, we have

$$\xi^{s\dagger}\sigma_z\xi^{s'} = \pm\xi^{s\dagger}\xi^{s'} = \pm\delta^{ss'} \tag{A.2.3}$$

and for an antiparticle, we have

$$\xi^{s\dagger}\sigma_z\xi^{s'} = \mp\xi^{s\dagger}\xi^{s'} = \mp\delta^{ss'} \tag{A.2.4}$$

More generically, let's identify $\eta = \varepsilon\xi^*_{\bar{\chi}}$. ε is the antisymmetric tensor and σ satisfies the relation: $\sigma^i\varepsilon = -\varepsilon(\sigma^i)^*$.

$$\eta^\dagger\vec{\sigma}\eta = (\varepsilon\xi^*_{\bar{\chi}})^\dagger\vec{\sigma}(\varepsilon\xi^*_{\bar{\chi}}) = \xi^T_{\bar{\chi}}\varepsilon\vec{\sigma}\varepsilon\xi^*_{\bar{\chi}} = \xi^T_{\bar{\chi}}(-\vec{\sigma}^*)\xi^*_{\bar{\chi}} \tag{A.2.5}$$

Now this is a scalar quantity so we are free to transpose it and this gives us $-\xi^\dagger_{\bar{\chi}}\vec{\sigma}\xi_{\bar{\chi}}$, where this $\vec{\sigma}$ gets identified with the spin matrix $\vec{S}$. From this, we see that the minus sign naturally arises when looking at $\eta^\dagger\vec{\sigma}\eta$ for any generic state, and not just the z eigenstates.

A.3 Feynman Diagrammatic Argument for Sommerfeld Enhancement

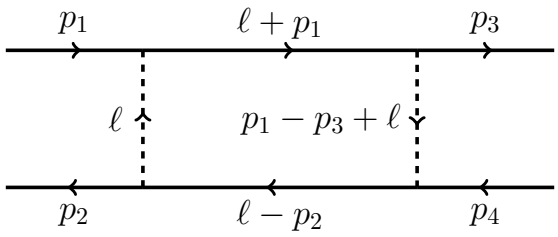

Figure A.1: The box diagram corresponds to the first diagram in the infinite set of ladder diagrams being resummed by our procedure. Sommerfeld enhancement arises when this diagram gives a contribution that is comparable to or larger than the tree level contribution to the scattering process.

There are a few lines of evidence supporting our claim that Sommerfeld enhancement is absent in the pseudoscalar case. We can show this analytically by computing the box diagram in Figure $A.1$. The general amplitude for this diagram is given by

$$\mathcal{M}_{1-\text{loop}} \sim g^4 \int \frac{\mathrm{d}^4 l}{(2\pi)^4} \frac{\mathcal{N}}{[(p_1+l)^2 - m_\chi^2][(l-p_2)^2 - m_\chi^2][l^2 - m_\varphi^2][(p_1 - p_3 + l)^2 - m_\varphi^2]} \tag{A.3.1}$$

where the numerator $\mathcal{N}$ is

$$\mathcal{N} = \overline{u}(p_3)\left(\Gamma(\not{p}_1 + \not{l} + m_\chi)\Gamma\right)u(p_1) \times \overline{v}(p_2)\left(\Gamma(\not{l} - \not{p}_2 + m_\chi)\Gamma\right)v(p_4) \tag{A.3.2}$$

The Γ matrices represent the matrix structure arising from the vertices. We will focus on two cases: the Yukawa interaction, where Γ is the identity matrix, and the pseudoscalar case, where $\Gamma = \gamma^5$.

On the equations of motion, for the pseudoscalar case, the numerator simplifies to

$$\overline{u}(p_3)\not{l}u(p_1)\overline{v}(p_2)\not{l}v(p_4). \tag{A.3.3}$$

We introduce Feynman parameters and perform the integral over the loop momentum. Since we are interested in the nonrelativistic regime, we take the $v \to 0$ limit of the amplitude. This allows us to perform the integration over two of the Feynman parameters and we are left with the following expression.

$$\begin{aligned}\mathcal{M}_{1-\text{loop}} \sim &- ig^4\overline{u}(p_3)\gamma_\mu u(p_1)\overline{v}(p_2)\gamma^\mu v(p_4)\int_0^1 \mathrm{d}w\int_0^{1-w}\mathrm{d}x\frac{(1-w-x)}{32\pi^2(m_\chi^2(w-x)^2+m_\varphi^2(1-w-x))}\\ &+ ig^4\overline{u}(p_3)u(p_1)\overline{v}(p_2)v(p_4)\int_0^1 \mathrm{d}w\int_0^{1-w}\mathrm{d}x\frac{m_\chi^2(w-x)^2(1-w-x)}{16\pi^2(m_\chi^2(w-x)^2+m_\varphi^2(1-w-x))^2}.\end{aligned} \tag{A.3.4}$$

In the nonrelativistic limit, the leading term from the γ matrices comes from the γ^0. We also define

$\xi = m_\chi^2/m_\varphi^2$. This allows us to combine the two terms into

$$\mathcal{M}_{1-\text{loop}} \sim \frac{ig^4\overline{u}(p_3)u(p_1)\overline{v}(p_2)v(p_4)}{32\pi^2 m_\varphi^2}\int_0^1 \mathrm{d}w \int_0^{1-w} \mathrm{d}x \frac{\xi(w-x)^2(1-w-x)-(1-w-x)^2}{(\xi(w-x)^2+(1-w-x))^2}. \tag{A.3.5}$$

This integral can be computed analytically and we obtain the following result

$$\begin{aligned}\frac{1}{2\xi^2\sqrt{-1+4\xi}}\Bigg((2-6\xi)\arctan\Big[\frac{1}{\sqrt{-1+4\xi}}\Big]+(-2+6\xi)\arctan\Big[\frac{1-2\xi}{\sqrt{-1+4\xi}}\Big]+\\ \sqrt{-1+4\xi}(2\xi+\log\xi-\xi\log\xi)\Bigg).\end{aligned} \tag{A.3.6}$$

A series expansion around large ξ yields

$$\frac{1}{2}\left(\frac{2-\log\xi}{\xi}-\frac{3}{2}\pi\Big(\frac{1}{\xi}\Big)^{3/2}+\frac{3+2\log\xi}{2\xi^2}+\mathcal{O}\Big(\frac{1}{\xi}\Big)^{5/2}\right). \tag{A.3.7}$$

The box diagram then gives a contribution to the matrix element scaling as

$$\mathcal{M}_{1-\text{loop}} \sim \frac{g^4}{32\pi^2}\log\frac{m_\chi^2}{m_\varphi^2}. \tag{A.3.8}$$

This should be compared with the tree-level amplitude, which scales as $\mathcal{M}_{\text{tree}} \sim g^2$. Note that although the t-channel contribution to the tree-level amplitude is momentum suppressed in the nonrelativistic limit, the s-channel contribution is not. Hence $\mathcal{M}_{1-\text{loop}}/\mathcal{M}_{\text{tree}}$ is on the order of a naive, log-enhanced loop factor, and nonrelativistic effects do not enhance the cross section predicted by perturbative QFT.

By contrast, for the scalar case, we expect to find a Sommerfeld enhancement. The numerator simplifies to[1]

$$\mathcal{N} = \overline{u}(p_3)(\not{l} + 2m_\chi)u(p_1)\overline{v}(p_2)(\not{l} + 2m_\chi)v(p_4). \tag{A.3.9}$$

Computing the integral over Feynman parameters analytically for the scalar case yields

$$\begin{aligned} -\frac{1}{2\xi^2\sqrt{-1+4\xi}}\Bigg(&(-2+6\xi-32\xi^3)\arctan\left[\frac{1}{\sqrt{-1+4\xi}}\right]+ \\ &(2-6\xi+32\xi^3)\arctan\left[\frac{1-2\xi}{\sqrt{-1+4\xi}}\right]+\sqrt{-1+4\xi}(-2\xi-\log\xi+\xi\log\xi)\Bigg). \end{aligned} \tag{A.3.10}$$

For large ξ, this behaves like $4\pi\sqrt{\xi}$. This means that the Sommerfeld enhancement can be important for low mediator masses, when

$$\frac{\mathcal{M}_{1-\text{loop}}}{\mathcal{M}_{\text{tree}}} \gtrsim 1 \quad \Rightarrow \quad m_\varphi \lesssim \frac{g^2 m_\chi}{4\pi}. \tag{A.3.11}$$

This is consistent with the standard claim about the regime of nonrelativistic enhancement for a Yukawa potential (e.g., [3,84]).

One can understand the origin of the enhancement as follows: the numerator of the integral scales as ξ and the denominator as ξ^2, so in most of the integration region one expects a suppressed contribution at large ξ. However, when $(w-x)^2 \sim \xi^{-1}$, the denominator takes order-one values and the

[1] In the vector case, a priori the Γ should be γ_μ, but in the nonrelativistic limit, the dominant contribution comes from γ_0. Therefore, even the vector case maps back down to the scalar case and the argument goes through in the same manner which is why we get Sommerfeld enhancement for an attractive Yukawa potential which can be generated by scalar and vector mediators.

integrand is of order ξ. This occurs only in a region of size $\xi^{-1/2}$ within the overall integration region, and accounts for an integral of size $\sqrt{\xi}$. This did not occur in the pseudoscalar case, where one can check that, precisely when the denominator becomes of order one, the numerator is suppressed as well.

B

Appendices to Chapter 3

B.1 Higher Derivative Terms and the Potential Involving Scalars

Scalars do not possess any intrinsic spin. As a result, the non-relativistic limit of the amplitude can only depend on the vector q^i. In particular, the amplitude, and hence $\tilde{V}(\vec{q})$, can be parameterized in the following manner

$$\tilde{V}(\vec{q}) = \frac{f(q^2)}{q^2 + m^2} = \sum_{n=0}^{\infty} \frac{a_n q^{2n}}{q^2 + m^2} \tag{B.1.1}$$

m is the mass of the mediator and $f(q^2)$ is a function that can be determined by the specific structure of the interactions in the QFT. We will show explicitly that the first few terms in this series are nonsingular and then generalize to the case of arbitrary n.

For concreteness, we will consider an example where $f(q^2) = a_0 + a_1 q^2 + a_2 q^4$. We find that

$$\tilde{V}(\vec{q}) = \frac{a_0 + a_1 q^2 + a_2 q^4}{q^2 + m^2} = a_2 q^2 + a_1 - a_2 m^2 + \frac{a_0 - a_1 m^2 + a_2 m^4}{q^2 + m^2} \tag{B.1.2}$$

The last term generates a Yukawa potential and the constant terms generate $\delta^3(\vec{r})$. Both of these potentials are nonsingular. The first term is nontrivial. It generates a term proportional to $\nabla^2 \delta^3(\vec{r})$. To show that the first Born approximation in Equation 3.1.5 is finite, we will evaluate the integrand

$$\nabla^2 \delta(r) r^{\ell+\ell'} = \frac{1}{r}\frac{\partial^2}{\partial r^2}\left(\delta(r) r^{\ell+\ell'+1}\right) = (\ell + \ell')(\ell + \ell' - 1)\delta(r) r^{\ell+\ell'-2} \tag{B.1.3}$$

The integral is divergent when $\ell + \ell' < 2$, but we see that the coefficient vanishes for those choices of ℓ and ℓ'. We can generalize these results to higher order q^2 terms. The expression in Equation B.1.1 can be rewritten as follows

$$\tilde{V}(\vec{q}) = \sum_{n=0}^{\infty} \frac{a_n q^{2n}}{q^2 + m^2} = \frac{\tilde{a}_{-1}}{q^2 + m^2} + \sum_{n=0}^{\infty} \tilde{a}_n q^{2n} \tag{B.1.4}$$

The q^{2n} terms generate terms in the potential proportional to $\nabla^{2n}\delta^3(\vec{r})$. Evaluating the integrand, we find

$$\nabla^{2n} \delta(r) r^{\ell+\ell'} = (\ell + \ell')(\ell + \ell' - 1) \cdots (\ell + \ell' + 1 - 2n)\delta(r) r^{\ell+\ell'-2n} \tag{B.1.5}$$

This integral is divergent for $\ell + \ell' < 2n$, which happens to be where the coefficient vanishes. Therefore, all the higher derivative terms are well-behaved and produce finite nonsingular first Born approximations.

We can construct a similar argument for the scalar-fermion case as well. Due to the fermion's spin, $q \cdot S$ exists as an additional independent operator. Therefore, the general amplitude can be parameterized as follows

$$\tilde{V}(\vec{q}) = \frac{f(q^2)(1 + \alpha q \cdot S)}{q^2 + m^2} = \sum_{n=0}^{\infty} \frac{a_n q^{2n}}{q^2 + m^2} + \frac{b_n q^{2n} q \cdot S}{q^2 + m^2} \tag{B.1.6}$$

The second set of terms in this sum generate terms proportional to $S \cdot \hat{r} \partial_r \nabla^2 \delta^3(\vec{r})$. Evaluating the integrand, and using the results of Equation B.1.5, we find

$$\begin{aligned} S \cdot \hat{r} \partial_r \nabla^{2n} \delta(r) r^{\ell+\ell'} &= S \cdot \hat{r}(\ell + \ell')(\ell + \ell' - 1) \cdots (\ell + \ell' + 1 - 2n) \partial_r \delta(r) r^{\ell+\ell'-2n} \\ &= S \cdot \hat{r}(\ell + \ell')(\ell + \ell' - 1) \cdots (\ell + \ell' + 1 - 2n)(\ell + \ell' - 2n - 1) \delta(r) r^{\ell+\ell'-2n-1} \end{aligned} \tag{B.1.7}$$

This integral is divergent for $\ell + \ell' < 2n + 1$. The coefficient vanishes for $\ell + \ell' < 2n$ as before. $\ell + \ell' = 2n$ seems problematic, but here we note that an additional operator exists for this potential. In particular, $S \cdot \hat{r}$ links states with angular momenta that differ by one unit. Therefore, $\ell + \ell'$ must be odd, but $2n$ is manifestly even, and the operator prevents the singularity from arising for this combination of states.

B.2 Evaluating the derivatives on $\delta^3(\vec{r})$

As an example, we explicitly evaluate the derivatives on the following position space potential:

$$\frac{\lambda}{m_1 m_2 \Lambda^2}(\vec{S}_1 \cdot \vec{\nabla})(\vec{S}_2 \cdot \vec{\nabla})\delta^3(\vec{r}) \tag{B.2.1}$$

We make use of the following relations

$$\delta^3(\vec{r}) = \frac{\delta(r)}{4\pi r^2}, \quad -r\delta'(r) = \delta(r), \quad r^2\delta''(r) = 2\delta(r) \tag{B.2.2}$$

In particular, we want to show that the first Born approximation in Equation 3.1.5 is finite. For clarity of notation, we will omit overall factors.

$$\int_0^a dr s_{\ell'}(kr)(\vec{S}_1 \cdot \vec{\nabla})(\vec{S}_2 \cdot \vec{\nabla})\delta^3(\vec{r}) s_\ell(kr) \approx S_1^i S_2^j \int_0^a dr \nabla_i \nabla_j \frac{\delta(r)}{r^2}(kr)^{\ell+1}(kr)^{\ell'+1} \tag{B.2.3}$$

Now we isolate and evaluate the integrand.

$$\begin{aligned}
\nabla_i \nabla_j \delta(r) r^{\ell+\ell'} &= \delta(r)\partial_i\partial_j r^{\ell+\ell'} + \partial_i r^{\ell+\ell'}\partial_j\delta(r) + \partial_j r^{\ell+\ell'}\partial_i\delta(r) + r^{\ell+\ell'}\partial_i\partial_j\delta(r) \\
&= \delta(r) r^{\ell+\ell'-2}\Big[(\ell+\ell'-1)\delta_{ij} + (3 + (\ell+\ell')(\ell+\ell'-4))\hat{r}_i\hat{r}_j\Big]
\end{aligned} \tag{B.2.4}$$

We see that the integral is divergent when $\ell + \ell' < 2$. If $\ell = \ell' = 0$, the operator simplifies to $\mathcal{O}_T$ which vanishes when sandwiched between states of $\ell = \ell' = 0$. If $\ell = 1$ or $\ell' = 1$, then the integrand also vanishes. The cancellation is nontrivial in both cases and the operator structure conspires to produce a nonsingular first Born approximation. We have checked explicitly that the other potentials in Section 3.2.2 also produce nonsingular first Born approximations.

C

Appendices to Chapter 4

C.1 Next-Order Velocity Expansion of the Annihilation Cross Section

As established, to leading order in dark matter velocity, the annihilation signal is set by the pseudoscalar coupling $\mathrm{Im}[y_{b\chi}]$ (and subdominantly by $g_{Z\chi}$), while spin-independent scattering is set by the scalar coupling $\mathrm{Re}[y_{b\chi}]$. However, we would also like to understand whether we can generate the annihilation signal at all in the limit that $y_{b\chi}$ is real. In this limit, the leading velocity independent term

vanishes, and we need to consider terms of higher order in the halo velocity v.

For this argument we will neglect the contribution of the Z portal; a $g_{Z\chi}$ consistent with spin-dependent constraints cannot generate a thermal relic annihilation cross section, as it does not have a mass resonance.[1] Thus, for hypothetically viable parameter space it is safe to assume that the Z-mediated annihilation is subdominant.

When $y_{h\chi}$ has vanishing imaginary part, the leading contribution to the spin averaged annihilation amplitude squared is

$$|\mathcal{M}|^2_{\chi\chi\to f\bar{f}} = \frac{4y_{hf}^2 y_{h\chi}^2 m_\chi^2 (m_\chi^2 - m_f^2) v^2}{(m_h^2 - 4m_\chi^2)^2 + m_h^2 \Gamma_h^2} + \mathcal{O}(v^4). \tag{C.1.1}$$

This term is suppressed by the non-relativistic speeds of dark matter, for typical values $v^2 \sim 10^{-6}$, and the magnitude of the purely real coupling is stringently constrained by direct detection. Thus, any allowed parameter space would require precise fine-tuning of the dark matter mass. However, the enhancement obtained from the $m_\chi \to m_h/2$ resonance is limited by the finite width of the Higgs, which is ~ 4 MeV in the SM [371]. Since the branching ratio of $h \to \chi\chi$ near the resonance is vanishingly small due to phase space suppression, we may take 4 MeV as a conservative bound for the Higgs width. Thus, the comparative ratio between annihilation and scattering cross sections, given in Equations 4.2.4 and 4.2.13, can be bounded by

[1] In fact, the $\mathcal{O}(v^2)$ Z-coupling term does have a mediator resonance, but enhancement is limited by the significantly larger width of the Z boson.

$$\left.\frac{\langle\sigma v\rangle_{\rm ann}}{\sigma_{SI}}\right|_{{\rm Im}[y_{h\chi}]=0} \sim \frac{6\times 10^4\ {\rm GeV}^2\ m_\chi^2}{(m_h^2-4m_\chi^2)^2+m_h^2\Gamma_h^2} < \frac{10^5\ {\rm GeV}^2\ m_\chi^2}{m_h^2\Gamma_h^2} \approx 10^9. \tag{C.1.2}$$

As the current direct detection limits bound the spin-independent scattering rate at $\leq 10^{-10}$ pb, a model without CP-violation may exhibit an annihilation cross section of at most $\mathcal{O}(0.1)$ pb. We emphasize here that these statements are specifically valid for Majorana fermion dark matter, and dark matter models with a different CP-structure could certainly achieve the required hierarchy between annihilation and scattering with sufficient tuning on this resonance.

D

Appendices to Chapter 5

D.1 Classification of QULE box diagrams

This appendix lists all possible quantum numbers of the new vectorlike fermions and complex scalars we introduced to generate $(q \cdot \ell)(\bar{u}\bar{e})$ or $(q\bar{e}) \cdot (\ell\bar{u})$ operators through a box diagram. We will make the simplifying assumption that the particles are either (anti-)fundamental or singlet under $SU(3)$ and $SU(2)$. Even with this assumption, there are infinitely many possibilities as a function of a free

parameter Y, the hypercharge of one of the particles. Two different criteria are then used to constrain the value of Y. The first is to make at least one of the particles an electrically-neutral color singlet, such that all particles can decay to Standard Model particles and the neutral particle. The second is to make at least one of particles couple to a pair of Standard Model particles, such that all particles can decay back to the Standard Model.

For every set of quantum numbers, we also check for three potentially problematic behaviors. The first is whether the particles also generate $(q\cdot\ell)(\bar{u}\bar{e})$ or $(q\bar{e})\cdot(\ell\bar{u})$ operators at tree-level, thus an electron EDM at 1-loop. The second is whether the particles generate C_S operator at tree-level, which can be more dominant than the two-loop electron EDM even after applying the suppression factors in (5.6.4). The third is whether the particles cause proton decay. Tree-level proton decay can be caused by scalar particles alone, while loop-level proton decay can happen when the fermions and scalars also generate, through a box diagram, the 4-fermion operators that lead to proton decay. However, no case in this appendix has been found where the particles cause loop-level proton decay without causing tree-level proton decay. Therefore, from this point on, "proton decay" will always refer to a tree-level process.

Finally, we note that, as discussed around Fig. 5.9, in some models a coupling of $\psi_1\psi_2$ to the Higgs boson is allowed, which can generate a 1-loop EDM. This is always true for the models in §D.1.2 and §D.1.4 below. On the other hand, the models in §D.1.1 and §D.1.3 have an intermediate state $\psi_1\psi_2$ with the quantum numbers of $\bar{\ell}u$ or ℓq, and as such do not generate 1-loop contributions to the EDM in the same way. Furthermore, because there is no possibility for Higgs couplings for either the two-fermion or two-scalar intermediate states obtained by cutting these diagrams, these models do not lead to Barr-Zee contributions. Hence, these are the models in which (unless otherwise flagged in the

tables below) we expect the 2-loop EDM generated from the QULE operator to dominate.

For clarity, we list below the quantum numbers of the scalar particle that can cause one or more of the problematic behaviors. The quantum number of scalar mediators for tree-level $(q \cdot \ell)(\bar{u}\bar{e})$ or $(q\bar{e}) \cdot (\ell\bar{u})$ were discussed in §5.6 and for proton decay were discussed in [59]. For tree-level C_S, it is equivalent to finding scalar mediators that generate $(\bar{d}q) \cdot (\bar{\ell}e)$, $(q \cdot \ell)(\bar{u}\bar{e})$, $(q\bar{e}) \cdot (\ell\bar{u})$, or $(q\bar{u}) \cdot (\ell\bar{e})$, as discussed in §5.6.1 and at the beginning of §5.6.

Quantum number of scalar	EDM at 1-loop?	Tree-level C_S?	Proton decay?
$(3, 3, -1/3)$	No	No	Yes
$(3, 2, 7/6)$	Yes	Yes	No
$(3, 2, 1/6)$	No	No	Yes
$(3, 2, -5/6)$	No	No	Yes
$(3, 1, -1/3)$	Yes	Yes	Yes
$(3, 1, -4/3)$	No	No	Yes
$(1, 2, 1/2)$	No	Yes	No
$(1, 2, -1/2)$	No	Yes	No

We also list here all possible renormalizable couplings to Standard Model particles for each quantum number pattern that appears in the box diagram. Couplings which only differ by exchanging $\varphi(\psi)$ and $\varphi^\dagger(\bar{\psi})$ are considered distinct, because in the box diagram, the hypercharge of $\varphi(\psi)$ is in general a

linear equation in the hypercharge of other particles, and choosing $\varphi(\psi)$ or $\varphi^\dagger(\bar{\psi})$ couplings will give different hypercharge value.

φ charge	coupling and Y value		coupling and Y value	
$(3,2)_Y$	$\varphi \cdot \ell\bar{u}, \varphi^\dagger q\bar{e}$	$Y = 7/6$	$\varphi \cdot \ell\bar{d}$	$Y = 1/6$
$(3,1)_Y$	$\varphi\bar{u}\bar{e}, \varphi^\dagger q \cdot \ell$	$Y = -1/3$	$\varphi\bar{d}\bar{e}$	$Y = -4/3$
$(1,2)_Y$	$\varphi \cdot q\bar{u}, \varphi^\dagger q\bar{d}, \varphi^\dagger \ell\bar{e}$	$Y = 1/2$	$\varphi \cdot q\bar{d}, \varphi \cdot \ell\bar{e}, \varphi^\dagger q\bar{u}$	$Y = -1/2$
$(1,1)_Y$	$\varphi\ell \cdot \ell$	$Y = 1$	$\varphi\bar{e}\bar{e}$	$Y = -2$
	$\varphi^\dagger \ell \cdot \ell$	$Y = -1$	$\varphi^\dagger\bar{e}\bar{e}$	$Y = 2$

ψ charge	coupling and Y value		coupling and Y value	
$(3,2)_Y$	$h \cdot \psi\bar{u}, h^\dagger\psi\bar{d}$	$Y = 1/6$	$h^\dagger\psi\bar{u}$	$Y = 7/6$
	$h \cdot \psi\bar{d}$	$Y = -5/6$	N/A	N/A
$(3,1)_Y$	$q \cdot h\bar{\psi}$	$Y = 2/3$	$h^\dagger q\bar{\psi}$	$Y = -1/3$
$(1,2)_Y$	$h \cdot \psi\bar{e}$	$Y = -3/2$	$h^\dagger\psi\bar{e}$	$Y = -1/2$
	$h \cdot \bar{\psi}\bar{e}$	$Y = 3/2$	$h^\dagger\bar{\psi}\bar{e}$	$Y = 1/2$
$(1,1)_Y$	$h^\dagger\ell\psi$	$Y = 1$	$h^\dagger\ell\bar{\psi}$	$Y = -1$

D.1.1 $(q \cdot \ell)(\bar{e}\bar{u})$

The box diagram that generates this operator is

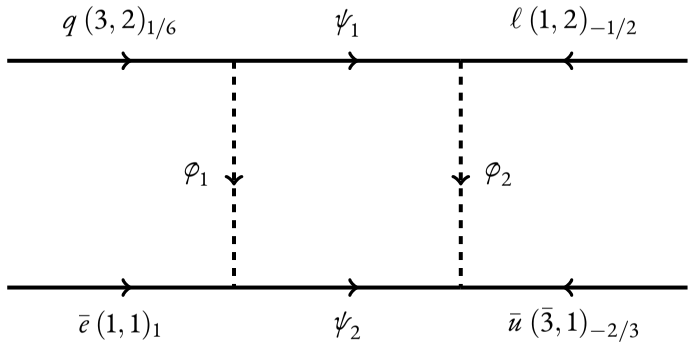

The most general quantum numbers for this diagram are:

φ_1	φ_2	ψ_1	ψ_2
$(3,2)_Y$	$(1,2)_{-1/3-Y}$	$(1,1)_{1/6-Y}$	$(3,2)_{1+Y}$
$(3,1)_Y$	$(1,1)_{-1/3-Y}$	$(1,2)_{1/6-Y}$	$(3,1)_{1+Y}$
$(1,1)_Y$	$(3,1)_{-1/3-Y}$	$(3,2)_{1/6-Y}$	$(1,1)_{1+Y}$
$(1,2)_Y$	$(3,2)_{-1/3-Y}$	$(3,1)_{1/6-Y}$	$(1,2)_{1+Y}$

D.1.1.1 Y assignment that makes at least one particle electrically-neutral and color singlet

Y	φ_1	φ_2	ψ_1	ψ_2	EDM at 1-loop?	Tree-level C_S?	Proton decay?
$1/6$	$(3,2)_{1/6}$	$(1,2)_{-1/2}$	$(1,1)_0$	$(3,2)_{7/6}$	No	Yes	Yes
$-1/3$	$(3,1)_{-1/3}$	$(1,1)_0$	$(1,2)_{1/2}$	$(3,1)_{2/3}$	Yes, $(q\cdot\ell)(\bar{u}\bar{e})$	Yes	Yes
$2/3$	$(3,1)_{2/3}$	$(1,1)_{-1}$	$(1,2)_{-1/2}$	$(3,1)_{5/3}$	No	No	No
0	$(1,1)_0$	$(3,1)_{-1/3}$	$(3,2)_{1/6}$	$(1,1)_1$	Yes, $(q\cdot\ell)(\bar{u}\bar{e})$	Yes	Yes
-1	$(1,1)_{-1}$	$(3,1)_{2/3}$	$(3,2)_{7/6}$	$(1,1)_0$	No	No	No
$1/2$	$(1,2)_{1/2}$	$(3,2)_{-5/6}$	$(3,1)_{-1/3}$	$(1,2)_{3/2}$	No	Yes	Yes
$-1/2$	$(1,2)_{-1/2}$	$(3,2)_{1/6}$	$(3,1)_{2/3}$	$(1,2)_{1/2}$	No	Yes	Yes
$-3/2$	$(1,2)_{-3/2}$	$(3,2)_{7/6}$	$(3,1)_{5/3}$	$(1,2)_{-1/2}$	Yes, $(q\bar{e})\cdot(\ell\bar{u})$	Yes	No

D.1.1.2 Y assignment that couples at least one particle to a pair of Standard Model particles

For this section, each row of the general table is given a separate table.

$(q \cdot \ell)(\bar{e}\bar{u})$ Row 1							
Y	SM coupling				EDM at 1-loop?	Tree-level C_S?	Proton decay?
	$\varphi_1\,(3,2)_Y$	$\varphi_2\,(1,2)_{-1/3-Y}$	$\psi_1\,(1,1)_{1/6-Y}$	$\psi_2\,(3,2)_{1+Y}$			
$-5/6$	N/A	$\varphi \cdot q\bar{u}, \varphi^\dagger q\bar{d}, \varphi^\dagger \ell \bar{e}$	$h^\dagger \ell \psi$	$h \cdot \psi\bar{u}, h^\dagger \psi \bar{d}$	No	Yes	Yes
$1/6$	$\varphi \cdot \ell\bar{d}$	$\varphi \cdot q\bar{d}, \varphi \cdot \ell\bar{e}, \varphi^\dagger q\bar{u}$	N/A	$h^\dagger \psi \bar{u}$	No	Yes	Yes
$7/6$	$\varphi \cdot \ell\bar{u}, \varphi^\dagger q\bar{e}$	N/A	$h^\dagger \ell \bar{\psi}$	N/A	Yes, $(q\bar{e}) \cdot (\ell\bar{u})$	Yes	No
$-11/6$	N/A	N/A	N/A	$h \cdot \psi\bar{d}$	No	No	No

$(q \cdot \ell)(\bar{e}\bar{u})$ Row 2							
Y	SM coupling				EDM at 1-loop?	Tree-level C_S?	Proton decay?
	$\varphi_1\,(3,1)_Y$	$\varphi_2\,(1,1)_{-1/3-Y}$	$\psi_1\,(1,2)_{1/6-Y}$	$\psi_2\,(3,1)_{1+Y}$			
$-1/3$	$\varphi\bar{u}\bar{e}$, $\varphi^\dagger q \cdot \ell$	N/A	$h^\dagger\bar{\psi}\bar{e}$	$q \cdot h\bar{\psi}$	Yes, $(q \cdot \ell)(\bar{u}\bar{e})$	Yes	Yes
$-4/3$	$\varphi\bar{d}\bar{e}$	$\varphi\ell \cdot \ell$	$h \cdot \bar{\psi}\bar{e}$	$h^\dagger q\bar{\psi}$	No	No	Yes
$5/3$	N/A	$\varphi\bar{e}\bar{e}$	$h \cdot \psi\bar{e}$	N/A	No	No	No
$2/3$	N/A	$\varphi^\dagger\ell \cdot \ell$	$h^\dagger\psi\bar{e}$	N/A	No	No	No
$-7/3$	N/A	$\varphi^\dagger\bar{e}\bar{e}$	N/A	N/A	No	No	No

$(q \cdot \ell)(\bar{e}\bar{u})$ Row 3							
Y	SM coupling				EDM at 1-loop?	Tree-level C_S?	Proton decay?
	$\varphi_1\,(1,1)_Y$	$\varphi_2\,(3,1)_{-1/3-Y}$	$\psi_1\,(3,2)_{1/6-Y}$	$\psi_2\,(1,1)_{1+Y}$			
1	$\varphi\ell \cdot \ell$	$\varphi\bar{d}\bar{e}$	$h \cdot \psi\bar{d}$	N/A	No	No	Yes
0	N/A	$\varphi\bar{u}\bar{e}, \varphi^\dagger q \cdot \ell$	$h \cdot \psi\bar{u}, h^\dagger\psi\bar{d}$	$h^\dagger\ell\psi$	Yes, $(q \cdot \ell)(\bar{u}\bar{e})$	Yes	Yes
-1	$\varphi^\dagger\ell \cdot \ell$	N/A	$h^\dagger\psi\bar{u}$	N/A	No	No	No
-2	$\varphi\bar{e}\bar{e}$	N/A	N/A	$h^\dagger\ell\bar{\psi}$	No	No	No
2	$\varphi^\dagger\bar{e}\bar{e}$	N/A	N/A	N/A	No	No	No

$(q \cdot \ell)(\bar{e}\bar{u})$ Row 4							
Y	SM coupling				EDM at 1-loop?	Tree-level C_S?	Proton decay?
	$\varphi_1\,(1,2)_Y$	$\varphi_2\,(3,2)_{-1/3-Y}$	$\psi_1\,(3,1)_{1/6-Y}$	$\psi_2\,(1,2)_{1+Y}$			
$1/2$	$\varphi \cdot q\bar{u}, \varphi^\dagger q\bar{d}, \varphi^\dagger \ell\bar{e}$	N/A	$h^\dagger q\bar{\psi}$	$h \cdot \bar{\psi}\bar{e}$	No	Yes	Yes
$-1/2$	$\varphi \cdot q\bar{d}, \varphi \cdot \ell\bar{e}, \varphi^\dagger q\bar{u}$	$\varphi \cdot \ell\bar{d}$	$q \cdot h\bar{\psi}$	$h^\dagger\bar{\psi}\bar{e}$A	No	Yes	Yes
$-3/2$	N/A	$\varphi \cdot \ell\bar{u}, \varphi^\dagger q\bar{e}$	N/A	$h^\dagger\psi\bar{e}$	Yes, $(q \cdot \ell)(\bar{u}\bar{e})$	Yes	No
$-5/2$	N/A	N/A	N/A	$h \cdot \psi\bar{e}$	No	No	No

D.1.2 $(q \cdot \ell)(\bar{u}\bar{e})$

$(q \cdot \ell)(\bar{u}\bar{e})$ is equivalent to $(q \cdot \ell)(\bar{e}\bar{u})$ operator in §D.1.1, except here we are considering a different diagram:

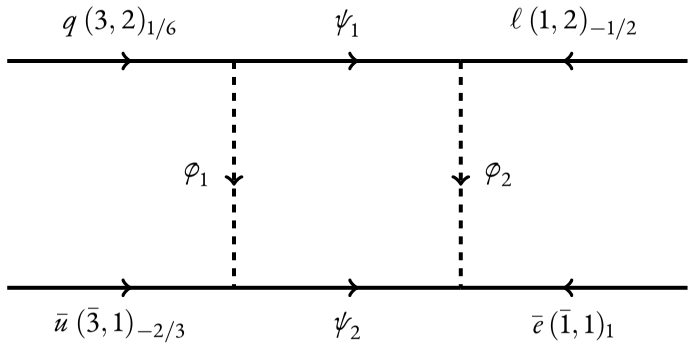

This case is somewhat less interesting, in that the quantum numbers allow for a Yukawa coupling of $\psi_1\psi_2$ to the Higgs boson and hence a 1-loop EDM. The most general quantum numbers for this diagram are:

φ_1	φ_2	ψ_1	ψ_2
$(3,2)_Y$	$(1,2)_{-1/3-Y}$	$(1,1)_{1/6-Y}$	$(1,2)_{Y-2/3}$
$(3,1)_Y$	$(1,1)_{-1/3-Y}$	$(1,2)_{1/6-Y}$	$(1,1)_{Y-2/3}$
$(1,1)_Y$	$(3,1)_{-1/3-Y}$	$(3,2)_{1/6-Y}$	$(\bar{3},1)_{Y-2/3}$
$(1,2)_Y$	$(3,2)_{-1/3-Y}$	$(3,1)_{1/6-Y}$	$(\bar{3},2)_{Y-2/3}$

D.1.2.1 Y assignment that makes at least one particle electrically-neutral and color singlet

Y	φ_1	φ_2	ψ_1	ψ_2	EDM at 1-loop?	Tree-level C_S?	Proton decay?
$1/6$	$(3,2)_{1/6}$	$(1,2)_{-1/2}$	$(1,1)_0$	$(1,2)_{-1/2}$	No	Yes	Yes
$-1/3$	$(3,1)_{-1/3}$	$(1,1)_0$	$(1,2)_{1/2}$	$(1,1)_{-1}$	Yes, $(q\cdot\ell)(\bar{u}\bar{e})$	Yes	Yes
$2/3$	$(3,1)_{2/3}$	$(1,1)_{-1}$	$(1,2)_{-1/2}$	$(1,1)_0$	No	No	No
0	$(1,1)_0$	$(3,1)_{-1/3}$	$(3,2)_{1/6}$	$(\bar{3},1)_{-2/3}$	Yes, $(q\cdot\ell)(\bar{u}\bar{e})$	Yes	Yes
$1/2$	$(1,2)_{1/2}$	$(3,2)_{-5/6}$	$(3,1)_{-1/3}$	$(\bar{3},2)_{-1/6}$	No	Yes	Yes
$-1/2$	$(1,2)_{-1/2}$	$(3,2)_{1/6}$	$(3,1)_{2/3}$	$(\bar{3},2)_{-7/6}$	No	Yes	Yes

D.1.2.2 Y assignment that couples at least one particle to a pair of Standard Model particles

For this section, each row of the general table is given a separate table.

$(q \cdot \ell)(\bar{u}\bar{e})$ Row 1							
Y	SM coupling				EDM at 1-loop?	Tree-level C_S?	Proton decay?
	$\varphi_1\,(3,2)_Y$	$\varphi_2\,(1,2)_{-1/3-Y}$	$\psi_1\,(1,1)_{1/6-Y}$	$\psi_2\,(1,2)_{Y-2/3}$			
$-5/6$	N/A	$\varphi \cdot q\bar{u}$, $\varphi^\dagger q\bar{d}$, $\varphi^\dagger \ell\bar{e}$	$h^\dagger \ell\psi$	$h \cdot \psi\bar{e}$	No	Yes	Yes
$1/6$	$\varphi \cdot \ell\bar{d}$	$\varphi \cdot q\bar{d}$, $\varphi \cdot \ell\bar{e}$, $\varphi^\dagger q\bar{u}$	N/A	$h^\dagger \psi\bar{e}$	No	Yes	Yes
$7/6$	$\varphi \cdot \ell\bar{u}$, $\varphi^\dagger q\bar{e}$	N/A	$h^\dagger \ell\bar{\psi}$	$h^\dagger \bar{\psi}\bar{e}$	Yes, $(q\bar{e}) \cdot (\ell\bar{u})$	Yes	No
$13/6$	N/A	N/A	N/A	$h \cdot \bar{\psi}\bar{e}$	No	No	No

$(q \cdot \ell)(\overline{u}\overline{e})$ Row 2							
Y	SM coupling				EDM at 1-loop?	Tree-level C_S?	Proton decay?
	$\varphi_1\,(3,1)_Y$	$\varphi_2\,(1,1)_{-1/3-Y}$	$\psi_1\,(1,2)_{1/6-Y}$	$\psi_2\,(1,1)_{Y-2/3}$			
$-4/3$	$\varphi\bar{d}\bar{e}$	$\varphi\ell \cdot \ell$	$h \cdot \bar{\psi}\bar{e}$	N/A	No	No	Yes
$-1/3$	$\varphi\overline{u}\overline{e}$, $\varphi^\dagger q \cdot \ell$	N/A	$h^\dagger\bar{\psi}\bar{e}$	$h^\dagger\ell\bar{\psi}$	Yes, $(q \cdot \ell)(\overline{u}\overline{e})$	Yes	Yes
$5/3$	N/A	$\varphi\overline{e}\overline{e}$	$h \cdot \psi\bar{e}$	$h^\dagger\ell\psi$	No	No	No
$2/3$	N/A	$\varphi^\dagger\ell \cdot \ell$	$h^\dagger\psi\bar{e}$	N/A	No	No	No
$-7/3$	N/A	$\varphi^\dagger\overline{e}\overline{e}$	N/A	N/A	No	No	No

$(q \cdot \ell)(\overline{u}\overline{e})$ Row 3							
Y	SM coupling				EDM at 1-loop?	Tree-level C_S?	Proton decay?
	$\varphi_1\,(1,1)_Y$	$\varphi_2\,(3,1)_{-1/3-Y}$	$\psi_1\,(3,2)_{1/6-Y}$	$\psi_2\,(\bar{3},1)_{Y-2/3}$			
1	$\varphi\ell \cdot \ell$	$\varphi\bar{d}\bar{e}$	$h \cdot \psi\bar{d}$	$h^\dagger q\psi$	No	No	Yes
0	N/A	$\varphi\overline{u}\overline{e}, \varphi^\dagger q \cdot \ell$	$h \cdot \psi\bar{u}, h^\dagger\psi\bar{d}$	$q \cdot h\psi$	Yes, $(q \cdot \ell)(\overline{u}\overline{e})$	Yes	Yes
-1	$\varphi^\dagger\ell \cdot \ell$	N/A	$h^\dagger\psi\bar{u}$	N/A	No	No	No
-2	$\varphi\overline{e}\overline{e}$	N/A	N/A	N/A	No	No	No
2	$\varphi^\dagger\overline{e}\overline{e}$	N/A	N/A	N/A	No	No	No

$(q \cdot \ell)(\bar{u}\bar{e})$ Row 4							
Y	SM coupling				EDM at 1-loop?	Tree-level C_S?	Proton decay?
	$\varphi_1\,(1,2)_Y$	$\varphi_2\,(3,2)_{-1/3-Y}$	$\psi_1\,(3,1)_{1/6-Y}$	$\psi_2\,(\bar{3},2)_{Y-2/3}$			
$1/2$	$\varphi \cdot q\bar{u}, \varphi^\dagger q\bar{d}, \varphi^\dagger \ell\bar{e}$	N/A	$h^\dagger q\bar{\psi}$	$h \cdot \bar{\psi}\bar{u}, h^\dagger\bar{\psi}\bar{d}$	No	Yes	Yes
$-1/2$	$\varphi \cdot q\bar{d}, \varphi \cdot \ell\bar{e}, \varphi^\dagger q\bar{u}$	$\varphi \cdot \ell\bar{d}$	$q \cdot h\bar{\psi}$	$h^\dagger\bar{\psi}\bar{u}$	No	Yes	Yes
$-3/2$	N/A	$\varphi \cdot \ell\bar{u}, \varphi^\dagger q\bar{e}$	N/A	N/A	Yes, $(q \cdot \ell)(\bar{u}\bar{e})$	Yes	No
$3/2$	N/A	N/A	N/A	$h \cdot \bar{\psi}\bar{d}$	No	No	No

D.1.3 $(q\bar{e}) \cdot (\ell\bar{u})$

The box diagram that generates this operator is

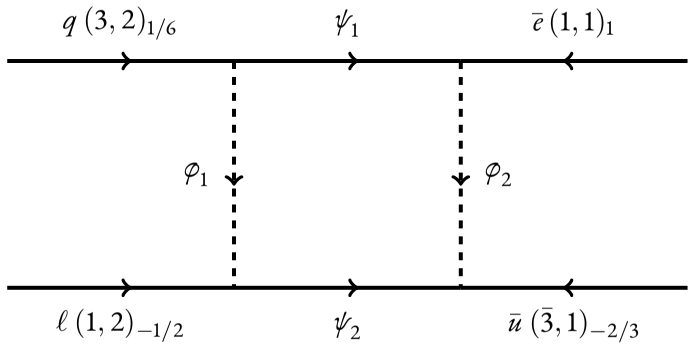

The most general quantum numbers for this diagram are:

φ_1	φ_2	ψ_1	ψ_2
$(1,1)_Y$	$(3,2)_{7/6-Y}$	$(3,2)_{1/6-Y}$	$(1,2)_{Y-1/2}$
$(1,2)_Y$	$(3,1)_{7/6-Y}$	$(3,1)_{1/6-Y}$	$(1,1)_{Y-1/2}$
$(3,2)_Y$	$(1,1)_{7/6-Y}$	$(1,1)_{1/6-Y}$	$(3,1)_{Y-1/2}$
$(3,1)_Y$	$(1,2)_{7/6-Y}$	$(1,2)_{1/6-Y}$	$(3,2)_{Y-1/2}$

D.1.3.1 Y assignment that makes at least one particle electrically-neutral and color singlet

Y	φ_1	φ_2	ψ_1	ψ_2	EDM at 1-loop?	Tree-level C_S?	Proton decay?
0	$(1,1)_0$	$(3,2)_{7/6}$	$(3,2)_{1/6}$	$(1,2)_{-1/2}$	Yes, $(q\bar{e})\cdot(\ell\bar{u})$	Yes	No
1/2	$(1,2)_{1/2}$	$(3,1)_{2/3}$	$(3,1)_{-1/3}$	$(1,1)_0$	No	Yes	No
−1/2	$(1,2)_{-1/2}$	$(3,1)_{5/3}$	$(3,1)_{2/3}$	$(1,1)_{-1}$	No	Yes	No
1/6	$(3,2)_{1/6}$	$(1,1)_1$	$(1,1)_0$	$(3,1)_{-1/3}$	No	No	No
7/6	$(3,2)_{7/6}$	$(1,1)_0$	$(1,1)_{-1}$	$(3,1)_{2/3}$	Yes, $(q\bar{e})\cdot(\ell\bar{u})$	Yes	No
−1/3	$(3,1)_{-1/3}$	$(1,2)_{3/2}$	$(1,2)_{1/2}$	$(3,2)_{-5/6}$	No	Yes	Yes
2/3	$(3,1)_{2/3}$	$(1,2)_{1/2}$	$(1,2)_{-1/2}$	$(3,2)_{1/6}$	No	Yes	No
5/3	$(3,1)_{5/3}$	$(1,2)_{-1/2}$	$(1,2)_{-3/2}$	$(3,2)_{7/6}$	No	Yes	No

D.1.3.2 Y assignment that couples at least one particle to a pair of Standard Model particles

For this section, each row of the general table is given a separate table.

$(q\bar{e}) \cdot (\ell\bar{u})$ Row 1							
Y	SM coupling				EDM at 1-loop?	Tree-level C_S?	Proton decay?
	$\varphi_1\,(1,1)_Y$	$\varphi_2\,(3,2)_{7/6-Y}$	$\psi_1\,(3,2)_{1/6-Y}$	$\psi_2\,(1,2)_{Y-1/2}$			
1	$\varphi\ell \cdot \ell$	$\varphi \cdot \ell\bar{d}$	$h \cdot \psi\bar{d}$	$h^\dagger\bar{\psi}\bar{e}$	No	No	Yes
0	N/A	$\varphi \cdot \ell\bar{u}$, $\varphi^\dagger q\bar{e}$	$h \cdot \psi\bar{u}$, $h^\dagger\psi\bar{d}$	$h^\dagger\psi\bar{e}$	Yes, $(q\bar{e}) \cdot (\ell\bar{u})$	Yes	No
-1	$\varphi^\dagger\ell \cdot \ell$	N/A	$h^\dagger\psi\bar{u}$	$h \cdot \psi\bar{e}$	No	No	No
-2	$\varphi\bar{e}\bar{e}$	N/A	N/A	N/A	No	No	No
2	$\varphi^\dagger\bar{e}e$	N/A	N/A	$h \cdot \bar{\psi}\bar{e}$	No	No	Yes

$(q\bar{e}) \cdot (\ell\bar{u})$ Row 2							
Y	SM coupling				EDM at 1-loop?	Tree-level C_S?	Proton decay?
	$\varphi_1\,(1,2)_Y$	$\varphi_2\,(3,1)_{7/6-Y}$	$\psi_1\,(3,1)_{1/6-Y}$	$\psi_2\,(1,1)_{Y-1/2}$			
$-1/2$	$\varphi \cdot q\bar{d}, \varphi \cdot \ell\bar{e}, \varphi^\dagger q\bar{u}$	N/A	$q \cdot h\bar{\psi}$	$h^\dagger \ell\bar{\psi}$	No	Yes	No
$1/2$	$\varphi \cdot q\bar{u}, \varphi^\dagger q\bar{d}, \varphi^\dagger \ell\bar{e}$	N/A	$h^\dagger q\bar{\psi}$	N/A	No	Yes	No
$3/2$	N/A	$\varphi\bar{u}\bar{e}, \varphi^\dagger q \cdot \ell$	N/A	$h^\dagger \ell\psi$	Yes, $(q \cdot \ell)(\bar{u}\bar{e})$	Yes	Yes
$5/2$	N/A	$\varphi\bar{d}\bar{e}$	N/A	N/A	No	No	Yes

$(q\bar{e}) \cdot (\ell\bar{u})$ Row 3							
Y	SM coupling				EDM at 1-loop?	Tree-level C_S?	Proton decay?
	$\varphi_1\,(3,2)_Y$	$\varphi_2\,(1,1)_{7/6-Y}$	$\psi_1\,(1,1)_{1/6-Y}$	$\psi_2\,(3,1)_{Y-1/2}$			
$1/6$	$\varphi \cdot \ell\bar{d}$	$\varphi\ell \cdot \ell$	N/A	$h^\dagger q\bar{\psi}$	No	No	Yes
$7/6$	$\varphi \cdot \ell\bar{u}, \varphi^\dagger q\bar{e}$	N/A	$h^\dagger \ell\bar{\psi}$	$q \cdot h\bar{\psi}$	Yes, $(q\bar{e}) \cdot (\ell\bar{u})$	Yes	No
$-5/6$	N/A	$\varphi^\dagger \bar{e}\bar{e}$	$h^\dagger \ell\psi$	N/A	No	No	Yes
$13/6$	N/A	$\varphi^\dagger \ell \cdot \ell$	N/A	N/A	No	No	No
$19/6$	N/A	$\varphi\bar{e}\bar{e}$	N/A	N/A	No	No	No

$(q\bar{e}) \cdot (\ell\bar{u})$ Row 4							
Y	SM coupling				EDM at 1-loop?	Tree-level C_S?	Proton decay?
	$\varphi_1\,(3,1)_Y$	$\varphi_2\,(1,2)_{7/6-Y}$	$\psi_1\,(1,2)_{1/6-Y}$	$\psi_2\,(3,2)_{Y-1/2}$			
$-1/3$	$\varphi\bar{u}\bar{e}, \varphi^\dagger q \cdot \ell$	N/A	$h^\dagger\bar{\psi}\bar{e}$	$h \cdot \psi\bar{d}$	Yes, $(q \cdot \ell)(\bar{u}\bar{e})$	Yes	Yes
$2/3$	N/A	$\varphi \cdot q\bar{u}, \varphi^\dagger q\bar{d}, \varphi^\dagger \ell\bar{e}$	$h^\dagger\psi\bar{e}$	$h \cdot \psi\bar{u}, h^\dagger\psi\bar{d}$	No	Yes	No
$-4/3$	$\varphi\bar{d}\bar{e}$	N/A	$h \cdot \bar{\psi}\bar{e}$	N/A	No	No	Yes
$5/3$	N/A	$\varphi \cdot q\bar{d}, \varphi \cdot \ell\bar{e}, \varphi^\dagger q\bar{u}$	$h \cdot \psi\bar{e}$	$h^\dagger\psi\bar{u}$	No	Yes	No

D.1.4 $(q\bar{e}) \cdot (\bar{u}\ell)$

$(q\bar{e}) \cdot (\bar{u}\ell)$ is equivalent to $(q\bar{e}) \cdot (\ell\bar{u})$ in §D.1.3, except here we are considering a different diagram:

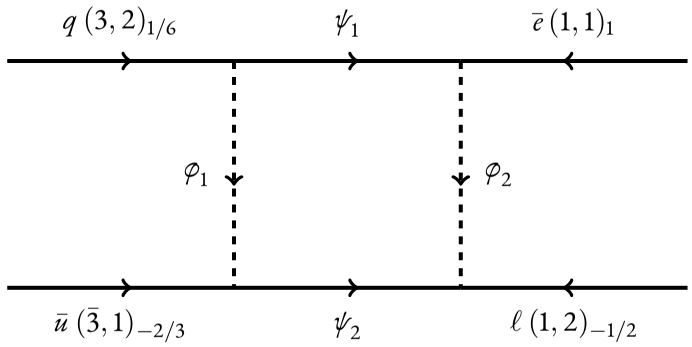

This case is somewhat less interesting, in that the quantum numbers allow for a Yukawa coupling of $\psi_1\psi_2$ to the Higgs boson and hence a 1-loop EDM. The most general quantum numbers for this diagram are:

φ_1	φ_2	ψ_1	ψ_2
$(1,1)_Y$	$(3,2)_{7/6-Y}$	$(3,2)_{1/6-Y}$	$(\bar{3},1)_{-2/3+Y}$
$(1,2)_Y$	$(3,1)_{7/6-Y}$	$(3,1)_{1/6-Y}$	$(\bar{3},2)_{-2/3+Y}$
$(3,2)_Y$	$(1,1)_{7/6-Y}$	$(1,1)_{1/6-Y}$	$(1,2)_{-2/3+Y}$
$(3,1)_Y$	$(1,2)_{7/6-Y}$	$(1,2)_{1/6-Y}$	$(1,1)_{-2/3+Y}$

D.1.4.1 Y assignment that makes at least one particle electrically-neutral and color singlet

For this section, each row of the general table is given a separate table.

Y	φ_1	φ_2	ψ_1	ψ_2	EDM at 1-loop?	Tree-level C_S?	Proton decay?
0	$(1,1)_0$	$(3,2)_{7/6}$	$(3,2)_{1/6}$	$(\bar{3},1)_{-2/3}$	Yes	Yes	No
1/2	$(1,2)_{1/2}$	$(3,1)_{2/3}$	$(3,1)_{-1/3}$	$(\bar{3},2)_{-1/6}$	No	Yes	No
−1/2	$(1,2)_{-1/2}$	$(3,1)_{5/3}$	$(3,1)_{2/3}$	$(\bar{3},2)_{-7/6}$	No	Yes	No
1/6	$(3,2)_{1/6}$	$(1,1)_1$	$(1,1)_0$	$(1,2)_{-1/2}$	No	No	No
7/6	$(3,2)_{7/6}$	$(1,1)_0$	$(1,1)_{-1}$	$(1,2)_{1/2}$	Yes, $(q\bar{e})\cdot(\ell\bar{u})$	Yes	No
−1/3	$(3,1)_{-1/3}$	$(1,2)_{3/2}$	$(1,2)_{1/2}$	$(1,1)_{-1}$	Yes, $(q\cdot\ell)(\bar{u}\bar{e})$	Yes	Yes
2/3	$(3,1)_{2/3}$	$(1,2)_{1/2}$	$(1,2)_{-1/2}$	$(1,1)_0$	No	Yes	No
5/3	$(3,1)_{5/3}$	$(1,2)_{-1/2}$	$(1,2)_{-3/2}$	$(1,1)_1$	No	Yes	No

D.1.4.2 Y assignment that couples at least one particle to a pair of Standard Model particles

$(q\bar{e}) \cdot (\bar{u}\ell)$ Row 1							
Y	SM coupling				EDM at 1-loop?	Tree-level C_S?	Proton decay?
	$\varphi_1\,(1,1)_Y$	$\varphi_2\,(3,2)_{7/6-Y}$	$\psi_1\,(3,2)_{1/6-Y}$	$\psi_2\,(\bar{3},1)_{-2/3+Y}$			
1	$\varphi\ell \cdot \ell$	$\varphi \cdot \ell\bar{d}$	$h \cdot \psi\bar{d}$	$h^\dagger q\psi$	No	No	Yes
0	N/A	$\varphi \cdot \ell\bar{u}, \varphi^\dagger q\bar{e}$	$h \cdot \psi\bar{u}, h^\dagger\psi\bar{d}$	$q \cdot h\psi$	Yes, $(q\bar{e}) \cdot (\ell\bar{u})$	Yes	No
-1	$\varphi^\dagger\ell \cdot \ell$	N/A	$h^\dagger\psi\bar{u}$	N/A	No	No	No
2	$\varphi^\dagger\overline{e}\overline{e}$	N/A	N/A	N/A	No	No	Yes
-2	$\varphi\overline{e}\overline{e}$	N/A	N/A	N/A	No	No	No

$(q\bar{e}) \cdot (\bar{u}\ell)$ Row 2							
Y	SM coupling				EDM at 1-loop?	Tree-level C_S?	Proton decay?
	$\varphi_1\,(1,2)_Y$	$\varphi_2\,(3,1)_{7/6-Y}$	$\psi_1\,(3,1)_{1/6-Y}$	$\psi_2\,(\bar{3},2)_{-2/3+Y}$			
$-1/2$	$\varphi \cdot q\bar{d}, \varphi \cdot \ell\bar{e}, \varphi^\dagger q\bar{u}$	N/A	$q \cdot h\bar{\psi}$	$h^\dagger\bar{\psi}\bar{u}$	No	Yes	No
$1/2$	$\varphi \cdot q\bar{u}, \varphi^\dagger q\bar{d}, \varphi^\dagger \ell\bar{e}$	N/A	$h^\dagger q\bar{\psi}$	$h \cdot \bar{\psi}\bar{u}, h^\dagger\bar{\psi}\bar{d}$	No	Yes	No
$3/2$	N/A	$\varphi\bar{u}\bar{e}, \varphi^\dagger q \cdot \ell$	N/A	$h \cdot \bar{\psi}\bar{d}$	Yes, $(q \cdot \ell)(\bar{u}\bar{e})$	Yes	Yes
$5/2$	N/A	$\varphi\bar{d}\bar{e}$	N/A	N/A	No	No	Yes

$(q\bar{e}) \cdot (\bar{u}\ell)$ Row 3							
Y	SM coupling				EDM at 1-loop?	Tree-level C_S?	Proton decay?
	$\varphi_1\,(3,2)_Y$	$\varphi_2\,(1,1)_{7/6-Y}$	$\psi_1\,(1,1)_{1/6-Y}$	$\psi_2\,(1,2)_{-2/3+Y}$			
$1/6$	$\varphi \cdot \ell\bar{d}$	$\varphi\ell \cdot \ell$	N/A	$h^\dagger\psi\bar{e}$	No	No	Yes
$7/6$	$\varphi \cdot \ell\bar{u}$, $\varphi^\dagger q\bar{e}$	N/A	$h^\dagger\ell\bar{\psi}$	$h^\dagger\bar{\psi}\bar{e}$	Yes, $(q\bar{e}) \cdot (\ell\bar{u})$	Yes	Yes
$-5/6$	N/A	$\varphi^\dagger\bar{e}\bar{e}$	$h^\dagger\ell\psi$	$h \cdot \psi\bar{e}$	No	No	Yes
$13/6$	N/A	$\varphi^\dagger\ell \cdot \ell$	N/A	$h \cdot \bar{\psi}\bar{e}$	No	No	No
$19/6$	N/A	$\varphi\bar{e}\bar{e}$	N/A	N/A	No	No	No

$(q\bar{e}) \cdot (\bar{u}\ell)$ Row 4							
Y	SM coupling				EDM at 1-loop?	Tree-level C_S?	Proton decay?
	$\varphi_1\,(3,1)_Y$	$\varphi_2\,(1,2)_{7/6-Y}$	$\psi_1\,(1,2)_{1/6-Y}$	$\psi_2\,(1,1)_{-2/3+Y}$			
$-1/3$	$\varphi\bar{u}\bar{e}$, $\varphi^\dagger q \cdot \ell$	N/A	$h^\dagger\bar{\psi}\bar{e}$	$h^\dagger\ell\bar{\psi}$	Yes, $(q \cdot \ell)(\bar{u}\bar{e})$	Yes	Yes
$-4/3$	$\varphi\bar{d}\bar{e}$	N/A	$h \cdot \bar{\psi}\bar{e}$	N/A	No	No	Yes
$2/3$	N/A	$\varphi \cdot q\bar{u}$, $\varphi^\dagger q\bar{d}$, $\varphi^\dagger\ell\bar{e}$	$h^\dagger\psi\bar{e}$	N/A	No	Yes	No
$5/3$	N/A	$\varphi \cdot q\bar{d}$, $\varphi \cdot \ell\bar{e}$, $\varphi^\dagger q\bar{u}$	$h \cdot \psi\bar{e}$	$h^\dagger\ell\psi$	No	Yes	No

E

Appendices to Chapter 7

E.1 Analytic Estimate of Mixing

The calculation of $\langle \chi^2 \rangle$ can be broken into a few steps. In order to compare with the string constructions, we chose a particle spectrum that included states with charges $(Q_a, \pm|Q_b|)$. This led to the contribution we see in Equation 7.3.4. The first step then is to find the distribution of $r = c_+/c_-$. In statistics, this is known as the ratio distribution. For two random variables X and Y, the distribution

of $R = X/Y$ is given by

$$P_R(R) = \int_0^\infty f_y(y) f_x(Ry) y dy \tag{E.1.1}$$

where we have made use of the fact that c_+ and c_- are independent variables so their joint PDF is just the product of their individual PDFs. To compute this ratio distribution, we have to consider the cases $r > 1$ and $r < 1$ separately. For $r < 1$, we integrate over a triangle in the $c_+ - c_-$ plane defined by $c_+ \in [0, rc_-]$ and $c_- \in [0, 1]$. Computing the integral in Equation E.1.1, we find

$$P_r(r) = \frac{1 + e^{(1+r)\beta}(-1 + \beta + r\beta)}{(1+r)^2(e^\beta - 1)^2} \qquad r < 1 \tag{E.1.2}$$

The $r > 1$ case is slightly more involved. The region we integrate over is a trapezoid. We can break this into two regions. The first is defined by $c_+ \in [0, rc_-]$ and $c_- \in [0, r^{-1}]$. The second is defined by $c_+ \in [0, 1]$ and $c_- \in [r^{-1}, 1]$. Finding the CDF and differentiating with respect to r, we find

$$P_r(r) = \frac{r + e^{\beta(1+r^{-1})}(r(\beta - 1) + \beta)}{(1+r)^2 r(e^\beta - 1)^2} \qquad r > 1 \tag{E.1.3}$$

Given the probability distribution of r, we can find the probability distribution of χ which is a function of r. Suppose we take

$$\chi = -\frac{1}{k}\log(r) \quad \rightarrow \quad r = \exp(-k\chi) \qquad k = \frac{48\pi^2}{g_a g_b Q_a Q_b} \tag{E.1.4}$$

If we take $\chi = g(r)$, then we have

$$P_\chi(\chi) = P_r\left(g^{-1}(\chi)\right)\left|\frac{d}{d\chi}g^{-1}(\chi)\right| = |k|\exp(-k\chi)\,P_r(\exp(-k\chi)) \tag{E.1.5}$$

Symmetrizing with respect to r and r^{-1}, we find the results in Equation 7.3.5. With $P_\chi(\chi)$ in hand, we can compute $\langle\chi_{ij}^2\rangle$ by evaluating

$$\langle\chi_{ij}^2\rangle = \int_{-\infty}^{\infty}\chi_{ij}^2 P(\chi_{ij})d\chi_{ij} = \int_{-\infty}^{0}\chi_{ij}^2 P(\chi_{ij})d\chi_{ij} + \int_{0}^{\infty}\chi_{ij}^2 P(\chi_{ij})d\chi_{ij} \tag{E.1.6}$$

$P_\chi(\chi)$ is piecewise defined, so we split our integral into two at $\chi = 0$, which corresponds to $r = 1$. Since $P_\chi(\chi) = P_\chi(-\chi)$ and the integrand is even, we can consider just one of these regions, which provides us the computational benefit of having to only consider $r > 1$ *or* $r < 1$. Computing this integral gives us the results in Equation 7.3.6. Finally, to compute $\langle\chi^2\rangle$, we have to integrate $\langle\chi_{ij}^2\rangle$ over the $\beta < 1$ ellipse. Since we have already taken into account states with charges $\pm|Q_b|$, we focus on the half-ellipse where $Q_b > 0$. Integrating over this region, we arrive at the results in Equation 7.3.7.

E.2 CY 3-form bases and Siegel's Fundamental Domain

We begin by recalling the symplectic basis transformations that act on the real 3-form basis of a CY manifold. For a CY manifold with Hodge number $h^{2,1}$, there are $2(h^{2,1}+1)$ 3-forms in real cohomol-

ogy that we label (α_i, β^j) with $i, j = 0, \ldots, h^{2,1}$. These have the following pairing relations:

$$\int_{\text{CY}} \alpha_i \wedge \beta^j = \delta_i^j; \qquad \int_{\text{CY}} \alpha_i \wedge \alpha_j = 0; \qquad \int_{\text{CY}} \beta^i \wedge \beta^j = 0 \tag{E.2.1}$$

which are preserved by transformations under the symplectic group $Sp(2h^{2,1} + 2; \mathbb{Z})$. For a matrix in $Sp(2h^{2,1} + 2; \mathbb{Z})$, the action on the (α_i, β^j) and the complex matrix $\mathcal{M}$ defined in 7.4.15 is given by:

$$\begin{pmatrix} \alpha \\ \\ \beta \end{pmatrix} \to \begin{pmatrix} A & B \\ \\ C & D \end{pmatrix} \cdot \begin{pmatrix} \alpha \\ \\ \beta \end{pmatrix}; \qquad \mathcal{M} \to (A\mathcal{M} + B)(C\mathcal{M} + D)^{-1}. \tag{E.2.2}$$

As briefly mentioned previously, we work with the matrix $\mathcal{M}^*$ which has the same transformation as above with the replacement $\mathcal{M} \to \mathcal{M}^*$. The matrix $\mathcal{M}^*$ takes values in Siegel's upper half space of genus (or degree) $h^{2,1} + 1$ defined to be the subset of $(h^{2,1} + 1) \times (h^{2,1} + 1)$ complex matrices that are symmetric with a positive definite imaginary part. The latter condition ensures that $\text{Im}\mathcal{M}$ is negative definite which is required for the gauge kinetic terms to have the correct sign. The symplectic action preserves these conditions. As a familiar example, one can consider the genus 1 case of Siegel's upper half space which is the well-known Teichmüller space describing the complex structure of the torus with the usual $PSL(2, \mathbb{Z})$ action.

As in the case of the upper half plane, a natural question to ask is: what is the fundamental domain of Siegel's half space under the symplectic action? It turns out that the conditions defining one such fundamental domain provide a choice of electric-magnetic duality frame that matches our needs. This

also resolves the issue related to basis-dependence. We now specialize to the case of interest, i.e. genus 2, and summarize these conditions (see for example [370,183,275] for a more detailed account) and their physical meaning.

Definition (Siegel's fundamental domain for genus 2): Let $\mathcal{M}_{ij} = X_{ij} + iY_{ij}$ be a 2×2 complex matrix that is symmetric, with Y positive definite. Then $\mathcal{M}$ is said to be in the fundamental domain if:

1. $|X_{ij}| \leq \frac{1}{2}$
2. The matrix Y has elements that satisfy $Y_{11} \geq Y_{00} \geq 2Y_{10} > 0$
3. $|\det(C\Omega + D)| \geq 1$ for matrices C and D that are submatrices of a symplectic matrix, as shown above.

Given that the real part of $\mathcal{M}$ is the coefficient of the topological terms in the 4D action, the first condition amounts to using the periodicity of the θ angles so that they are not arbitrarily large. The second condition guarantees that the first $U(1)$ has a smaller gauge coupling than the second and that the mixing is small compared to the gauge couplings. Finally, the third condition ensures that the matrix $\mathcal{M}$ gives the most weakly coupled theory, although this is harder to demonstrate without considering the details of the algorithm provided in [183].

The algorithm to reduce a matrix to Siegel's fundamental domain proceeds by repeatedly carrying out a few simple operations. The first operation is Minkowski reduction which is simply a basis change not related to electric-magnetic duality. Using integer coefficients, the fields are redefined to ensure that the two $U(1)$'s are as orthogonal as possible with gauge couplings and kinetic mixing satisfying the

second condition in the definition above. This is followed by shifting the theta angles to ensure that the real part of the matrix lies in the range $[-\frac{1}{2}, \frac{1}{2}]$. These latter transformations are the analogue of T transformations for the genus 1 case. Finally, one has to ensure that the third condition is satisfied. Naïvely, this seems to require checking an infinite number of inequalities, however Gottschling[242] showed that one only needs to verify this for a finite set of 19 matrices. Correspondingly, there is a series of 19 transformations (analogous to the S transformations of genus 1) that are carried out whenever one of Gottschling's conditions is not satisfied. This algorithm is iterated until all three conditions are simultaneously satisfied.

References

[1] Combined LEP Chargino Results, up to 208 GeV for Large m0.

[2] Combined LEP Chargino Results, up to 208 GeV for Low DM.

[3] Aaboud, M. et al. (2018). Measurement of the W-boson mass in pp collisions at $\sqrt{s} = 7$ TeV with the ATLAS detector. *Eur. Phys. J. C*, 78(2), 110. [Erratum: Eur.Phys.J.C 78, 898 (2018)].

[4] Aad, G. et al. (2012). Observation of a new particle in the search for the Standard Model Higgs boson with the ATLAS detector at the LHC. *Phys. Lett. B*, 716, 1–29.

[5] Aaij, R. et al. (2017). Test of lepton universality with $B^0 \to K^{*0}\ell^+\ell^-$ decays. *JHEP*, 08, 055.

[6] Aaij, R. et al. (2019). Search for lepton-universality violation in $B^+ \to K^+\ell^+\ell^-$ decays. *Phys. Rev. Lett.*, 122(19), 191801.

[7] Aaij, R. et al. (2022a). Measurement of the W boson mass. *JHEP*, 01, 036.

[8] Aaij, R. et al. (2022b). Test of lepton universality in beauty-quark decays. *Nature Phys.*, 18(3), 277–282.

[9] Aaltonen, T. et al. (2022). High-precision measurement of the W boson mass with the CDF II detector. *Science*, 376(6589), 170–176.

[10] Aaltonen, T. A. et al. (2013). Combination of CDF and Do W-Boson Mass Measurements. *Phys. Rev. D*, 88(5), 052018.

[11] Aaltonen, T. A. et al. (2014). Precise Measurement of the W -Boson Mass with the Collider Detector at Fermilab. *Phys. Rev. D*, 89(7), 072003.

[12] Aartsen, M. et al. (2017). Search for annihilating dark matter in the Sun with 3 years of IceCube data. *Eur. Phys. J. C*, 77(3), 146. [Erratum: Eur.Phys.J.C 79, 214 (2019)].

[13] Abazajian, K. N., Canac, N., Horiuchi, S., & Kaplinghat, M. (2014). Astrophysical and Dark Matter Interpretations of Extended Gamma-Ray Emission from the Galactic Center. *Phys. Rev. D*, 90(2), 023526.

[14] Abazajian, K. N., Horiuchi, S., Kaplinghat, M., Keeley, R. E., & Macias, O. (2020). Strong constraints on thermal relic dark matter from Fermi-LAT observations of the Galactic Center.

[15] Abe, T. (2020). The effect of the early kinetic decoupling in a fermionic dark matter model.

[16] Abe, T., Hisano, J., Kitahara, T., & Tobioka, K. (2014). Gauge invariant Barr-Zee type contributions to fermionic EDMs in the two-Higgs doublet models. *JHEP*, 01, 106. [Erratum: JHEP04,161(2016)].

[17] Abe, T., Kitano, R., & Sato, R. (2015). Discrimination of dark matter models in future experiments. *Phys. Rev. D*, 91(9), 095004. [Erratum: Phys.Rev.D 96, 019902 (2017)].

[18] Abel, S., Goodsell, M., Jaeckel, J., Khoze, V., & Ringwald, A. (2008a). Kinetic Mixing of the Photon with Hidden U(1)s in String Phenomenology. *JHEP*, 07, 124.

[19] Abel, S. A., Jaeckel, J., Khoze, V. V., & Ringwald, A. (2008b). Illuminating the Hidden Sector of String Theory by Shining Light through a Magnetic Field. *Phys. Lett. B*, 666, 66–70.

[20] Abel, S. A. & Schofield, B. W. (2004). Brane anti-brane kinetic mixing, millicharged particles and SUSY breaking. *Nucl. Phys. B*, 685, 150–170.

[21] Abi, B. et al. (2021). Measurement of the Positive Muon Anomalous Magnetic Moment to 0.46 ppm. *Phys. Rev. Lett.*, 126(14), 141801.

[22] Ade, P. A. R. et al. (2016). Planck 2015 results. XIII. Cosmological parameters. *Astron. Astrophys.*, 594, A13.

[23] Aghanim, N. et al. (2018). Planck 2018 results. VI. Cosmological parameters.

[24] Agrawal, P., Bagherian, H., Cesarotti, C., DePorzio, N., Lu, Q., Muñoz, J. B., Parikh, A., Reece, M., & Xu, W. L. (2021). The Swapland.

[25] Agrawal, P., Chacko, Z., Kilic, C., & Mishra, R. K. (2010). A Classification of Dark Matter Candidates with Primarily Spin-Dependent Interactions with Matter.

[26] Agrawal, P., Cyr-Racine, F.-Y., Randall, L., & Scholtz, J. (2017). Make Dark Matter Charged Again. *JCAP*, 05, 022.

[27] Agrawal, P., Parikh, A., & Reece, M. (2020). Systematizing the Effective Theory of Self-Interacting Dark Matter. *JHEP*, 10, 191.

[28] Aguilar, M. et al. (2016). Antiproton Flux, Antiproton-to-Proton Flux Ratio, and Properties of Elementary Particle Fluxes in Primary Cosmic Rays Measured with the Alpha Magnetic Spectrometer on the International Space Station. *Phys. Rev. Lett.*, 117(9), 091103.

[29] Ajello, M. et al. (2016). Fermi-LAT Observations of High-Energy γ-Ray Emission Toward the Galactic Center. *Astrophys. J.*, 819(1), 44.

[30] Akerib, D. et al. (2016). Results on the Spin-Dependent Scattering of Weakly Interacting Massive Particles on Nucleons from the Run 3 Data of the LUX Experiment. *Phys. Rev. Lett.*, 116(16), 161302.

[31] Akerib, D. et al. (2017). Results from a search for dark matter in the complete LUX exposure. *Phys. Rev. Lett.*, 118(2), 021303.

[32] Akerib, D. et al. (2020). Projected WIMP sensitivity of the LUX-ZEPLIN dark matter experiment. *Phys. Rev. D*, 101(5), 052002.

[33] Albahri, T. et al. (2021). Measurement of the anomalous precession frequency of the muon in the Fermilab Muon g-2 Experiment. *Phys. Rev. D*, 103(7), 072002.

[34] Alonso, R., Jenkins, E. E., Manohar, A. V., & Trott, M. (2014). Renormalization Group Evolution of the Standard Model Dimension Six Operators III: Gauge Coupling Dependence and Phenomenology. *JHEP*, 04, 159.

[35] Altmannshofer, W., Carena, M., Gori, S., & de la Puente, A. (2011). Signals of CP Violation Beyond the MSSM in Higgs and Flavor Physics. *Phys. Rev.*, D84, 095027.

[36] Altmannshofer, W., Harnik, R., & Zupan, J. (2013). Low Energy Probes of PeV Scale Sfermions. *JHEP*, 11, 202.

[37] Alwall, J., Ballestrero, A., Bartalini, P., Belov, S., Boos, E., et al. (2007). A Standard format for Les Houches event files. *Comput.Phys.Commun.*, 176, 300–304.

[38] Alwall, J., Frederix, R., Frixione, S., Hirschi, V., Maltoni, F., Mattelaer, O., Shao, H. S., Stelzer, T., Torrielli, P., & Zaro, M. (2014). The automated computation of tree-level and next-to-leading order differential cross sections, and their matching to parton shower simulations. *JHEP*, 07, 079.

[39] Alwall, J., Herquet, M., Maltoni, F., Mattelaer, O., & Stelzer, T. (2011). MadGraph 5 : Going Beyond. *JHEP*, 06, 128.

[40] Ambrogi, F. et al. (2018). SModelS v1.2: long-lived particles, combination of signal regions, and other novelties.

[41] Ambrogi, F., Kraml, S., Kulkarni, S., Laa, U., Lessa, A., Magerl, V., Sonneveld, J., Traub, M., & Waltenberger, W. (2017). SModelS v1.1 user manual.

[42] Amole, C. et al. (2017). Dark matter search results from the PICO−60 c_3f_8 bubble chamber. *Phys. Rev. Lett.*, 118, 251301.

[43] Amole, C. et al. (2019). Dark matter search results from the complete exposure of the pico-60 c_3f_8 bubble chamber. *Phys. Rev. D*, 100, 022001.

[44] Andreev, V. et al. (2018). Improved limit on the electric dipole moment of the electron. *Nature*, 562(7727), 355–360.

[45] Antoniadis, I., Leontaris, G., & Rizos, J. (1990). A Three generation SU(4) x O(4) string model. *Phys. Lett. B*, 245, 161–168.

[46] Aprile, E. et al. (2017). First Dark Matter Search Results from the XENON1T Experiment. *Phys. Rev. Lett.*, 119(18), 181301.

[47] Aprile, E. et al. (2018). Dark Matter Search Results from a One Ton-Year Exposure of XENON1T. *Phys. Rev. Lett.*, 121(11), 111302.

[48] Aprile, E. et al. (2019). Constraining the spin-dependent WIMP-nucleon cross sections with XENON1T. *Phys. Rev. Lett.*, 122(14), 141301.

[49] Aprile, E. et al. (2020). Projected WIMP Sensitivity of the XENONnT Dark Matter Experiment.

[50] Arcadi, G., Dutra, M., Ghosh, P., Lindner, M., Mambrini, Y., Pierre, M., Profumo, S., & Queiroz, F. S. (2018). The waning of the WIMP? A review of models, searches, and constraints. *Eur. Phys. J. C*, 78(3), 203.

[51] Archambault, J. P., Czarnecki, A., & Pospelov, M. (2004). Electric dipole moments of leptons in the presence of majorana neutrinos. *Phys. Rev.*, D70, 073006.

[52] Arkani-Hamed, N., Blum, K., D'Agnolo, R. T., & Fan, J. (2013). 2:1 for Naturalness at the LHC? *JHEP*, 01, 149.

[53] Arkani-Hamed, N., Cheng, H.-C., Luty, M., & Thaler, J. (2005a). Universal dynamics of spontaneous Lorentz violation and a new spin-dependent inverse-square law force. *JHEP*, 07, 029.

[54] Arkani-Hamed, N., Dimopoulos, S., Giudice, G. F., & Romanino, A. (2005b). Aspects of split supersymmetry. *Nucl. Phys.*, B709, 3–46.

[55] Arkani-Hamed, N., Finkbeiner, D. P., Slatyer, T. R., & Weiner, N. (2009). A Theory of Dark Matter. *Phys. Rev. D*, 79, 015014.

[56] Arkani-Hamed, N., Motl, L., Nicolis, A., & Vafa, C. (2007). The String landscape, black holes and gravity as the weakest force. *JHEP*, 06, 060.

[57] Arkani-Hamed, N. & Weiner, N. (2008). LHC Signals for a SuperUnified Theory of Dark Matter. *JHEP*, 12, 104.

[58] Arnold, J. M., Fornal, B., & Wise, M. B. (2013a). Phenomenology of scalar leptoquarks. *Phys. Rev.*, D88, 035009.

[59] Arnold, J. M., Fornal, B., & Wise, M. B. (2013b). Simplified models with baryon number violation but no proton decay. *Phys. Rev.*, D87, 075004.

[60] ATLAS Collaboration (2019). *Reproducing searches for new physics with the ATLAS experiment through publication of full statistical likelihoods*. Technical Report ATL-PHYS-PUB-2019-029, CERN, Geneva. https://cds.cern.ch/record/2684863.

[61] Atwood, D., Burgess, C. P., Hamazaou, C., Irwin, B., & Robinson, J. A. (1990). One loop P and T odd W+- electromagnetic moments. *Phys. Rev.*, D42, 3770–3777.

[62] Awramik, M., Czakon, M., & Freitas, A. (2006). Electroweak two-loop corrections to the effective weak mixing angle. *JHEP*, 11, 048.

[63] Awramik, M., Czakon, M., Freitas, A., & Weiglein, G. (2004). Precise prediction for the W boson mass in the standard model. *Phys. Rev. D*, 69, 053006.

[64] Baak, M., Cúth, J., Haller, J., Hoecker, A., Kogler, R., Mönig, K., Schott, M., & Stelzer, J. (2014). The global electroweak fit at NNLO and prospects for the LHC and ILC. *Eur. Phys. J. C*, 74, 3046.

[65] Baak, M., Goebel, M., Haller, J., Hoecker, A., Ludwig, D., Moenig, K., Schott, M., & Stelzer, J. (2012). Updated Status of the Global Electroweak Fit and Constraints on New Physics. *Eur. Phys. J. C*, 72, 2003.

[66] Badertscher, A., Crivelli, P., Fetscher, W., Gendotti, U., Gninenko, S., Postoev, V., Rubbia, A., Samoylenko, V., & Sillou, D. (2007). An Improved Limit on Invisible Decays of Positronium. *Phys. Rev. D*, 75, 032004.

[67] Ball, A. et al. (2016). A Letter of Intent to Install a milli-charged Particle Detector at LHC P5.

[68] Banerjee, S., Matsumoto, S., Mukaida, K., & Tsai, Y.-L. S. (2016). WIMP Dark Matter in a Well-Tempered Regime: A case study on Singlet-Doublets Fermionic WIMP. *JHEP*, 11, 070.

[69] Barbieri, R., Frigeni, M., & Giudice, G. F. (1989). Dark Matter Neutralinos in Supergravity Theories. *Nucl. Phys.*, B313, 725–735.

[70] Barbieri, R., Pomarol, A., Rattazzi, R., & Strumia, A. (2004). Electroweak symmetry breaking after LEP-1 and LEP-2. *Nucl. Phys. B*, 703, 127–146.

[71] Baron, J. et al. (2014). Order of Magnitude Smaller Limit on the Electric Dipole Moment of the Electron. *Science*, 343, 269–272.

[72] Barr, S. M. & Zee, A. (1990). Electric Dipole Moment of the Electron and of the Neutron. *Phys. Rev. Lett.*, 65, 21–24. [Erratum: Phys. Rev. Lett.65,2920(1990)].

[73] Bartels, R., Krishnamurthy, S., & Weniger, C. (2016). Strong support for the millisecond pulsar origin of the Galactic center GeV excess. *Phys. Rev. Lett.*, 116(5), 051102.

[74] Bartels, R., Storm, E., Weniger, C., & Calore, F. (2018). The Fermi-LAT GeV excess as a tracer of stellar mass in the Galactic bulge. *Nature Astron.*, 2(10), 819–828.

[75] Basirnia, A., Macaluso, S., & Shih, D. (2017). Dark Matter and the Higgs in Natural SUSY. *JHEP*, 03, 073.

[76] Bastai, A., Bertocchi, L., Fubini, S., Furlan, G., & Tonin, M. (1963). On the treatment of singular bethe-salpeter equations. *Il Nuovo Cimento (1955-1965)*, 30(6), 1512–1531.

[77] Bauer, M. & Neubert, M. (2016). Minimal Leptoquark Explanation for the $R_{D^{(*)}}$, R_K , and $(g-2)_g$ Anomalies. *Phys. Rev. Lett.*, 116(14), 141802.

[78] Bedaque, P. F., Buchoff, M. I., & Mishra, R. K. (2009). Sommerfeld enhancement from Goldstone pseudo-scalar exchange. *JHEP*, 11, 046.

[79] Belanger, G., Boudjema, F., Pukhov, A., & Semenov, A. (2014). micrOMEGAs_3: A program for calculating dark matter observables. *Comput. Phys. Commun.*, 185, 960–985.

[80] Bellazzini, B., Cliche, M., & Tanedo, P. (2013). Effective theory of self-interacting dark matter. *Phys. Rev.*, D88(8), 083506.

[81] Benakli, K., Branchina, C., & Lafforgue-Marmet, G. (2020). U(1) mixing and the Weak Gravity Conjecture. *Eur. Phys. J. C*, 80(12), 1118.

[82] Bennett, G. W. et al. (2006). Final Report of the Muon E821 Anomalous Magnetic Moment Measurement at BNL. *Phys. Rev. D*, 73, 072003.

[83] Berg, M., Marsh, D., McAllister, L., & Pajer, E. (2011). Sequestering in String Compactifications. *JHEP*, 06, 134.

[84] Berlin, A., Gori, S., Lin, T., & Wang, L.-T. (2015). Pseudoscalar Portal Dark Matter. *Phys. Rev. D*, 92, 015005.

[85] Bernstein, J., Brown, L. S., & Feinberg, G. (1985). Cosmological heavy-neutrino problem. *Phys. Rev. D*, 32, 3261–3267.

[86] Binder, T., Bringmann, T., Gustafsson, M., & Hryczuk, A. (2017). Early kinetic decoupling of dark matter: when the standard way of calculating the thermal relic density fails. *Phys. Rev. D*, 96(11), 115010. [Erratum: Phys.Rev.D 101, 099901 (2020)].

[87] Bishara, F., Brod, J., Grinstein, B., & Zupan, J. (2017a). Chiral Effective Theory of Dark Matter Direct Detection. *JCAP*, 1702(02), 009.

[88] Bishara, F., Brod, J., Grinstein, B., & Zupan, J. (2017b). From quarks to nucleons in dark matter direct detection. *JHEP*, 11, 059.

[89] Bjerrum-Bohr, N., Donoghue, J. F., & Holstein, B. R. (2003). Quantum gravitational corrections to the nonrelativistic scattering potential of two masses. *Phys. Rev. D*, 67, 084033. [Erratum: Phys.Rev.D 71, 069903 (2005)].

[90] Blank, T. & Hollik, W. (1998). Precision observables in SU(2) x U(1) models with an additional Higgs triplet. *Nucl. Phys. B*, 514, 113–134.

[91] Blinov, N. & Morrissey, D. E. (2014). Vacuum Stability and the MSSM Higgs Mass. *JHEP*, 03, 106.

[92] Blum, K., D'Agnolo, R. T., & Fan, J. (2015). Vacuum stability bounds on Higgs coupling deviations in the absence of new bosons. *JHEP*, 03, 166.

[93] Blum, K., Delaunay, C., Losada, M., Nir, Y., & Tulin, S. (2010). CP violation Beyond the MSSM: Baryogenesis and Electric Dipole Moments. *JHEP*, 05, 101.

[94] Blum, K., Sato, R., & Slatyer, T. R. (2016). Self-consistent Calculation of the Sommerfeld Enhancement. *JCAP*, 1606(06), 021.

[95] Boehm, C., Dolan, M. J., McCabe, C., Spannowsky, M., & Wallace, C. J. (2014). Extended gamma-ray emission from Coy Dark Matter. *JCAP*, 05, 009.

[96] Bolton, P. D., Deppisch, F. F., & Hati, C. (2020). Probing new physics with long-range neutrino interactions: an effective field theory approach. *JHEP*, 07, 013.

[97] Boudaud, M., Génolini, Y., Derome, L., Lavalle, J., Maurin, D., Salati, P., & Serpico, P. D. (2020). AMS-02 antiprotons are consistent with a secondary astrophysical origin. *Phys. Rev. Res.*, 2, 023022.

[98] Boylan-Kolchin, M., Bullock, J. S., & Kaplinghat, M. (2011). Too big to fail? The puzzling darkness of massive Milky Way subhaloes. *Mon. Not. Roy. Astron. Soc.*, 415, L40.

[99] Branco, G. C., Ferreira, P. M., Lavoura, L., Rebelo, M. N., Sher, M., & Silva, J. P. (2012). Theory and phenomenology of two-Higgs-doublet models. *Phys. Rept.*, 516, 1–102.

[100] Brax, P., Fichet, S., & Pignol, G. (2018). Bounding Quantum Dark Forces. *Phys. Rev.*, D97(11), 115034.

[101] Brennan, T. D., Carta, F., & Vafa, C. (2017). The String Landscape, the Swampland, and the Missing Corner. *PoS*, TASI2017, 015.

[102] Brooks, A. M., Papastergis, E., Christensen, C. R., Governato, F., Stilp, A., Quinn, T. R., & Wadsley, J. (2017). How to Reconcile the Observed Velocity Function of Galaxies with Theory. *Astrophys. J.*, 850(1), 97.

[103] Brooks, A. M. & Zolotov, A. (2014). Why Baryons Matter: The Kinematics of Dwarf Spheroidal Satellites. *Astrophys. J.*, 786, 87.

[104] Buckley, A. (2013). PySLHA: a Pythonic interface to SUSY Les Houches Accord data.

[105] Buckley, M. R. & Fox, P. J. (2010). Dark Matter Self-Interactions and Light Force Carriers. *Phys. Rev. D*, 81, 083522.

[106] Burgess, C. P., Godfrey, S., Konig, H., London, D., & Maksymyk, I. (1994a). A Global fit to extended oblique parameters. *Phys. Lett. B*, 326, 276–281.

[107] Burgess, C. P., Godfrey, S., Konig, H., London, D., & Maksymyk, I. (1994b). Model independent global constraints on new physics. *Phys. Rev. D*, 49, 6115–6147.

[108] Burrage, C., Jaeckel, J., Redondo, J., & Ringwald, A. (2009). Late time CMB anisotropies constrain mini-charged particles. *JCAP*, 11, 002.

[109] Buschmann, M., Rodd, N. L., Safdi, B. R., Chang, L. J., Mishra-Sharma, S., Lisanti, M., & Macias, O. (2020). Foreground Mismodeling and the Point Source Explanation of the Fermi Galactic Center Excess.

[110] Cacciapaglia, G., Csaki, C., Marandella, G., & Strumia, A. (2006). The Minimal Set of Electroweak Precision Parameters. *Phys. Rev. D*, 74, 033011.

[111] Cai, C., Yu, Z.-H., & Zhang, H.-H. (2017). Cepc precision of electroweak oblique parameters and weakly interacting dark matter: The fermionic case. *Nuclear Physics B*, 921, 181–210.

[112] Cairncross, W. B., Gresh, D. N., Grau, M., Cossel, K. C., Roussy, T. S., Ni, Y., Zhou, Y., Ye, J., & Cornell, E. A. (2017). Precision Measurement of the Electron's Electric Dipole Moment Using Trapped Molecular Ions. *Phys. Rev. Lett.*, 119(15), 153001.

[113] Calibbi, L., Mariotti, A., & Tziveloglou, P. (2015). Singlet-Doublet Model: Dark matter searches and LHC constraints. *JHEP*, 10, 116.

[114] Calore, F., Cholis, I., & Weniger, C. (2015). Background Model Systematics for the Fermi GeV Excess. *JCAP*, 03, 038.

[115] Candelas, P., De La Ossa, X. C., Green, P. S., & Parkes, L. (1991). A Pair of Calabi-Yau manifolds as an exactly soluble superconformal theory. *Nucl. Phys. B*, 359, 21–74.

[116] Cao, J., Shang, L., Wu, P., Yang, J. M., & Zhang, Y. (2015). Supersymmetry explanation of the Fermi Galactic Center excess and its test at LHC run II. *Phys. Rev. D*, 91(5), 055005.

[117] Carena, M., Megevand, A., Quiros, M., & Wagner, C. E. M. (2005). Electroweak baryogenesis and new TeV fermions. *Nucl. Phys.*, B716, 319–351.

[118] Carena, M., Osborne, J., Shah, N. R., & Wagner, C. E. M. (2018). Supersymmetry and LHC Missing Energy Signals. *Phys. Rev.*, D98(11), 115010.

[119] Carena, M., Osborne, J., Shah, N. R., & Wagner, C. E. M. (2019). Return of the WIMP: Missing energy signals and the Galactic Center excess. *Phys. Rev.*, D100(5), 055002.

[120] Caruso, F., Martins, J., & Oguri, V. (2013). On the existence of hydrogen atoms in higher dimensional euclidean spaces. *Physics Letters A*, 377(9), 694–698.

[121] Casas, J. A., Lleyda, A., & Munoz, C. (1996). Problems for supersymmetry breaking by the dilaton in strings from charge and color breaking. *Phys. Lett.*, B380, 59–67.

[122] Casimir, H. & Polder, D. (1948). The Influence of retardation on the London-van der Waals forces. *Phys. Rev.*, 73, 360–372.

[123] Caswell, W. E. & Lepage, G. P. (1986). Effective Lagrangians for Bound State Problems in QED, QCD, and Other Field Theories. *Phys. Lett.*, 167B, 437–442.

[124] Chang, D., Keung, W.-Y., & Pilaftsis, A. (1999). New two loop contribution to electric dipole moment in supersymmetric theories. *Phys. Rev. Lett.*, 82, 900–903. [Erratum: Phys. Rev. Lett.83,3972(1999)].

[125] Chang, D., Keung, W.-Y., & Yuan, T. C. (1991). Two loop bosonic contribution to the electron electric dipole moment. *Phys. Rev.*, D43, R14–R16.

[126] Chang, J. H., Essig, R., & McDermott, S. D. (2018). Supernova 1987A Constraints on Sub-GeV Dark Sectors, Millicharged Particles, the QCD Axion, and an Axion-like Particle. *JHEP*, 09, 051.

[127] Chatrchyan, S. et al. (2012). Observation of a New Boson at a Mass of 125 GeV with the CMS Experiment at the LHC. *Phys. Lett. B*, 716, 30–61.

[128] Cheung, C., Papucci, M., Sanford, D., Shah, N. R., & Zurek, K. M. (2014). NMSSM Interpretation of the Galactic Center Excess. *Phys. Rev.*, D90(7), 075011.

[129] Cheung, C. & Sanford, D. (2014). Simplified Models of Mixed Dark Matter. *JCAP*, 02, 011.

[130] Chia, S. P. & Nandi, S. (1982). Neutron Electric Dipole Moment in Supersymmetric Theories. *Phys. Lett.*, 117B, 45–50.

[131] Chiu, H.-Y. (1966). Symmetry between particle and anti-particle populations in the universe. *Phys. Rev. Lett.*, 17, 712.

[132] Cho, G.-C., Hagiwara, K., Matsumoto, Y., & Nomura, D. (2011). The MSSM confronts the precision electroweak data and the muon g-2. *JHEP*, 11, 068.

[133] Cho, P. L. & Simmons, E. H. (1995). Searching for G3 in $t\bar{t}$ production. *Phys. Rev. D*, 51, 2360–2370.

[134] Choi, K. & Hong, J.-y. (1991). Electron electric dipole moment and Theta (QCD). *Phys. Lett.*, B259, 340–344.

[135] Choi, K.-w., Kaplan, D. B., & Nelson, A. E. (1993). Is CP a gauge symmetry? *Nucl. Phys.*, B391, 515–530.

[136] Cholis, I., Hooper, D., & Linden, T. (2014). A New Determination of the Spectra and Luminosity Function of Gamma-Ray Millisecond Pulsars.

[137] Cholis, I., Hooper, D., & Linden, T. (2015). Challenges in Explaining the Galactic Center Gamma-Ray Excess with Millisecond Pulsars. *JCAP*, 06, 043.

[138] Cholis, I., Linden, T., & Hooper, D. (2019). A Robust Excess in the Cosmic-Ray Antiproton Spectrum: Implications for Annihilating Dark Matter. *Phys. Rev. D*, 99(10), 103026.

[139] Choudhury, D., Tait, T. M. P., & Wagner, C. E. M. (2002). Beautiful mirrors and precision electroweak data. *Phys. Rev. D*, 65, 053002.

[140] Chowdhury, D., Godbole, R. M., Mohan, K. A., & Vempati, S. K. (2014). Charge and Color Breaking Constraints in MSSM after the Higgs Discovery at LHC. *JHEP*, 02, 110. [Erratum: JHEP03,149(2018)].

[141] Chu, X., Garcia-Cely, C., & Murayama, H. (2019a). A Practical and Consistent Parametrization of Dark Matter Self-Interactions.

[142] Chu, X., Garcia-Cely, C., & Murayama, H. (2019b). Velocity Dependence from Resonant Self-Interacting Dark Matter. *Phys. Rev. Lett.*, 122(7), 071103.

[143] Chu, X., Garcia-Cely, C., & Murayama, H. (2020). Finite-size dark matter and its effect on small-scale structure. *Phys. Rev. Lett.*, 124(4), 041101.

[144] Chupp, T., Fierlinger, P., Ramsey-Musolf, M., & Singh, J. (2019). Electric dipole moments of atoms, molecules, nuclei, and particles. *Rev. Mod. Phys.*, 91(1), 015001.

[145] Chupp, T. & Ramsey-Musolf, M. (2015). Electric Dipole Moments: A Global Analysis. *Phys. Rev.*, C91(3), 035502.

[146] Cirelli, M., Del Nobile, E., & Panci, P. (2013). Tools for model-independent bounds in direct dark matter searches. *JCAP*, 10, 019.

[147] Ciuchini, M., Franco, E., Mishima, S., & Silvestrini, L. (2013). Electroweak Precision Observables, New Physics and the Nature of a 126 GeV Higgs Boson. *JHEP*, 08, 106.

[148] Claudson, M., Hall, L. J., & Hinchliffe, I. (1983). Low-Energy Supergravity: False Vacua and Vacuous Predictions. *Nucl. Phys.*, B228, 501–528.

[149] Cohen, T., Kearney, J., Pierce, A., & Tucker-Smith, D. (2012). Singlet-Doublet Dark Matter. *Phys. Rev.*, D85, 075003.

[150] Conlon, J. P. (2008). Mirror Mediation. *JHEP*, 03, 025.

[151] Costantino, A. & Fichet, S. (2020). The Neutrino Casimir Force. *JHEP*, 09, 122.

[152] Costantino, A., Fichet, S., & Tanedo, P. (2020). Exotic Spin-Dependent Forces from a Hidden Sector. *JHEP*, 03, 148.

[153] Crivellin, A., Hoferichter, M., Manzari, C. A., & Montull, M. (2020). Hadronic Vacuum Polarization: $(g-2)_\mu$ versus Global Electroweak Fits. *Phys. Rev. Lett.*, 125(9), 091801.

[154] Cui, X. et al. (2017). Dark Matter Results From 54-Ton-Day Exposure of PandaX-II Experiment. *Phys. Rev. Lett.*, 119(18), 181302.

[155] Cuoco, A., Heisig, J., Klamt, L., Korsmeier, M., & Krämer, M. (2019). Scrutinizing the evidence for dark matter in cosmic-ray antiprotons. *Phys. Rev. D*, 99(10), 103014.

[156] Cuoco, A., Heisig, J., Korsmeier, M., & Krämer, M. (2017). Probing dark matter annihilation in the Galaxy with antiprotons and gamma rays. *JCAP*, 10, 053.

[157] Cyr-Racine, F.-Y., Sigurdson, K., Zavala, J., Bringmann, T., Vogelsberger, M., & Pfrommer, C. (2016). ETHOS–an effective theory of structure formation: From dark particle physics to the matter distribution of the Universe. *Phys. Rev.*, D93(12), 123527.

[158] Daido, R. & Takahashi, F. (2017). The sign of the dipole–dipole potential by axion exchange. *Phys. Lett.*, B772, 127–129.

[159] Dave, R., Spergel, D. N., Steinhardt, P. J., & Wandelt, B. D. (2001). Halo properties in cosmological simulations of selfinteracting cold dark matter. *Astrophys. J.*, 547, 574–589.

[160] Davidson, S., Hannestad, S., & Raffelt, G. (2000). Updated bounds on millicharged particles. *JHEP*, 05, 003.

[161] Daylan, T., Finkbeiner, D. P., Hooper, D., Linden, T., Portillo, S. K. N., Rodd, N. L., & Slatyer, T. R. (2016). The characterization of the gamma-ray signal from the central Milky Way: A case for annihilating dark matter. *Phys. Dark Univ.*, 12, 1–23.

[162] de Blas, J., Ciuchini, M., Franco, E., Mishima, S., Pierini, M., Reina, L., & Silvestrini, L. (2016). Electroweak precision observables and Higgs-boson signal strengths in the Standard Model and beyond: present and future. *JHEP*, 12, 135.

[163] de Gouvea, A., Hernandez, D., & Tait, T. M. P. (2014). Criteria for Natural Hierarchies. *Phys. Rev.*, D89(11), 115005.

[164] Dedes, A. & Karamitros, D. (2014). Doublet-Triplet Fermionic Dark Matter. *Phys. Rev.*, D89(11), 115002.

[165] Dekens, W., de Vries, J., Jung, M., & Vos, K. K. (2019). The phenomenology of electric dipole moments in models of scalar leptoquarks. *JHEP*, 01, 069.

[166] del Aguila, F., Gavela, M. B., Grifols, J. A., & Mendez, A. (1983). Specifically Supersymmetric Contribution to Electric Dipole Moments. *Phys. Lett.*, 126B, 71. [Erratum: Phys. Lett.129B,473(1983)].

[167] Del Popolo, A., Pace, F., Le Delliou, M., & Lee, X. (2018). Energy transfer from baryons to dark matter as a unified solution to small-scale structure issues of the ΛCDM model. *Phys. Rev.*, D98(6), 063517.

[168] Del Zotto, M., Heckman, J. J., Kumar, P., Malekian, A., & Wecht, B. (2017). Kinetic Mixing at Strong Coupling. *Phys. Rev. D*, 95(1), 016007.

[169] Demir, D. A., Lebedev, O., Olive, K. A., Pospelov, M., & Ritz, A. (2004). Electric dipole moments in the MSSM at large tan beta. *Nucl. Phys.*, B680, 339–374.

[170] D'Eramo, F. (2007). Dark matter and Higgs boson physics. *Phys. Rev. D*, 76, 083522.

[171] Di Mauro, M. (2021). The characteristics of the Galactic center excess measured with 11 years of Fermi-LAT data.

[172] Díaz Rivero, A., Dvorkin, C., Cyr-Racine, F.-Y., Zavala, J., & Vogelsberger, M. (2018). Gravitational Lensing and the Power Spectrum of Dark Matter Substructure: Insights from the ETHOS N-body Simulations. *Phys. Rev.*, D98(10), 103517.

[173] Dienes, K. R., Kolda, C. F., & March-Russell, J. (1997). Kinetic mixing and the supersymmetric gauge hierarchy. *Nucl. Phys. B*, 492, 104–118.

[174] Dine, M., Leigh, R. G., & MacIntire, D. A. (1992). Of CP and other gauge symmetries in string theory. *Phys. Rev. Lett.*, 69, 2030–2032.

[175] Dixon, L. J., Kaplunovsky, V., & Louis, J. (1991). Moduli dependence of string loop corrections to gauge coupling constants. *Nucl. Phys. B*, 355, 649–688.

[176] Dobrescu, B. A. & Mocioiu, I. (2006). Spin-dependent macroscopic forces from new particle exchange. *JHEP*, 11, 005.

[177] Dong, S.-H., Ma, Z.-Q., & Esposito, G. (1999). Exact Solutions of the Schrödinger Equation with Inverse-Power Potential. *Found. Phys. Lett.*, 12(5), 465–474.

[178] Donoghue, J. F. (1978). T Violation in SU(2) x U(1) Gauge Theories of Leptons. *Phys. Rev.*, D18, 1632.

[179] Doršner, I., Fajfer, S., Greljo, A., Kamenik, J. F., & Košnik, N. (2016). Physics of leptoquarks in precision experiments and at particle colliders. *Phys. Rept.*, 641, 1–68.

[180] Dubovyk, I., Freitas, A., Gluza, J., Riemann, T., & Usovitsch, J. (2016). The two-loop electroweak bosonic corrections to $\sin^2\theta$

b_eff. *Phys.Lett.B*, 762, 184 – –189.

[181] Dubovyk, I., Freitas, A., Gluza, J., Riemann, T., & Usovitsch, J. (2018). Complete electroweak two-loop corrections to Z boson production and decay. *Phys. Lett. B*, 783, 86–94.

[182] Duerr, M., Fileviez Pérez, P., & Smirnov, J. (2016). Gamma-Ray Excess and the Minimal Dark Matter Model. *JHEP*, 06, 008.

[183] Dupont, R. (2006). *Moyenne arithmético-géométrique, suites de Borchardt et applications*. PhD thesis, PhD thesis, École polytechnique.

[184] Dutta, J., Kraml, S., Lessa, A., & Waltenberger, W. (2018). SModelS extension with the CMS supersymmetry search results from Run 2. *LHEP*, 1(1), 5–12.

[185] Dzuba, V., Flambaum, V., & Harabati, C. (2011). Relations between matrix elements of different weak interactions and interpretation of the parity-nonconserving and electron electric-dipole-moment measurements in atoms and molecules. *Phys. Rev.*, A84(5), 052108.

[186] Egana-Ugrinovic, D. (2017). The minimal fermionic model of electroweak baryogenesis. *JHEP*, 12, 064.

[187] Ehret, K. et al. (2010). New ALPS Results on Hidden-Sector Lightweights. *Phys. Lett. B*, 689, 149–155.

[188] Ellis, J., Nagata, N., & Olive, K. A. (2018). Uncertainties in WIMP Dark Matter Scattering Revisited. *Eur. Phys. J. C*, 78(7), 569.

[189] Ellis, J. R., Ferrara, S., & Nanopoulos, D. V. (1982). CP Violation and Supersymmetry. *Phys. Lett.*, 114B, 231–234.

[190] Ellis, J. R., Lee, J. S., & Pilaftsis, A. (2008). Electric Dipole Moments in the MSSM Reloaded. *JHEP*, 10, 049.

[191] Ellis, S. A. R. & Kane, G. L. (2016). Theoretical Prediction and Impact of Fundamental Electric Dipole Moments. *JHEP*, 01, 077.

[192] Enberg, R., Fox, P., Hall, L., Papaioannou, A., & Papucci, M. (2007). Lhc and dark matter signals of improved naturalness. *Journal of High Energy Physics*, 2007(11), 014–014.

[193] Engel, J., Ramsey-Musolf, M. J., & van Kolck, U. (2013). Electric Dipole Moments of Nucleons, Nuclei, and Atoms: The Standard Model and Beyond. *Prog. Part. Nucl. Phys.*, 71, 21–74.

[194] Epelbaum, E., Hammer, H.-W., & Meissner, U.-G. (2009). Modern Theory of Nuclear Forces. *Rev. Mod. Phys.*, 81, 1773–1825.

[195] Erler, J. & Schott, M. (2019). Electroweak Precision Tests of the Standard Model after the Discovery of the Higgs Boson. *Prog. Part. Nucl. Phys.*, 106, 68–119.

[196] Esposito, G. (1998). Scattering from singular potentials in quantum mechanics. *J. Phys.*, A31, 9493–9504.

[197] Essig, R., Schuster, P., & Toro, N. (2009). Probing Dark Forces and Light Hidden Sectors at Low-Energy e+e- Colliders. *Phys. Rev.*, D80, 015003.

[198] Esteban, I., Gonzalez-Garcia, M. C., Maltoni, M., Martinez-Soler, I., & Schwetz, T. (2017). Updated fit to three neutrino mixing: exploring the accelerator-reactor complementarity. *JHEP*, 01, 087.

[199] Fabbrichesi, M., Gabrielli, E., & Lanfranchi, G. (2020). The Dark Photon.

[200] Fadeev, P., Stadnik, Y. V., Ficek, F., Kozlov, M. G., Flambaum, V. V., & Budker, D. (2019). Revisiting spin-dependent forces mediated by new bosons: Potentials in the coordinate-space representation for macroscopic- and atomic-scale experiments. *Phys. Rev.*, A99(2), 022113.

[201] Fan, J. & Reece, M. (2013). Probing Charged Matter Through Higgs Diphoton Decay, Gamma Ray Lines, and EDMs. *JHEP*, 06, 004.

[202] Fan, J., Reece, M., & Wang, L.-T. (2010). Non-relativistic effective theory of dark matter direct detection. *JCAP*, 1011, 042.

[203] Fan, J., Reece, M., & Wang, L.-T. (2015a). Possible Futures of Electroweak Precision: ILC, FCC-ee, and CEPC. *JHEP*, 09, 196.

[204] Fan, J., Reece, M., & Wang, L.-T. (2015b). Precision Natural SUSY at CEPC, FCC-ee, and ILC. *JHEP*, 08, 152.

[205] Faraggi, A. E. (1992). A New standard - like model in the four-dimensional free fermionic string formulation. *Phys. Lett. B*, 278, 131–139.

[206] Faraggi, A. E. (1993). Gauge coupling unification in superstring derived standard - like models. *Phys. Lett. B*, 302, 202–208.

[207] Farina, M., Pappadopulo, D., & Strumia, A. (2013). A modified naturalness principle and its experimental tests. *JHEP*, 08, 022.

[208] Feinberg, G. & Sucher, J. (1968). Long-Range Forces from Neutrino-Pair Exchange. *Phys. Rev.*, 166, 1638–1644.

[209] Feinberg, G., Sucher, J., & Au, C. K. (1989). The dispersion theory of dispersion forces. *Physics Reports*, 180(2), 83–157.

[210] Feng, J. L., Kaplinghat, M., & Yu, H.-B. (2010). Halo Shape and Relic Density Exclusions of Sommerfeld-Enhanced Dark Matter Explanations of Cosmic Ray Excesses. *Phys. Rev. Lett.*, 104, 151301.

[211] Ferrer, F. & Grifols, J. (1998). Long range forces from pseudoscalar exchange. *Phys. Rev. D*, 58, 096006.

[212] Feynman, R. (1963). Quantum theory of gravitation. *Acta Phys. Polon.*, 24, 697–722.

[213] Fichet, S. (2018). Quantum Forces from Dark Matter and Where to Find Them. *Phys. Rev. Lett.*, 120(13), 131801.

[214] Fischbach, E. (1996). Long range forces and neutrino mass. *Annals Phys.*, 247, 213–291.

[215] Fitzpatrick, A. L., Haxton, W., Katz, E., Lubbers, N., & Xu, Y. (2013). The Effective Field Theory of Dark Matter Direct Detection. *JCAP*, 1302, 004.

[216] Flacher, H., Goebel, M., Haller, J., Hocker, A., Monig, K., & Stelzer, J. (2009). Revisiting the Global Electroweak Fit of the Standard Model and Beyond with Gfitter. *Eur. Phys. J. C*, 60, 543–583. [Erratum: Eur.Phys.J.C 71, 1718 (2011)].

[217] Flores, R. A. & Primack, J. R. (1994). Observational and theoretical constraints on singular dark matter halos. *Astrophys. J.*, 427, L1–4.

[218] Fox, P. J., Kribs, G. D., & Martin, A. (2014). Split Dirac Supersymmetry: An Ultraviolet Completion of Higgsino Dark Matter. *Phys. Rev.*, D90(7), 075006.

[219] Frank, W. M., Land, D. J., & Spector, R. M. (1971). Singular potentials. *Rev. Mod. Phys.*, 43, 36–98.

[220] Fraser, K., Parikh, A., & Xu, W. L. (2021). A Closer Look at CP-Violating Higgs Portal Dark Matter as a Candidate for the GCE. *JHEP*, 03, 123.

[221] Freitas, A., Westhoff, S., & Zupan, J. (2015). Integrating in the Higgs Portal to Fermion Dark Matter. *JHEP*, 09, 015.

[222] Freytsis, M. & Ligeti, Z. (2011). On dark matter models with uniquely spin-dependent detection possibilities. *Phys. Rev.*, D83, 115009.

[223] Freytsis, M., Ligeti, Z., & Ruderman, J. T. (2015). Flavor models for $\bar{B} \to D^{(*)}\tau\bar{\nu}$. *Phys. Rev.*, D92(5), 054018.

[224] Fuyuto, K., Ramsey-Musolf, M., & Shen, T. (2019). Electric Dipole Moments from CP-Violating Scalar Leptoquark Interactions. *Phys. Lett.*, B788, 52–57.

[225] Gavela, M. B. & Georgi, H. (1982). CP Violation in the Lepton Sector. *Phys. Lett.*, 119B, 141–143.

[226] Gherghetta, T., Kersten, J., Olive, K., & Pospelov, M. (2019). Evaluating the price of tiny kinetic mixing. *Phys. Rev. D*, 100(9), 095001.

[227] Gherghetta, T., von Harling, B., Medina, A. D., Schmidt, M. A., & Trott, T. (2015). SUSY implications from WIMP annihilation into scalars at the Galactic Center. *Phys. Rev.*, D91, 105004.

[228] Ghosh, D. & Sato, R. (2018). Lepton Electric Dipole Moment and Strong CP Violation. *Phys. Lett.*, B777, 335–339.

[229] Ghosh, M., Grossman, Y., & Tangarife, W. (2019). Probing the two-neutrino exchange force using atomic parity violation.

[230] Giudice, G. F., Luty, M. A., Murayama, H., & Rattazzi, R. (1998). Gaugino mass without singlets. *JHEP*, 12, 027.

[231] Giudice, G. F. & Rattazzi, R. (1999). Theories with gauge mediated supersymmetry breaking. *Phys. Rept.*, 322, 419–499.

[232] Giudice, G. F. & Romanino, A. (2006). Electric dipole moments in split supersymmetry. *Phys. Lett.*, B634, 307–314.

[233] Gninenko, S. (2018a). *Addendum to the NA64 Proposal: Search for the A' $\to$ invisible and $X \to e^+e^-$ decays in 2021*. Technical Report CERN-SPSC-2018-004. SPSC-P-348-ADD-2, CERN, Geneva.

[234] Gninenko, S. (2018b). *Addendum to the Proposal P348: Search for dark sector particles weakly coupled to muon with NA64μ*. Technical Report CERN-SPSC-2018-024. SPSC-P-348-ADD-3, CERN, Geneva.

[235] Golden, M. & Randall, L. (1991). Radiative Corrections to Electroweak Parameters in Technicolor Theories. *Nucl. Phys. B*, 361, 3–23.

[236] Gondolo, P. & Gelmini, G. (1991). Cosmic abundances of stable particles: Improved analysis. *Nucl. Phys. B*, 360, 145–179.

[237] Gonul, B., Ozer, O., Kocak, M., Tutcu, D., & Cancelik, Y. (2001). Supersymmetry and the relationship between a class of singular potentials in arbitrary dimensions. *J. Phys.*, A34, 8271–8279.

[238] Goodenough, L. & Hooper, D. (2009). Possible Evidence For Dark Matter Annihilation In The Inner Milky Way From The Fermi Gamma Ray Space Telescope.

[239] Goodsell, M., Jaeckel, J., Redondo, J., & Ringwald, A. (2009). Naturally Light Hidden Photons in LARGE Volume String Compactifications. *JHEP*, 11, 027.

[240] Goodsell, M., Ramos-Sanchez, S., & Ringwald, A. (2012). Kinetic Mixing of U(1)s in Heterotic Orbifolds. *JHEP*, 01, 021.

[241] Gordon, C. & Macias, O. (2013). Dark Matter and Pulsar Model Constraints from Galactic Center Fermi-LAT Gamma Ray Observations. *Phys. Rev. D*, 88(8), 083521. [Erratum: Phys.Rev.D 89, 049901 (2014)].

[242] Gottschling, E. (1959). Explizite bestimmung der randflächen des fundamentalbereiches der modulgruppe zweiten grades. *Mathematische Annalen*, 138, 103–124.

[243] Governato, F. et al. (2010). At the heart of the matter: the origin of bulgeless dwarf galaxies and Dark Matter cores. *Nature*, 463, 203–206.

[244] Griest, K. & Seckel, D. (1991). Three exceptions in the calculation of relic abundances. *Phys. Rev. D*, 43, 3191–3203.

[245] Grifols, J., Masso, E., & Toldra, R. (1996). Majorana neutrinos and long range forces. *Phys. Lett. B*, 389, 563–565.

[246] Grimm, T. W. (2005). The Effective action of type II Calabi-Yau orientifolds. *Fortsch. Phys.*, 53, 1179–1271.

[247] Grimm, T. W., Ha, T.-W., Klemm, A., & Klevers, D. (2009). The D5-brane effective action and superpotential in N=1 compactifications. *Nucl. Phys. B*, 816, 139–184.

[248] Grinstein, B. & Wise, M. B. (1991). Operator analysis for precision electroweak physics. *Phys. Lett. B*, 265, 326–334.

[249] Grzadkowski, B., Iskrzynski, M., Misiak, M., & Rosiek, J. (2010). Dimension-Six Terms in the Standard Model Lagrangian. *JHEP*, 10, 085.

[250] Guo, J., Li, J., Li, T., & Williams, A. G. (2015). NMSSM explanations of the Galactic center gamma ray excess and promising LHC searches. *Phys. Rev. D*, 91(9), 095003.

[251] Haggard, D., Heinke, C., Hooper, D., & Linden, T. (2017). Low Mass X-Ray Binaries in the Inner Galaxy: Implications for Millisecond Pulsars and the GeV Excess. *JCAP*, 05, 056.

[252] Haller, J., Hoecker, A., Kogler, R., Mönig, K., Peiffer, T., & Stelzer, J. (2018). Update of the global electroweak fit and constraints on two-Higgs-doublet models. *Eur. Phys. J. C*, 78(8), 675.

[253] Han, Z. (2008). Effective Theories and Electroweak Precision Constraints. *Int. J. Mod. Phys. A*, 23, 2653–2685.

[254] Han, Z. & Skiba, W. (2005). Effective theory analysis of precision electroweak data. *Phys. Rev. D*, 71, 075009.

[255] Heckman, J. J. & Vafa, C. (2019). Fine Tuning, Sequestering, and the Swampland. *Phys. Lett. B*, 798, 135004.

[256] Heidenreich, B., Reece, M., & Rudelius, T. (2016). Sharpening the Weak Gravity Conjecture with Dimensional Reduction. *JHEP*, 02, 140.

[257] Heidenreich, B., Reece, M., & Rudelius, T. (2017). Evidence for a sublattice weak gravity conjecture. *JHEP*, 08, 025.

[258] Heisig, J., Korsmeier, M., & Winkler, M. W. (2020). Dark matter or correlated errors? Systematics of the AMS-02 antiproton excess.

[259] Hill, R. J. & Solon, M. P. (2015). Standard Model anatomy of WIMP dark matter direct detection II: QCD analysis and hadronic matrix elements. *Phys. Rev. D*, 91, 043505.

[260] Hisano, J., Matsumoto, S., & Nojiri, M. M. (2003). Unitarity and higher order corrections in neutralino dark matter annihilation into two photons. *Phys. Rev.*, D67, 075014.

[261] Hisano, J., Matsumoto, S., & Nojiri, M. M. (2004). Explosive dark matter annihilation. *Phys. Rev. Lett.*, 92, 031303.

[262] Hisano, J., Matsumoto, S., Nojiri, M. M., & Saito, O. (2005). Non-perturbative effect on dark matter annihilation and gamma ray signature from galactic center. *Phys. Rev.*, D71, 063528.

[263] Holdom, B. (1986). Two U(1)'s and Epsilon Charge Shifts. *Phys. Lett. B*, 166, 196–198.

[264] Holdom, B. (1991). Oblique electroweak corrections and an extra gauge boson. *Phys. Lett. B*, 259, 329–334.

[265] Holdom, B. & Terning, J. (1990). Large corrections to electroweak parameters in technicolor theories. *Phys. Lett. B*, 247, 88–92.

[266] Hoogeveen, F. (1990). The Standard Model Prediction for the Electric Dipole Moment of the Electron. *Nucl. Phys.*, B341, 322–340.

[267] Hooper, D. & Goodenough, L. (2011). Dark Matter Annihilation in The Galactic Center As Seen by the Fermi Gamma Ray Space Telescope. *Phys. Lett.*, B697, 412–428.

[268] Hooper, D., Leane, R. K., Tsai, Y.-D., Wegsman, S., & Witte, S. J. (2019). A Systematic Study of Hidden Sector Dark Matter: Application to the Gamma-Ray and Antiproton Excesses.

[269] Hooper, D. & Linden, T. (2011). On The Origin Of The Gamma Rays From The Galactic Center. *Phys. Rev. D*, 84, 123005.

[270] Hsu, S. D. & Sikivie, P. (1994). Long range forces from two neutrino exchange revisited. *Phys. Rev. D*, 49, 4951–4953.

[271] Huang, W.-C., Urbano, A., & Xue, W. (2014). Fermi Bubbles under Dark Matter Scrutiny Part II: Particle Physics Analysis. *JCAP*, 04, 020.

[272] Hut, P. (1977). Limits on Masses and Number of Neutral Weakly Interacting Particles. *Phys. Lett. B*, 69, 85.

[273] Ibrahim, T. & Nath, P. (2008). CP Violation From Standard Model to Strings. *Rev. Mod. Phys.*, 80, 577–631.

[274] Iwasaki, Y. (1971). Quantum theory of gravitation vs. classical theory. - fourth-order potential. *Prog. Theor. Phys.*, 46, 1587–1609.

[275] Jaber, C. (2017). *Algorithmic approaches to Siegel's fundamental domain*. PhD thesis, Bourgogne Franche-Comté.

[276] Jaeckel, J., Jankowiak, M., & Spannowsky, M. (2013). LHC probes the hidden sector. *Phys. Dark Univ.*, 2, 111–117.

[277] Janot, P. & Jadach, S. (2020). Improved Bhabha cross section at LEP and the number of light neutrino species. *Phys. Lett. B*, 803, 135319.

[278] Jenkins, E. E., Manohar, A. V., & Trott, M. (2013). Renormalization Group Evolution of the Standard Model Dimension Six Operators I: Formalism and lambda Dependence. *JHEP*, 10, 087.

[279] Jenkins, E. E., Manohar, A. V., & Trott, M. (2014). Renormalization Group Evolution of the Standard Model Dimension Six Operators II: Yukawa Dependence. *JHEP*, 01, 035.

[280] Jockers, H. & Louis, J. (2005). The Effective action of D7-branes in N = 1 Calabi-Yau orientifolds. *Nucl. Phys. B*, 705, 167–211.

[281] Joglekar, A., Schwaller, P., & Wagner, C. E. M. (2012). Dark Matter and Enhanced Higgs to Diphoton Rate from Vector-like Leptons. *JHEP*, 12, 064.

[282] Joglekar, A., Schwaller, P., & Wagner, C. E. M. (2013). A Supersymmetric Theory of Vector-like Leptons. *JHEP*, 07, 046.

[283] Jung, M. (2013). A robust limit for the electric dipole moment of the electron. *JHEP*, 05, 168.

[284] Jung, M. & Pich, A. (2014). Electric Dipole Moments in Two-Higgs-Doublet Models. *JHEP*, 04, 076.

[285] Junnarkar, P. & Walker-Loud, A. (2013). Scalar strange content of the nucleon from lattice QCD. *Phys. Rev.*, D87, 114510.

[286] Kachru, S., McAllister, L., & Sundrum, R. (2007). Sequestering in String Theory. *JHEP*, 10, 013.

[287] Kahlhoefer, F., Schmidt-Hoberg, K., Frandsen, M. T., & Sarkar, S. (2014). Colliding clusters and dark matter self-interactions. *Mon. Not. Roy. Astron. Soc.*, 437(3), 2865–2881.

[288] Kahlhoefer, F., Schmidt-Hoberg, K., & Wild, S. (2017). Dark matter self-interactions from a general spin-0 mediator. *JCAP*, 1708(08), 003.

[289] Kaplan, D. B. (1991). Flavor at SSC energies: A New mechanism for dynamically generated fermion masses. *Nucl. Phys.*, B365, 259–278.

[290] Kaplan, D. B. (1992). A Single explanation for both the baryon and dark matter densities. *Phys. Rev. Lett.*, 68, 741–743.

[291] Kaplinghat, M., Tulin, S., & Yu, H.-B. (2016). Dark Matter Halos as Particle Colliders: Unified Solution to Small-Scale Structure Puzzles from Dwarfs to Clusters. *Phys. Rev. Lett.*, 116(4), 041302.

[292] Kaplunovsky, V. S. (1988). One Loop Threshold Effects in String Unification. *Nucl. Phys. B*, 307, 145–156. [Erratum: Nucl.Phys.B 382, 436–438 (1992)].

[293] Karwin, C., Murgia, S., Tait, T. M. P., Porter, T. A., & Tanedo, P. (2017). Dark Matter Interpretation of the Fermi-LAT Observation Toward the Galactic Center. *Phys. Rev. D*, 95(10), 103005.

[294] Katz, A., Reece, M., & Sajjad, A. (2014). Naturalness, $b \to s\gamma$, and SUSY heavy Higgses. *JHEP*, 10, 102.

[295] Kelly, K. J. & Tsai, Y.-D. (2019). Proton fixed-target scintillation experiment to search for millicharged dark matter. *Phys. Rev. D*, 100(1), 015043.

[296] Kennedy, D. C. & Lynn, B. W. (1989). Electroweak Radiative Corrections with an Effective Lagrangian: Four Fermion Processes. *Nucl. Phys. B*, 322, 1–54.

[297] Khandker, Z. U., Li, D., & Skiba, W. (2012). Electroweak Corrections from Triplet Scalars. *Phys. Rev. D*, 86, 015006.

[298] Khosa, C. K., Kraml, S., Lessa, A., Neuhuber, P., & Waltenberger, W. (2020). SModelS database update v1.2.3. *to appear in LHEP.* .

[299] Kitano, R., Ooguri, H., & Ookouchi, Y. (2010). Supersymmetry Breaking and Gauge Mediation. *Ann. Rev. Nucl. Part. Sci.*, 60, 491–511.

[300] Klypin, A. A., Kravtsov, A. V., Valenzuela, O., & Prada, F. (1999). Where are the missing Galactic satellites? *Astrophys. J.*, 522, 82–92.

[301] Kozyryev, I. & Hutzler, N. R. (2017). Precision Measurement of Time-Reversal Symmetry Violation with Laser-Cooled Polyatomic Molecules. *Phys. Rev. Lett.*, 119(13), 133002.

[302] Krall, R. & Reece, M. (2018). Last Electroweak WIMP Standing: Pseudo-Dirac Higgsino Status and Compact Stars as Future Probes. *Chin. Phys.*, C42(4), 043105.

[303] Kraml, S., Kulkarni, S., Laa, U., Lessa, A., Magerl, W., Proschofsky, D., & Waltenberger, W. (2014). SModelS: a tool for interpreting simplified-model results from the LHC and its application to supersymmetry. *Eur.Phys.J.*, C74, 2868.

[304] Kuzio de Naray, R., Martinez, G. D., Bullock, J. S., & Kaplinghat, M. (2010). The Case Against Warm or Self-Interacting Dark Matter as Explanations for Cores in Low Surface Brightness Galaxies. *Astrophys. J.*, 710, L161.

[305] Le Thien, Q. & Krause, D. E. (2019). Spin-Independent Two-Neutrino Exchange Potential with Mixing and *CP*-Violation. *Phys. Rev. D*, 99(11), 116006.

[306] Leane, R. K. & Slatyer, T. R. (2019). Revival of the Dark Matter Hypothesis for the Galactic Center Gamma-Ray Excess. *Phys. Rev. Lett.*, 123(24), 241101.

[307] Leane, R. K. & Slatyer, T. R. (2020a). Spurious Point Source Signals in the Galactic Center Excess.

[308] Leane, R. K. & Slatyer, T. R. (2020b). The Enigmatic Galactic Center Excess: Spurious Point Sources and Signal Mismodeling.

[309] Lebedev, O. & Pospelov, M. (2002). Electric dipole moments in the limit of heavy superpartners. *Phys. Rev. Lett.*, 89, 101801.

[310] Lee, B. W. & Weinberg, S. (1977). Cosmological Lower Bound on Heavy Neutrino Masses. *Phys. Rev. Lett.*, 39, 165–168.

[311] Lee, S. K., Lisanti, M., & Safdi, B. R. (2015). Distinguishing Dark Matter from Unresolved Point Sources in the Inner Galaxy with Photon Statistics. *JCAP*, 05, 056.

[312] Lee, S. K., Lisanti, M., Safdi, B. R., Slatyer, T. R., & Xue, W. (2016). Evidence for Unresolved γ-Ray Point Sources in the Inner Galaxy. *Phys. Rev. Lett.*, 116(5), 051103.

[313] Leigh, R. G., Paban, S., & Xu, R. M. (1991). Electric dipole moment of electron. *Nucl. Phys.*, B352, 45–58.

[314] Lepage, G. P. (1997). How to renormalize the Schrodinger equation. In *Nuclear physics. Proceedings, 8th Jorge Andre Swieca Summer School, Sao Jose dos Campos, Campos do Jordao, Brazil, January 26-February 7, 1997* (pp. 135–180).

[315] Li, Y., Profumo, S., & Ramsey-Musolf, M. (2008). Higgs-Higgsino-Gaugino Induced Two Loop Electric Dipole Moments. *Phys. Rev.*, D78, 075009.

[316] Lim, J., Almond, J., Trigatzis, M., Devlin, J., Fitch, N., Sauer, B., Tarbutt, M., & Hinds, E. (2018). Laser Cooled YbF Molecules for Measuring the Electron's Electric Dipole Moment. *Phys. Rev. Lett.*, 120(12), 123201.

[317] Lin, T. (2019). Dark matter models and direct detection. *PoS*, 333, 009.

[318] List, F., Rodd, N. L., Lewis, G. F., & Bhat, I. (2020). The GCE in a New Light: Disentangling the γ-ray Sky with Bayesian Graph Convolutional Neural Networks.

[319] Liu, Z.-P., Wu, Y.-L., & Zhou, Y.-F. (2013). Sommerfeld enhancements with vector, scalar and pseudoscalar force-carriers. *Phys. Rev.*, D88, 096008.

[320] Loeb, A. & Weiner, N. (2011). Cores in Dwarf Galaxies from Dark Matter with a Yukawa Potential. *Phys. Rev. Lett.*, 106, 171302.

[321] Lopez Honorez, L., Tytgat, M. H. G., Tziveloglou, P., & Zaldivar, B. (2018). On Minimal Dark Matter coupled to the Higgs. *JHEP*, 04, 011.

[322] Macias, O., Gordon, C., Crocker, R. M., Coleman, B., Paterson, D., Horiuchi, S., & Pohl, M. (2018). Galactic bulge preferred over dark matter for the Galactic centre gamma-ray excess. *Nature Astron.*, 2(5), 387–392.

[323] Macias, O., Horiuchi, S., Kaplinghat, M., Gordon, C., Crocker, R. M., & Nataf, D. M. (2019). Strong Evidence that the Galactic Bulge is Shining in Gamma Rays. *JCAP*, 09, 042.

[324] Magill, G., Plestid, R., Pospelov, M., & Tsai, Y.-D. (2019). Millicharged particles in neutrino experiments. *Phys. Rev. Lett.*, 122(7), 071801.

[325] Mahbubani, R. & Senatore, L. (2006). The Minimal model for dark matter and unification. *Phys. Rev.*, D73, 043510.

[326] Maksymyk, I., Burgess, C. P., & London, D. (1994). Beyond S, T and U. *Phys. Rev. D*, 50, 529–535.

[327] Markevitch, M., Gonzalez, A. H., David, L., Vikhlinin, A., Murray, S., Forman, W., Jones, C., & Tucker, W. (2002). A Textbook example of a bow shock in the merging galaxy cluster 1E0657-56. *Astrophys. J. Lett.*, 567, L27.

[328] McKeen, D., Pospelov, M., & Ritz, A. (2013). Electric dipole moment signatures of PeV-scale superpartners. *Phys. Rev.*, D87(11), 113002.

[329] Mishra-Sharma, S. & Cranmer, K. (2020). Semi-parametric γ-ray modeling with Gaussian processes and variational inference.

[330] Moody, J. E. & Wilczek, F. (1984). New Macroscopic Forces? *Phys. Rev.*, D30, 130.

[331] Moore, B. (1994). Evidence against dissipationless dark matter from observations of galaxy haloes. *Nature*, 370, 629.

[332] Moore, B., Ghigna, S., Governato, F., Lake, G., Quinn, T. R., Stadel, J., & Tozzi, P. (1999). Dark matter substructure within galactic halos. *Astrophys. J.*, 524, L19–L22.

[333] Mount, B. J. et al. (2017). LUX-ZEPLIN (LZ) Technical Design Report.

[334] Nagata, N. & Shirai, S. (2015). Higgsino Dark Matter in High-Scale Supersymmetry. *JHEP*, 01, 029.

[335] Naghdi, M. (2014). Nucleon-nucleon interaction: A typical/concise review. *Phys. Part. Nucl.*, 45, 924–971.

[336] Nakai, Y. & Reece, M. (2017). Electric Dipole Moments in Natural Supersymmetry. *JHEP*, 08, 031.

[337] Ng, D. & Ng, J. N. (1996). A Note on Majorana neutrinos, leptonic CKM and electron electric dipole moment. *Mod. Phys. Lett.*, A11, 211–216.

[338] Nilles, H. P. & Vaudrevange, P. K. S. (2015). Geography of Fields in Extra Dimensions: String Theory Lessons for Particle Physics. *Mod. Phys. Lett. A*, 30(10), 1530008.

[339] Nir, Y. & Rattazzi, R. (1996). Solving the supersymmetric CP problem with Abelian horizontal symmetries. *Phys. Lett.*, B382, 363–368.

[340] Nussinov, S. (1985). Technocosmology: Could a technibaryon excess provide a 'natural' missing mass candidate? *Phys. Lett.*, 165B, 55–58.

[341] Oman, K. A. et al. (2015). The unexpected diversity of dwarf galaxy rotation curves. *Mon. Not. Roy. Astron. Soc.*, 452(4), 3650–3665.

[342] Ong, R. A. et al. (2018). The GAPS Experiment to Search for Dark Matter using Low-energy Antimatter. *PoS*, ICRC2017, 914. [35,914(2017)].

[343] Pais, A. & Primack, J. R. (1973). Cp violation and electric dipole moments in gauge theories of weak interactions. *Phys. Rev.*, D8, 3063–3074.

[344] Palti, E. (2019). The Swampland: Introduction and Review. *Fortsch. Phys.*, 67(6), 1900037.

[345] Panico, G., Riembau, M., & Vantalon, T. (2018). Probing light top partners with CP violation. *JHEP*, 06, 056.

[346] Pardo Vega, J. & Villadoro, G. (2015). SusyHD: Higgs mass Determination in Supersymmetry. *JHEP*, 07, 159.

[347] Peskin, M. E. & Schroeder, D. V. (1995). *An Introduction to Quantum Field Theory*. Reading, USA: Addison-Wesley.

[348] Peskin, M. E. & Takeuchi, T. (1990). A New constraint on a strongly interacting Higgs sector. *Phys. Rev. Lett.*, 65, 964–967.

[349] Peskin, M. E. & Takeuchi, T. (1992). Estimation of oblique electroweak corrections. *Phys. Rev. D*, 46, 381–409.

[350] Polchinski, J. (2007). *String theory. Vol. 2: Superstring theory and beyond*. Cambridge Monographs on Mathematical Physics. Cambridge University Press.

[351] Polchinski, J. & Wise, M. B. (1983). The Electric Dipole Moment of the Neutron in Low-Energy Supergravity. *Phys. Lett.*, 125B, 393–398.

[352] Porod, W. (2003). SPheno, a program for calculating supersymmetric spectra, SUSY particle decays and SUSY particle production at e+ e- colliders. *Comput. Phys. Commun.*, 153, 275–315.

[353] Porod, W. & Staub, F. (2012). SPheno 3.1: Extensions including flavour, CP-phases and models beyond the MSSM. *Comput. Phys. Commun.*, 183, 2458–2469.

[354] Pospelov, M. & Ritz, A. (2005). Electric dipole moments as probes of new physics. *Annals Phys.*, 318, 119–169.

[355] Pospelov, M. & Ritz, A. (2014). CKM benchmarks for electron electric dipole moment experiments. *Phys. Rev.*, D89(5), 056006.

[356] Pospelov, M. E. & Khriplovich, I. B. (1991). Electric dipole moment of the W boson and the electron in the Kobayashi-Maskawa model. *Sov. J. Nucl. Phys.*, 53, 638–640. [Yad. Fiz.53,1030(1991)].

[357] Prinz, A. A. et al. (1998). Search for millicharged particles at SLAC. *Phys. Rev. Lett.*, 81, 1175–1178.

[358] Åkesson, T. et al. (2018a). *Dark Sector Physics with a Primary Electron Beam Facility at CERN*. Technical Report CERN-SPSC-2018-023. SPSC-EOI-018, CERN, Geneva.

[359] Åkesson, T. et al. (2018b). Light Dark Matter eXperiment (LDMX).

[360] Randall, L. & Sundrum, R. (1999). Out of this world supersymmetry breaking. *Nucl. Phys.*, B557, 79–118.

[361] Raubenheimer, T., Beukers, A., Fry, A., Hast, C., Markiewicz, T., Nosochkov, Y., Phinney, N., Schuster, P., & Toro, N. (2018). DASEL: Dark Sector Experiments at LCLS-II.

[362] Read, J. I., Walker, M. G., & Steger, P. (2018). Dark matter heats up in dwarf galaxies. *Mon. Not. Roy. Astron. Soc.*

[363] Rubin, V. C. & Ford, Jr., W. K. (1970). Rotation of the Andromeda Nebula from a Spectroscopic Survey of Emission Regions. *Astrophys. J.*, 159, 379–403.

[364] Rubin, V. C., Thonnard, N., & Ford, Jr., W. K. (1980). Rotational properties of 21 SC galaxies with a large range of luminosities and radii, from NGC 4605 /R = 4kpc/ to UGC 2885 /R = 122 kpc/. *Astrophys. J.*, 238, 471.

[365] Safronova, M. S., Budker, D., DeMille, D., Kimball, D. F. J., Derevianko, A., & Clark, C. W. (2018). Search for New Physics with Atoms and Molecules. *Rev. Mod. Phys.*, 90(2), 025008.

[366] Sawala, T. et al. (2016). The APOSTLE simulations: solutions to the Local Group's cosmic puzzles. *Mon. Not. Roy. Astron. Soc.*, 457(2), 1931–1943.

[367] Schael, S. et al. (2006). Precision electroweak measurements on the Z resonance. *Phys. Rept.*, 427, 257–454.

[368] Scherrer, R. J. & Turner, M. S. (1986). On the Relic, Cosmic Abundance of Stable Weakly Interacting Massive Particles. *Phys. Rev. D*, 33, 1585. [Erratum: Phys.Rev.D 34, 3263 (1986)].

[369] Segarra, A. & Bernabéu, J. (2020). Absolute neutrino mass and the Dirac/Majorana distinction from the weak interaction of aggregate matter. *Phys. Rev. D*, 101(9), 093004.

[370] Siegel, C. L. (1964). *Symplectic Geometry*. New York: Academic Press.

[371] Sirunyan, A. M. et al. (2019). Measurements of the Higgs boson width and anomalous HVV couplings from on-shell and off-shell production in the four-lepton final state. *Phys. Rev. D*, 99(11), 112003.

[372] Skands, P. Z., Allanach, B., Baer, H., Balazs, C., Belanger, G., et al. (2004). SUSY Les Houches accord: Interfacing SUSY spectrum calculators, decay packages, and event generators. *JHEP*, 0407, 036.

[373] Sommerfeld, A. (1931). Über die beugung und bremsung der elektronen. *Annalen der Physik*, 403(3), 257–330.

[374] Spergel, D. N. & Steinhardt, P. J. (2000). Observational evidence for selfinteracting cold dark matter. *Phys. Rev. Lett.*, 84, 3760–3763.

[375] Srednicki, M., Watkins, R., & Olive, K. A. (1988). Calculations of Relic Densities in the Early Universe. *Nucl. Phys. B*, 310, 693.

[376] Stadnik, Y. V. (2018). Probing Long-Range Neutrino-Mediated Forces with Atomic and Nuclear Spectroscopy. *Phys. Rev. Lett.*, 120(22), 223202.

[377] Staub, F. (2008). SARAH.

[378] Staub, F. (2014). SARAH 4 : A tool for (not only SUSY) model builders. *Comput. Phys. Commun.*, 185, 1773–1790.

[379] Staub, F. (2015). Exploring new models in all detail with SARAH. *Adv. High Energy Phys.*, 2015, 840780.

[380] Steigman, G. (1979). Cosmology Confronts Particle Physics. *Ann. Rev. Nucl. Part. Sci.*, 29, 313–338.

[381] Steigman, G., Dasgupta, B., & Beacom, J. F. (2012). Precise Relic WIMP Abundance and its Impact on Searches for Dark Matter Annihilation. *Phys. Rev. D*, 86, 023506.

[382] Steinhauser, M. (1998). Leptonic contribution to the effective electromagnetic coupling constant up to three loops. *Phys. Lett. B*, 429, 158–161.

[383] Tulin, S. & Yu, H.-B. (2018). Dark Matter Self-interactions and Small Scale Structure. *Phys. Rept.*, 730, 1–57.

[384] Tulin, S., Yu, H.-B., & Zurek, K. M. (2013). Beyond Collisionless Dark Matter: Particle Physics Dynamics for Dark Matter Halo Structure. *Phys. Rev. D*, 87(11), 115007.

[385] Vinyoles, N. & Vogel, H. (2016). Minicharged Particles from the Sun: A Cutting-Edge Bound. *JCAP*, 03, 002.

[386] Vissani, F. (1998). Do experiments suggest a hierarchy problem? *Phys. Rev.*, D57, 7027–7030.

[387] Vitale, V. & Morselli, A. (2009). Indirect Search for Dark Matter from the center of the Milky Way with the Fermi-Large Area Telescope. In *Fermi gamma-ray space telescope. Proceedings, 2nd Fermi Symposium, Washington, USA, November 2-5, 2009*.

[388] Vogel, H. & Redondo, J. (2014). Dark Radiation constraints on minicharged particles in models with a hidden photon. *JCAP*, 02, 029.

[389] Vogelsberger, M., Zavala, J., Cyr-Racine, F.-Y., Pfrommer, C., Bringmann, T., & Sigurdson, K. (2016). ETHOS – an effective theory of structure formation: dark matter physics as a possible explanation of the small-scale CDM problems. *Mon. Not. Roy. Astron. Soc.*, 460(2), 1399–1416.

[390] Vutha, A. C., Horbatsch, M., & Hessels, E. A. (2018). Oriented polar molecules in a solid inert-gas matrix: a proposed method for measuring the electric dipole moment of the electron. *Atoms*, 6, 3.

[391] Weinberg, S. (1989). Larger Higgs Exchange Terms in the Neutron Electric Dipole Moment. *Phys. Rev. Lett.*, 63, 2333.

[392] Weinberg, S. (2005). *The Quantum theory of fields. Vol. 1: Foundations*. Cambridge University Press.

[393] Wells, J. D. & Zhang, Z. (2016). Effective theories of universal theories. *JHEP*, 01, 123.

[394] Wolfram, S. (1979). Abundances of Stable Particles Produced in the Early Universe. *Phys. Lett. B*, 82, 65–68.

[395] Yamanaka, N. (2013). Two-loop level rainbowlike supersymmetric contribution to the fermion electric dipole moment. *Phys. Rev.*, D87(1), 011701.

[396] Zeldovich, Y. (1965). *Survey of Modern Cosmology*, volume 3, (pp. 241–379).

[397] Zhong, Y.-M., McDermott, S. D., Cholis, I., & Fox, P. J. (2020). A New Mask for An Old Suspect: Testing the Sensitivity of the Galactic Center Excess to the Point Source Mask. *Phys. Rev. Lett.*, 124(23), 231103.

[398] Zurek, K. M. (2014). Asymmetric Dark Matter: Theories, Signatures, and Constraints. *Phys. Rept.*, 537, 91–121.

[399] Zyla, P. et al. (2020a). Review of Particle Physics. *Progress of Theoretical and Experimental Physics*, 2020(8). 083C01.

[400] Zyla, P. et al. (2020b). Review of Particle Physics. *PTEP*, 2020(8), 083C01. and 2021 update.